

# **Interference Modelling for Indoor Wireless Systems using the Finite-Difference Time-Domain Method**

*A thesis submitted to The University of Auckland, New Zealand, in fulfilment of the requirements for the degree of Doctor of Philosophy in Electrical and Electronic Engineering.*

Andrew Charles Mallory Austin

June 2011



# Abstract

The performance of modern wireless systems within buildings is primarily limited by interference from other users and other systems operating in close physical proximity. In order to estimate system performance in the presence of interference, *reliable* models to predict signal strengths (and other channel parameters) are required. Currently, empirical models based on experimental measurements are widely used. However, these models inherently lack an electromagnetic or physical basis and can vary considerably between buildings. Indoor environments can be very complex, and improved accuracy and a more thorough understanding of how the radio waves propagate may be gained through an electromagnetic approach. However, the high computational costs of fully-electromagnetic techniques, such as the Finite-Difference Time-Domain (FDTD) method, limits their applicability for day-to-day system planning purposes at this stage.

The research presented in this thesis describes a series of FDTD investigations of the indoor radio channel, using two- and three-dimensional geometries, with the aim of identifying the dominant mechanisms governing propagation within buildings. Mechanistic models are proposed by developing computationally efficient approximations for each mechanism. The complexity of the propagation processes can make conclusive identification of the mechanisms difficult, however various visualisation techniques developed in this thesis can be used to infer the dominant propagation paths. Central to the development of mechanistic models is a thorough assessment of the limitations of the FDTD method to model propagation within buildings, particularly the use of two-dimensional representations of the geometry, the impact of furniture and other details, and comparisons with experimental measurements.



# Acknowledgments

First and foremost I wish to thank my supervisors, Michael Neve and Gerard Rowe, for their contributions and discussions over the past four years. Their guidance in all aspects of this journey has been invaluable.

I also wish to acknowledge:

- The NZ Tertiary Education Commission for awarding me a scholarship;
- Professor Durgin and Dr Pirkle for hosting me in Atlanta and for their assistance in making experimental measurements;
- Ying Yang for sharing her measurement data;
- Dr Eva Lai for her many useful and thought-provoking discussions and comments;
- Ramin, Salim, Hazim, Rav and Claudio for their friendship, advice and approximately  $10^3$  ‘tea-breaks’;
- Other members from the Telecommunications and Electromagnetics Group who have provided constructive criticism;
- Members of the technical staff, especially R. Henry, E. Lo, G. Smith, J. Walker, P. Wigan and W.-L. Yeung who have provided assistance; and
- N. Smith and Y. Halytskyy from the Centre for eResearch at The University of Auckland for helping set up my simulations on the BeSTGRID Cluster.

Finally, I would like to thank my family for their never ceasing support and encouragement.

Andrew Austin  
June 2011



# Glossary

## Acronyms

BER	Bit Error Rate
CDF	Cumulative Distribution Function
CDMA	Code Division Multiple Access
CIR	Carrier-to-Interference Ratio
FAF	Floor Attenuation Factor
FDTD	Finite-Difference Time-Domain
FSS	Frequency Selective Surface
GO	Geometrical Optics
ISM	Industrial, Scientific and Medical
ITU	International Telecommunications Union
LOS	Line-of-Sight
MRTD	Multi-Resolution Time-Domain
OFDM	Orthogonal Frequency Division Multiplexing
PRBS	Pseudo-Random Binary Sequence
PSTD	Pseudo-Spectral Time-Domain
RMS	Root Mean Square
SIR	Signal-to-Interference Ratio
$\text{TE}_z$	Transverse Electric
$\text{TM}_z$	Transverse Magnetic
U-NII	Unlicensed National Information Infrastructure
UHF	Ultra-High Frequency
UPML	Uniaxial Perfectly Matched Layer
UTD	Uniform Theory of Diffraction
WLAN	Wireless Local Area Network

## Symbols

$A_0$	calibration constant between FDTD and GO field values
$c_0$	speed of light in a vacuum ( $299,792,458 \text{ ms}^{-1}$ )
$d_0$	reference distance
$d$	distance
$D$	diffraction coefficient
$D$	mean excess delay
$\text{erfc}(\cdot)$	complementary error function

<b>E</b>	vector electric field
$E$	electric field component
$f$	frequency
$h$	height
<b>H</b>	vector magnetic field
$H$	magnetic field component
$I_0(\cdot)$	zero order Bessel function
$j$	$\sqrt{-1}$
$k$	wave-number
$K$	Rician K-factor
$L$	generalised loss
$L$	transmitter-receiver separation distance
$n$	distance-dependency exponent
$\vec{p}(\cdot)$	position
$P_{\text{out}}$	outage probability
$P_r$	received power
$P_t$	transmitted power
$PL$	path-loss
$P_h(\tau)$	power-delay-profile
$r$	radial distance from source
$S$	delay spread
<b>S</b>	Poynting vector
$t$	time
$t_0$	pulse lead-in time
$t_w$	pulse width
$T$	floor thickness
$U(\cdot)$	unit step function
$\Delta$	lattice cell dimensions
$\Delta t$	time-step
$\epsilon_0$	permittivity of free-space ( $8.854187 \times 10^{-12}$ F/m)
$\epsilon_r$	relative permittivity
$\eta_0$	impedance of free-space ( $376.73031$ $\Omega$ )
$\theta$	azimuth angle
$\lambda$	wavelength
$\mu_0$	permeability of free-space ( $4\pi \times 10^{-7}$ H/m)
$\mu_r$	relative permeability
$\pi$	3.1415926
$\rho$	correlation coefficient
$\sigma^2$	mean power
$\sigma_{\text{E}}$	electric conductivity
$\sigma_{\text{M}}$	magnetic loss
$\tau$	time-delay
$\phi$	elevation angle
$\phi$	diffraction angle
$\phi'$	incident angle
$\omega$	angular frequency

# Contents

<b>1</b>	<b>Introduction</b>	<b>1</b>
<b>2</b>	<b>Indoor Wireless Systems: Propagation and Interference</b>	<b>7</b>
2.1	Introduction . . . . .	7
2.2	Propagation within Buildings . . . . .	7
2.2.1	The Indoor Environment . . . . .	7
2.2.2	Variation in the Received Signal with Distance . . . . .	9
2.2.3	Multi-Path Fading . . . . .	11
2.2.4	The Channel Impulse Response . . . . .	11
2.3	System Performance Estimation . . . . .	13
2.3.1	Co-Channel Interference . . . . .	13
2.3.2	Wireless Networks . . . . .	13
2.3.3	Inter-Floor Interference . . . . .	14
2.4	Interference Mitigation . . . . .	15
2.4.1	Deployment Strategies . . . . .	15
2.4.2	Frequency Selective Surfaces and Metal Shielding . . . . .	15
2.5	Summary . . . . .	16
<b>3</b>	<b>Mechanistic Propagation Modelling</b>	<b>17</b>
3.1	Introduction . . . . .	17
3.2	Empirical Models . . . . .	17
3.2.1	Path-Loss Prediction . . . . .	17
3.2.2	Discussion . . . . .	20
3.3	Deterministic Models . . . . .	20
3.3.1	Analytical Methods . . . . .	21
3.3.2	Ray-Optical Methods . . . . .	21
3.3.3	Time-Domain Methods . . . . .	22
3.3.4	Other Deterministic Methods . . . . .	24
3.4	Mechanistic Modelling . . . . .	25
3.5	Contributions of this Thesis . . . . .	26
3.6	Summary . . . . .	26
<b>4</b>	<b>The Finite Difference Time Domain Method</b>	<b>27</b>
4.1	Introduction . . . . .	27
4.2	The Finite-Difference Time-Domain Method . . . . .	28
4.2.1	Maxwell's Equations in Three Dimensions . . . . .	28
4.2.2	Reduction to Two Dimensions . . . . .	29

4.2.3	The Yee Algorithm . . . . .	29
4.2.4	Dispersion and Stability . . . . .	31
4.2.5	Lattice Excitation . . . . .	32
4.3	Boundary Conditions . . . . .	32
4.3.1	The Perfectly Matched Layer . . . . .	33
4.3.2	UPML Performance . . . . .	34
4.4	Parallel Implementation of the FDTD Method . . . . .	34
4.4.1	Computational Requirements . . . . .	34
4.4.2	High Performance Computing . . . . .	35
4.4.3	Field Exchange . . . . .	36
4.4.4	Parallel Efficiency . . . . .	37
4.5	Validation of the Codes . . . . .	37
4.5.1	2D and 3D Distance Dependency . . . . .	38
4.5.2	3D Radiation Pattern . . . . .	38
4.5.3	Diffraction by a Single PEC Knife Edge . . . . .	38
4.6	Summary . . . . .	38
<b>5</b>	<b>Indoor Propagation Modelling with the FDTD Method</b>	<b>41</b>
5.1	Introduction . . . . .	41
5.2	Propagation Modelling with the FDTD Method . . . . .	41
5.2.1	Field Magnitude and Phase . . . . .	41
5.2.2	Path-Loss . . . . .	42
5.2.3	Impulse Response . . . . .	42
5.3	Visualising Propagation . . . . .	43
5.3.1	Phase Plots . . . . .	43
5.3.2	Poynting Vectors . . . . .	43
5.3.3	Streamline Visualisations of the Poynting Vector . . . . .	44
5.3.4	Propagation Through an Infinite Lossy Dielectric Slab . . . . .	45
5.4	Material Modelling . . . . .	46
5.5	Interference Modelling and Mitigation . . . . .	46
5.5.1	Propagation Study A—Within the Building Perimeter (2D) . . . . .	47
5.5.2	Propagation Study B—External to the Building Perimeter (2D) . . . . .	48
5.5.3	Propagation Study C—Within the Building Perimeter (3D) . . . . .	49
5.5.4	Interference Prediction and Mitigation . . . . .	49
5.6	Summary . . . . .	50
<b>6</b>	<b>Propagation Study A: Within the Building Perimeter (2D)</b>	<b>51</b>
6.1	Introduction . . . . .	51
6.2	Inter-Floor Propagation . . . . .	51
6.2.1	FDTD Analysis . . . . .	52
6.2.2	Propagation Paths . . . . .	53
6.2.3	Path-Loss versus Distance . . . . .	57
6.2.4	Floor Thickness, Concrete Conductivity and Frequency . . . . .	57
6.3	Detailed Models . . . . .	60
6.4	Propagation through Internal Shafts . . . . .	61
6.5	Mechanistic Models and Experimental Validation . . . . .	64
6.5.1	Ray-Based Models . . . . .	64

6.5.2	Experimental Comparison . . . . .	65
6.6	Discussion . . . . .	66
6.7	Summary . . . . .	68
<b>7</b>	<b>Propagation Study B: External to the Building Perimeter (2D)</b>	<b>69</b>
7.1	Introduction . . . . .	69
7.2	FDTD Analysis . . . . .	69
7.2.1	External Propagation Paths . . . . .	69
7.2.2	Description of the Environment Investigated . . . . .	70
7.2.3	Simulation Configuration . . . . .	70
7.3	Narrowband Results . . . . .	71
7.4	Wideband Results . . . . .	75
7.5	Development of a Mechanistic Model . . . . .	79
7.6	Experimental Validation . . . . .	80
7.6.1	Narrow-band Comparison . . . . .	80
7.6.2	Wide-band Comparison . . . . .	80
7.7	Discussion . . . . .	85
7.8	Summary . . . . .	86
<b>8</b>	<b>Propagation Study C: Within the Building Perimeter (3D)</b>	<b>87</b>
8.1	Introduction . . . . .	87
8.2	Description of the Environment Investigated . . . . .	88
8.3	Propagation on the Same Floor . . . . .	88
8.3.1	The Effects of Clutter . . . . .	88
8.3.2	Propagation in Corridors . . . . .	92
8.4	Propagation to Adjacent Floors . . . . .	93
8.5	Comparisons with Experimental Measurements . . . . .	93
8.5.1	Qualitative Comparisons . . . . .	96
8.5.2	Direct Comparisons . . . . .	96
8.6	Path-Loss Prediction Models . . . . .	99
8.6.1	Path-Loss versus Distance . . . . .	99
8.6.2	Distance-Dependency Models . . . . .	99
8.7	Fading Distributions . . . . .	102
8.8	Summary . . . . .	104
<b>9</b>	<b>System Performance Estimation for Indoor Wireless Systems with the FDTD Method</b>	<b>105</b>
9.1	Introduction . . . . .	105
9.2	Modelling Interference for Indoor Wireless Systems . . . . .	106
9.2.1	Interference Within Buildings . . . . .	106
9.2.2	FDTD Propagation Analysis . . . . .	106
9.2.3	Carrier-to-Interference Ratio . . . . .	107
9.2.4	Outage Probability . . . . .	107
9.3	Deployment Strategies (2D) . . . . .	109
9.3.1	Isolated Building . . . . .	109
9.3.2	Propagation through Internal Shafts . . . . .	112
9.4	Deployment Strategies (3D) . . . . .	114

9.4.1	Staggered and Aligned Base-Stations . . . . .	114
9.4.2	Comparisons with Experimental Measurements . . . . .	117
9.5	Interference Mitigation . . . . .	117
9.6	Correlated Shadowing . . . . .	120
9.7	Consequences for System Planning . . . . .	123
9.8	Summary . . . . .	123
<b>10</b>	<b>Discussion and Recommendations for Future Investigation</b>	<b>125</b>
10.1	Introduction . . . . .	125
10.2	Mechanistic Propagation Models . . . . .	125
10.2.1	Overview . . . . .	125
10.2.2	Propagation Studies—Summary . . . . .	126
10.2.3	Assumptions and Applicability . . . . .	127
10.3	Recommendations for Future Investigation . . . . .	128
10.3.1	Refinement of the Mechanistic Models . . . . .	128
10.3.2	Reducing Computational Requirements . . . . .	129
10.3.3	Modelling Propagation in the Presence of Clutter . . . . .	131
10.4	Summary . . . . .	132
<b>11</b>	<b>Conclusions</b>	<b>133</b>
<b>A</b>	<b>FDTD Update Equations</b>	<b>135</b>
<b>B</b>	<b>The Uniaxial Perfectly Matched Layer</b>	<b>137</b>
B.1	Derivation of the Update Equations . . . . .	137
B.2	UPML Update Equations . . . . .	139
<b>C</b>	<b>Free-Space Calibration</b>	<b>141</b>
C.1	Two-Dimensions . . . . .	141
C.2	Three-Dimensions . . . . .	141
<b>D</b>	<b>Including Details in the Propagation Environment</b>	<b>143</b>
D.1	Reinforcing Bars . . . . .	143
D.2	Hanging Panels . . . . .	143
<b>E</b>	<b>2.5D Field Expansion</b>	<b>147</b>
<b>F</b>	<b>Localised Effects of Clutter</b>	<b>149</b>
<b>G</b>	<b>Inter-floor Propagation: Basic Geometry</b>	<b>151</b>
<b>H</b>	<b>Path-Loss versus Distance</b>	<b>153</b>
<b>I</b>	<b>Monte Carlo Sensitivity Analysis—2D Feasibility Study</b>	<b>155</b>
<b>References</b>		<b>158</b>

# Chapter 1

## Introduction

The incessant demand for information has been (and remains) the driving force behind the development of reliable methods to communicate over long distances. Early technological advances, such as Cooke and Wheatstone's electric telegraph in 1837 [1, pp. 59–60], helped extend the range (and speed) information could reach; and by the end of the 19th century communication networks—in the form of terrestrial and undersea telegraphic cables—connected continents and spanned the globe. However, in the year before the first trans-Pacific cable was completed (1902)—connecting Australia and New Zealand with the United States—Marconi demonstrated the use of radio waves to transmit messages across the Atlantic ocean [1, p. 94]. Further 'demonstration' experiments, communicating to mobile receivers such as ships, aircraft and automobiles, confirmed the potential capabilities of radio and sparked the commercial interest that remains to this day.

Although the first (civilian) land-mobile radio communication systems were installed in the 1920s—initially for police departments in the United States—these were usually not available to the general public<sup>1</sup> [2, pp. 2–3]. Furthermore, these early systems could only support an extremely limited number of users over relatively small geographic areas, and lacked connectivity to other networks. The public interest in radio communications, coupled with technologies developed for the early systems (including frequency modulation and superheterodyne receivers) and advancements in manufacturing, led to the deployment of the first commercial mobile radio-telephone system in 1946 [1, p. 144]. This system operated at 152 MHz, and as a single transmitter was used to cover an entire metropolitan area, capacity was extremely limited [3, p. 3]. Despite the major technological advances, mobile radio systems did not improve significantly over the next 30 years, e.g. in 1976 the Bell Mobile Phone system for New York City could only support 543 users (demand remained high, with over 3700 people on the waiting list at that time) [2, p. 4]. The ability to provide wireless connectivity to the entire population was not possible until Bell Laboratories developed and refined the cellular concept in the 1960s and 1970s, although the first cellular systems were not installed until the 1980s [2, pp. 4–6]. Cellular systems divide the coverage area into a series of smaller regions (termed cells); and by reusing frequencies—in non-adjacent cells to reduce interference—a greater number of users can be supported with the same bandwidth. The cell size depends on the user density as typically each cell can only service a fixed number of users [4, pp. 16–19]. The first 'generation' of cellular systems—such as the Advanced Mobile Phone System (AMPS) in the United States, or the

---

<sup>1</sup>In the United States the allocation of radio frequencies was controlled by the Department of Commerce; and from 1934 by the Federal Communications Commission (FCC).

Nordic Mobile Telephone (NMT) system in Scandinavia—were based on analogue technology, and operated in the lower UHF bands (typically 450 or 800 MHz) [3, p. 12]. Despite their size (in comparison to the mobile phones of today) cellular phones turned out to be extremely popular, and new systems and standards—often incompatible with each other—were introduced to improve spectral efficiency and better accommodate the near exponential demand. For example, second-generation digital cellular networks—such as Digital-AMPS and IS-95 in the USA, and GSM<sup>2</sup> in Europe—were introduced in the early 1990s, and although these systems still focused on voice transmission, packet data services were also supported [3, pp. 12–13]. In contrast, current third- and future fourth-generation cellular systems are largely focused on providing high-speed data connections, where voice traffic is treated as a data stream.

The optimal allocation of frequency channels—particularly in regions with high user density, such as urban/metropolitan areas and within buildings—remains a challenge for modern cellular systems. To improve capacity, the physical region covered by each cell can be reduced, accordingly lower power is required from the base-stations. Macro-cells are designed to provide outdoor coverage for rural, suburban and urban environments. A typical coverage area is between 1–10 km, and accordingly the antennas are usually mounted above the surrounding terrain and buildings [5, pp. 15–16]. To provide better coverage for users in urban environments, a large macro-cell can be split into several micro-cells. In this case the base-station typically provides coverage over a range of less than 1 km, and the antennas are usually mounted at street level [5, p. 18]. However, regions with high traffic density (e.g. train-stations and airports) are not well serviced by macro- or micro-cells. To extend coverage to these regions, pico-cells—typically with a maximum range between 20–200 m—can be deployed [5, pp. 30–33]. Achieving adequate coverage and reliable system performance within buildings with micro- and pico-cells is particularly challenging as, though the users are relatively stationary, the traffic density can be extremely high. Furthermore, because the transmitters are generally located outside, large penetration losses are often encountered when propagating a signal into a building. To improve cellular system performance within buildings, a further decrease in the cell size has been suggested. Femto-cells have a maximum range between 10–50 m and are designed to be located indoors to provide improved coverage within small buildings, or across several floors of larger buildings [5, pp. 33–35]. Femto-cells still operate in the licensed portions of the frequency spectrum; however, as the frequency reuse distances are generally smaller this leads to increased levels of co-channel interference.

The proliferation of cellular systems has been paralleled by the development of wireless computer networks operating in unlicensed portions of the spectrum. Wireless Local Area Networks (WLAN) are often deployed within buildings to provide wireless connectivity to existing networks or the internet [3, pp. 15–16]. The current generation of WLANs are based on the IEEE 802.11 ‘family’ of standards, and were originally introduced in the mid 1990s. Successive improvements—e.g. IEEE 802.11b (CDMA, 2.45 GHz), 802.11a (OFDM, 5.8 GHz), 802.11g (OFDM, 2.45 GHz) and 802.11n (OFDM/MIMO, 2.45 GHz)<sup>3</sup>—have seen a steady increase in performance, although in comparison to contemporary wired networking, the maximum data rates are still relatively low [3, pp. 15–16]. Moreover, systems operating in the unlicensed frequency bands are prone to interference from other systems and devices operating in close physical proximity.

---

<sup>2</sup>GSM was originally an acronym for Groupe Spécial Mobile; it now stands for Global System for Mobile Communications.

<sup>3</sup>Abbreviations—CDMA: code-division multiple-access; OFDM: orthogonal frequency-division multiplexing; MIMO: multiple-input multiple-output.

Buildings represent challenging environments for contemporary indoor wireless systems, and decisions made at the time of deployment remain critically important to overall success. In particular, achieving adequate coverage (for WLANs or femto-cells) is usually not an issue within buildings as the distances are considerably shorter. However, to support a high number of users, multiple base-stations are often required [6]. Frequency reuse introduces interference, which detrimentally affects the system performance, reducing the reliability, maximum transmission rates, and number of users that can be supported. Accurately predicting the effects of this interference depends heavily on correctly characterising radio-wave propagation within the environment. Numerous propagation studies have attempted to characterise the indoor radio channel statistically using experimental measurements [7, 8]. Unfortunately, not only are such measurements time consuming and expensive, they also have no analytical basis to explain the physical observations, and cannot therefore be transported to other environments without additional validation [6]. In contrast, deterministic characterisations of the indoor radio channel are based on the underlying electromagnetics, and accordingly, may provide more accurate and reliable results. Furthermore, a better understanding of the mechanisms governing radio-wave propagation within buildings can be used to improve the planning and deployment of existing (and future) systems.

To formulate deterministic models to characterise the indoor radio channel it is necessary to start from Maxwell's equations (formulated by James Clerk Maxwell in the 1860s). These equations characterise all macroscopic electromagnetic phenomena—including the propagation of radio-waves—by describing, in abstract form, the relationships between electric and magnetic fields. Maxwell's equations also provide a mathematical framework to explain the earlier experimental observations of Faraday, Ampere and Gauss [9, pp. 112–113]. However, analytical solutions to Maxwell's equations are difficult, if not impossible, to obtain for anything other than simple cases, due to boundary condition complexity [10, p. 2, 105–106]. Consequently, there is considerable interest in developing numerical solutions to Maxwell's equations and applying these techniques to new problems. The development and current success of numerical electromagnetic techniques has been strongly influenced by the growth in computing technology [11, pp. 3–6].

The primary focus of this thesis is the application of computational electromagnetic techniques to deterministically model radio-wave propagation within buildings and thereby predict interference. Grid-based numerical electromagnetic techniques, such as the Finite-Difference Time Domain (FDTD) method, are known to provide highly accurate results [11, pp. 6–16], but have not been widely applied to model indoor propagation due to their high computational requirements [12]. However, advances in computing technology—in particular, high performance computer clusters—are making their application to the indoor propagation problem tractable. It is important to note that the ability to numerically simulate propagation in electromagnetically large structures is not, in itself, sufficient for use in routine system planning. The key element is to use the understanding obtained via this exhaustive analysis to derive simpler *mechanistic* models which represent the dominant effects adequately—thereby guaranteeing prediction accuracy to within an acceptable limit—but have a low computational overhead and are thus suitable in routine system planning [13].

Chapter 2 reviews radio-wave propagation within buildings from a systems perspective focusing on typical propagation paths, the variation in the received signal with distance, and multi-path fading. The use of models—characterising aspects of the indoor radio channel—to predict interference arising from other users and systems, particularly those operating on adja-

cent (or nearly adjacent) floors, is discussed in some detail. A brief summary of methods and tools to mitigate indoor interference by reducing the strength of interfering signal paths is also presented.

With this background on propagation within buildings, the literature related to modelling the indoor radio channel is reviewed in chapter 3. Several widely used empirical models to predict the signal strengths are considered, followed by a discussion on the limitations of the empirical modelling approach. Deterministic models based on electromagnetic theory can potentially offer better predictions, but are often more difficult to apply. An alternative approach to characterising propagation within buildings (mechanistic modelling) is discussed, and the major contributions of this thesis are outlined.

Chapter 4 introduces the FDTD method and derives the update expressions from Maxwell's equations in two- and three-dimensions. Boundary conditions are also considered, as terminating the lattice is important for unbounded problems. One of the major limitations of the FDTD method is its computational requirements, which are often in excess of a single computer; chapter 4 therefore, also discusses the parallelisation of the FDTD algorithm for implementation on computer clusters. The results for several validation cases are presented and compared against analytical and other numerical solutions.

Having introduced the FDTD method, chapter 5 discuss how it can be applied to model propagation within buildings. In particular, this chapter treats the conversion of time-domain electromagnetic fields to quantities relevant for propagation prediction. Visualisation techniques to determine the dominant propagation paths are also analysed. Chapter 5 concludes by outlining the roadmap of propagation studies considered in this thesis to characterise the indoor radio channel, focusing in particular on inter-floor propagation paths.

The first propagation study is investigated in chapter 6, and considers propagation on a single two-dimensional vertical 'slice' through a multi-storey building. The dominant propagation paths are identified, and the resulting mechanistic models are compared against experimental measurements of the received power. Environmental details and clutter are often difficult to characterise on a two-dimensional slice, and consequently have largely been ignored from the propagation study examined in this chapter.

Chapter 7 extends the propagation geometry examined in chapter 6 to include possible reflection and scattering paths from nearby buildings. Due to computational limitations, this problem is examined in two-dimensions. The results are generalised to formulate appropriate mechanistic models, and these are compared against experimental measurements of the received power and the channel impulse response.

A three-dimensional investigation of the indoor radio channel with the FDTD method is presented in chapter 8, however, computational limitations restrict the analysis to three floors of a multi-storey building. The impact of including some internal details/clutter on the dominant propagation paths, received power and fading distributions have also been considered. Also examined in chapter 8 are direct comparisons between the FDTD simulation results and experimental measurements.

Chapter 9 presents a feasibility study focusing on the application of the FDTD method to directly estimate system performance in the presence of interfering signals. Various base-station deployment strategies are examined with two- and three-dimensional implementations of the FDTD method. Also considered in chapter 9 is the deployment of partial metal shielding to occlude interfering signal paths; the improvement in performance is quantified and compared with experimental measurements.

On the basis of results presented in chapters 6–9, the mechanistic modelling approach is reviewed from a system planning perspective, and recommendations for future investigation are presented in chapter 10. This discussion is followed by brief concluding remarks in chapter 11.



## Chapter 2

# Indoor Wireless Systems: Propagation and Interference

### 2.1 Introduction

Chapter 1 has provided a historical overview of wireless communication systems, starting with analogue outdoor mobile radio and finishing with contemporary multi-user digital wireless systems. The goal of this chapter is to extend this discussion and examine issues related to the deployment of modern wireless systems within buildings, in particular radio-wave propagation, and the problem of co-channel interference. Although many of the techniques developed to characterise the outdoor propagation environment can be readily applied within buildings, there are important distinctions to be considered, and these are also addressed in this chapter. This work is extended in chapter 3, which examines models to predict indoor radio-wave propagation and outlines the contributions of this thesis.

Section §2.2 examines how the indoor environment can influence the propagation of signals, specifically examining the variation in mean power with distance, statistical distributions to characterise multi-path fading, and the channel impulse response. Section §2.3 focuses on the performance of wireless systems in the presence of interference. Also addressed in section §2.3 is the problem of inter-floor interference (where two users are transmitting with the same frequency on different floors). Section §2.4 reviews the literature related to interference characterisation for indoor environments, in particular the use of experimental measurements to improve deployment strategies. Also examined in section §2.4 are techniques to reduce the power of interfering signals, such as the use of frequency selective surfaces and metal shielding. The major findings of the chapter are summarised in section §2.5.

### 2.2 Propagation within Buildings

#### 2.2.1 The Indoor Environment

Indoor wireless systems typically operate over shorter ranges than outdoor macro- and micro-cellular or broadcast systems. However, indoor environments are inherently three-dimensional in topology and arguably more cluttered. Furthermore, in most cases no line-of-sight path exists [2, p. 123]. As a result, large losses can be experienced over very short distances (e.g.

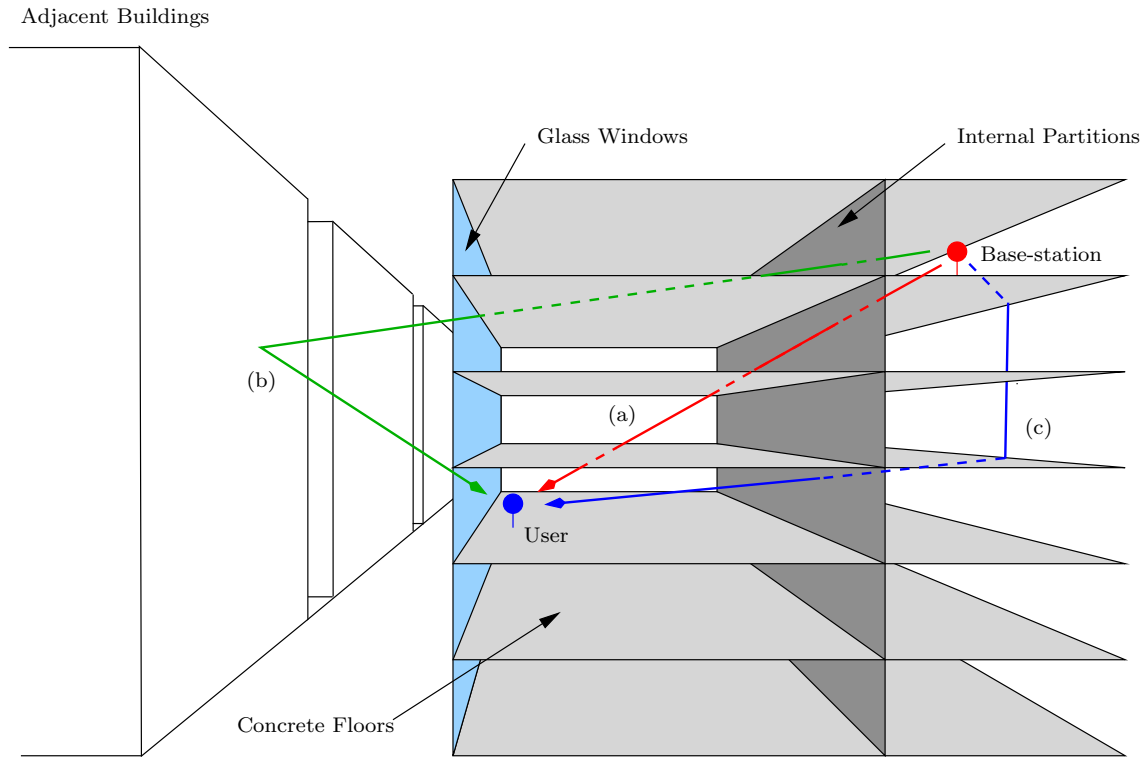


Figure 2.1: Generalised depiction of the indoor propagation environment showing some of the key physical features, and potential propagation paths.

propagation through thick concrete walls). A generalised depiction of the indoor propagation environment is shown in Fig. 2.1, which also indicates some of the physical features characterising most indoor environments, namely

1. Fixed access points/base-stations, typically mounted 1.0–3.0 m above the floor (on ceilings or walls);
2. Mobile users, typically operating 1.0–2.0 m above the floor;
3. Concrete walls and floors, drywall and timber internal partitions, and glass exterior windows;
4. Randomly positioned dielectric and metal clutter, e.g. office furniture, pipes, ducts and fittings;
5. People moving within the building; and
6. Propagation path lengths typically between 0–100 m<sup>1</sup>.

Also identified in Fig. 2.1 are several of the key propagation phenomena thought to be responsible for delivering power from the base-station to the users and vice-versa [14, pp. 195–199] [2, pp. 123–127], namely

- (a) Penetration through walls, floors and other obstacles;
- (b) Reflection from objects, including adjacent buildings; and

<sup>1</sup>This includes possible propagation paths external to the building perimeter.

- (c) Diffraction around objects, including walls and floors.

Other propagation mechanisms, such as wave-guiding in corridors have not been depicted, but may exist in some buildings [15, 16]. The combination of multiple propagation paths, and the significant levels of signal attenuation through objects, can lead to greater than free-space path-loss and significant spatial variations in the received power.

### 2.2.2 Variation in the Received Signal with Distance

Fig. 2.2 shows the variation in received signal with distance (at 1.0 GHz) for a hypothetical indoor environment. Objects in the environment tend to reflect, diffract and scatter the propagating radio-waves, and the phasor superposition of these multi-path components leads to rapid fluctuations in the received power over short distances ( $1\text{--}10\lambda$ ). This phenomena is termed *fading* [14, pp. 114–119] and the distance between successive fades is usually between 0.5–1.0 $\lambda$ , with fades typically 25 dB below the mean signal level.

The sector mean<sup>2</sup> is calculated by averaging the signal over  $5\lambda$  sectors<sup>3</sup>. As observed in Fig. 2.2(a) the sector mean decreases with distance from the transmitting antenna. In many environments the mean received power,  $P_r$ , is observed to vary with the transmitter-receiver separation distance  $d$ , according to a power-law [2, pp. 102–104], given by

$$P_r \propto \frac{1}{d^n}, \quad (2.1)$$

where  $n$  is the distance-dependency exponent. The physical environment is known to play a significant role in determining  $n$ , and Table 2.1 lists values of  $n$  observed in various scenarios. For indoor environments, the distance-dependency exponent is generally determined by the large scale geometry of the building [18].

Table 2.1: Distance-dependency exponent for various physical environments

Scenario	$n$
Free-space	2.0
Plane-earth <sup>a</sup>	2.0, $d < \frac{8h_r h_t}{\lambda}$ 4.0, $d > \frac{8h_r h_t}{\lambda}$
Diffraction over multiple knife edges [19]	3.9
Waveguide <sup>b</sup>	0.0

<sup>a</sup>Where  $h_t$  and  $h_r$  are the transmitter and receiver antenna heights respectively [2, pp. 85–90].

<sup>b</sup>In an ideal waveguide fields propagate as plane-waves. Waveguide-*like* behaviour can arise in urban canyons or long corridors, where values of  $n$  between 0–2 have been observed [15].

In outdoor environments electrically large objects, such as buildings or hills, can cast radio shadows over significant distances, causing fluctuations in the sector mean over the medium-range (50–100 m); this phenomena is termed shadowing. For indoor environments the range is typically less than 50 m, and it becomes difficult to separate shadowing from multi-path fading. Consequently, for the research presented in this thesis, shadowing (as a separate effect) is ignored.

<sup>2</sup>The sector mean is also referred to as the local mean [17].

<sup>3</sup>This averaging process is essentially a spatial smoothing filter. The filter needs to remove the deep nulls introduced by multi-path fading, but should not distort the medium-term variations in the fields.

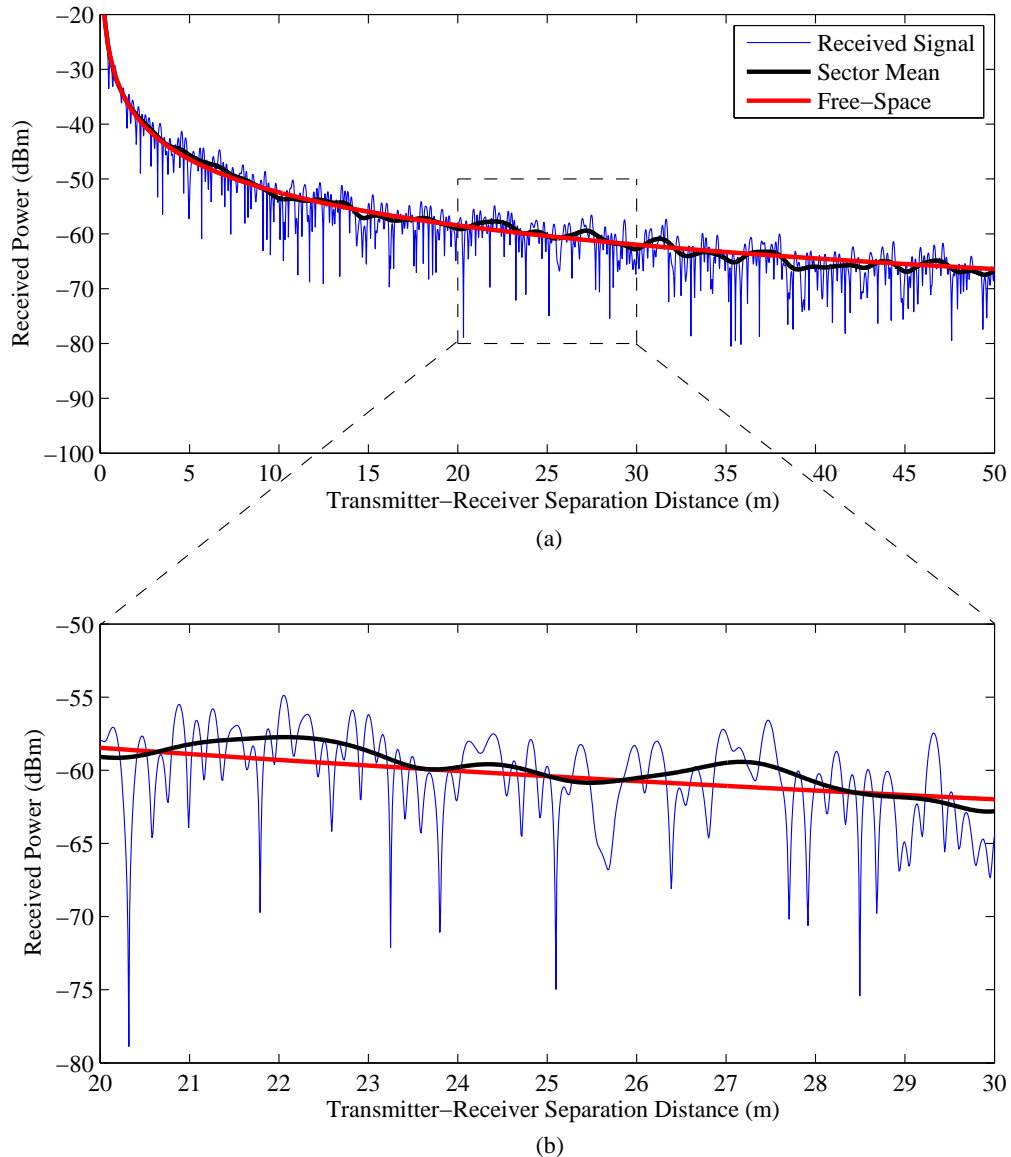


Figure 2.2: Received signal at 1.0 GHz (a) 0–50 m, and (b) 20–30 m from the transmitter for a hypothetical indoor environment. The  $5\lambda$  sector mean is shown in black and free-space (given by the Friis equation [2, p. 71]) in red (adapted from [20, p. 13]).

### 2.2.3 Multi-Path Fading

The complex multi-path phenomena causing fading can be difficult and impractical to analyse deterministically. However, the received signal envelope [14, pp. 125–127] often follows known statistical distributions, and Rayleigh and Rician distributions are frequently used to characterise multi-path fading for indoor environments [6, 21] [14, pp. 201–202]. When a specular component is stronger than the scattered components—for example, on a line-of-sight (LOS) path—the probability density function (PDF) of the signal envelope  $x(t)$ , follows a Rician distribution, given by

$$f(x) = \frac{x}{\sigma^2} \exp\left(\frac{-x^2 + s^2}{2\sigma^2}\right) I_0\left(\frac{xs}{\sigma^2}\right), \quad (2.2)$$

where  $s^2$  is the power of the dominant component,  $2\sigma^2$  is the mean scattered power, and  $I_0$  is the zero-th order Bessel function of the first kind. The Rician  $K$ -factor is defined as the ratio of specular power to scattered power,  $K = \frac{s^2}{2\sigma^2}$ , and can be determined from measurement data using [21]

$$\frac{\mathbb{E}[x]}{\mathbb{E}[x^2]} = \sqrt{\frac{\pi}{4(K+1)}} \exp\left(-\frac{K}{2}\right) \left[ (1+K)I_0\left(\frac{K}{2}\right) + KI_1\left(\frac{K}{2}\right) \right],$$

where  $\mathbb{E}[x^2]$  is the average square amplitude,  $\mathbb{E}[x]$  is the average amplitude, and  $I_m$  is the  $m$ -th order Bessel function of the first kind. In the case where no single component dominates ( $K = 0$ ), the PDF of the signal envelope follows a Rayleigh distribution, given by

$$f(x) = \frac{x}{\sigma^2} \exp\left(-\frac{x^2}{2\sigma^2}\right), \quad (2.3)$$

where  $\sigma^2$  is the mean power. For outdoor environments, shadowing is observed to follow a log-normal distribution, given by [14, p. 232]

$$f(x) = \frac{20}{x\sigma_v \log_e 10 \sqrt{2\pi}} \exp\left(-\frac{(20 \log_{10} x - m_v)^2}{2\sigma_v^2}\right), \quad (2.4)$$

where  $m_v$  and  $\sigma_v$  are the mean and standard deviation of the received signal in dB.

### 2.2.4 The Channel Impulse Response

The path lengths for each component in a multi-path environment are all slightly different, and as the speed of propagation is constant, each component arrives at the receiver with different delays. The impulse response of a radio channel provides a temporal characterisation of the multi-path environment, and can (sometimes) provide insight into the propagation mechanisms. As the radio channel can be modelled as a linear (time-varying) filter, the impulse response can also be used to predict and compare the performance of different wireless systems.

The impulse response can be measured in the time-domain directly by exciting the channel with a short-duration RF pulse, however this approach is sensitive to noise and interference and does not preserve the phase information [14, pp. 234–235]. Alternatively, by measuring the frequency response of the channel (via a frequency sweep on a vector network analyser), the impulse response can be calculated via an inverse Fourier transform. This approach preserves the phase information, but the system requires careful calibration and synchronisation, which limits the separation distance between the transmitting and receiving antennas [2, pp. 158–159].

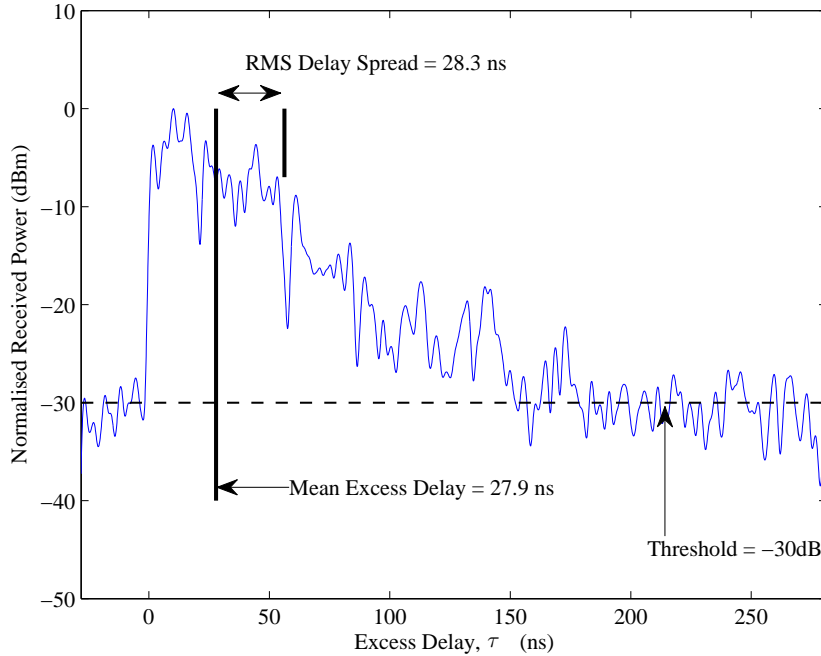


Figure 2.3: A power delay profile measured within a building using a sliding correlator channel sounder. Annotations show the mean excess delay, delay spread and threshold.

Another widely used method to measure the impulse response is the spread spectrum sliding correlator channel sounder, which exploits the auto-correlation property of pseudo-random binary sequences (PRBS)<sup>4</sup>. A PRBS is generated at a particular chip frequency, modulated and then transmitted. At the receiver, a locally generated PRBS<sup>5</sup>, is mixed with a local oscillator and then multiplied by the received signal. The resultant is then filtered to complete the correlation operation to produce an estimate of the channel impulse response [14, pp. 236–239].

The power delay profile is formed by aligning and averaging several impulse response measurements, and is usually normalised to the peak power and plotted against the excess delay,  $\tau$  (where  $\tau$  is measured from the first received echo). Fig. 2.3 shows an example of a power-delay profile measured inside a building using a sliding-correlator channel sounder—with centre frequency 4.5 GHz and 800 MHz 3 dB bandwidth—with several key parameters identified. The mean excess delay is the first central moment of the power delay profile,  $P_h(\tau)$ , given by [14, pp. 184–188]

$$D = \frac{\int_0^\infty \tau P_h(\tau) d\tau}{\int_0^\infty P_h(\tau) d\tau}, \quad (2.5)$$

and the delay spread is the second central moment of  $P_h(\tau)$ , given by [14, pp. 184–188]

$$S = \sqrt{\frac{\int_0^\infty (\tau - D)^2 P_h(\tau) d\tau}{\int_0^\infty P_h(\tau) d\tau}}. \quad (2.6)$$

<sup>4</sup>The auto-correlation of a PRBS has a peak at  $t = 0$  (when the sequences are aligned), and low values for all other shifts.

<sup>5</sup>The receiver-side PRBS is clocked slightly slower. The difference in clock frequencies causes the sequences to slide past each other.

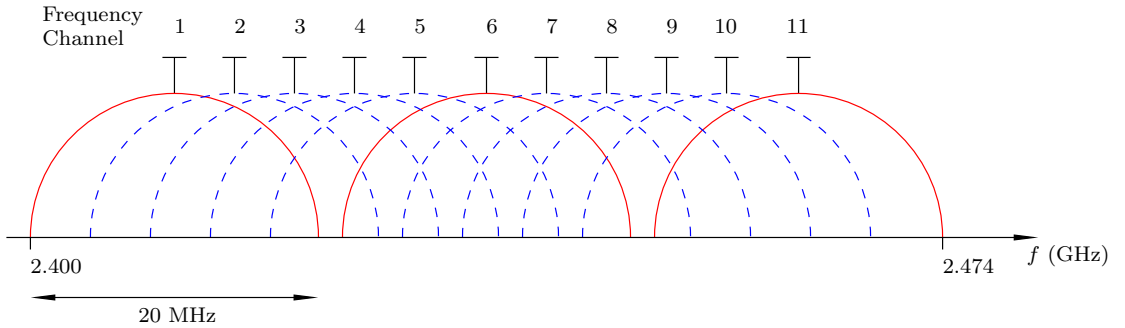


Figure 2.4: Graphical representation of the 2.4 GHz frequency channels in the 802.11 standard. Each channel can support multiple users by separating them via CDMA or OFDM (adapted from [23, pp. 679–680]). The three channels identified in red do not overlap in frequency, and hence do not interfere with each other.

A threshold of  $-30$  dB is also identified and represents the artificial noise floor introduced by the auto-correlation. The mean delay and delay spread give an indication of the multi-path environment, e.g. cluttered channels will tend to have a higher mean delay and delay spread. The delay spread can also affect the maximum bit-rates for a digital wireless system by causing inter-symbol interference (ISI). ISI occurs when energy from previous bits arrives after the bit-transition. Indoor channels typically have delay spreads between 10–100 ns, while the delay spread in urban environments is between 10–25  $\mu$ s [2, pp. 160–162].

## 2.3 System Performance Estimation

### 2.3.1 Co-Channel Interference

As the radio spectrum is a finite resource, the increasing demand for wireless communication services has necessitated reuse of the spectrum [4, p. 16]. Frequency reuse causes co-channel interference, which is detrimental to system performance, reducing the reliability, throughput and the number of users that can be supported. Frequency reuse is widely used in outdoor cellular systems, but the resulting co-channel interference from neighbouring base-stations can be reduced with careful deployment strategies [4, pp. 16–19]. However, reducing co-channel interference for systems operating indoors is a challenge, as deployment tends to be rather more *ad hoc*. Furthermore, the reuse distances indoors are typically much smaller<sup>6</sup>, and all transceivers are located in close physical proximity. It should also be noted that achieving adequate coverage (i.e. sufficient desired signal strength at the receiver) for indoor systems is usually not an issue, rather it is interference (typically from physically adjacent co-channel systems) that constrains performance [22].

### 2.3.2 Wireless Networks

The IEEE 802.11 standard outlines communication protocols for wireless local area networks (WLANs) operating in the unlicensed portions of the 2.4 GHz industrial, scientific and medical (ISM) frequency band, and the 5.8 GHz unlicensed national information infrastructure (U-NII) band [23]. Systems supporting the 802.11 standard are widely deployed within buildings to provide wireless connectivity.

<sup>6</sup>Although it should be noted that the transmitting powers are also reduced.

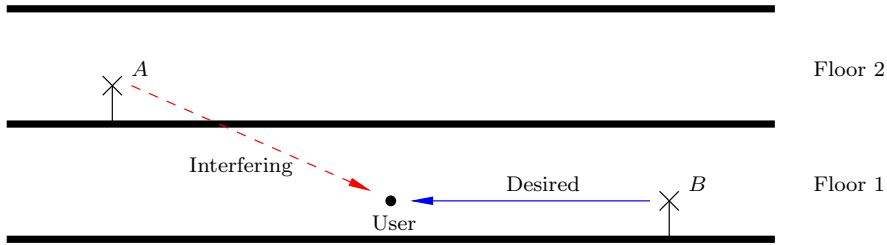


Figure 2.5: Generalised depiction of inter-floor interference arising in multi-storey building.

Fig. 2.4 shows how the 802.11 standard divides the 2.4 GHz band into 11 channels<sup>7</sup> with 20 MHz bandwidth/channel. Each channel can support multiple users simultaneously by separating the users with different spreading codes (code-division multiple-access, CDMA) or, in frequency with orthogonal sub-carriers (orthogonal frequency division multiplexing, OFDM). It should be noted that there is considerable overlap between adjacent channels, e.g. in the 2.4 GHz band shown in Fig. 2.4, only three channels (1, 6 and 11, identified in red) do not overlap in frequency. Therefore, when more than three channels are allocated to base-stations, frequencies are reused and varying levels of adjacent-channel interference could arise.

Another wireless technology planned for indoor environments are *femto-cells* [5]. Femto-cells are low-powered, short-range (10–50 m) cellular-network base-stations installed within buildings and designed to connect mobile devices to an operator’s network via existing wired connections<sup>8</sup>. The deployment of femto-cell systems is driven by capacity constraints and the (sometimes frequent) poor performance of existing macro-cellular systems for users operating within buildings. However, interference arising from neighbouring femto-cells and existing cellular networks remains a concern [5, pp. 145–178].

### 2.3.3 Inter-Floor Interference

Unlike two-dimensional planar frequency reuse strategies developed for outdoor cellular systems, multi-storey buildings encourage a three-dimensional approach to system planning [6]. Each storey in the building is treated as a ‘cell’, with the floors forming natural boundaries [6]. However, signals can ‘leak’ onto adjacent (or nearly adjacent) floors. Fig. 2.5 shows a generalised two-dimensional representation of a multi-storey building, with two base-stations (A and B) identified. It is assumed both base-stations are operating in the same frequency band (thereby interfering with each other), and users connect to base-stations on the same floor. In the scenario presented in Fig. 2.5, signals propagating from base-station A to Floor 1 appear as interference to the user operating on Floor 1.

The quality of service provided to the users will depend on the strength of the desired signal and the relative strength of the interfering signal. The ratio between the desired and interfering signal powers is termed the signal-to-interference ratio (SIR). However, due to multi-path fading on the desired and interfering propagation paths, the instantaneous SIR will fluctuate.

An alternative measure of system performance, in the presence of interference, is the outage probability, which quantifies the probability of failure to deliver acceptable performance [24]. In digital systems this usually is defined as a bit-error-rate (BER) above a certain threshold, typically  $10^{-3}$  [6]. Expressions for the outage probability are derived by superimposing the

<sup>7</sup>The USA version of the standard divides the 2.4 GHz band into 11 channels; in other areas of the world up to 14 channels can be used [23].

<sup>8</sup>Femto-cells can be declared ‘private’, allowing only *known* devices to connect.

probability density functions characterising multi-path fading, (2.2)–(2.4), on estimates for the sector mean. Predicting the sector mean and fading distributions for indoor environments is complicated by the large variability in building layout, architectural styles, and building materials.

## 2.4 Interference Mitigation

### 2.4.1 Deployment Strategies

Appropriate deployment strategies for wireless access-points can reduce co-channel interference arising from physically adjacent systems [4, pp. 16–19]. The experimental study published by Butterworth *et al.* [6] was a significant contribution, as unlike many previous studies it addressed the problem of inter-floor interference. Measurements of the received signal in four multi-storey buildings were collected at 1.8 GHz from multiple transmitters located on each floor. The down- and up-link outage probabilities for a variable number of users were computed from this dataset. It was found that the majority of inter-floor interference arrived from transmitters located on immediately adjacent floors. Correlations in the mean signal level were also observed, depending on the vertical configuration of the base-stations. This led to the conclusion that vertically aligning the base-stations would result in significantly lower levels of outage probability, compared to other configurations, such as vertically offsetting the base-stations. Further studies have investigated the interference from systems outside the building [25], and the use of directional base-station antennas [26]. It should be noted that developing deployment strategies requires extensive experimental measurements, or good predictions of the received signals in the buildings of interest.

### 2.4.2 Frequency Selective Surfaces and Metal Shielding

Modifying the indoor propagation environment, by deploying frequency selective surfaces (FSSs), has been suggested as another way to reduce the levels of co-channel interference [27–30]. FSSs behave as passive<sup>9</sup> electromagnetic filters, and could be applied to walls and floors to block co-channel interference from neighbouring wireless systems, while still allowing other services, such as safety systems (e.g. fire-service radio communications), cellular phones and terrestrial TV and radio, to operate [29]. FSSs have been studied extensively since the 1960s, and typically consist of thin conducting elements tessellated on a dielectric substrate [31, pp. 2–8]. Fig. 2.6(a) shows a photograph of a hexagonal loop, band-stop FSS, designed to operate at 5.8 GHz. The hexagonal elements are made from thin aluminium foil and are attached to a sheet of cardboard for support. Fig 2.6(b) shows a typical frequency response for the transmission coefficient through a band-stop FSS. At the resonant frequency,  $f_c$ , incident waves are reflected off the surface (at resonance, the FSS behaves similar to a metal sheet), while at other frequencies the FSS is nominally transparent.

The deployment of FSSs to shield indoor environments from interference is hindered by the electromagnetic interactions arising between the surface and the walls and floors it is applied against [29, 30]. These complex interactions detune the FSS, shifting the resonant frequency, increasing angular dependence and lowering the maximum attenuation [29, 30]. As the internal

---

<sup>9</sup>Some modern FSS designs incorporate active elements enabling the frequency properties to be changed while deployed.

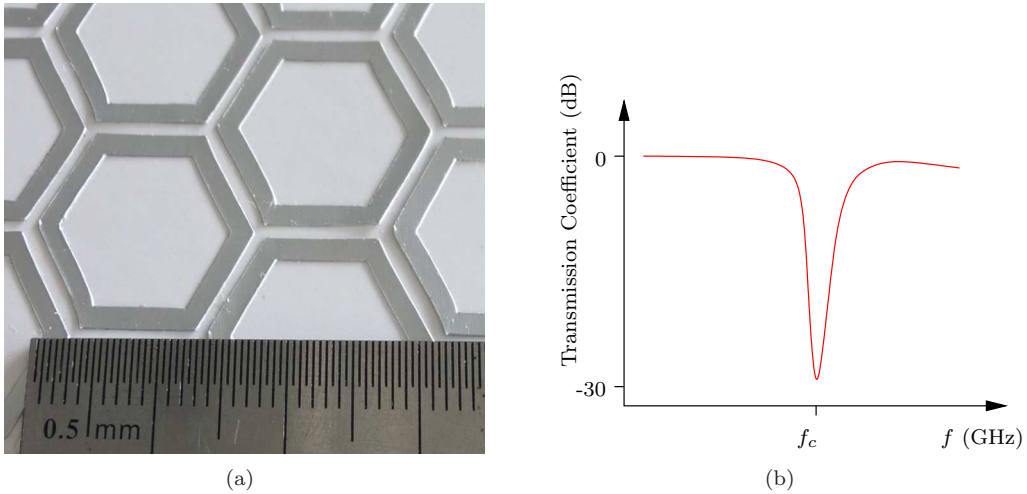


Figure 2.6: (a) Hexagonal loop FSS. (b) Illustration of the frequency response for a band-stop FSS with resonant frequency  $f_c$ .

structure of walls differ considerably, it is not always possible to achieve the required performance. Furthermore, the fabrication costs of large FSS panels remain high.

As an alternative to FSSs, metal shields can also be used increase the isolation between physically adjacent cells, enhancing coverage and reducing interference<sup>10</sup> [22]. By identifying and shielding only the propagation paths that contribute significant levels of interference, the total length of shielding deployed can be minimised<sup>11</sup>. The deployment process may have to be iterated, as the addition of shields may introduce new interference paths [22]. It should be noted that inter-floor interference was not considered in [22].

## 2.5 Summary

This chapter has examined issues related to the deployment of contemporary wireless systems within buildings. The indoor propagation environment is considerably more compact than outdoor environments, and interference from neighbouring systems is the major limiting factor. Therefore understanding how radio waves propagate within buildings, and give rise to co-channel interference, is important to better design and deploy wireless systems. It is also noted that modelling radio-wave propagation within buildings is complicated by varying architectural styles and the range of materials encountered. Chapter 3 will review existing models to predict the signal strength and other propagation parameters, and outline the contributions of this thesis.

<sup>10</sup>Metal shields modelled as perfect electric conductors (PEC) can be considered *ideal* FSSs operated in their resonant state.

<sup>11</sup>Complete electromagnetic isolation could be achieved by shielding all surfaces, however this solution is costly and impractical.

# Chapter 3

## Mechanistic Propagation Modelling

### 3.1 Introduction

As discussed in chapter 2, accurate propagation models that can predict relevant statistical parameters, such as the signal-to-interference ratio (SIR) and outage probability, are essential to the development and successful implementation of future wireless systems. Therefore, there is a need for *reliable* models to predict signal strengths within buildings. Currently, empirical models based on experimental measurements are popular [32], however, indoor environments can be very complex, and improved accuracy and a more thorough understanding of how the radio waves propagate may be gained through an electromagnetic approach. As electromagnetic methods are generally difficult to apply, this chapter introduces a *mechanistic* modelling approach. Mechanistic models are derived from a detailed electromagnetic characterisation of the indoor radio channel, but are more appropriate for day-to-day system planning.

Section §3.2 outlines some of the widely used empirical models to predict signal strengths within buildings, followed by a short discussion on the limitations of such models. The application of site-specific deterministic models (based on electromagnetic theory) to predict relevant propagation parameters is discussed in section §3.3; this section briefly reviews analytical techniques and ray-based methods, followed by a literature survey on the application of the FDTD method to model indoor radio-wave propagation. The mechanistic modelling approach is discussed in section §3.4, and the contributions of this thesis are outlined in section §3.5. The chapter is briefly summarised in section §3.6.

### 3.2 Empirical Models

#### 3.2.1 Path-Loss Prediction

Empirical models to predict the path-loss are generally developed from narrow-band experimental measurements of the received signal strength. For indoor measurements, the power is typically recorded at several hundred locations throughout the building [6, 7, 33], and the receiving antenna is usually rotated [6, 33], or moved linearly [7, 34] to average out the effects of multi-path fading and obtain an estimate of the sector-averaged mean [17]. By deploying

multiple transmitters, with appropriately spaced frequencies, the path-loss from multiple transmitter locations can be collected with a single sweep [6]. Similar to outdoor/urban propagation models [35], the power is converted to path-loss, and is typically modelled as varying exponentially with the transmitter-receiver separation distance, with additional terms to account for penetration losses. The resulting empirical models are generally straight forward to apply, and prediction results can be computed relatively easily. There have been numerous experimental studies of the indoor radio channel, and this section outlines several relevant, noteworthy empirical propagation models developed to predict signal strengths for indoor environments. Literature surveys of earlier research (pre-1990s)<sup>1</sup> can be found in [36] and [37].

### Motley and Keenan (1988) [34]

The Motley and Keenan model is based on experimental measurements of the received power/path-loss in a multi-storey office building at 900 and 1700 MHz. The path-loss was observed to follow a logarithmic relationship with distance [34],

$$PL = S + 10n \log_{10} d + kF, \quad (3.1)$$

where  $S$  is path-loss measured at a distance of 1.0 m,  $n$  is the distance dependency exponent,  $F$  is the loss encountered propagating through a floor, and  $k$  is the number of floors penetrated. The parameters  $n$  and  $F$  are found by fitting (3.1) to the experimental measurements via linear regression. At 900 MHz the parameters were found to be  $S = 16$  dB,  $F = 10$  dB and  $n = 4.0$ ; whereas at 1700 MHz,  $S = 21$  dB,  $F = 16$  dB and  $n = 3.5$  [34]. It is noted that higher losses are predicted at 1700 MHz, and for the limited number of floors considered in [34], the path-loss was observed to increase linearly with the number of floors penetrated.

### LaFortune and Lecours (1990) [8]

The models proposed in [8] to predict the sector-averaged path-loss are based on experimental measurements made in two multi-storey university buildings (containing a mix of laboratories, offices and classrooms) at 917 MHz. The measurement set was divided into a number of canonical regions (e.g. propagation in corridors, penetration through soft and hard internal partitions and propagation to adjacent floors) and models to predict the sector-averaged path-loss were fitted to the measurements. When the transmitter and receiver are located on different floors, the loss in excess of free-space is given by [8]

$$L = -1.5n - 10.7 \log_{10} d - 23.8 - 41.7 \log_{10} p, \quad (3.2)$$

where  $n$  and  $p$  are the number of (internal, soft partitioned) walls and concrete floors in the transmission path respectively, and  $d$  is the transmitter-receiver separation distance. In contrast to the model proposed in (3.1), the floor attenuation is observed to decrease as more floors separate the transmitter and receiver. The effects of antenna polarisation (on propagation to adjacent floors) was also considered, and it was shown the loss introduced by vertically polarised antennas is approximately 2 dB larger than horizontally polarised antennas (in the same location) [8]. Further results suggest that propagation through metallic (and non-metallic) furniture and clutter can reduce the received power by 1–4 dB.

---

<sup>1</sup>Circa 1990 the focus of research shifted from characterising the outdoor-to-indoor radio channel to also include systems operating within buildings.

### Seidel and Rappaport (1992) [7]

Based on experimental measurements in two multi-storey buildings, Seidel and Rappaport proposed a distance-dependency model for the sector-averaged path-loss [7]. The measurements were conducted at 914 MHz; however, it was suggested the model could be extended to the low microwave bands (1.0–5.0 GHz). Other authors have found the Seidel model can be applied with similar accuracy at frequencies higher than 914 MHz [6]. The Seidel model for multi-storey buildings is given by [7]

$$PL = PL(d_0) + 10 \times n_{\text{sf}} \times \log_{10} \left( \frac{d}{d_0} \right) + \text{FAF}, \quad (3.3)$$

where  $PL(d_0)$  is the path-loss at a reference distance ( $d_0$ ) and includes all the losses and gains in the system,  $d$  is the transmitter-receiver separation distance,  $n_{\text{sf}}$  is the (constant) distance-dependency exponent for data measured on the *same floor* as the transmitter, and FAF is the floor attenuation factor representing losses encountered propagating through a number of floors<sup>2</sup>. Table 3.1 presents values for the FAF reported in the literature [6, 7].

Table 3.1: Seidel Model: Floor Attenuation Factors (dB).

Floor Separation	Seidel (914 MHz) [7] Building 1	Seidel (914 MHz) [7] Building 2	Butterworth (1.8 GHz) [6]
1	12.9	16.2	16.0
2	18.7	27.5	22.1
3	24.4	31.6	
4	27.0		

It is noted that the FAF's shown in Table 3.1 depend on the building and the number of floors separating the transmitter and receiver. As all floors in the buildings examined are identical, if penetration through the floors was the only dominant propagation path, the FAF should increase linearly. However, it is observed that the incremental FAF decreases as more floors are penetrated, suggesting lower loss paths/mechanisms dominate the propagation to adjacent (or nearly adjacent) floors [7, 38]. Since the publication of the Seidel model in 1992, various improvements have been suggested, e.g. additional terms to account for correlated shadowing [6, 39], the angular dependence of attenuation factors [33], increased loss with distance [2, p. 130], and diffraction around structural corners [33]. However, the Seidel model in (3.3) remains widely used and forms the basis of the International Telecommunications Union (ITU) model for mean path-loss prediction in multi-storey buildings [32].

### ITU Model [32]

The ITU model is based on a number of experimental studies conducted in a wide range of buildings throughout the world at various frequencies. The sector-averaged path-loss is given by [32]

$$PL = 20 \log_{10} f + n \log_{10} d + L_f(k) - 28 \quad (\text{dB}), \quad (3.4)$$

<sup>2</sup>An alternative form for the Seidel model, that does not include FAF, is

$$PL(d) = PL(d_0) + 10 \times n_{\text{mf}} \times \log_{10} \left( \frac{d}{d_0} \right),$$

where  $n_{\text{mf}}$  is the distance-dependency exponent. It should be noted that  $n_{\text{mf}}$  is not constant and changes depending on the number of floors separating the transmitter and receiver.

where  $n$  is the distance dependency exponent,  $f$  is frequency (in MHz),  $d$  is the transmitter-receiver separation distance,  $L_f$  is the floor penetration loss, and  $k$  is the number of floors separating the transmitter and receiver. Table 3.2 shows values for  $n$  and  $L_f$  at typical operating frequencies, though it is suggested that better performance can often be obtained if the model in (3.4) is tuned by incorporating experimental measurements for  $n$  and  $L_f$  from the buildings of interest [32].

Table 3.2: ITU Model: Distance-Dependency Exponents and Floor Attenuation Factors.

Frequency (GHz)	Distance Dependency, $n$	Floor Attenuation, $L_f$ (dB)
0.9	33	9 (1 floor)
		19 (2 floors)
		24 (3 floors)
1.8–2.0	30	$15 + 4(n - 1)$
5.2	31	16 (1 floor)

Similar to the models proposed by LaFortune [8] and Seidel [7], at lower frequencies the floor attenuation is observed to vary with the number of floors separating the transmitter and receiver. However at higher frequencies, the ITU model suggests a linear dependence with the number of floors.

### 3.2.2 Discussion

Although empirical models are simple to apply, they lack a physical basis for the phenomena observed and thus cannot be easily generalised. For example, many of the terms and parameters in the empirical models outlined in this section lack an electromagnetic basis, and vary considerably between buildings. Consequently, the applicability of empirical models in buildings where measurements were not taken (or in buildings that differ radically in architectural style) is questionable. When used in practise to predict co-channel interference for systems operating on adjacent floors, empirical models have been found to result in pessimistic estimates of the outage probability [6]. More accurate findings have been reported when the empirical models were complemented with physical factors, such as correlated shadowing [39]. Furthermore, the collection of sufficient experimental data to allow statistically valid conclusions is time-consuming and expensive. Despite these limitations, empirical models remain widely used for system planning purposes (e.g. optimisation of base-station locations [40]).

## 3.3 Deterministic Models

Deterministic models are based on an electromagnetic analysis of the indoor propagation environment (or a representative canonical environment). Deterministic models have been the subject of recent research, and are considered more widely applicable, robust and accurate compared to empirical models [41]. However, the complexity of indoor environments makes the application of analytical electromagnetic techniques difficult, and consequently numerical solutions are increasingly favoured [41, 42]. The disadvantages of numerical electromagnetic modelling include the complexity of the models, lengthy simulation times, and restricted problem sizes (due to limited computing resources). It should also be noted that the results obtained

are generally specific to the building/environment considered. Thus, fully-electromagnetic models are generally not suitable to analyse the physical channel in day-to-day planning applications (at the present time), but may provide considerable insight into the indoor radio channel.

### 3.3.1 Analytical Methods

The application of analytical electromagnetics to model indoor radio-wave propagation is difficult, as only a narrow range of problems can be investigated analytically due to the complex geometries (and boundary conditions) defining the problems. The complex propagation environments found within buildings necessitates a simplification of the problem to canonical geometries.

#### **Honcharenko *et al.* (1992) [18]**

The study reported in [18] examined propagation in the vertical clear space between the floor and ceiling using a simplified two-dimensional geometry. The clutter typically present in most indoor environments was modelled as a series of two-dimensional perfectly absorbing screens attached to the floor and ceiling. The fields propagating in the clear space were calculated using Kirchhoff-Huygens aperture integration<sup>3</sup>. As the transmitter-receiver separation distance increases, a greater proportion of the first Fresnel zone is obscured by the screens. Correspondingly, the path-loss increases, suggesting a two-slope model may be appropriate [18]. However, the difficulty in extending the aperture field integration technique to predict propagation in more realistic (and inherently more complex) geometries limits its applicability.

#### **Porrat and Cox (2004) [15]**

Analytical methods have also been used to model propagation in corridors [15]. As a first approximation the corridors were assumed to be empty with electrically smooth dielectric walls (the floor and ceiling were assumed to be conducting). At UHF frequencies, this environment forms an over-moded dielectric-slab waveguide, and can be analysed using modal techniques. Surface roughness was included on the walls to better represent realistic corridors, and was modelled using a mode coupling approach [15]. The models were also extended to include propagation around and through ‘L’ and ‘T’ junctions. Along relatively long corridors (lengths greater than 30 m), the waveguide models were shown to agree well with experimental measurements, however propagation into rooms was not considered [15].

### 3.3.2 Ray-Optical Methods

The application of ray-optical methods—such as Geometrical Optics and the Uniform Theory of Diffraction (GO/UTD)—to predict the key propagation parameters (e.g. the sector mean, fading distributions and delay spreads) for indoor environments has been well established in the literature [14, pp. 203–210] [18, 38, 42–45]. Modelling indoor propagation with ray-optical methods requires a detailed architectural database containing information about the location and material properties for all the significant objects in the environment. Accordingly, there is an inherent trade-off between the level of detail included in the model, the accuracy of the results and computational cost [14, p. 209] [42, 45].

---

<sup>3</sup>The field in the aperture of each successive screen is calculated by integrating over the field in the previous aperture, with a line source used to calculate the fields in the aperture of the first screen. This process can be repeated for any number of screens, similar to the approach suggested in [19].

For each pair of transmitter and receiver locations the received power is calculated by considering each ray-trajectory separately, and summing the fields predicted by each path [14, pp. 203–210]. Penetration through, reflection from and diffraction around objects in the propagation environment are taken into account with appropriate transmission, reflection and diffraction coefficients. As ray-optical methods approximate the physical propagation paths, the delay spread and other parameters can be calculated directly. In typical indoor environments many propagation paths between the transmitter and receiver may exist. However, usually a small number of these paths carry significant levels of power, and a number of techniques to reduce the computational burden by identifying only high-contribution paths have been proposed [14, pp. 203–210].

Ray-optical methods must be applied to the indoor propagation problem with caution, as many of the assumptions and approximations used in their derivation are not valid for typical indoor environments. For example, structural corners made from lossy dielectric materials (such as concrete) are frequently encountered in indoor environments, however, dielectric wedge diffraction is known to be a non ray-optical process [46]. Correctly predicting the diffracted fields is important, as in some circumstances (e.g. deeply shadowed regions) the received power is dominated by diffracted components [14, pp. 209–210].

### 3.3.3 Time-Domain Methods

Time-domain methods are based on numerical approximations to Maxwell's equations on a spatial lattice. The spatial derivatives in Maxwell's equations can be approximated using: central differences, as in the Finite-Difference Time-Domain (FDTD) method [47]; discrete Fourier or Chebyshev transforms, as in the Psedu-Spectral Time-Domain (PSTD) method [11, pp. 847–882] [48]; and wavelets, as in the Multi-Resolution Time-Domain (MRTD) method [41]. However, the FDTD method remains widely used for a range of electromagnetic problems, and offers many advantages as a modelling, simulation and analysis tool [11, pp. 3–16], including:

1. Accurate estimates of the electric and magnetic field distributions for arbitrary two- or three-dimensional geometries;
2. Frequency dependent constitutive parameters, allowing a wide range of materials to be specified (including lossy dielectrics, magnetic materials and anisotropic materials);
3. Broadband characterisation of the problem with a single simulation run; and
4. Insights into the propagation processes using appropriate data visualisation techniques.

While the main disadvantage of the FDTD method to solve electrically large problems is excessive computational requirements [49], advances in processing capabilities are making their application to the indoor propagation problem tractable.

The FDTD method was originally proposed in 1966 [47], however, the first reported application for modelling propagation within buildings was not published until 1994 [50]; the high computational cost precluding earlier investigations<sup>4</sup>. Compared to ray-tracing, the application of the FDTD and related time-domain methods to characterise the indoor radio channel are not as well established in the literature. However, a number of studies have been reported, and Table 3.3 summarises several of the more significant publications. While most of the studies outlined in Table 3.3 employ the FDTD method, there has been some work with related techniques,

---

<sup>4</sup>The study reported in [50] (1994) required approximately 20 MB of memory and 10 hours on a 150 MHz MIPS-R4400 processor.

Table 3.3: Application of Time-Domain Methods to Model Propagation Within Buildings.

Investigators	Year of Publication	Method	Frequency	Environment	Contribution/Parameters Investigated
Lauer <i>et al.</i> [50, 51]	1994 and 1995	FDTD	1.0 GHz	2D floor plan of an office building with ‘soft’ internal walls.	Channel impulse response and power delay profiles.
Wang <i>et al.</i> [52, 53]	2000 and 2002	Hybrid GO/FDTD	1.3 GHz	2D model of a typical office.	Received power, fading distributions and comparisons with experimental measurements.
Yun <i>et al.</i> [54]	2004	FDTD	900 MHz	2D floor plan of an office building with complex internal walls.	Received power, fading distributions and capacity analysis for MIMO systems.
Schäfer and Wiesbeck [55]	2005	FDTD	42.6–300 MHz	3D models of shielded rooms in hospitals.	Power radiated from medical equipment within shielded enclosures (and leakage to other rooms).
Zygiridis <i>et al.</i> [56]	2006	FDTD	2.5–5.8 GHz	2D model of a typical office.	Power coverage, fading distributions and RMS delay-spread over 2.5–5.8 GHz.
Zhao <i>et al.</i> [57]	2007	FDTD	3–11 GHz	2D model of a typical office environment with furniture.	Power delay profiles and the channel frequency response over 3–11 GHz.
Alighanbari and Sarris [41, 58]	2007 and 2009	MRTD/ FDTD	900 MHz	2D floor plan of an office building with ‘soft’ internal walls.	Power coverage, path-loss prediction and fading distributions. Comparisons between the FDTD and MRTD methods.
Thiel and Sarabandi [59, 60]	2008 and 2009	Hybrid GO/FDTD	1.0 GHz	2D and 3D representations of single storey buildings.	Power coverage, path-loss variation and fading distributions.
Stowell <i>et al.</i> [61]	2008	FETD	1.0 GHz	3D model of a two-storey residential building.	Time-domain visualisations of the indoor radio channel.
Lai <i>et al.</i> [62]	2008	FDTD	1.0 GHz	2D floor plan of an office building with ‘hard’ and ‘soft’ internal walls.	Power coverage and the development of models to predict the path-loss.
Austin <i>et al.</i> [12, 63, 64]	2008, 2009	FDTD	1.0, 2.5 and 4.5 GHz	2D vertical slices through multi-storey buildings.	Power coverage, path-loss prediction and channel impulse response. Verified against experimental measurements.

such as the MRTD method [41] and the Finite-Element Time-Domain (FETD) method [61]. Hybrid GO/FDTD methods, which use geometrical optics to predict fields on LOS paths, and the FDTD method to predict propagation through detailed structures (with appropriate field coupling), have also been proposed to reduce the computation burden [52, 53, 59, 60].

As noted in Table 3.3, most applications of time-domain methods to model propagation within buildings have limited analysis to two-dimensional horizontal ‘slices’ through the geometry. The high computational costs of the FDTD (and related) methods generally precludes a three-dimensional investigation<sup>5</sup>. However, the focus has largely been on characterising propagation on the same floor as the transmitter, and in these cases a two-dimensional representation may be adequate<sup>6</sup>. Typically the floor plan of a generalised building is considered, with internal walls dividing the space into rooms/offices and corridors. The internal walls and partitions are usually modelled as lossy dielectric materials [41], and there has been some work in characterising propagation through inhomogeneous dielectric walls [54]. Office furniture, wiring, pipes/ducts and other dielectric and metallic clutter have largely been ignored, as it is difficult to adequately model propagation around these objects on a two-dimensional slice. Two-dimensional Transverse Magnetic ( $\text{TM}_z$ ) polarisation<sup>7</sup> is usually assumed, as an electric field source in a  $\text{TM}_z$  FDTD lattice radiates isotropically. The majority of the studies summarised in Table 3.3 are conducted around 1.0 GHz. To reduce dispersion error and prevent numerical instability the FDTD lattice size is typically a fraction of a wavelength (usually  $\lambda/15$ ). At higher frequencies, smaller lattice sizes are required, which results in increased computational requirements.

The primary focus for most studies presented in Table 3.3 is performance estimation for contemporary wireless systems (e.g. cordless phones, cellular networks and WLANs) operating within buildings. Accordingly, the FDTD simulation results tend to focus on characterising the indoor radio channel using coverage maps of the received power [56, 62], with appropriate statistical distributions to describe the multi-path fading envelope [41, 54, 56]. The FDTD method is also well suited to characterising the channel in the time-domain through power-delay profiles and calculations of the delay spread and frequency response [57, 58]. However, it should also be noted that few of the FDTD simulations presented in Table 3.3 have been verified against experimental measurements.

### 3.3.4 Other Deterministic Methods

The materials and geometries typically encountered within buildings are relatively simple, and a number of other electromagnetic techniques could be applied to characterise indoor radio-wave propagation [45], for example:

- Other grid-based approximations, such as the Finite Element Method, Finite Integration Technique and Transmission Line Matrix method;
- Integral equation techniques, such as the Method of Moments (MoM)<sup>8</sup> and the Partial Element Equivalent Circuit method; and

<sup>5</sup>It should be noted that the three-dimensional simulations reported in [61] required 2.1 TB of memory, 1536 processors and approximately 19 hours of wall time on a computer cluster.

<sup>6</sup>The implications of this assumption will be explored further in chapter 8.

<sup>7</sup>A two-dimensional implementation of the FDTD method supports propagation on both Transverse Magnetic ( $\text{TM}_z$ ) and Transverse Electric ( $\text{TE}_z$ ) polarised lattices.

<sup>8</sup>While the MoM has not been widely applied to model propagation within buildings [45], it is well suited to modelling propagation through electrically fine structures, such as frequency selective surfaces.

- Statistical scattering methods based on Boltzmann or diffusion equations [65].

Similar to ray-tracing and the FDTD method, most alternative computational electromagnetic techniques require extensive databases of the material locations and constitutive parameters. The application of the techniques outlined above (and others) to characterise the indoor radio channel is outside the scope of this thesis.

### 3.4 Mechanistic Modelling

Deterministic and empirical approaches to modelling the indoor radio channel make different trade-offs between accuracy and complexity. Empirical models are straightforward to apply and do not require detailed information about the building layout and materials, however, transportability to other buildings remains a concern [6, 33]. In contrast, deterministic models/methods can provide extremely accurate estimates of the fields, but require specific information about the building, including the locations and constitutive parameters of the walls and other large objects [45]. Furthermore, the high computational costs of full-wave electromagnetic techniques, such as the FDTD method, limits their applicability for day-to-day system planning purposes at this time.

The mechanistic modelling approach advocated in this thesis addresses the trade-offs between accuracy and complexity. The received signal at any given location in a typical indoor environment is usually comprised of a number of separate components, each propagating over a different path. In some (often a majority of) circumstances, a small number of components will contribute significantly toward the received power, and are hereafter termed *mechanisms*. This assumption originates from experimental characterisations of the outdoor mobile radio environment. Measurements of urban/suburban radio channels with directional antennas indicate energy arrives on, at most, 3–4 distinct propagation paths [66, 67]. Common paths include, line-of-sight from the transmitter, diffraction over the top or around large buildings, and reflections from buildings and other large objects (e.g. hills/mountains); and in most circumstances one or two components dominate the (sector-averaged) received power [66].

It must be understood that the purpose of a mechanistic model is **not** to predict the instantaneous received power at a point. As noted in section §2.2, objects in the propagation environment will scatter the received signals, leading to multi-path fading. While precisely predicting the fading envelope would require characterising *all* scattering objects, this is not necessary as fading can usually be modelled with appropriate statistical distributions superimposed on the sector-averaged signal level. Therefore, a mechanistic model only needs to reliably estimate the sector-mean to accurately predict system performance parameters, such as the SIR and outage probability. Components that do not contribute significantly toward the sector-mean are not considered mechanisms, and are disregarded from the mechanistic model.

The dominant mechanisms are identified by a thorough analysis of in-building radio-wave propagation with two- and three-dimensional implementations of the FDTD method. The FDTD method is more applicable to general buildings than most analytical techniques and, unlike ray-based methods, makes no *a priori* assumptions about the propagation paths. The complexity of the propagation processes can make conclusive identification of the mechanisms difficult, however various visualisation techniques developed in this thesis can be used to infer the dominant propagation paths. The mechanistic model is formed by developing appropriate, computationally efficient, approximations for each mechanism. As many mechanisms identified

are likely to remain the same for similar environments in different locations [66], a significant advantage of the mechanistic modelling approach is transportability to other buildings.

### 3.5 Contributions of this Thesis

As noted in Table 3.3, the FDTD method has been used to model indoor propagation previously, however, there has been little work on generalising these results to identify the dominant mechanisms governing propagation within buildings. Noticeably absent from Table 3.3 (other than work by the author and reported in this thesis) is the use of the FDTD method to model propagation between floors in multi-storey buildings. However, as noted in chapter 2, interference arising from co-channel transmitters on adjacent (or nearly adjacent) floors can be significant, and this behaviour is generally not well characterised with existing propagation models. The major contribution of this thesis is, therefore, the development of mechanistic models to characterise the indoor radio channel, particularly focusing on inter-floor propagation and the prediction of system performance. Other contributions include:

- developing and verifying parallel two- and three-dimensional FDTD codes suitable for use on computing facilities at the University of Auckland;
- developing techniques to visualise the propagating fields (to help infer the dominant propagation mechanisms);
- experimental characterisations of the indoor radio channel (with the aim of confirming the results obtained with the FDTD method); and
- investigating the use of the FDTD method to directly estimate system performance.

Central to these goals, however, is a thorough assessment of the limitations of the FDTD method to model propagation within buildings, particularly the use of two-dimensional representations of the geometry, and the impact of furniture and other details.

### 3.6 Summary

Models to predict key propagation parameters, especially the sector mean, are important for the deployment of indoor wireless systems. This chapter has reviewed a number of empirical and deterministic models to predict signal strengths within buildings. Deterministic models potentially offer improved accuracy and a better understanding of the propagation processes, but are practically more difficult to apply than empirical models, which accordingly, remain widely used. The mechanistic modelling approach outlined in this chapter aims to develop simple models for the dominant propagation mechanisms, which are identified via an FDTD analysis of the indoor radio channel. The major contributions of this thesis are an assessment of the FDTD method to model radio-wave propagation in buildings, and the development of mechanistic models to predict system performance. Chapter 4 will introduce the FDTD method in more detail, focusing on aspects relevant to modelling propagation within buildings.

## Chapter 4

# The Finite Difference Time Domain Method

### 4.1 Introduction

Chapter 2 outlined several methods currently used to predict propagation within buildings, namely models based on experimental measurements, site-specific models based on computationally efficient electromagnetic approximations (e.g. geometrical optics and the uniform theory of diffraction) and the application of full wave electromagnetic techniques, such as the Finite Difference Time Domain (FDTD) method. As stated in chapter 3, one of the contributions of this thesis is to develop computationally efficient *mechanistic* models to predict propagation within buildings. In order to formulate these *mechanistic* models it is necessary to adequately model the electromagnetic nature of the propagation process, without any *a priori* assumptions. In this regard, full wave electromagnetics can be used to gain considerable insight into how the physical building structure can influence the propagating fields. This chapter introduces the FDTD method and outlines the implementation and validation of the numerical codes developed.

The FDTD method was first proposed by Yee in 1966 [47], however the high computational cost precluded extensive use and investigation of the method at that time. Since the publication of the stability bounds and an absorbing boundary condition by Taflove in 1975 [68], there has been renewed interest in applying the FDTD method to larger and more complex problems [11, pp 3–5]. This chapter focuses on aspects of the FDTD method relevant for modelling propagation within buildings (a complete description of the FDTD method can be found in [11]).

Section §4.2 outlines the derivation of the update expressions from Maxwell's equations in two- and three-dimensions. Also briefly discussed are the stability and dispersion criteria which set bounds for the space and time steps. The boundary conditions terminating the lattice are also important when examining unbounded problems with the FDTD method, and section §4.3 discusses the uniaxial perfectly matched layer (UPML) absorbing boundary. The computational requirements of the FDTD method often exceed the resources available on a single computer, and section §4.4 discusses the parallelisation of the FDTD algorithm for implementation on a computer cluster. Section §4.5 outlines several test cases used to validate the numerical codes. The major findings of the chapter are presented in section §4.6.

## 4.2 The Finite-Difference Time-Domain Method

### 4.2.1 Maxwell's Equations in Three Dimensions

In a source free region, Maxwell's equations in differential form are given by [11, pp. 51–52]

$$\frac{\partial \mathbf{B}}{\partial t} = -\nabla \times \mathbf{E} - \sigma_E \mathbf{E} \quad (4.1)$$

$$\frac{\partial \mathbf{D}}{\partial t} = \nabla \times \mathbf{H} - \sigma_M \mathbf{H} \quad (4.2)$$

$$\nabla \cdot \mathbf{D} = 0 \quad (4.3)$$

$$\nabla \cdot \mathbf{B} = 0, \quad (4.4)$$

where

$\mathbf{E}$  : electric field (V/m)

$\mathbf{H}$  : magnetic field (A/m)

$\mathbf{D}$  : electric flux density (C/m<sup>2</sup>)

$\mathbf{B}$  : magnetic flux density (Wb/m<sup>2</sup>)

$\sigma_E$  : electric conductivity (S/m)

$\sigma_M$  : magnetic loss ( $\Omega$ /m).

In a medium containing stored electric charge, (4.3) is modified to  $\nabla \cdot \mathbf{D} = \rho_v$ , where  $\rho_v$  is the volume charge density (in C/m<sup>3</sup>). Furthermore, in linear, isotropic, and non-dispersive materials,  $\mathbf{E}$  and  $\mathbf{H}$  are related to  $\mathbf{D}$  and  $\mathbf{B}$  via the constitutive equations, given by

$$\mathbf{D} = \epsilon \mathbf{E} = \epsilon_0 \epsilon_r \mathbf{E} \quad (4.5)$$

$$\mathbf{B} = \mu \mathbf{H} = \mu_0 \mu_r \mathbf{H}, \quad (4.6)$$

where

$\mu_0$  : permeability of free-space,  $4\pi \times 10^{-7}$  (H/m)

$\mu_r$  : relative permeability of the medium

$\epsilon_0$  : permittivity of free-space,  $8.85418782 \times 10^{-12}$  (F/m)

$\epsilon_r$  : relative permittivity of the medium.

Substituting (4.5) into (4.1), (4.6) into (4.2) and expanding the curl operators in Cartesian co-ordinates leads to six coupled differential equations,

$$\frac{\partial E_x}{\partial t} = \frac{1}{\epsilon_0 \epsilon_r} \left[ \frac{\partial H_z}{\partial y} - \frac{\partial H_y}{\partial z} - \sigma_E E_x \right] \quad (4.7)$$

$$\frac{\partial E_y}{\partial t} = \frac{1}{\epsilon_0 \epsilon_r} \left[ \frac{\partial H_x}{\partial z} - \frac{\partial H_z}{\partial x} - \sigma_E E_y \right] \quad (4.8)$$

$$\frac{\partial E_z}{\partial t} = \frac{1}{\epsilon_0 \epsilon_r} \left[ \frac{\partial H_y}{\partial x} - \frac{\partial H_x}{\partial y} - \sigma_E E_z \right] \quad (4.9)$$

$$\frac{\partial H_x}{\partial t} = \frac{1}{\mu_0 \mu_r} \left[ \frac{\partial E_y}{\partial z} - \frac{\partial E_z}{\partial y} - \sigma_M H_x \right] \quad (4.10)$$

$$\frac{\partial H_y}{\partial t} = \frac{1}{\mu_0 \mu_r} \left[ \frac{\partial E_z}{\partial x} - \frac{\partial E_x}{\partial z} - \sigma_M H_y \right] \quad (4.11)$$

$$\frac{\partial H_z}{\partial t} = \frac{1}{\mu_0 \mu_r} \left[ \frac{\partial E_x}{\partial y} - \frac{\partial E_y}{\partial x} - \sigma_M H_z \right]. \quad (4.12)$$

Analytical solutions to (4.7)–(4.12) are difficult, if not impossible, to obtain for anything other than simple cases, due to boundary condition complexity [10, p. 2, 105–106].

### 4.2.2 Reduction to Two Dimensions

If the structure being modelled extends to infinity in the **z**-direction with no change in the cross-section and the incident wave is also uniform in **z**, then all  $\frac{\partial \cdot}{\partial z}$  terms in (4.7)–(4.12) will reduce to zero. Depending on the polarisation of the lattice and incident fields, two solutions are possible: the transverse magnetic ( $\text{TM}_z$ ) and transverse electric ( $\text{TE}_z$ ) modes.

Equations (4.9), (4.10) and (4.11) (which only involve  $H_x$ ,  $H_y$  and  $E_z$  field terms) represent the  $\text{TM}_z$  mode with respect to **z**:

$$\begin{aligned}\frac{\partial H_x}{\partial t} &= \frac{1}{\mu_0 \mu_r} \left[ -\frac{\partial E_z}{\partial y} - \sigma_{\text{M}} H_x \right] \\ \frac{\partial H_y}{\partial t} &= \frac{1}{\mu_0 \mu_r} \left[ \frac{\partial E_z}{\partial x} - \sigma_{\text{M}} H_y \right] \\ \frac{\partial E_z}{\partial t} &= \frac{1}{\epsilon_0 \epsilon_r} \left[ \frac{\partial H_y}{\partial x} - \frac{\partial H_x}{\partial y} - \sigma_{\text{E}} E_z \right].\end{aligned}$$

Similarly, equations (4.7), (4.8) and (4.12) (which only involve  $E_x$ ,  $E_y$  and  $H_z$  field terms) represent the  $\text{TE}_z$  mode with respect to **z**:

$$\begin{aligned}\frac{\partial E_x}{\partial t} &= \frac{1}{\epsilon_0 \epsilon_r} \left[ \frac{\partial H_z}{\partial y} - \sigma_{\text{E}} E_x \right] \\ \frac{\partial E_y}{\partial t} &= \frac{1}{\epsilon_0 \epsilon_r} \left[ -\frac{\partial H_z}{\partial x} - \sigma_{\text{E}} E_y \right] \\ \frac{\partial H_z}{\partial t} &= \frac{1}{\mu_0 \mu_r} \left[ \frac{\partial E_x}{\partial y} - \frac{\partial E_y}{\partial x} - \sigma_{\text{M}} H_z \right].\end{aligned}$$

It is important to note there are no common field components between the  $\text{TM}_z$  and  $\text{TE}_z$  modes, and so both modes can simultaneously exist independently (in two-dimensions).

### 4.2.3 The Yee Algorithm [47]

The Yee algorithm uses second order accurate central difference approximations in time and space to discretise the temporal and spatial partial differentiation operators of (4.7)–(4.12) on a rectangular lattice. For spatial grid separations  $\Delta x$ ,  $\Delta y$  and  $\Delta z$  and time increment  $\Delta t$ , a field component,  $U$ , may be written as

$$U(x, y, z, t) = U(i\Delta x, j\Delta y, k\Delta z, n\Delta t) = U|_{i,j,k}^n. \quad (4.13)$$

Fig. 4.1 shows the positions of the interleaved electric and magnetic field components on a unit cell of the Yee lattice, with ● and ● representing electric and magnetic field components respectively. Each **E** component is surrounded by four circulating **H** components; and similarly, each **H** component is surrounded by four circulating **E** components. The leapfrog algorithm proposed by Yee interleaves the **E** and **H** fields in time, where the magnetic fields are evaluated at integer time steps, while electric fields are evaluated at half-integer time steps.

It should be noted that the zero-divergence conditions of (4.3) and (4.4) do not need to be explicitly enforced by the FDTD algorithm. This is because the staggered arrangement of the

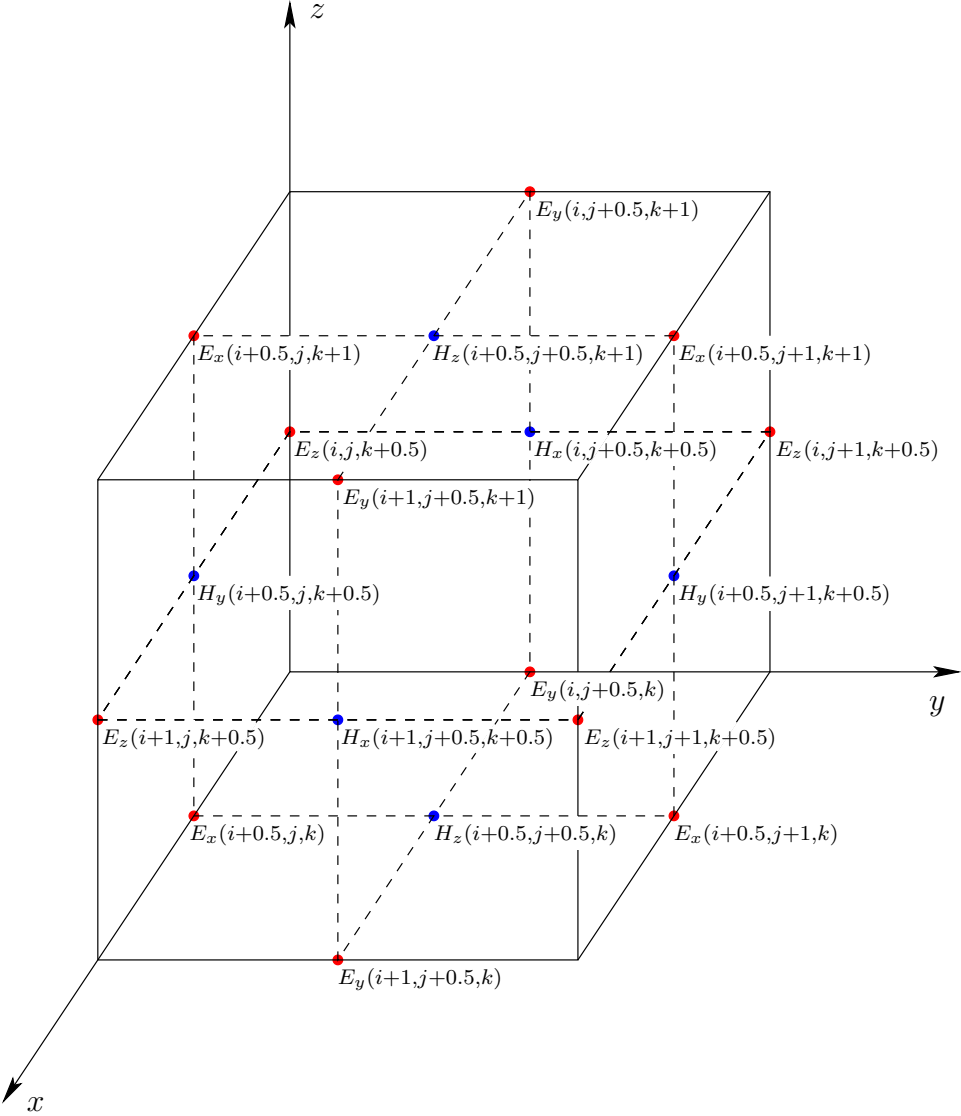


Figure 4.1: Positions of the field components in a unit cell of the Yee lattice, • and ● represent the electric and magnetic field components.

electric and magnetic fields in the Yee lattice ensures each unit cell satisfies the zero-divergence conditions (i.e. electric and magnetic charge are not stored) [11, pp. 78–79]

The update equation for the  $E_z$  field component is derived starting from (4.9), namely

$$\frac{\partial E_z}{\partial t} = \frac{1}{\epsilon_0 \epsilon_r} \left[ \frac{\partial H_y}{\partial x} - \frac{\partial H_x}{\partial y} - \sigma_E E_z \right],$$

and applying central differences with the notation used in (4.13), leading to

$$\begin{aligned} \frac{E_z|_{i,j,k+0.5}^{n+0.5} - E_z|_{i,j,k+0.5}^{n-0.5}}{\Delta t} &= \frac{1}{\epsilon_0 \epsilon_r|_{i,j,k+0.5}} \left[ \frac{H_y|_{i+0.5,j+0.5,k+0.5}^n - H_y|_{i-0.5,j+0.5,k+0.5}^n}{\Delta x} \right. \\ &\quad \left. - \frac{H_x|_{i,j+0.5,k+0.5}^n - H_x|_{i,j-0.5,k+0.5}^n}{\Delta y} - \sigma_E|_{i,j,k+0.5} E_z|_{i,j,k+0.5}^n \right]. \end{aligned} \quad (4.14)$$

However,  $E_z|_{i,j,k+0.5}^n$  is not known, as electric fields are only updated on half-integer time steps. A semi-implicit approximation is used to estimate the electric field at time step  $n$ , i.e.

$$E_z|_{i,j,k+0.5}^n = \frac{E_z|_{i,j,k+0.5}^{n+0.5} + E_z|_{i,j,k+0.5}^{n-0.5}}{2}. \quad (4.15)$$

Substituting (4.15) into (4.14) and solving for  $E_z|_{i,j,k+0.5}^{n+0.5}$  gives the update equation for  $E_z$  as

$$\begin{aligned} E_z|_{i,j,k+0.5}^{n+0.5} &= \left( \frac{2\epsilon_0\epsilon_r|_{i,j,k+0.5} - \Delta t \sigma_E|_{i,j,k+0.5}}{2\epsilon_0\epsilon_r|_{i,j,k+0.5} + \Delta t \sigma_E|_{i,j,k+0.5}} \right) E_z|_{i,j,k+0.5}^{n-0.5} + \left( \frac{2\Delta t}{2\epsilon_0\epsilon_r|_{i,j,k+0.5} + \Delta t \sigma_E|_{i,j,k+0.5}} \right) \\ &\times \left[ \frac{H_y|_{i+0.5,j+0.5,k+0.5}^n - H_y|_{i-0.5,j+0.5,k+0.5}^n}{\Delta x} - \frac{H_x|_{i,j+0.5,k+0.5}^n - H_x|_{i,j-0.5,k+0.5}^n}{\Delta y} \right]. \end{aligned} \quad (4.16)$$

Similar expressions can be derived for the remaining electric and magnetic field components, as presented in appendix A.

#### 4.2.4 Dispersion and Stability

The FDTD algorithm introduces non-physical numerical dispersion, which can influence the components of the **E** and **H** fields [11, p. 107]. In a free-space lattice<sup>1</sup>, dispersion causes the phase velocity to depend on the frequency, direction of propagation and grid discretisation. The extent of these effects can be quantified by comparing finite-difference solutions of monochromatic plane wave propagation with analytical solutions. It has been found that the spatial sampling density greatly influences the numerical dispersion error [11, pp 120–128]. In particular, the dispersion error decreases with increased sampling density, and reduces to zero, in the limit, as the grid size approaches zero. It has been found that errors due to the phase velocity and anisotropy can be constrained below 1% (for all lattice cells) with sampling densities greater than 12 points per wavelength [11, pp 120–128].

To ensure the numerical stability of the FDTD method outlined in (A.1)–(A.6), the time increment cannot exceed the Courant limit [68]. For a three-dimensional FDTD lattice, with cell size  $\Delta x \times \Delta y \times \Delta z$ , the stability bound is

$$\Delta t \leq \Delta t_{\text{Courant}} = \frac{1}{c_0 \sqrt{\frac{1}{(\Delta x)^2} + \frac{1}{(\Delta y)^2} + \frac{1}{(\Delta z)^2}}},$$

where  $c_0$  is the speed of light in free-space. For a two-dimensional ( $\text{TM}_z$  or  $\text{TE}_z$ ) lattice the stability bound is

$$\Delta t \leq \Delta t_{\text{Courant}} = \frac{1}{c_0 \sqrt{\frac{1}{(\Delta x)^2} + \frac{1}{(\Delta y)^2}}}.$$

In practice a time step of  $\Delta t = 0.95\Delta t_{\text{Courant}}$  is used to ensure any finite-precision rounding errors do not cause numerical instability.

---

<sup>1</sup> $\epsilon_r = 1.0$ ,  $\mu_r = 1.0$ ,  $\sigma_E = 0.0$  and  $\sigma_M = 0.0$ .

#### 4.2.5 Lattice Excitation

Initially all field components in the lattice are zero, and propagating waves are excited by applying time domain sources at appropriate points in the lattice. As the FDTD method operates in the time domain, applying a source from  $t = 0$  is akin to multiplying the steady-state excitation by a unit step function,  $U(t)$ . The spectrum of  $U(t)$  is infinite in extent, and should such a source be directly applied to the lattice, increased dispersion will distort the results. Furthermore, non-zero DC fields can be stored in the lattice if the excitation source has a DC component<sup>2</sup>. Two types of sources have been used in this thesis: the modulated Gaussian pulse and the ramped sinusoid function.

In discrete time the modulated Gaussian pulse is given by

$$p(n) = \exp \left[ -0.5 \left( \frac{n - t_0}{t'_w} \right)^2 \right] \sin(2\pi f n \Delta t) U(n), \quad (4.17)$$

where  $n$  is the step number,  $t'_w$  is the pulse width in units of  $n$ ,  $t_0$  is the lead-in time (typically 3–5  $t'_w$ ),  $f$  is the centre frequency,  $\Delta t$  is the time increment, and  $U(n)$  is the unit step function. The pulse width is found by taking the Fourier Transform of (4.17) and solving for  $t_w$  given the 3 dB bandwidth,  $f_b$ . The expression for  $t_w$  (in s) is thus

$$t_w = \sqrt{\frac{-\log_e 0.5}{2f_b^2 \pi^2}} \quad (\text{s}).$$

To reduce the impact of the step-function, the sinusoidal excitation source is multiplied by a smooth ramping-function, which rises from a small value to 1.0. The ramping function employed in this thesis is the complementary error function,  $\text{erfc}(\cdot)$ , and the source applied is thus

$$p(n) = \left[ 1 - 0.5 \text{erfc} \left( \frac{n - t_0}{t'_w} \right) \right] \sin(2\pi f n \Delta t) U(n).$$

If the sinusoid is applied without the ramping function, dispersion errors and a significant DC component will be induced [69].

### 4.3 Boundary Conditions

Any computer implementation of the FDTD technique requires suitable boundary conditions for fields on the perimeter of the computational space. In particular, when applying the FDTD method to unbounded problems (where the outgoing waves are assumed to travel to infinity) the lattice must be truncated, and boundary conditions that minimise spurious reflections are required. By applying appropriate boundary conditions to numerically simulate an electromagnetic wave propagating out of the FDTD lattice, reflection errors below  $10^{-5}$  can be achieved [11].

There are two major classes of boundary conditions: analytical and the perfectly matched layer (PML). Analytical boundary conditions (such as the Mur technique [70]) typically use one-way wave equations to numerically cancel the outgoing wave. The reflection error from analytical boundary conditions is between  $10^{-2} - 10^{-4}$ , however, the performance degrades

---

<sup>2</sup>The FDTD lattice is divergence free *in the absence of sources*, however a source with a DC component will deposit charge in the lattice in accordance with Maxwell's Equations [69].

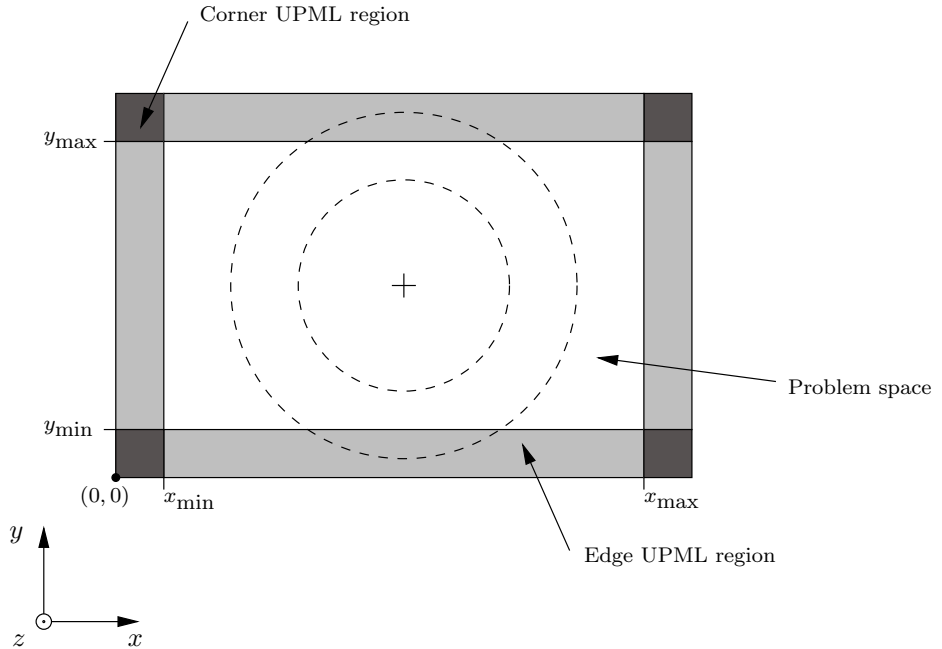


Figure 4.2: Two-dimensional FDTD computational domain surrounded by UPML boundary conditions. The corner regions are formed by overlapping edge regions (adapted from [11, p. 280]).

when the wave impinges on the boundary at glancing incidence [11, pp 245–251]. For this reason, boundary conditions incorporating the PML are usually required.

### 4.3.1 The Perfectly Matched Layer

The PML boundary condition was proposed by Berenger in 1994 [71], and uses an artificial material designed to absorb outgoing waves and minimise any reflections. The computational space is completely surrounding with a thin layer (10–15 cells thick) of a lossy material characterised by electrical conductivity  $\sigma_E$  and magnetic loss  $\sigma_M$ . By relating these parameters via

$$\frac{\sigma_E}{\epsilon_0} = \frac{\sigma_M}{\mu_0},$$

the intrinsic impedance of the medium is matched to free-space, and reflectionless transmission of a normally incident plane wave into the layer can be achieved. Once in the layer, the incident wave is rapidly attenuated. To absorb waves at oblique incidence, Berenger's PML splits transverse field components into two parts, normal and tangential to the boundary, and only the normal component is attenuated [71]. This formulation, although non-Maxwellian<sup>3</sup>, can achieve reflection errors below  $10^{-5}$  [11, 71].

This thesis uses an alternative (Maxwellian) formulation of Berenger's PML: the Uniaxial PML (UPML) [73]. Fig. 4.2 shows the structure of a two-dimensional computational lattice with the problem space surrounded by a thin layer of the UPML absorbing boundary. An abridged derivation of the UPML is presented in appendix B.

---

<sup>3</sup>Berenger's PML results in 12 coupled differential equations relating the **E** and **H** fields; these include dependent sources, rendering the medium active, and hence non-Maxwellian [72].

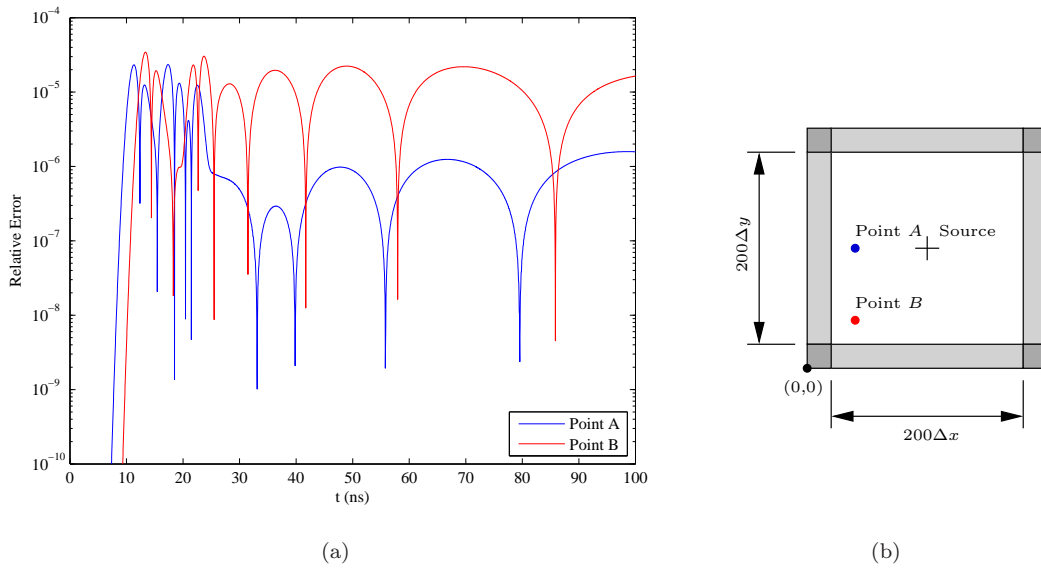


Figure 4.3: Relative reflection error observed for a 12-cell thick UPML operating a 2D  $\text{TM}_z$  lattice. The source is located at  $(100, 100)$ , Point  $A$  at  $(5, 100)$  and Point  $B$  at  $(5, 5)$ .

### 4.3.2 UPML Performance

Fig. 4.3(a) shows the performance of a two-dimensional,  $\text{TM}_z$  polarised, 12-cell thick UPML for two sample points,  $A$  and  $B$  as indicated on Fig. 4.3(b). A differentiated Gaussian pulse, given by  $p(t) = -2 \left[ \frac{t-t_0}{t_w} \right] \exp \left[ -\left( \frac{t-t_0}{t_w} \right)^2 \right]$ , is used to excite the lattice, where  $t_w = 1.23 \mu\text{s}$  and  $t_0 = 5t_w$ . The cell size is  $\Delta x = \Delta y = 0.01 \text{ m}$ , and the time increment  $\Delta t = 22.4 \text{ ps}$ . The simulation was run for 5000 time steps (112 ns) and the relative error ( $\xi$ ) is calculated over this period (for the  $E_z$  field component) using

$$\xi|_{i,j}^{n+0.5} = \frac{\left|E_z|_{i,j}^{n+0.5} - E_z^{\text{Ref}}|_{i,j}^{n+0.5}\right|}{\max\left|E_z^{\text{Ref}}|_{i,j}^{n+0.5}\right|},$$

where the reference solution,  $E_z^{\text{Ref}}$ , is calculated by solving a problem space sufficiently large such that reflections from the boundaries are not present in the first 5000 time steps. Larger errors are observed in Fig. 4.3(a) for point  $B$ , and this observation is consistent with other numerical experiments conducted with the UPML [11, pp. 313–323]. The UPML parameters found to give the lowest error in this case are:  $\kappa_{\max} = 3.0$  and  $\sigma_{\max} = 0.64$ . The performance of the UPML is observed to degrade with higher angles of incidence. However, in most cases the relative error is bounded below  $10^{-4}$ .

#### 4.4 Parallel Implementation of the FDTD Method

#### 4.4.1 Computational Requirements

One of the major limitations of the FDTD method, particularly when applied to electrically large problems, is computational requirements that often exceed the capability of a single-processor computer. To illustrate this, each three-dimensional lattice cell requires memory to

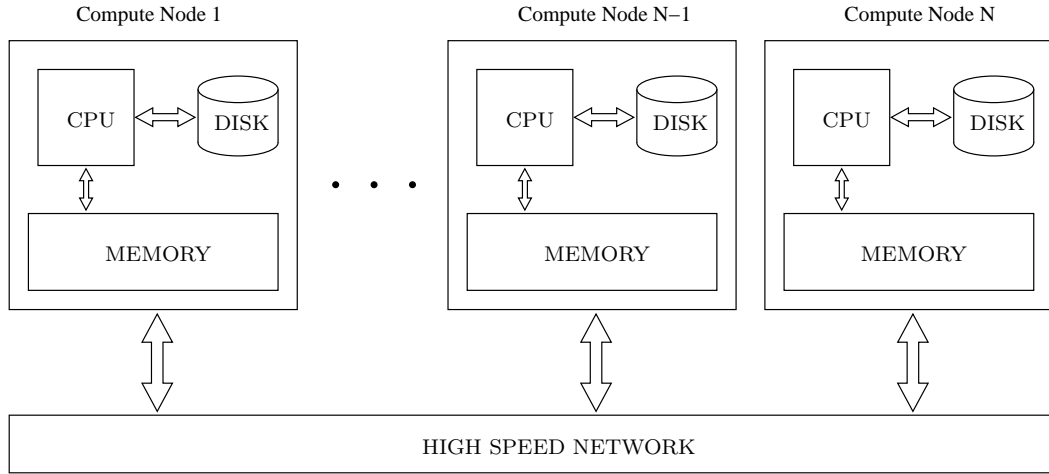


Figure 4.4: Architecture of a Beowulf computer cluster. Adapted from [49, 120–125]

store six field components (for two-dimensional  $\text{TM}_z$  or  $\text{TE}_z$  lattices only three components must be stored). As the FDTD method is iterative and to minimise round-off errors, floating point numbers must be stored with double precision to correctly represent the fields. Each field component thus requires 64 bits (8 bytes), and in a three-dimensional lattice, each unit cell requires 48 bytes of memory. For an electrically large, three-dimensional, problem the number of mesh cells required to represent the geometry may exceed  $3 \times 10^9$ , and the corresponding memory required is in excess of 150 gigabytes. This number represents a lower bound, as in practise additional storage is required for auxiliary variables and the implementation of the UPML. In some cases the simulation must be run for more than 20,000 time steps before the fields reach steady-state. Solving problems of this scale using a single processor computer is not currently feasible. One solution to this challenge is to use parallel computing to split the computations over multiple processors. Fortunately, the FDTD method is well suited for parallelisation with only minor changes to the algorithm.

#### 4.4.2 High Performance Computing

High Performance Computing (HPC) is a generic term for systems utilising parallel computers to more efficiently solve large computational problems. One of the more recent developments in HPC has been the use of clusters composed of many (relatively) inexpensive computers connected via a high speed network; this is typically termed a *Beowulf*<sup>4</sup> cluster. Unlike dedicated parallel computers, *Beowulf* clusters use software and communications protocols to present the programmer with a single ‘virtual’ computer, where many of the details of the physical connections have been abstracted away. The cluster runs an operating system (in most cases GNU/Linux) and the nodes communicate by requesting and sending messages (containing data) over the network. One of the most widely used communications protocol for HPC *Beowulf* clusters is the Message Passing Interface (MPI). Several implementations of the MPI exist, and the research reported in this thesis has used MPICH2 [74].

As illustrated in Fig. 4.4, each compute node in a Beowulf computer cluster contains separate processing (CPU), local storage (disk) and memory elements. The nodes are linked together

<sup>4</sup>The name *Beowulf* comes from the main character in the Old English epic poem of the same name; *Beowulf* is described as having “thirty men’s heft of grasp in the gripe of his hand.”

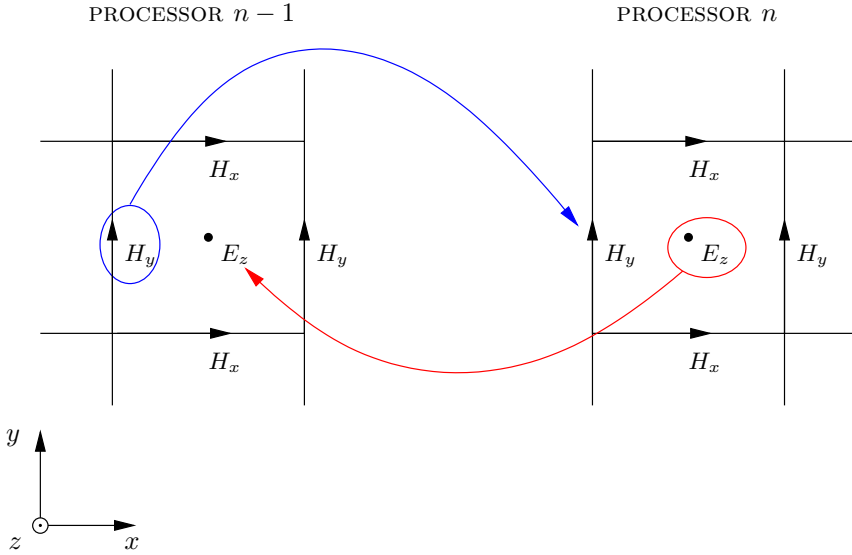


Figure 4.5:  $\text{TM}_z$  parallelization with field exchange in the  $x$  direction.

via a high speed network (e.g. Gigabit Ethernet or InfiniBand) over which the MPI messages are passed. Each block labelled CPU may contain multiple processors; in this case the memory within that node is shared and directly addressed. However, data stored in another node cannot be directly addressed and must be requested via MPI.

#### 4.4.3 Field Exchange

As each field component depends only on the immediately adjacent components, the FDTD lattice can be straightforwardly subdivided into smaller sub-domains, each within the computational limits of a single computer. The sub-domains are assigned to separate compute nodes on a *Beowulf* cluster, and the boundary fields exchanged every time step, thereby allowing field propagation between the sub-domains [49, 145–150].

Fig. 4.5 shows the electric and magnetic field exchanges between processor  $n - 1$  and  $n$  for a  $\text{TM}_z$  lattice parallelized in the  $x$  direction. A single layer of cells overlap on the boundary between processors  $n - 1$  and  $n$ . The electric fields are updated in both processors using (4.16). The updated  $E_z$  fields on the left boundary of processor  $n$  are passed back to processor  $n - 1$ , overwriting the existing electric fields on the right boundary. The magnetic fields are then updated in both processors using (A.4)–(A.5). The  $H_y$  fields on the right boundary of processor  $n - 1$  are passed forward to processor  $n$ , overwriting the existing magnetic fields. The  $E_z$  fields are then updated, and the field-transfer process is repeated at every time step. This arrangement allows waves to propagate in both directions between the processors with no spurious reflections or distortions. It should be noted that, in this example,  $H_x$  fields do not need to be exchanged as these are normal to the ‘slice’ direction. For maximum efficiency in two-dimensions, fields are exchanged in both the  $x$  and  $y$  directions, which can be treated independently. This process can be readily extended to three-dimensions.

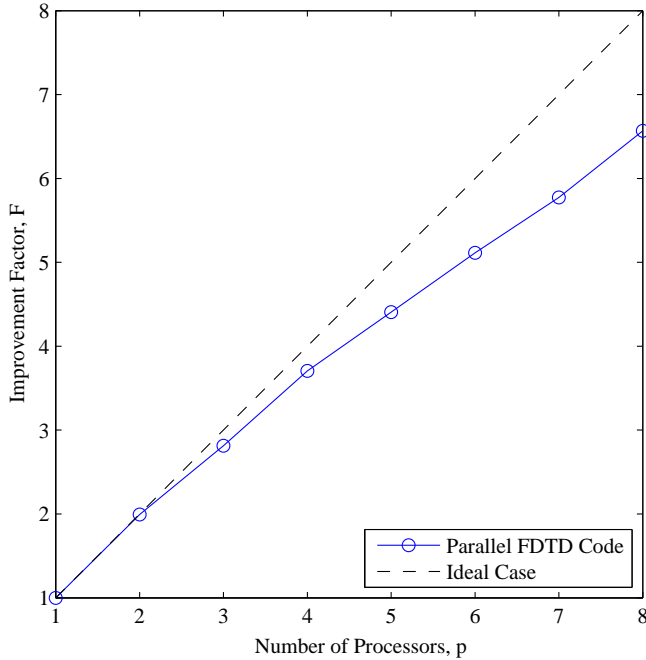


Figure 4.6: Improvement in simulation time versus the number of processors allocated for a 2D  $\text{TM}_z$  implementation in FORTRAN 90 with data passed between the processors using MPICH2.

#### 4.4.4 Parallel Efficiency

The efficiency of the two-dimensional implementation ( $\text{TM}_z$  polarisation) of the parallel FDTD method was validated by solving a  $1680 \times 1680$  cell test space. No materials were modelled and the edges of the simulation space were terminated with the UPML. The simulation was run for 20,000 time steps, with one to eight processors (Intel Xeon 2.00 GHz) allocated. An improvement factor  $F$ , was defined by

$$F(p) = \frac{T(1)}{T(p)},$$

where  $T(p)$  is the computational time when solving the test space with  $p$  processors. Fig. 4.6 shows the improvement in simulation time versus the number of processors allocated. In the ideal case, the improvement in simulation time should scale linearly with the number of processors allocated [49]. However, in practise, communication overheads between the processors will result in performance that is not quite as good as the ideal case.

## 4.5 Validation of the Codes

The FDTD codes developed in this thesis were implemented in Fortran 90 and compiled with version 10.1 of the Intel Fortran Compiler for Linux, with all speed optimisations enabled. This section presents the results for three test cases used to validate the implementation. The first two tests examine propagation in free-space, and are used to show the FDTD codes give the correct distance dependency and radiation patterns. The third test compares the FDTD code to a two-dimensional geometrical optics and uniform theory of diffraction (GO/UTD) code for

diffraction around a perfectly conducting knife edge.

#### 4.5.1 2D and 3D Distance Dependency

Fig. 4.7 shows plots of the electric field magnitude, measured as a function of distance from the source, for the two- and three-dimensional FDTD lattices. The applied source is a unit amplitude sinusoid with  $f = 1.0$  GHz, and the lattice cell size is 10 mm. A single  $E_z$  component is used to excite the three-dimensional and two-dimensional  $\text{TM}_z$  lattices; while a  $E_y$  component is used for the  $\text{TE}_z$  lattice. In free-space, the electric fields are known *a priori* to decrease exponentially with distance according to

$$|E| \propto \frac{1}{d^n}, \quad (4.18)$$

where  $d$  is the separation distance, and  $n$  is the distance dependency exponent. In two-dimensional free-space  $n = 0.5$ , and in three dimensions  $n = 1.0$ ; these values both agree with the results obtained from the FDTD simulations. It is observed in Fig. 4.7 that for small separation distances the electric fields do not follow the exponential relationship in (4.18). In the small region around the radiating component near-field effects dominate and cause deviations from (4.18).

#### 4.5.2 3D Radiation Pattern

Fig. 4.8 shows the azimuth and elevation radiation patterns extracted from a three-dimensional simulation of a short dipole radiating in free-space. A single  $E_z$  field component is used to excite the lattice with a sinusoid at a frequency of 1.0 GHz. The  $E_z$  field is measured on a radial distance,  $3\lambda$  from the source point. In the far field, the azimuth radiation pattern from a short dipole is omnidirectional; while the elevation pattern is given by  $E_\theta \propto \sin \theta$ , where  $\theta$  is the elevation angle. In Fig. 4.8 the theoretical radiation patterns have been scaled to the values extracted from the FDTD simulation. A good agreement exists for both the azimuth and elevation patterns.

#### 4.5.3 Diffraction by a Single PEC Knife Edge

Fig. 4.9 shows the magnitude of a two-dimensional  $\text{TM}_z$  polarised electric field at a radius of  $2\lambda$  around the tip of a PEC knife edge ( $\lambda/30$  thick) calculated using a two-dimensional geometrical optics and uniform theory of diffraction (GO/UTD) code and the two-dimensional  $\text{TM}_z$  FDTD code. The source point is located  $50\lambda$  from the tip at angle  $\phi = 75^\circ$ . Close agreement is observed between the FDTD and GO/UTD results. The small differences in the fields are likely due to the finite thickness ( $\Delta = 10$  mm) PEC knife edge in the FDTD lattice and numerical dispersion.

### 4.6 Summary

This chapter has focused on aspects of the FDTD method relevant for indoor propagation modelling. The FDTD update equations have been derived, and a brief overview of numerical dispersion and stability presented. Issues related to the excitation of the lattice with pulse and sinusoidal functions have also been examined. The importance of appropriate boundary

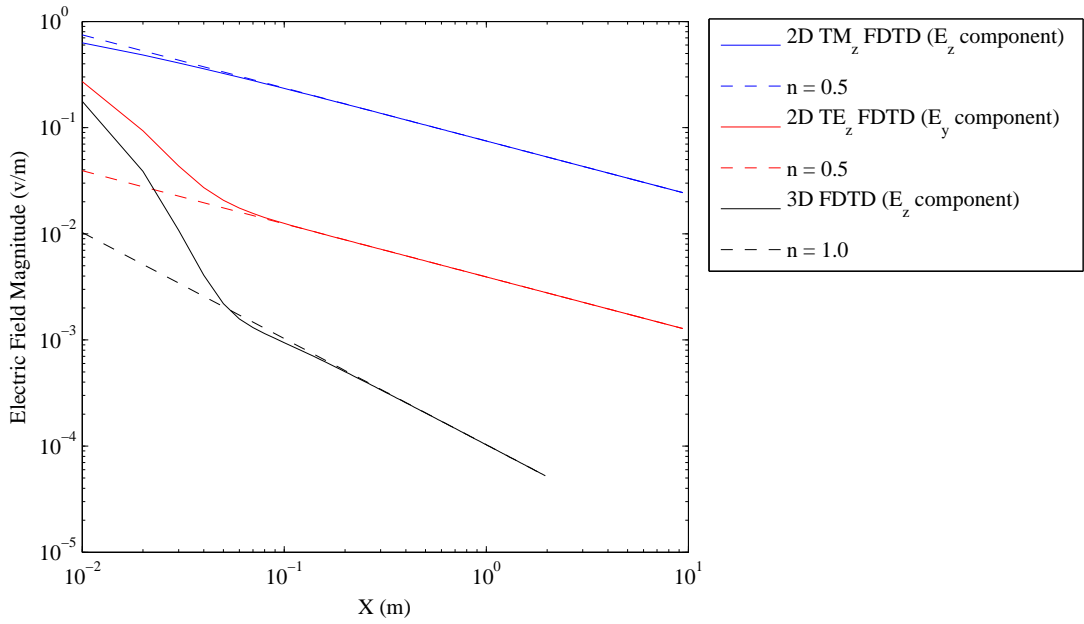


Figure 4.7: Electric field strengths measured in free-space for two- and three-dimensional FDTD method.

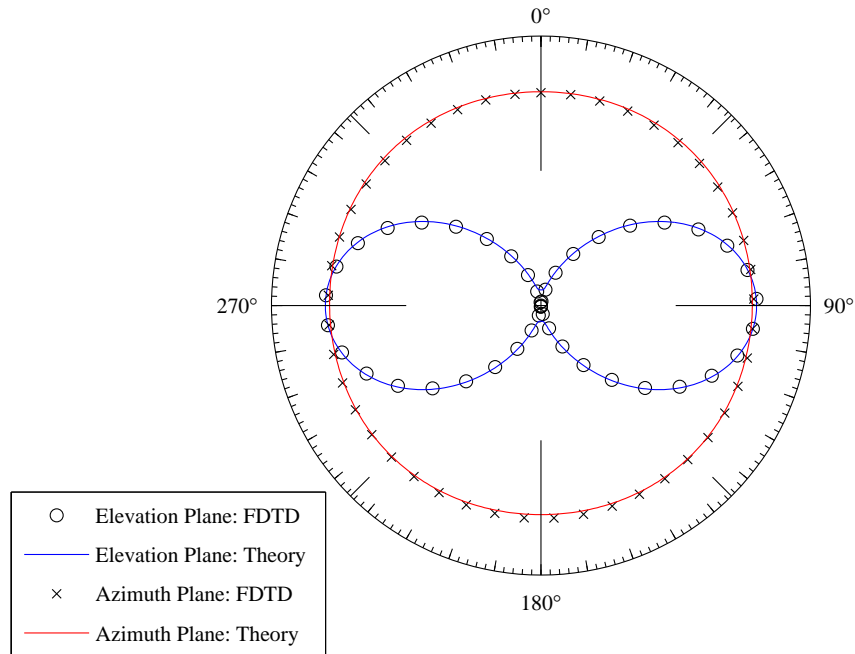


Figure 4.8: Comparison between calculated and theoretical azimuth and elevation radiation patterns from a short dipole antenna. A single  $E_z$  component in the 3D FDTD lattice is excited with a sinusoid at  $f = 1.0$  GHz. The lattice size is  $\Delta = 10$  mm.

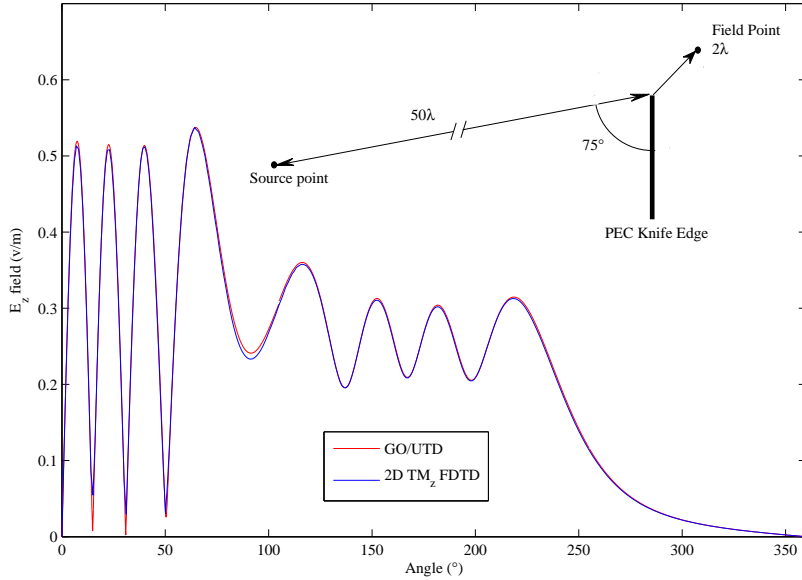


Figure 4.9:  $\text{TM}_z E_z$  field magnitude calculated  $2\lambda$  around the tip of a PEC knife edge using GO/UTD and FDTD codes. The source is located  $50\lambda$  from the tip at an angle of  $75^\circ$ .

conditions for unbounded problems is discussed, and a brief derivation of the UPML is provided in appendix B.

One of the major limitations of the FDTD method to model electrically large problems (such as indoor propagation) are computational requirements that can exceed the capabilities of a single computer. Hence, a portion of this chapter has focused on the implementation of the parallel FDTD method on *Beowulf* computer clusters. The implementation has been tested and shows good performance and parallel efficiency. Also presented in this chapter are the results for three test cases where analytical or alternative solutions are known; these are used to demonstrate the validity of the implementation. Chapter 5 will focus on the application of the FDTD method for indoor propagation modelling, and outline the propagation studies considered in this thesis.

# Chapter 5

## Indoor Propagation Modelling with the FDTD Method

### 5.1 Introduction

Chapter 4 introduced the FDTD algorithm, derived a set of update equations, discussed the implementation of the UPML absorbing boundary and outlined the parallelisation strategy. The boundary conditions and parallelisation are important aspects of the FDTD method when modelling unbounded and electrically large problems. However, chapter 4 has not explicitly considered how the FDTD method can be used to model radio-wave propagation in indoor environments. The goal of this chapter, therefore, is to show the reader how the FDTD method can be applied to characterise the indoor radio channel, and thereby address the goals of this thesis posed at the end of chapter 3.

Section §5.2 outlines the conversion of time-domain electromagnetic fields (as calculated by FDTD simulations) to quantities relevant for propagation prediction, such as the power and path-loss. Another major focus of this chapter (section §5.3) is the development of post-processing techniques to identify and visualise the dominant propagation mechanisms, e.g. density plots of the steady-state electric field phase and streamline visualisations of the Poynting vector. A brief overview of the electromagnetic properties of common building materials is provided in section §5.4. Section §5.5 describes the propagation studies examined in this thesis to characterise the indoor radio channel. It should be noted that the studies presented in section §5.5 will not be quantitatively examined in this chapter, rather, the goal is to outline the logical strategy followed in the remaining chapters of this thesis. The major findings of the chapter are presented in section §5.6.

### 5.2 Propagation Modelling with the FDTD Method

#### 5.2.1 Field Magnitude and Phase

The steady-state magnitude and phase of any field component can be found by taking a Fourier Transform of the time-history at each point in the lattice<sup>1</sup>. In continuous time, the Fourier

---

<sup>1</sup>This technique can be applied for both pulse and sinusoidal excitation sources.

Transform can be written as

$$U(\omega) = \int_{-\infty}^{\infty} u(t) \exp(-j\omega t) dt, \quad (5.1)$$

where  $\omega = 2\pi f$ . However, evaluating (5.1) at the conclusion of time-stepping requires the whole time-history to be recorded, and is an inefficient use of data storage. In discrete time ( $n\Delta t$ ) and space ( $i, j, k$ ), and for a fixed frequency,  $f$ , (5.1) can be written as a running sum

$$U_f|_{i,j,k} = U_f|_{i,j,k} + u|_{i,j,k}^n \times \exp(-j2\pi f n \Delta t), \quad (5.2)$$

where  $U_f|_{i,j,k} = 0$  initially. This approach only requires one additional variable ( $U_f$ ), which is declared as a complex double (128 bits). At the end of the simulation the magnitude and phase can be found by taking the absolute value, and argument, of  $U_f|_{i,j,k}$  respectively. The magnitude and phase throughout the lattice are normalised to the source point (assumed to be  $1\angle 0^\circ$  V/m)<sup>2</sup>.

### 5.2.2 Path-Loss

The link-budget equation for a wireless system can be represented generally as

$$P_r = P_t + G - L - P_L \quad (\text{dBm}),$$

where  $P_t$  and  $P_r$  are the transmitted and received powers (in dBm),  $G$  and  $L$  represent lumped gains and losses (e.g. antennas and cables), and  $P_L$  is the path-loss. Only the path-loss depends on the environment, and in three-dimensional<sup>3</sup> free-space, a comparison can be made between the FDTD results for the steady-state electric field magnitude and the Friis equation [2, p. 71] to determine the effective gains of a radiating element in the FDTD lattice. A single  $E_z$  field component is excited, and the field measured along a radial line in the normal plane. The Friis equation is given by

$$\frac{P_r}{P_t} = G_t G_r \left( \frac{\lambda}{4\pi d} \right)^2,$$

where  $P_t$  and  $P_r$  are the transmitted and received powers (in Watts),  $d$  is the separation distance between the transmitting and receiving antennas, and  $G_t$  and  $G_r$  are the transmitter and receiver antenna gains. To convert the FDTD results to power or path-loss (and to make valid comparisons against experimental measurements) a calibration needs to be run in free-space (for each combination of  $f$  and  $\Delta$ ) to determine the “effective values” of  $G_t$  and  $G_r$ . A brief overview of two- and three-dimensional free-space calibrations is presented in appendix C.

### 5.2.3 Impulse Response

The impulse response can be measured by recording the time history at desired points in the lattice when modulated-pulse excitation is used [49, pp. 97–100]. Although the magnitude of the impulse response could be extracted using an envelope detector, this approach would not preserve the phase information. The complex base-band impulse response can be found by

<sup>2</sup> $1\angle 0^\circ$  A/m in the case of magnetic field excitation.

<sup>3</sup>Two-dimensional results cannot be converted to path-loss and are typically presented with the source normalised to  $1\angle 0^\circ$  V/m.

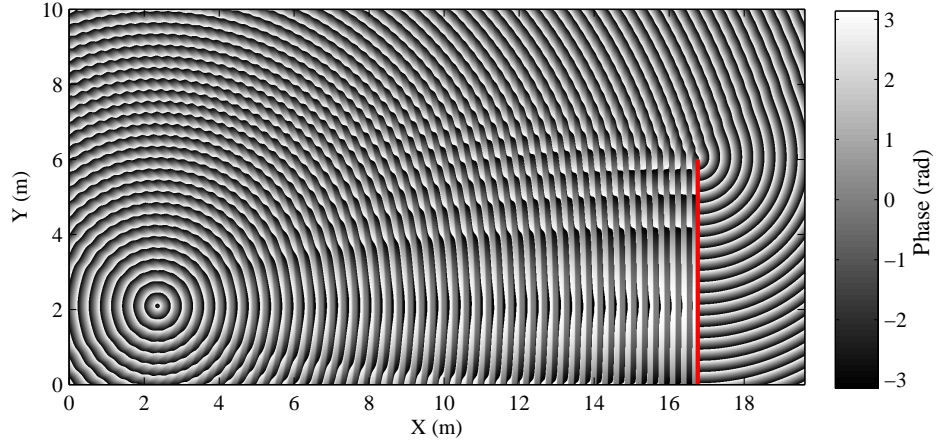


Figure 5.1: Density plot of the steady-state  $E_z$  phase around a PEC knife edge at 1.0 GHz. The knife edge is identified in red.

separating the time history into in-phase and quadrature components. The unwanted harmonic terms can be removed via digital filtering, and the magnitude and phase of the impulse response extracted by combining the in-phase and quadrature components in post processing.

## 5.3 Visualising Propagation

### 5.3.1 Phase Plots

Density plots of the steady-state magnitude (usually converted into path-loss and shown on a dB scale) are often used to determine the distribution of received power in a given geometry, and frequently form the basis of comparisons between FDTD simulations and experimental measurements. However, additional insights into the propagation processes may also be gained by examining the curvature of the phase-fronts in density plots of the steady state phase. As an example, Fig. 5.1 shows a density plot of the steady-state  $E_z$  field phase (in a two-dimensional  $\text{TM}_z$  lattice) for diffraction around a PEC knife edge (a depiction of the geometry is shown in Fig. 4.9). It is observed in Fig. 5.1 that most phase fronts above the source are radially centred, representing a cylindrically diverging field, and indicating the dominant propagation mechanism in these regions is line-of-sight propagation. Directly in front of the PEC knife edge the direct and reflected components have similar magnitude, and distinct changes in the phase are visible<sup>4</sup>. Moreover, phase fronts in the shadow region of the knife edge are radially centred on the tip, supporting the presence of an edge diffracted component (as might be predicted from the geometrical or uniform theory of diffraction).

### 5.3.2 Poynting Vectors

In some circumstances visualisations of the electric and magnetic fields can be used to determine the dominant propagation paths. However, the presence of strong multi-path components tends

<sup>4</sup>It should be noted that phase plots, such as Fig. 5.1, show the *net* phase caused by the vector summation of various components in the environment. This can lead to difficulties in interpreting the results.

to perturb the fields, making interpretation difficult. As discussed in this section, an alternative approach is to calculate the power flow through the environment from the full-wave FDTD simulation results. A measure of the power flow is given by the time averaged Poynting vector,

$$\mathbf{S} = \frac{1}{2} \Re[\mathbf{E} \times \mathbf{H}^*] \quad \text{W/m}^2, \quad (5.3)$$

where  $\mathbf{E}$  and  $\mathbf{H}$  are the steady-state (time-harmonic) vector electric and magnetic fields respectively, and  $*$  denotes the complex conjugate. As noted in section §4.2.3, and Fig. 4.1, the  $\mathbf{E}$  and  $\mathbf{H}$  field components are spatially staggered on the Yee lattice. To correctly calculate the Poynting vector the fields need to be co-located, and this is achieved by spatially averaging the  $\mathbf{E}$  and  $\mathbf{H}$  field components to  $(i + 0.5, j + 0.5, k + 0.5)$ . As an example, the spatially averaged  $E_x$  field is

$$E_x|_{i+0.5,j+0.5,k+0.5} = \frac{1}{4} \left[ E_x|_{i+0.5,j,k+1} + E_x|_{i+0.5,j+1,k+1} \right. \\ \left. + E_x|_{i+0.5,j+1,k} + E_x|_{i+0.5,j,k} \right].$$

Similar expressions for the remaining field components can be derived, and the steady-state magnitude and phase can be found by applying (5.2). Expanding (5.3) for the Poynting vector in Cartesian coordinates gives

$$S_x = \frac{1}{2} \Re[E_y^m \exp(jE_y^p) H_z^m \exp(-jH_z^p) - E_z^m \exp(jE_z^p) H_y^m \exp(-jH_y^p)] \\ S_y = \frac{1}{2} \Re[E_z^m \exp(jE_z^p) H_x^m \exp(-jH_x^p) - E_x^m \exp(jE_x^p) H_z^m \exp(-jH_z^p)] \\ S_z = \frac{1}{2} \Re[E_x^m \exp(jE_x^p) H_y^m \exp(-jH_y^p) - E_y^m \exp(jE_y^p) H_x^m \exp(-jH_x^p)],$$

where  $(\cdot)^m$  and  $(\cdot)^p$  are the steady-state magnitude and phase respectively.

The energy flow can be visualised by drawing an arrow in the direction of the Poynting vector at each point in the lattice. However, it can be difficult to correctly interpret this visualisation in complex geometries. An alternative approach (outlined in §5.3.3) is to project streamlines through the Poynting vector field.

### 5.3.3 Streamline Visualisations of the Poynting Vector

At each point in the field, the Poynting vector indicates the direction and magnitude of the *net* energy flow. Streamlines can be projected through this space by applying principles developed in fluid dynamics for studying steady flows [75]. A similar analysis using Poynting vector streamlines to visualise energy flow escaping backwards around a pyramidal horn antenna was shown in [76]. The local tangent to a streamline is the vector representing energy flow at that point, and in three-dimensions the differential equation governing a streamline is given by

$$\frac{d\vec{p}(a)}{da} = \mathbf{S}(\vec{p}(a)), \quad (5.4)$$

where  $\vec{p}$  is the position (in Cartesian coordinates),  $a$  is the parameter along the streamline, and  $\mathbf{S}(\vec{p})$  is the Poynting vector at  $\vec{p}$ .

Fig. 5.2 shows a graphical representation of the process to project the streamline through the Poynting vector field. Starting from an appropriate initial position,  $\vec{p}(a)$ , the streamline is computed by numerically solving (5.4) using forward differences (tracing the direction of the

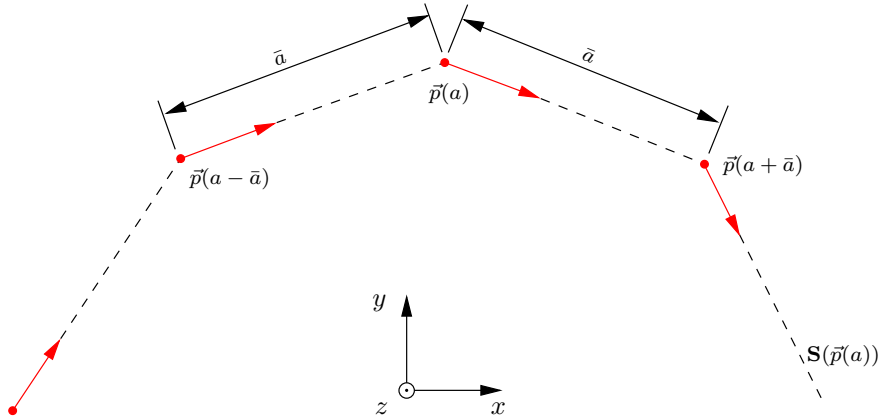


Figure 5.2: Streamlines are drawn by tracing a path through the Poynting vectors. This diagram shows the forward difference case.

physical propagation of the Poynting vector out of the lattice) or backward differences (tracing the Poynting vector back to the transmitting antenna). The forward difference expression is given by

$$\frac{\vec{p}(a + \bar{a}) - \vec{p}(a)}{\bar{a}} = \mathbf{S}(\vec{p}(a)), \quad (5.5)$$

and the backward difference by

$$\frac{\vec{p}(a) - \vec{p}(a - \bar{a})}{\bar{a}} = -\mathbf{S}(\vec{p}(a)). \quad (5.6)$$

A step size  $\bar{a} = 2\Delta$  (where  $\Delta$  is the lattice cell size) was found to be a good trade off between computational efficiency and accuracy. In the case where  $\mathbf{S}(\vec{p}(a + \bar{a}))$  does not lie on the rectangular FDTD lattice, it is interpolated using values from adjacent cells. Linear and cubic spline interpolation methods were implemented, and in both cases the resulting streamlines were very similar. A single initial position results in one streamline which may not be representative of the dominant propagation mechanism in a region. To assist in the visualisation of the net energy flow in a region of space 100 points in a  $3\lambda$  ‘cloud’ around the specified initial position are typically seeded.

### 5.3.4 Propagation Through an Infinite Lossy Dielectric Slab

Fig. 5.3 shows streamlines traced through an infinite dielectric slab<sup>5</sup> ( $\epsilon_r = 6.0$  and  $\sigma_e = 0.05$  S/m)<sup>6</sup> from 50 seed points (indicated by •) to the source point (indicated by ✕). A frequency of 1.0 GHz was used, with a mesh size  $\Delta = 5$  mm to minimise numerical dispersion. The streamlines are observed to bend toward the normal when passing through the vacuum-slab interface, and away from the normal at the slab-vacuum interface. These results agree with ray-optical refraction (Snell’s law). It is also observed that the streamlines (particularly in front of the slab) are not straight—the ripples develop as the Poynting vector is calculated in the time-domain—as these represent the *net* energy flow. In this case the net energy flow includes the specular reflection component from the slab interface.

<sup>5</sup>An infinite slab is modelled by extending the dielectric block into the UPML absorbing boundaries, thereby preventing spurious edge effects.

<sup>6</sup>These parameters are typical for concrete.

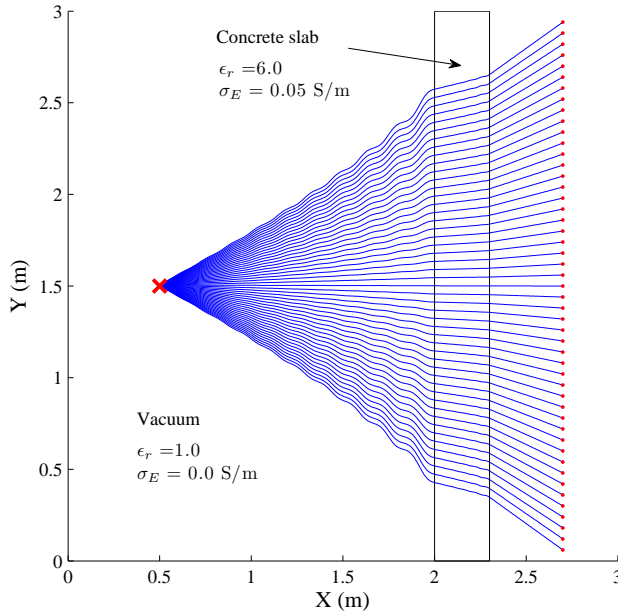


Figure 5.3: Streamlines of the Poynting vector, traced from seed points (●) to the source (✗) through a 0.30 m thick concrete slab for a two-dimensional  $\text{TM}_z$  lattice.

## 5.4 Material Modelling

The material properties for a general isotropic, homogeneous object in the FDTD lattice can be characterised by  $\epsilon_r$ ,  $\mu_r$ ,  $\sigma_E$  and  $\sigma_M$  in (A.1)–(A.6). Over the frequency range of interest (1.0–2.5 GHz), the electromagnetic properties of typical materials encountered within buildings can be modelled as frequency independent [32]. Furthermore, the majority of these materials can be classified as dielectric and non-magnetic, with  $\mu_r = 1.0$  and  $\sigma_M = 0.0$ . Experimental measurements of the electrical properties for typical building materials have been published by a number of authors, and there is often a large variation in the values reported, even at similar frequencies<sup>7</sup>. Table 5.1 lists some of the significant building materials used in the construction of multi-storey buildings, and presents nominal values for the electrical properties ( $\epsilon_r$  and  $\sigma_E$ ) as used in the FDTD simulations.

## 5.5 Interference Modelling and Mitigation with the FDTD Method

As stated in Chapter 3, the major motivations of this thesis are the characterisation and (possible) mitigation of interference arising from co-channel transmitters located on adjacent (or nearly adjacent)<sup>8</sup> floors in multi-storey buildings. However, it is first necessary to characterise the indoor radio channel, particularly focusing on inter-floor propagation. The following three chapters (6, 7 and 8) of this thesis are dedicated to investigating inter-floor propagation for var-

<sup>7</sup>The exact composition of many common building materials varies considerably, making correct classification difficult.

<sup>8</sup>It has been shown that the majority of received power (and thus interference) arrives from the immediately adjacent floors [6].

Table 5.1: Electrical Properties of Common Building Materials over 1.0 GHz–2.5 GHz

Material	Use	Electrical Properties		References
		$\epsilon_r$	$\sigma_E$ (mS/m)	
Concrete <sup>a</sup>	Floors <sup>b</sup> , internal structural supports and external walls.	4.0 <sup>c</sup> , 6.0	10.0–50.0	[32, 41, 77–79]
Glass	Exterior <sup>d</sup> and internal windows, usually not load bearing in multi-storey buildings.	3.0	2.0	[32, 78, 80]
Drywall <sup>e</sup>	Internal partitions, not load-bearing (typically nailed to both sides of a timber frame).	3.0	5.0	[32, 41, 78]
Timber	Framing for internal partitions, usually not load bearing in multi-storey buildings <sup>f</sup> . Also a major component of typical office furniture.	3.0	10.0	[32, 81]
Metal	Framing for windows, ducts and pipes, reinforcing bars, and a component of typical office furniture.	1.0	$10^{10}$	[82, p. 62]

<sup>a</sup>Concrete is a composite material composed of cement, aggregate (crushed stone with varying degrees of coarseness) and water, but is typically modelled as homogeneous when applying time-domain methods [41, 56, 58, 60, 77].

<sup>b</sup>Concrete has high strength under compressive loads, but is significantly weaker under tension; it is necessary to reinforce any structures likely to experience tension, such as floors, with metal bars (rebar), which is usually arranged in a grid mesh.

<sup>c</sup> $\epsilon_r = 4.0$  was used for three-dimensional simulations due to limits on the computational resources.

<sup>d</sup>Contemporary architectural styles use glass more extensively on exterior surfaces.

<sup>e</sup>Also known as plaster- or gib-board.

<sup>f</sup>An exception is a light-weight timber-framed top floor added to an existing multi-storey building.

ious scenarios with two- and three-dimensional implementations of the FDTD method. These three studies are followed by chapter 9, which outlines the use of the FDTD method to model interference and interference-mitigation tools, and the implications for modern wireless systems. A brief description of each study is outlined and accompanied by generalised depictions of the geometries investigated.

### 5.5.1 Propagation Study A—Within the Building Perimeter (2D)

This study considers a vertical two-dimensional ‘slice’ through a building, as illustrated in Fig. 5.4, and the analysis of this geometry forms the basis of chapter 6. The vertical slice consists of multiple concrete floors in free-space. The concrete floors are assumed to be homogeneous, and can be completely specified by their relative permittivity and conductivity (i.e. the electrical properties of the concrete are not frequency dependent). It is recognised that this geometry is simplistic, but it is broadly representative of many modern office buildings, and serves as a good starting point to identify the dominant inter-floor propagation mechanisms. The analysis of inter-floor propagation in similar two- and three-dimensional geometries has been considered previously using GO/UTD methods [38, 83].

The effects of architectural and structural details, such as glass windows, metal reinforcing bars and hanging panels, have also been considered in chapter 6. Buildings similar to those considered in Fig. 5.4 often have internal concrete structures, such as a services shaft containing

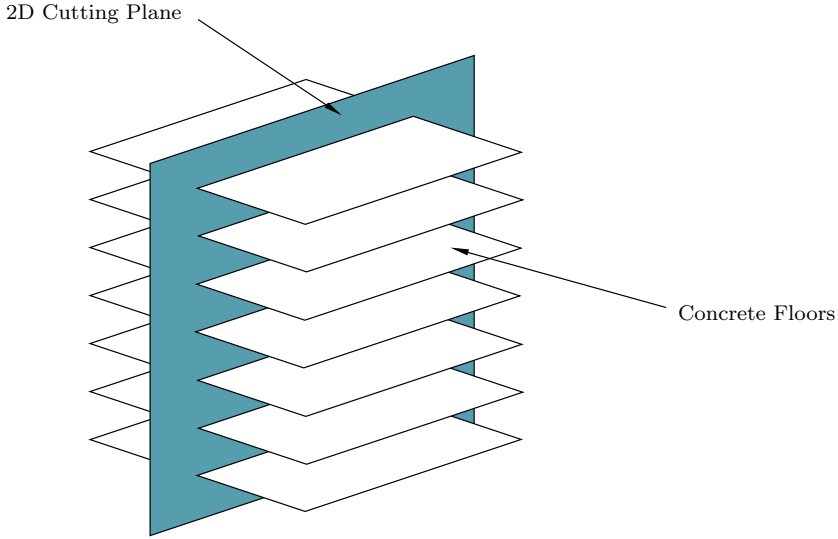


Figure 5.4: Propagation Study A—Within the Building Perimeter (2D).

lifts and stairwells. An initial, two-dimensional, approximation of a hollow concrete services shaft has also been studied as part of this geometry. However, small-scale internal details, such as office furniture and soft partitions, are more difficult to model correctly in two-dimensions. Consequently, an analysis involving the internal details is deferred until Chapter 8, when a three-dimensional geometry is considered.

It is also difficult to directly compare simulation results for this geometry with experimental measurements made within buildings. The 2.5D approximation outlined in appendix E is not applicable in this case, as most propagation paths are not in free-space. Instead, comparisons are made between experimental measurements of the path-loss and *mechanistic* models for path-loss developed from the FDTD simulations.

### 5.5.2 Propagation Study B—External to the Building Perimeter (2D)

The analysis of inter-floor propagation on paths contained within the building perimeter is considered in chapter 6. However, as more floors are penetrated, external paths are thought to contribute more toward the received power, because internal paths are significantly attenuated. In dense urban environments, nearby buildings in close proximity can potentially reflect strong signals back onto lower floors, and this argument is supported by previous measurement studies [84, 85].

Consequently, the propagation study examined in chapter 7 extends the two-dimensional slice, shown in Fig. 5.4, to include possible reflection and scattering paths from nearby buildings, as illustrated in Fig. 5.5. The two-dimensional geometry depicted in Fig. 5.5 considers partial models of two buildings, identified as A and B, separated by a distance  $d$ . The transmitter is located in Building A and reflections can potentially occur at the face of Building B. The internal details of the buildings have been ignored in this study, however, the role of surface irregularities (such as glass windows and architectural features) are examined in some detail.

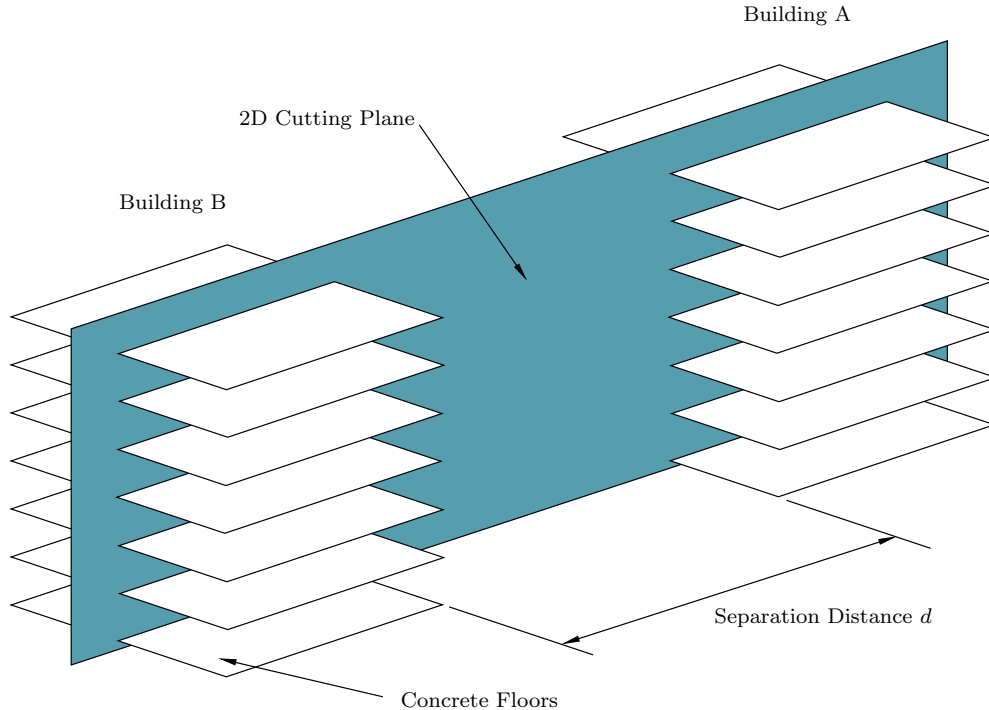


Figure 5.5: Propagation Study B—External to the Building Perimeter (2D).

### 5.5.3 Propagation Study C—Within the Building Perimeter (3D)

The propagation studies presented in chapters 6 and 7 largely focus on two-dimensional characterisations of the inter-floor radio channel. It is important to note that, unlike the single-floor case, no single two-dimensional slice through a multi-floor geometry can correctly account for all possible propagation paths. For example, many buildings have concrete shafts containing elevators and stairwells, and propagation to adjacent floors around (or through) such shafts can only be thoroughly examined in three dimensions. Accordingly, chapter 8 examines propagation between three floors<sup>9</sup> of a multi-storey building in three-dimensions. A depiction of the geometry investigated is shown in Fig. 5.6.

There has also been limited research into the impact of clutter in the environment (such as office furniture) has on propagation. Most applications of time-domain methods to model propagation within buildings have assumed these buildings to be empty [41, 54–56, 58, 60–62] (though [54, 60, 61] did assess the impact of different wall types). However, typical office buildings contain varying amounts of furniture and other metallic and dielectric clutter. Chapter 8 also makes comparisons between a basic FDTD model (with a similar level of detail to models in the existing literature) and a more detailed model that includes some furniture and similar objects.

### 5.5.4 Interference Prediction and Mitigation

Predicting wireless system performance in the presence of interference has traditionally been accomplished with empirical models based on experimental measurements. However, when used in practise, empirical models have frequently been found to result in pessimistic estimates of system performance [6]. More accurate findings have been reported when the empirical

---

<sup>9</sup>Only three floors have been examined in three-dimensions due current computing limitations.

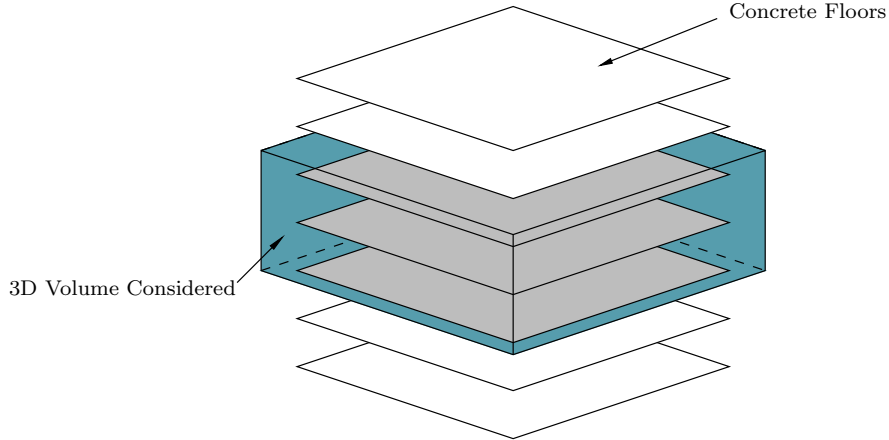


Figure 5.6: Propagation Study C—Within the Building Perimeter (3D).

models were complemented with physical factors, such as correlated shadowing [39]. While the propagation studies presented in chapters 6–8 have been used to formulate *mechanistic* models for indoor propagation, these are not yet sufficiently developed to replace empirical models for estimating system performance. Chapter 9 therefore presents a feasibility study, focusing on the application of FDTD-based simulation tools to model system performance in the presence of co-channel interference. Unlike experimental studies and empirical models, the FDTD method allows the propagation mechanisms causing interference to be explicitly identified. Many of the findings (such as optimal base-station placement) are therefore transportable to other buildings. Deployment strategies for interference-mitigation tools are also examined in chapter 9.

## 5.6 Summary

In this chapter the FDTD method implemented in chapter 4 has been extended to model radio-wave propagation within buildings, particularly focusing on the conversion of time-domain electromagnetic fields to quantities relevant for system planning. A method to extend two-dimensional results to 2.5D (allowing some comparison with experimental measurements) is also discussed. Another contribution of this chapter has been the development of post-processing techniques to determine and visualise the dominant propagation mechanisms, with the aim of using these findings to form *mechanistic* models. The chapter is concluded with a logical roadmap outlining the propagation studies investigated in chapters 6–9.

# Chapter 6

## Propagation Study A: Within the Building Perimeter (2D)

### 6.1 Introduction

Chapter 5 focused on the application of the FDTD method to model propagation within buildings, and outlined the three propagation studies considered in this thesis to characterise the indoor radio channel. As noted in chapter 2, determining the mechanisms governing inter-floor propagation is important to correctly predict co-channel interference arising from systems operating on adjacent (or nearly adjacent) floors in a multi-storey building. Accordingly, this chapter presents a two-dimensional FDTD investigation of inter-floor radio-wave propagation (where all propagation paths are contained within the building perimeter), with the aim of developing appropriate *mechanistic* models to describe the behaviours observed.

Section §6.2 introduces a simplified two-dimensional model of a multi-storey building and presents results obtained with a two-dimensional implementation of the FDTD method (with both  $\text{TM}_z$  and  $\text{TE}_z$  polarisations considered). In section §6.3, this simplified geometry is extended by considering the impacts of additional details, such as reinforcing bars (rebar), glass windows and other architectural features. The geometry is further extended to consider the impact of internal structural details (such as stairwells and elevator shafts) in section §6.4. Section §6.5 proposes *mechanistic* models to predict the field strengths on adjacent floors of a multi-storey building, and validates these findings against experimental measurements of the path-loss. The implications of the findings (for interference prediction) are discussed in section §6.6, and the chapter is briefly summarised in section §6.7.

### 6.2 Inter-Floor Propagation

Fig. 6.1(a) shows a photograph of the Engineering Tower at the University of Auckland. This is a typical 1960s office block, and the floors and internal structural shaft (not visible in the photograph) are made from reinforced concrete. Several features of the building have been identified, including the windows and hanging (decorative) panels. Fig. 6.1(b) is a reproduction of the illustration presented in Fig. 5.4, showing the two-dimensional vertical slice considered in this chapter (the dimensions of this problem are chosen to match the Engineering Tower). It is recognised that this geometry is a simplification of the real propagation environment, but it

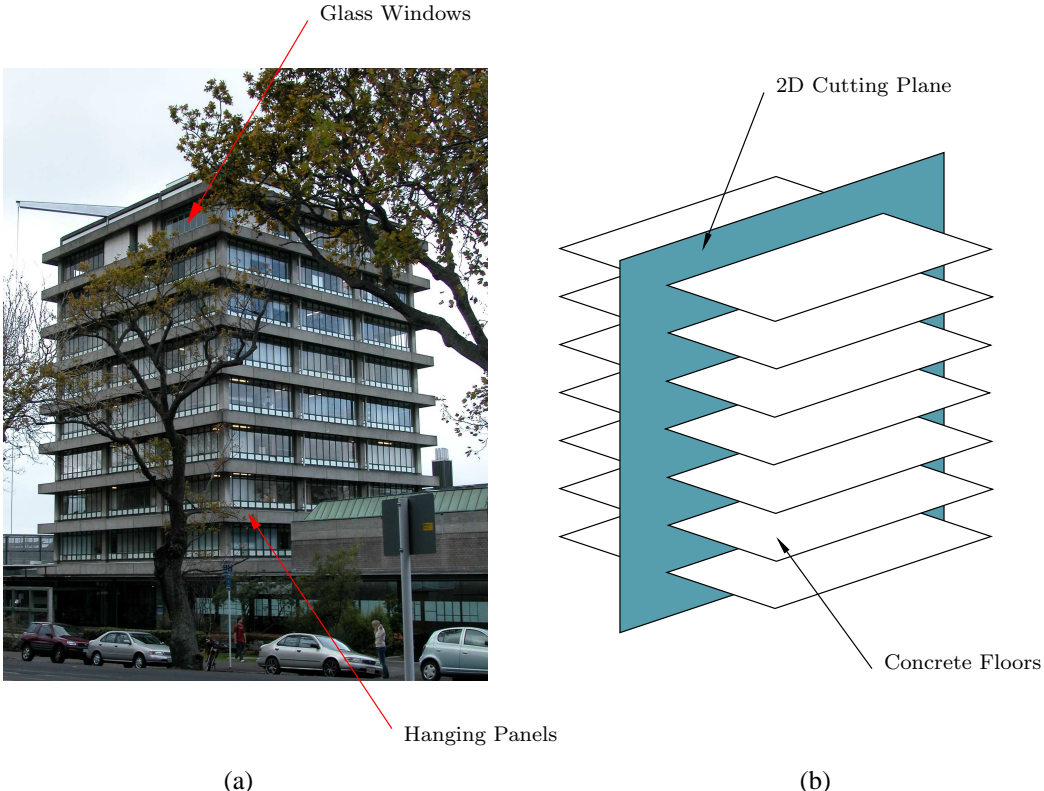


Figure 6.1: (a) Photograph of the Engineering Tower, (b) Two-dimensional vertical slice considered in this chapter.

serves as a useful starting point to identify the dominant propagation mechanisms. As noted in Fig. 6.1(b), the two-dimensional slice considers a building with an open floor plan, where many internal details (e.g. office furniture and fittings) have been ignored<sup>1</sup>. However, the complexity of the geometry is progressively increased by introducing two-dimensional representations of some details, such as rebar, windows, hanging panels and internal structural details (e.g. the central services shaft).

### 6.2.1 FDTD Analysis

Table 6.1 shows the parameters examined in this section to assess the impact of altering the frequency, floor thickness and concrete conductivity on the received power and propagation mechanisms. Both  $\text{TM}_z$  and  $\text{TE}_z$  polarisations were considered, and for each combination of  $T$  and  $\sigma_e$  all three frequencies (1.0, 1.8 and 2.5 GHz) were captured in a single simulation run. The permittivity of the concrete was held constant at  $\epsilon_r = 6.0$ , with an FDTD-lattice size of 5 mm to minimise dispersion. The floor separation distance was fixed at 2.70 m. Using the parallel FDTD code discussed in chapter 4, on a 36-core Beowulf cluster (with Intel Xeon 2.66 GHz quad-core processors), each simulation takes 5 hours to solve to steady state (75,000 time-steps). The total time to solve the 40 cases outlined in Table 6.1 is thus 200 hours (8.5 days), and this can be considered representative of a contemporary cluster.

Fig. 6.2(a) shows the steady-state power for an  $E_z$  component in a  $\text{TM}_z$  polarised lattice

<sup>1</sup>It is difficult to describe much of this clutter on a two-dimensional slice. A more thorough investigation with a three-dimensional geometry is considered in chapter 8.

Table 6.1: Parameters examined in the two-dimensional vertical slice simulations.

Polarization	$f$ (GHz)	$T$ (m)	$\sigma_E$ (mS/m)
$TM_z$	1.0	0.1, 0.2, 0.3, 0.4	0, 25, 50, 75, 100
	1.8	0.1, 0.2, 0.3, 0.4	0, 25, 50, 75, 100
	2.5	0.1, 0.2, 0.3, 0.4	0, 25, 50, 75, 100
$TE_z$	1.0	0.1, 0.2, 0.3, 0.4	0, 25, 50, 75, 100
	1.8	0.1, 0.2, 0.3, 0.4	0, 25, 50, 75, 100
	2.5	0.1, 0.2, 0.3, 0.4	0, 25, 50, 75, 100

at 1.0 GHz, and the corresponding phase is shown in Fig. 6.2(b). Nine storeys are considered, and the transmitter is located on the top floor, 1.5 m from the ceiling. The source has been normalised to  $1\angle 0^\circ$  v/m, and calibrated against the two-dimensional Green's function, as discussed in appendix C. In this case, the concrete floors have been modelled as lossy dielectric slabs with  $\epsilon_r = 6.0$ , and  $\sigma_E = 75$  mS/m. Similar plots of the power and phase for an  $E_y$  field component in a  $TE_z$  polarised lattice are shown in Fig. 6.3(a) and (b) respectively.

For both  $TM_z$  and  $TE_z$  polarised lattices, the power is observed to decrease with distance away from the transmitter, and from incremental attenuation encountered propagating through the floors. In the  $TM_z$  lattice the  $E_z$  field components are orthogonal to the page, and as shown in Fig. 6.3(b) the fields radiate cylindrically from the source. By contrast, the  $E_y$  source in the  $TE_z$  lattice acts as a short dipole antenna. This is evident in the density plot shown in Fig. 6.3(a), where the null in the dipole radiation pattern is visible directly under the transmitter. Fig. 6.3(b) also indicates the phase fronts, though centred on the source, are not cylindrical in shape.

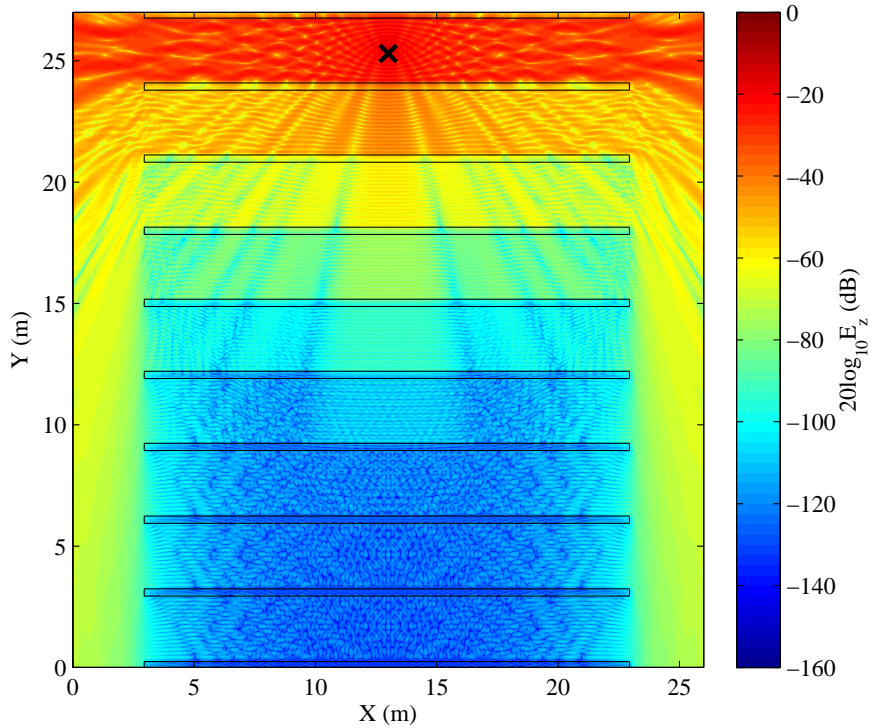
The bands of low and high power observed in Fig. 6.2(a)—appearing to originate from the source—can be attributed to strong specular reflections at the vacuum-concrete interfaces. These reflections cause localised variations in the received power of over 20 dB across a floor, and this behaviour is similar to multi-path fading, as discussed in chapter 2. However, the reflected and penetrating components have similar path lengths for varying horizontal displacement across the floor, and thus the fades can persist over multiple wavelengths. Although similar patterns in the received power can be observed in Fig. 6.3(a), the fade depths are typically smaller, as the  $E_y$  fields in a  $TE_z$  lattice are discontinuous over normal dielectric boundaries. For the case considered in Fig. 6.3, the magnitude of the  $E_y$  reflection coefficient from a dielectric slab will be lower than a similar  $TM_z$  polarised lattice [82, p. 188, 192].

### 6.2.2 Propagation Paths

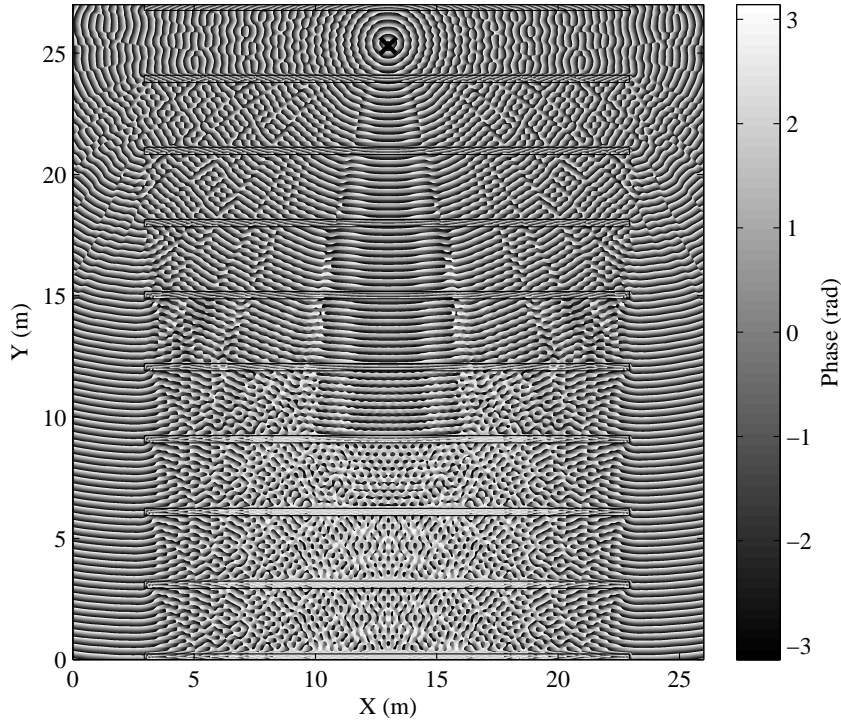
In the geometry considered, two propagation *paths* are possible: 1) transmission through the floors<sup>2</sup>; and 2) transmission via paths external to the building, e.g. diffraction down the outside face<sup>3</sup>. Paths involving a combination of penetration and diffraction are also possible. The power of the penetrating component decreases by a fixed amount per floor (in addition to free-space loss), and depending on thickness and concrete conductivity, this is between 10–20 dB/floor. Therefore, the power (in dBm) of the penetrating component decreases rapidly, but linearly, with the number of floors penetrated. By contrast, the power of the diffracted components will

<sup>2</sup>Transmission through the floors includes the direct and multiple-reflection paths, and is entirely contained within the building perimeter.

<sup>3</sup>In the geometry considered (isolated building) diffraction around the floors is the only external path possible.

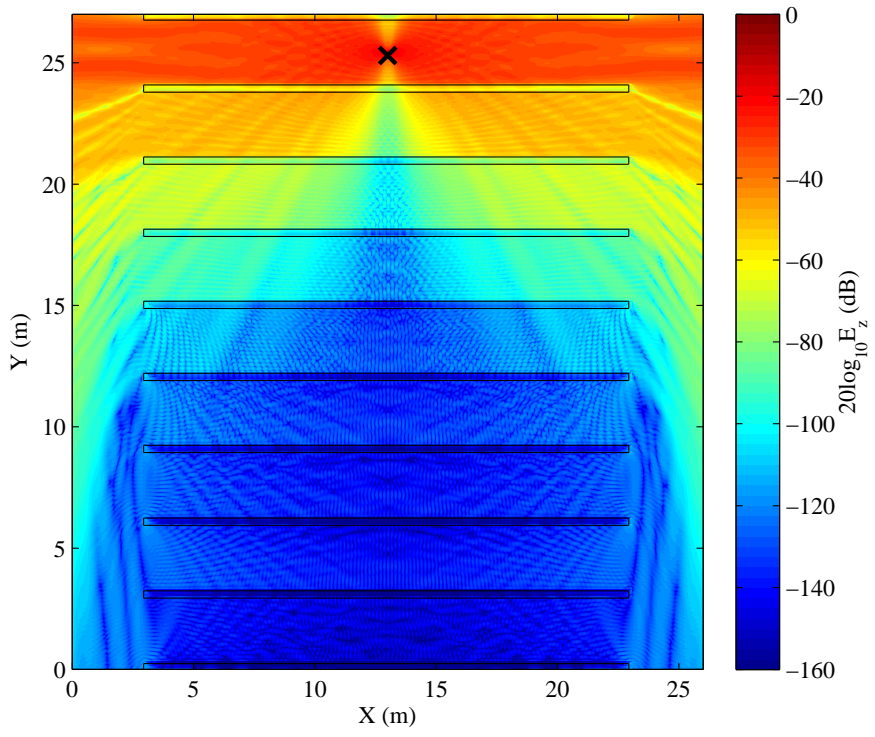


(a)

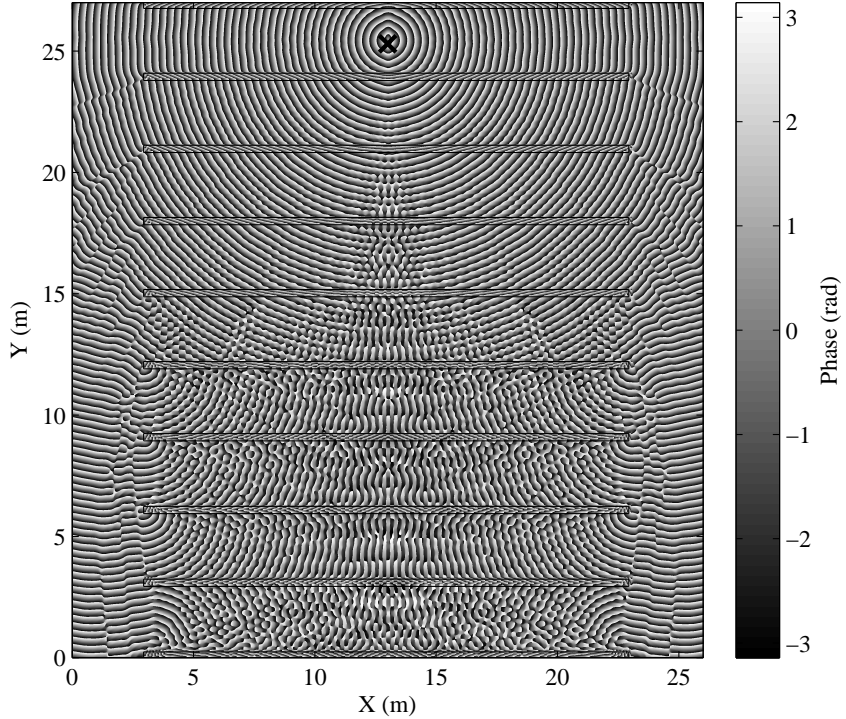


(b)

Figure 6.2: (a) Power and (b) Phase of the  $E_z$  field component ( $TM_z$  lattice polarisation) for 0.30 m thick floors ( $\epsilon_r = 6.0$ ,  $\sigma_E = 75$  mS/m) at  $f = 1.0$  GHz. The location of the transmitter is marked with  $\times$ .



(a)



(b)

Figure 6.3: (a) Power and (b) Phase of the  $E_y$  field component ( $TE_z$  lattice polarisation) for 0.30 m thick floors ( $\epsilon_r = 6.0$ ,  $\sigma_E = 75$  mS/m) at  $f = 1.0$  GHz. The location of the transmitter is marked with  $\times$ .

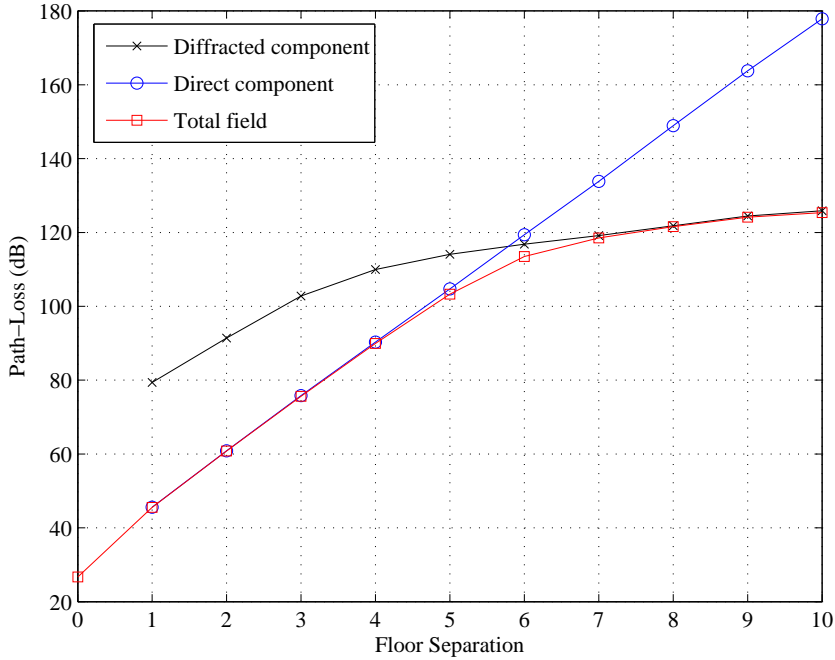


Figure 6.4: Isolating the total path-loss into direct and diffracted components. The direct component is isolated by running the concrete floors into the UPML and the diffracted component is isolated by placing a metal sheet in the concrete slab.

be significantly lower, but relatively constant with distance and (relatively) independent of the number of floors<sup>4</sup>. The combined effect causes the received power to decrease linearly, until the power of the diffracted component is approximately the same as the direct, at which point the rate of decrease in received power slows, and is dominated by the diffracted component.

This finding is supported by the results shown in Fig. 6.2(a) and Fig. 6.3(a). For example, Fig. 6.2(a) shows that for 1–5 floor separations the power decreases linearly with each additional floor (the attenuation introduced is approximately 15 dB/floor); it is also observed that beyond 5–6 floor separations the received power remains relatively constant. Similar observations can be made for the  $TE_z$  polarised lattice in Fig. 6.3(a). These results are also supported by Fig. 6.2(b) and Fig. 6.3(b), which show the steady-state phase for 1–5 floor separations remains radially centred on the transmitter, indicating the dominant propagation mechanism in this region is penetration through the concrete floors. Beyond five floor separations, the phase fronts indicate diffraction at the floor vertices dominates the received signal. The presence of external diffraction-based mechanisms that can propagate significant levels of power to other floors is a noteworthy finding, as it provides a deterministic, physical basis for behaviours reported in [7], e.g. floor-attenuation factors which vary as a function of the number of floors.

Fig. 6.4 shows the path-loss<sup>5</sup> recorded on each floor for a  $TM_z$  polarised lattice with 0.30 m thick,  $\sigma_E = 75$  mS/m concrete floors at 1.0 GHz. The penetrating and diffracting components have been isolated by considering two different geometries. The penetrating component is

<sup>4</sup>This mechanism could be influenced by external features, such as ledges and inset windows, which are discussed further in section §6.3.

<sup>5</sup>In two-dimensions the path-loss is defined as  $-20 \log_{10} |E|$ , where the source is normalised to  $1\angle0^\circ$ . It should be noted that these values of the two-dimensional path-loss cannot be directly compared against experimental measurements.

isolated by extending the concrete floors into the UPML absorbing boundary, thereby preventing any external propagation paths. In this case the average power is observed to decrease linearly with the number of floors penetrated. The diffracted component is isolated by placing a layer of PEC in the centre of the floor directly under the transmitter<sup>6</sup>, thereby preventing propagation through the floors. In the case considered, after 5–6 floor separations the total received power becomes dominated by the diffracted component.

### 6.2.3 Path-Loss versus Distance

Scatter plots of the  $(3\lambda)^2$  sector-averaged path-loss versus the transmitter-receiver separation distance,  $d$  are shown in Fig. 6.5 for (a)  $\text{TM}_z$  polarisation and (b)  $\text{TE}_z$  polarisation. The frequency is 1.0 GHz, and the floors are modelled as 0.30 m thick homogeneous slabs of concrete with  $\epsilon_r = 6.0$  and  $\sigma_E = 75 \text{ mS/m}$ . In both cases the path-loss is observed to increase with  $d$  and the number of floors penetrated. The maximum path-loss occurs after 6–7 floor separations, regardless of polarisation. However, as shown in Fig. 6.5(a), the maximum path-loss for the  $\text{TM}_z$  polarised lattice is approximately 120 dB, while the maximum for the  $\text{TE}_z$  lattice is 18 dB higher. This difference can be attributed to the radiation pattern of the dipole antenna, which (in the vertical orientation) tends to direct energy outwards. Similarly, Fig. 6.5(b) shows that in a  $\text{TE}_z$  polarised lattice, higher path-losses are observed in sectors directly under the transmitting antenna.

On the same floor as the transmitter, the sector-averaged path-loss for both  $\text{TE}_z$  and  $\text{TM}_z$  polarisations is observed to follow a free-space relationship with distance, i.e. the distance-dependency exponent,  $n$ , is 1.0<sup>7</sup>. In Fig. 6.5(a) several sectors are observed to have  $n < 1.0$ , in this case the electrically smooth floor and ceiling support strong reflected components which can reduce the path-loss. For  $\text{TM}_z$  polarisation,  $n$  remains approximately 1.0 for 1–3 floor separations, and the average attenuation introduced by each floor is 15.0 dB. This finding suggests the sector-averaged path-loss (for 1–3 floor separations) can be modelled as free-space with lumped attenuation-terms to account for propagation through the concrete floors. As  $n$  is found by fitting the path-loss to distance on a logarithmic scale, beyond four floor separations a distance-dependency model for the path-loss on each floor is no longer appropriate. Furthermore, after 4–5 floor separations the received power tends to be dominated by the diffracted components, which generally increases the spread in path-loss values observed.

### 6.2.4 Floor Thickness, Concrete Conductivity and Frequency

Fig. 6.6(a) shows the variation in the average path-loss recorded across a floor with increasing floor thickness (0.10–0.40 m). Similarly, Fig. 6.6(b) shows the variation as the concrete conductivity increases from 0–50 mS/m. In both plots  $\text{TM}_z$  polarisation is considered and the frequency is fixed at 1.8 GHz. It is observed that the increase in path-loss is linear with the number of floors separating the transceivers until approximately 100 dB. However, it is noted that the attenuation introduced by the first floor is 3–5 dB greater than the following floors. This observation can be attributed to the presence of strong specular reflections from the electrically smooth floor and ceiling<sup>8</sup>.

<sup>6</sup>The PEC sheet does not extend to the floor vertex to prevent spurious diffraction around the vertex of the PEC sheet.

<sup>7</sup>For a cylindrically propagating wave in free-space,  $E \propto \frac{1}{\sqrt{d}}$ , and therefore  $|n| = 1.0$  for power/path-loss.

<sup>8</sup>For  $\text{TE}_z$  polarisation, the attenuation introduced by the first floor is the same as the following floors. As already noted the reflection coefficients from the concrete slabs (in the configuration considered) are lower for  $\text{TE}_z$  polarisation, and consequently the average path-loss on floor 0 is 3–5 dB higher.

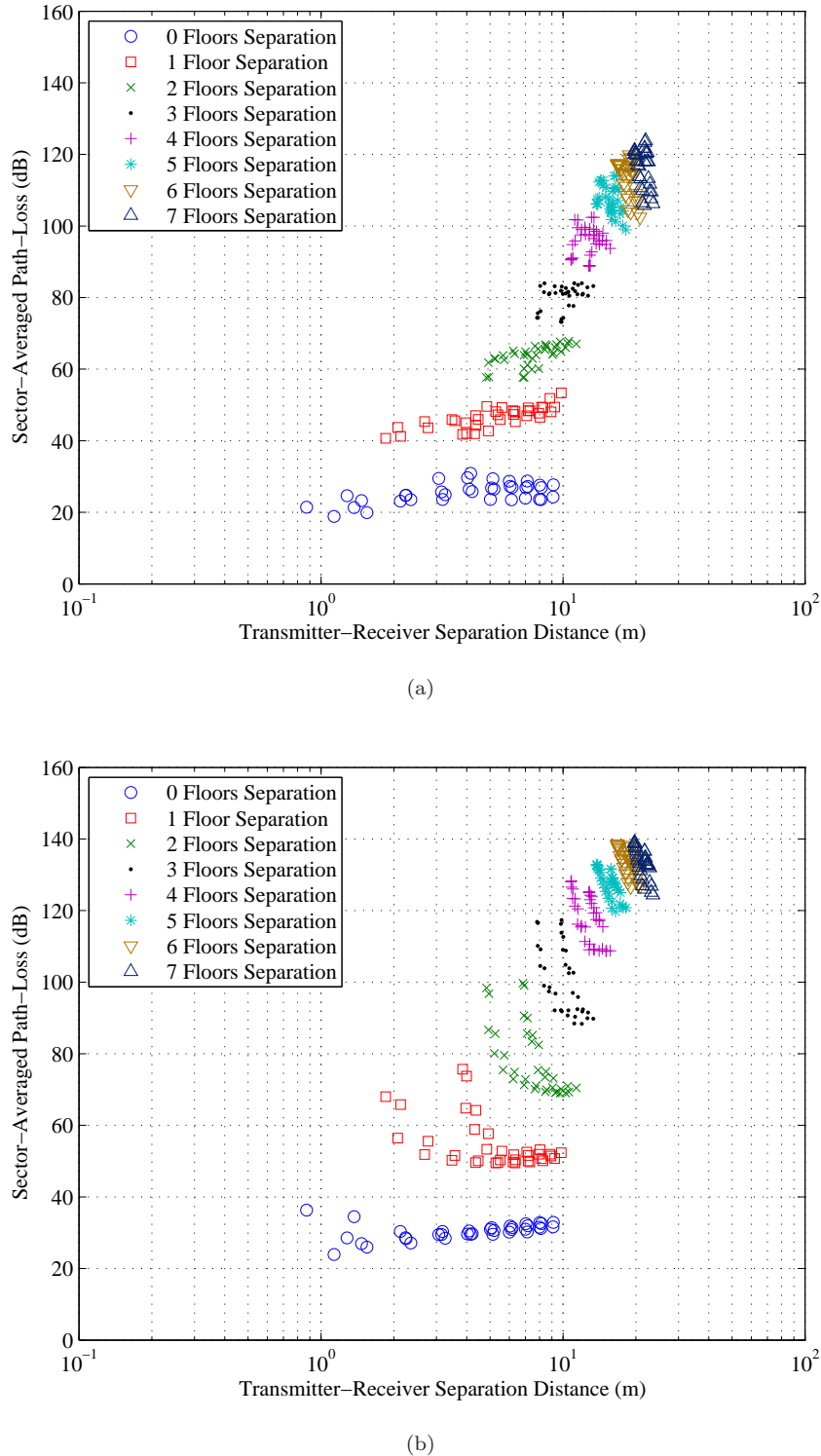
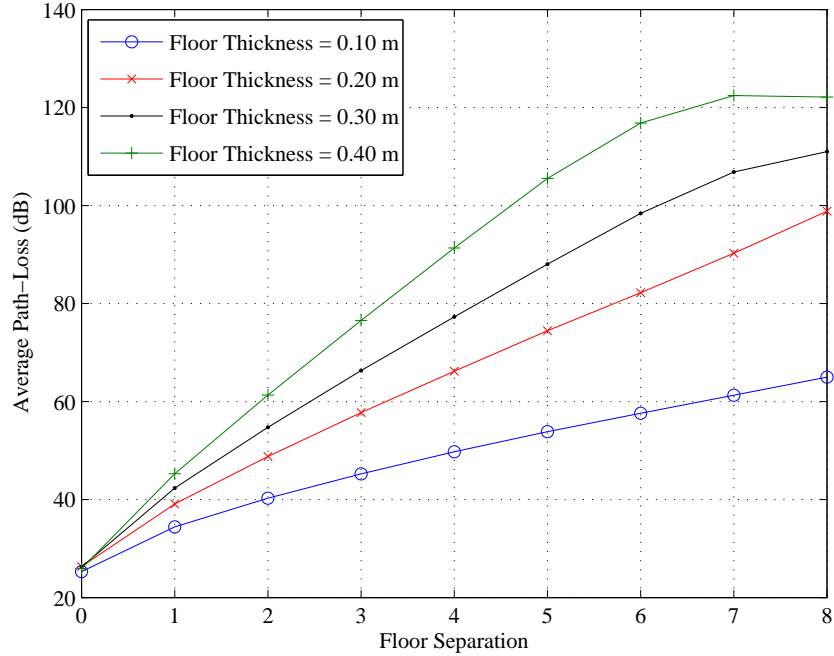
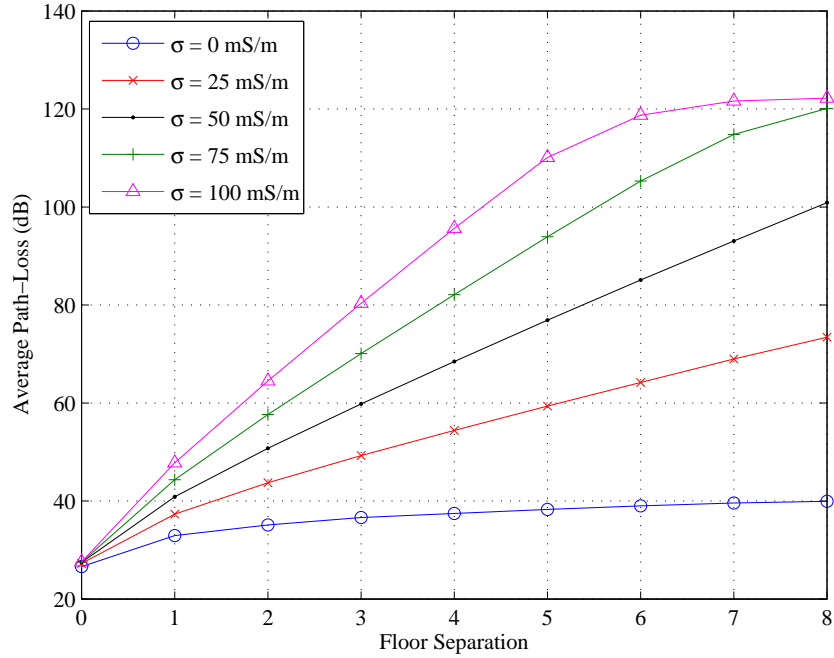


Figure 6.5: Scatter plot of the  $(3\lambda)^2$  sector-averaged path-loss plotted against the transmitter-receiver separation distance for (a) TM<sub>z</sub> polarisation and (b) TE<sub>z</sub> polarisation. In both cases  $f = 1.0$  GHz, floor thickness = 0.30 m and concrete conductivity = 75 mS/m.



(a)



(b)

Figure 6.6: Variation in the average path-loss over 0–8 floor separations at 1.8 GHz for  $\text{TM}_z$  polarisation with varying (a) floor thickness (conductivity fixed at 50 mS/m) and (b) concrete conductivity (thickness fixed at 0.20 m).

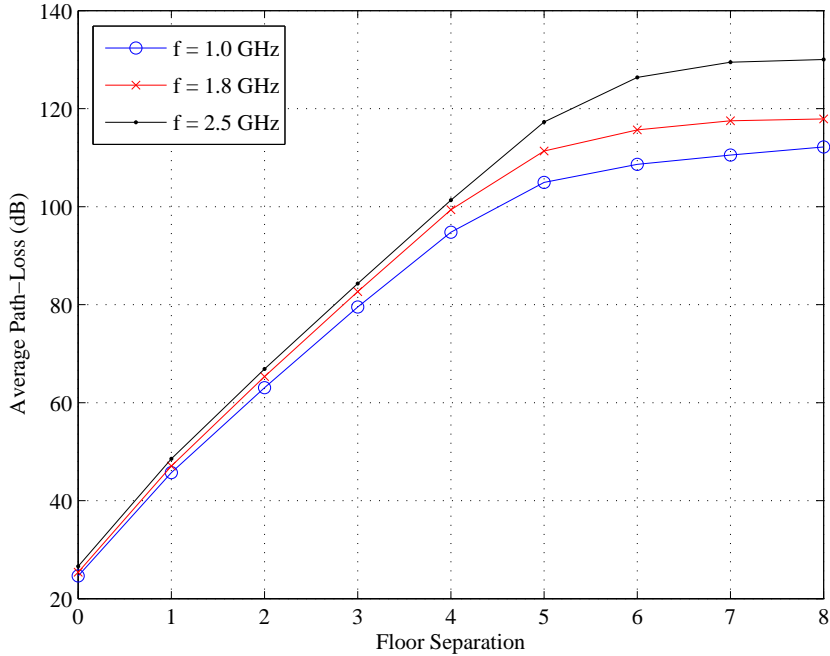


Figure 6.7: Floor-averaged path-loss for 0–8 floor separations at 1.0, 1.8 and 2.5 GHz for  $\text{TM}_z$  polarisation.

The attenuation introduced by each floor depends on the thickness and conductivity of the concrete. Increasing the thickness or conductivity increases the attenuation, and it is clear that to correctly predict the field strength on adjacent floors, good estimates of the floor attenuation are required. The floor thickness is relatively easy to determine, however, as noted in section §5.4, published values of the concrete conductivity vary considerably. In the scenarios presented in Fig. 6.6(a) and (b), it is noted that the variation in floor thickness does not have a significant effect on the magnitude of the diffracted components (for  $\text{TM}_z$  polarisation).

As shown in Fig. 6.7 the operating frequency can also have a significant impact on the average path-loss recorded on each floor. Three frequencies have been considered: 1.0, 1.8 and 2.5 GHz; and the results for  $\text{TM}_z$  polarisation, with  $\sigma_E = 75 \text{ mS/m}$ , 0.30 m thick floors are shown. The average path-loss recorded on each floor is observed to increase with frequency, with the increase being between 2–5 dB in the regions where the dominant propagation mechanism is penetration through the floors. However, the increase in diffraction loss at higher frequencies is observed to significantly increase the path-loss after 6–8 floor separations<sup>9</sup>. Accordingly, the transition point between the penetrating and diffracting components also increases.

### 6.3 Detailed Models

Many details present in real multi-storey buildings have been ignored in the simulations considered in section §6.2. These include glass exterior windows, internal partitions, office furniture and dielectric and metallic clutter. Although many of these details are inherently three-

<sup>9</sup>The diffraction loss generally increases with frequency, e.g. in the geometrical theory of diffraction (GTD) the magnitude of the diffraction coefficient (for a conducting wedge) is proportional to  $\frac{1}{\sqrt{f}}$  [82, p. 783].

Table 6.2: Additional Details Considered in the Two-Dimensional FDTD Model.

Additional Details	Description
Rebar	Modelled as a metal bar (with an $A \times A$ square cross-section) embedded within the concrete slab, and spaced $s$ m apart.
Glass Windows	Modelled as a 5 mm thick dielectric slab with properties $\epsilon_r = 3.0$ and $\sigma_E = 2 \text{ mS/m}$ .
Hanging Panels <sup>a</sup>	Modelled as $6 \times 50$ cm concrete slabs attached to the ends of each floor.
Internal Partitions	Modelled as a 6 cm thick block of solid gib-board ( $\epsilon_r = 3.0$ and $\sigma_E = 5 \text{ mS/m}$ ) extending between the floor and ceiling. Between 2–6 are randomly positioned <sup>b</sup> on each floor.
Metallic Clutter	Modelled as randomly sized metal blocks (dimensions vary between 10–50 cm). Between 1–10 metal blocks are randomly positioned on each floor.

<sup>a</sup>External decorative panels are discussed in further detail in appendix D.2.

<sup>b</sup>The results presented in Fig. 6.8 are the average of several simulation runs with the internal partitions in different locations.

dimensional, suitable two-dimensional representations can be included in the simulation geometries. This section aims to show that although the inclusion of these details can alter the locally received power, the dominant propagation paths (namely penetration through the floors and diffraction at the edges of the floor) do not change significantly. Table 6.2 outlines the additional details considered in this section.

Fig. 6.8 shows the average path-loss recorded across each floor for varying levels of internal detail. The addition of rebar (in this case with  $A = 5$  cm and  $s = 0.75$  m) has very little effect on the average path-loss, and no significant changes are observed as the parameters  $A$  or  $s$  are varied. However, as shown in appendix D the rebar can significantly alter the local fading patterns observed on adjacent floors. Similarly, the windows have minimal effect on the path-loss, though beyond five floor separations there is a consistent increase of 1.5 dB, which could be attributed to additional propagation loss through the glass. The most significant change is introduced by the hanging panels, which decrease the power carried on the diffracted components by approximately 8.0 dB. This phenomena is examined in more detail in appendix D. The introduction of gib-board internal partitions and metallic clutter increases the scatter in the environment, further reducing the received power.

## 6.4 Propagation through Internal Shafts

A common feature of many multi-storey buildings are internal services shafts containing elevators and stairwells. In the building considered in this chapter, the services shaft runs through the centre of the building, and provides structural support to the floors. Fig. 6.9(a) shows the distribution of the steady-state power (in a  $\text{TM}_z$  lattice<sup>10</sup>), when a two-dimensional representa-

<sup>10</sup>However, similar to section 6.2, many of the findings presented in this section are equally applicable to  $\text{TE}_z$  polarisation.

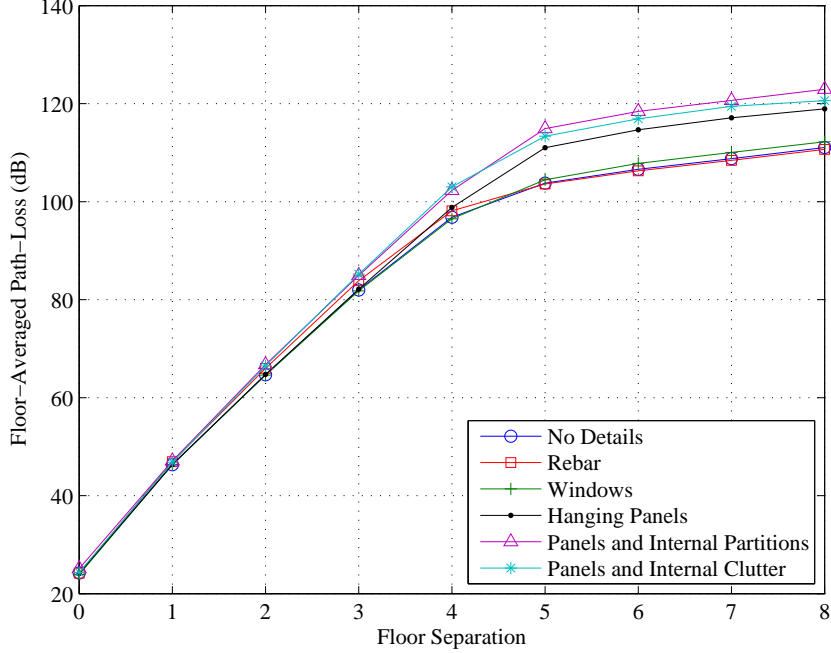


Figure 6.8: Floor-averaged path-loss over 0–8 floor separations for increasing levels of internal detail. The operating frequency is 1.0 GHz and the properties of the concrete floors are  $\epsilon_r = 6.0$  and  $\sigma_E = 75 \text{ mS/m}$ .

tion of the central services shaft is included in the geometry. Similar to Fig. 6.2, eight floors are considered, and the transmitter (marked by  $\times$ ) is located on the top floor. The floors and walls of the shaft are modelled as 0.30 m thick concrete slabs with  $\epsilon_r = 6.0$  and  $\sigma_E = 75 \text{ mS/m}$ . Two regions are identified in Fig. 6.9(a), Region A: on the transmitter side; and Region B: across the shaft.

Fig. 6.9(b) shows a scatter plot of the sector-averaged path-loss versus distance, where Regions A and B are separated. A comparison between Fig. 6.9(b) and Fig. 6.5(a) indicates the maximum sector-averaged path-loss is between 5–15 dB lower when the shaft is included. This observation is also supported by comparing Fig. 6.9(a) and Fig. 6.2(a). In Region A penetration through the floors dominates for three floor separations. However, beyond three floor separations, the received power is dominated by components internally reflected in the hollow services shaft<sup>11</sup>. In Region B the dominant propagation path is penetration through the services shaft, and the strong reflected components visible in Fig. 6.9(a) indicate multiple reflection within the shaft dominates on lower floors. The attenuation introduced by the walls of the shaft is approximately 40 dB, and consequently, for 1–4 floor separations the power received in Region B is lower than Region A. However, after five floor separations the received power in Regions A and B are comparable.

It should be noted that in the two-dimensional geometry considered, the only propagation path from Region A to B (and vice versa) is propagation into and through the services shaft. In reality, energy may also propagate around the shaft, however this behaviour cannot be

<sup>11</sup>It should be noted that the transmitter is closer to the edge of the floor in this case and more power may be carried on the diffracted component. However, comparisons against additional simulations (with the transmitter offset) indicate components reflected within the services shaft remain dominant.

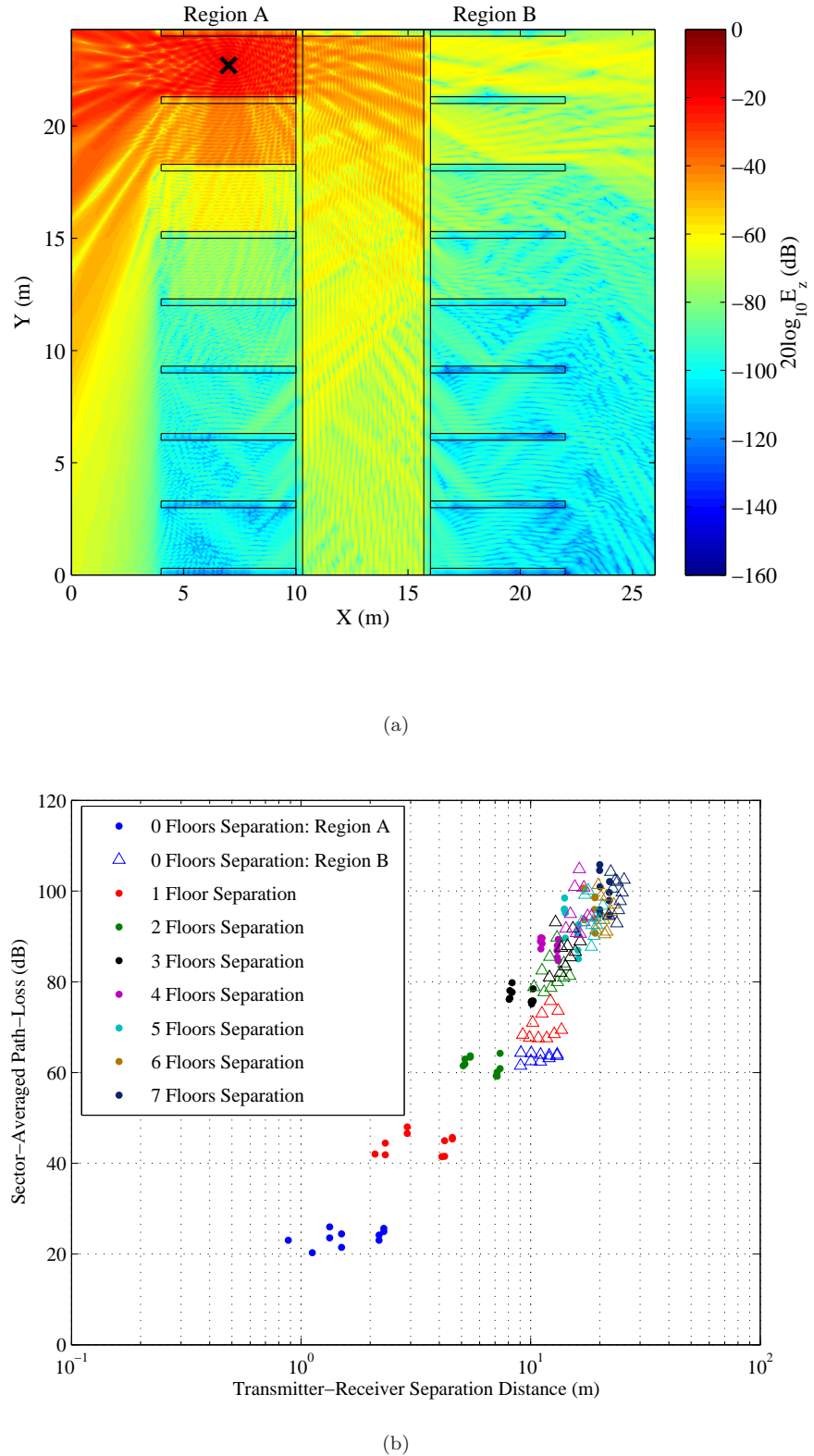


Figure 6.9: (a) Distribution of the steady-state power when the core is included in the geometry. The location of the transmitter is indicated by  $\times$ . (b) Steady-state power versus distance.

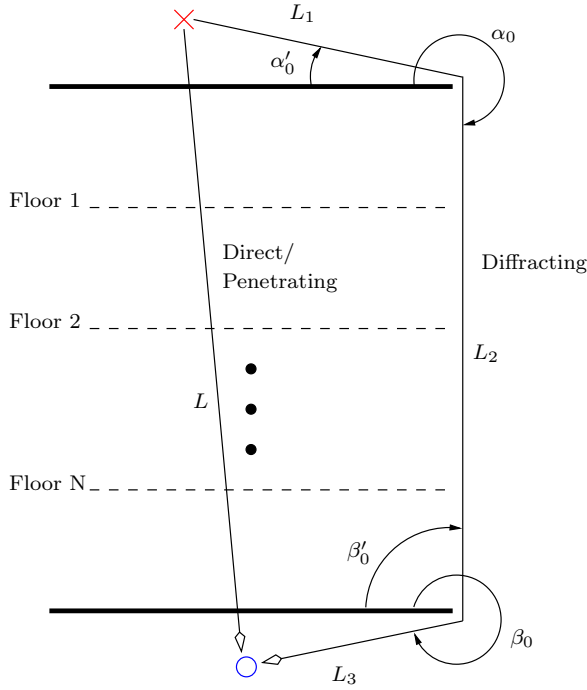


Figure 6.10: Propagation over multiple floor-edges. The location of the transmitter and receiver are marked by  $\times$  and  $\circ$  respectively.

captured on a single two-dimensional slice through the multi-floor geometry. A more thorough investigation of this behaviour with a three-dimensional implementation of the FDTD method is considered in chapter 8.

## 6.5 Mechanistic Models and Experimental Validation

### 6.5.1 Ray-Based Models

The results presented in the previous sections suggest the sector-averaged path-loss can be accurately predicted with a two component (penetration and diffraction) mechanistic model. A similar approach was considered in Honcharenko *et. al* [38], where a GO/UTD analysis of a simplified multi-storey building (similar to the geometry shown in Fig. 6.1) was used to show that diffracted paths propagating down the sides of the building could dominate the received power on lower floors. In the Honcharenko model, the diffracted components were modelled using the diffraction coefficient for an absorbing wedge, and the effects of multiple diffraction over the edges of the floors was not considered<sup>12</sup> [38].

The mechanistic model described in this section is a two-dimensional<sup>13</sup> version of the Honcharenko model. Fig. 6.10 shows a diagram of the geometry considered with the direct/penetrating and diffracting paths identified. In two-dimensions, the mechanistic model

<sup>12</sup>Extending the GO/UTD method to include the effects of multiple diffraction is difficult, as in many buildings the edges of the floors are vertically aligned, creating a case where the diffracting edges are co-linear (i.e. each edge is the transition region of another). This is a case where GO/UTD is known to fail [86, 87].

<sup>13</sup>The model reported in [38] is developed for three-dimensions, however to make a valid comparison with the two-dimensional FDTD simulations, the distance dependency and diffraction-spreading terms are adjusted to two-dimensions [82, p. 768].

is given by

$$P_{\text{total}} = P_{\text{direct}} + P_{\text{diffracted}} \quad (\text{W}). \quad (6.1)$$

The power of the direct component is given by

$$P_{\text{direct}} = \frac{A_0}{L} \prod_m T_{\text{Floor}(m)}^2 \prod_n T_{\text{Wall}(n)}^2, \quad (6.2)$$

where  $A_0$  is a constant to allow a valid comparison with the two-dimensional FDTD results,  $L$  is the direct distance between the transceivers,  $T_{\text{Floor}(m)}$  is the transmission coefficient through the  $m^{\text{th}}$  floor, and  $T_{\text{Wall}(n)}$  is the transmission coefficient through the  $n^{\text{th}}$  internal wall. The power of the diffracted component is given by

$$P_{\text{diffracted}} = \frac{A_0 D^2(\alpha, \alpha') D^2(\beta, \beta') \prod_j T_{\text{Glass}(j)}^2 \prod_k T_{\text{Wall}(k)}^2}{L_1 L_2 L_3}, \quad (6.3)$$

where  $L_{1-3}$  are the path lengths of the diffracted components,  $D(\phi, \phi')$  is the diffraction coefficient for a conducting wedge with incident angle  $\phi'$  and diffraction angle  $\phi$ , and  $T_{\text{Glass}(j)}$  is the transmission coefficient through the  $j^{\text{th}}$  glass window. The diffraction coefficient is dependent on the geometry and material properties, however, it was found a conducting wedge provides a good approximation in most scenarios<sup>14</sup> [88, pp. 167–169],

$$D(\phi, \phi') = -\frac{\exp\left(\frac{-j\pi}{4}\right)}{2\sqrt{2\pi k}} \left[ \frac{1}{\cos\left(\frac{\phi-\phi'}{2}\right)} - \frac{1}{\cos\left(\frac{\phi+\phi'}{2}\right)} \right], \quad (6.4)$$

where  $k$  is the wave-number.

Fig. 6.11 shows a comparison between the sector-averaged path-loss calculated using a two-dimensional implementation of the FDTD method, and the mechanistic model given by (6.1)–(6.4), at a frequency of 1.0 GHz. The glass windows and internal partitions have been ignored, and the material properties of the concrete are  $\epsilon_r = 6.0$ ,  $\sigma_e = 75 \text{ mS/m}$ ; the corresponding floor attenuation in (6.2) is 19.0 dB. The RMS error between the mechanistic model and FDTD simulated results is 5.2 dB, indicating good agreement in most regions. However, it is noted that the FDTD method generally predicts a larger spread in the (sector-averaged) path-loss. Furthermore, reflections from the surface of the floors/ceiling were not considered in the mechanistic model, which, consequently tends to under-predict the path-loss on the first three floors.

### 6.5.2 Experimental Comparison

To confirm the findings presented in the previous sections, experimental measurements of the sector-averaged path-loss were made at 1.8 GHz across five floors of the Engineering tower shown in Fig. 2.1(a). Two transmitters were deployed on each floor, and similar to [6], the transmitter carrier frequencies were spaced 400 kHz apart allowing path-loss from transmitters located on adjacent floors to be measured in a single sweep. Identical, vertically orientated, discone antennas were used in both transmitter and receiver, and located approximately 1.6 m from the floor. 52 measurements were made across the fifth floor, and the receiving antenna was rotated over a 1 m diameter circle to average out the effects of multi-path fading. Fig. 6.12(a) shows

---

<sup>14</sup>In most cases, GTD diffraction coefficients are sufficient, as the regions of interest are deeply shadowed by the floors.

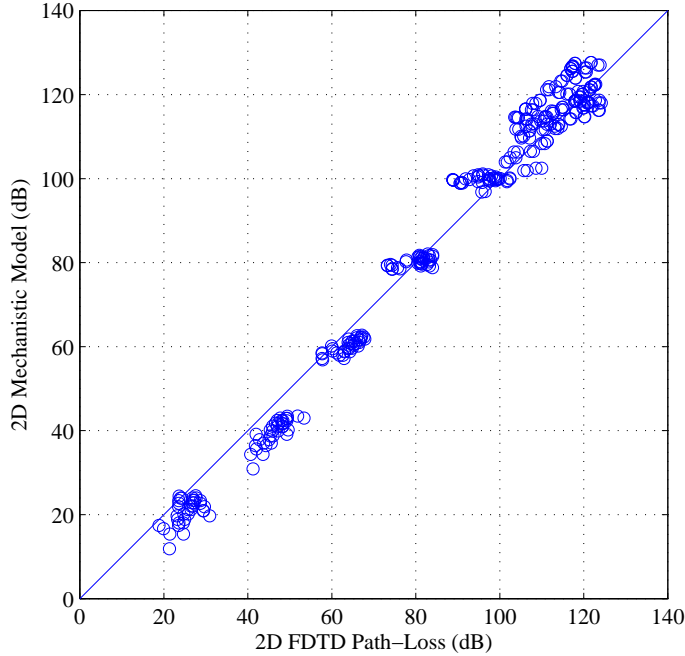


Figure 6.11: Scatter plot comparing the FDTD sector-averaged path-loss to values calculated with the Honcharenko model.

a floor plan of the Engineering Tower; the location of the transmitter indicated by  $\times$ , and the central services shaft divides the floor into *lit* and *shadowed* regions. As the models investigated in this chapter do not consider (possible) diffraction-based propagation paths travelling around the central services shaft, only measurement points in the lit regions are examined in this section. It should be noted that a direct comparison between the FDTD results (2D) and the experimental measurements (3D) is not possible due to their different dimensionality.

Fig. 6.12 shows a scatter plot of the sector-averaged path-loss measured in the lit regions, across five floors of the Engineering Tower. A qualitative comparison between Fig. 6.12(b) and FDTD simulation results in Fig. 6.5(a) shows several similarities, in particular, the apparent floor attenuation decreases as more floors separate the transmitter and receiver. On the same floor as the transmitter, the distance-dependency exponent,  $n$ , of the least-squares best-fit line is 2.9. The simulation results presented in section §6.2 suggest in this region free-space propagation dominates, and  $n = 2.0$  is expected. However, metallic and dielectric clutter present in the indoor propagation environment (but not considered in the two-dimensional vertical slice) can introduce additional attenuation, thereby increasing the perceived distance dependency exponent. Similarly, the spread in sector-averaged path-loss across each floor is also larger than predicted with the FDTD simulations.

## 6.6 Discussion

The FDTD analysis presented in this chapter shows diffracted components propagating down the outside face of a building can deliver a significant proportion of the total received power on adjacent (and nearly adjacent floors). Beyond 4–5 floor separations (for concrete floors with

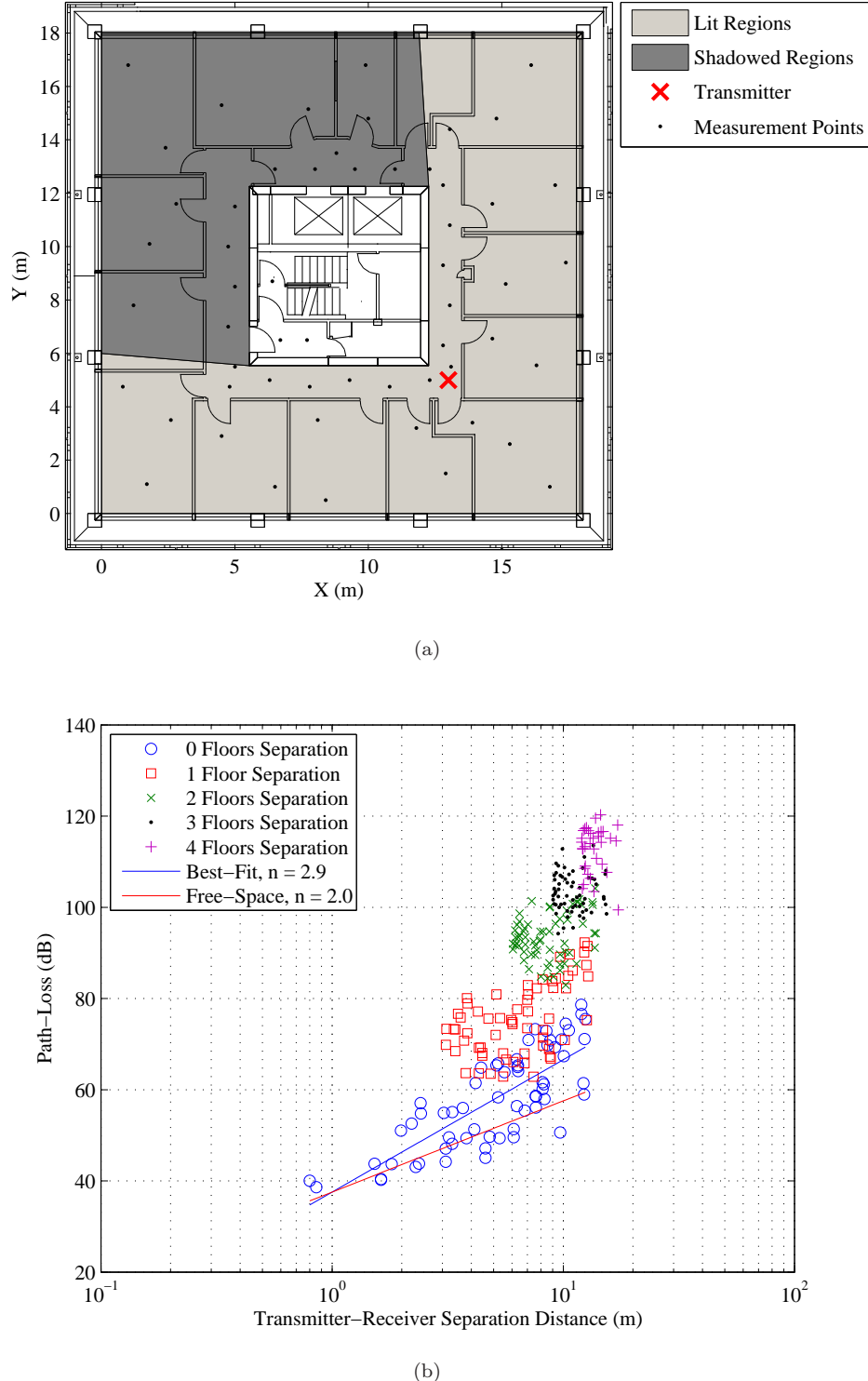


Figure 6.12: (a) Floor plan of the Engineering Tower. The location of the transmitter is indicated by  $\times$  and the lit and shadowed regions are identified. (b) Experimental measurements of the sector-averaged path-loss recorded across five floors of the Engineering Tower at 1.8 GHz.

typical material properties), these diffracted components dominate over components propagating through the floors. However, it must be noted that the power received via this diffraction mechanism is very low, e.g. in a two-dimensional  $\text{TM}_z$  case the power carried by the diffracted components is between  $-120$  to  $-90$  dBm.

In a typical multi-storey building, multiple co-channel base-stations may be deployed to ensure good coverage and throughput. The results presented in this chapter suggest that, in most circumstances, the majority of the inter-floor interference arises from transceivers located on immediately adjacent floors. In the simplified two-dimensional geometries considered in this chapter the dominant propagation path to an immediately adjacent floor is penetration through the (concrete) dielectric floor. In this case the diffracted components can be ignored when calculating the signal-to-interference ratio or the outage probability. However, it should be noted that propagation to adjacent floors around (or through) internal shafts, such as those considered in section §6.4, cannot be thoroughly modelled using a single two-dimensional slice; in this case a three-dimensional analysis may be required. Furthermore, propagation mechanisms other than penetration through the floors may dominate, e.g. reflection from surrounding buildings.

## 6.7 Summary

The propagation study considered in this chapter has focused on characterising inter-floor propagation on a two-dimensional vertical slice through a multi-storey building. Results from an FDTD analysis of a simplified indoor environment indicate inter-floor radio-wave propagation is supported by two distinct mechanisms: direct penetration and floor-edge diffraction. Additional environmental details, such as rebar, glass windows and ledges alter the field distributions, but not the propagation paths. Results also indicate these mechanisms can be adequately characterised with ray-based models, and a qualitative comparison with experimental measurements shows good agreement. However, all the propagation paths examined in this chapter are contained within the building perimeter, consequently the propagation study considered in chapter 7 extends the vertical slice to consider reflection and scattering from surrounding buildings.

# Chapter 7

## Propagation Study B: External to the Building Perimeter (2D)

### 7.1 Introduction

This chapter presents the second propagation study considered in this thesis to characterise the indoor radio channel, and (as in chapter 6) focuses on propagation between the floors of multi-storey buildings. Accurate models to predict inter-floor propagation are important to estimate co-channel interference arising from systems operating on adjacent floors. However, as noted in chapter 3, the parameters of many widely used empirical models lack an electromagnetic or physical basis and can vary considerably between different buildings, e.g. distance dependency exponents and floor attenuation factors (which also vary a function of the number of floors). The results presented in chapter 6 suggest propagation paths external to the building perimeter may (partly) account for this behaviour. Accordingly, this chapter presents a two-dimensional FDTD investigation of inter-floor propagation, extending the geometry examined in the previous chapter to consider possible reflection and scattering paths from nearby buildings, with the aim of developing computationally efficient mechanistic models.

Section §7.2 introduces the environment examined in this chapter, and outlines the FDTD simulation parameters. Narrow-band FDTD simulation results (at 1.0 GHz) are presented in section §7.3, followed by wide-band results in section §7.4. Exciting the FDTD lattice with a pulse waveform can give a useful estimate of the channel impulse response, which can be used to infer dominant propagation paths. On the basis of the results presented in sections §7.3 and §7.4, a mechanistic model that includes paths reflected from surrounding buildings is proposed in section §7.5. Experimental measurements of the received power and channel impulse response are used to validate the findings and are described in section §7.6. The implications of the findings are discussed in section §7.7, and the chapter is summarised in section §7.8.

### 7.2 FDTD Analysis

#### 7.2.1 External Propagation Paths

Chapter 6 considered propagation on a two-dimensional vertical slice though a multi-storey building. By virtue of the geometry, only propagation paths contained within the building

perimeter were considered—previous studies with other methods have used similar assumptions [38]—and the received power is dominated by two components: direct *penetration* through the floors and *diffraction* at the floor edges or window frames [38, 63]. As more floors are penetrated, external paths are thought to contribute more toward the received power, because internal paths are significantly attenuated [38]. In dense urban environments, nearby buildings in close proximity can potentially reflect strong signals back onto lower floors. Complicating the problem, the outside face of modern buildings can be cluttered and electromagnetically rough, which may cause local scattering. Previous measurement studies have shown that nearby buildings can increase the received power on adjacent (or nearly adjacent) floors [7, 85]. A simplified radar-cross-section model was proposed in [7], however it is noted that this model is not applicable when the buildings are close, such that the far-field approximation is violated.

### 7.2.2 Description of the Environment Investigated

The dimensions for the problem examined in this chapter are chosen to match the Chemistry Building<sup>1</sup> at The University of Auckland, and is hereafter referred to as Building I. The back face of Building I is surrounded by two sets of multi-storey buildings (Buildings II and III) indicated in Fig. 7.1. Building II is 20 m away and eight storeys high, while Building III is 8 m away, two storeys high and has a sheet metal roof. The front face of Building I overlooks a street, where the nearest buildings are 40 m away and single storey<sup>2</sup>. The outside faces of all three buildings are not smooth, e.g. Fig. 7.1 shows ledges, extending from the windows, which support large hanging concrete panels (as described in section §6.3). The area surrounding the glass windows is also made from concrete and rises 1.0 m from the floor. Internally, the floor-ceiling height is 4.0 m for the first floor, and 3.0 m for all subsequent floors. The floors are 0.30 m thick and made from steel-reinforced concrete. The internal partitions are made from drywall attached to timber frames. Office furniture, lab equipment and similar clutter were also present in measurement environment, but not included in the FDTD model.

### 7.2.3 Simulation Configuration

The FDTD method has been used to simulate propagation (for both  $\text{TM}_z$  and  $\text{TE}_z$  lattice polarisations) on a simplified two-dimensional geometry, shown in Fig. 7.2. Similar to chapter 6, this geometry considers a vertical ‘slice’ through the problem, consisting of five dielectric slabs (representing the concrete floors of Building I) and the various external features of Buildings II and III, including windows, ledges and hanging panels. The FDTD simulation space is surrounded by a uniaxial perfectly matched layer (UPML) as described in chapter 4. A single electric field component in the two-dimensional lattice acts as the transmitter. For  $\text{TM}_z$  lattice polarisation the fields radiate isotropically, however for  $\text{TE}_z$  polarisation the radiation pattern is similar (as expected) to a Hertzian dipole. Therefore, for a  $\text{TE}_z$  polarised lattice, more energy is directed azimuthally (toward the surrounding buildings), than through the floors. The concrete floors are modelled as homogeneous, lossy, dielectric slabs (0.3m thick) with permittivity  $\epsilon_r = 6.0$ , and conductivity  $\sigma_E = 50 \text{ mS/m}$  [41]. The metal reinforcing bars (rebar) have been modelled as  $\sigma_E = 10^7 \text{ S/m}$  blocks with a 4 cm square cross-section spaced 0.5 m

<sup>1</sup>Similar to the Engineering Tower examined in chapter 6, this is a typical 1960’s metal reinforced concrete-slab building.

<sup>2</sup>Wide-band measurements did not indicate any significant signals arriving on long delay paths that could be attributed to interactions with these distant buildings which have subsequently have been ignored.

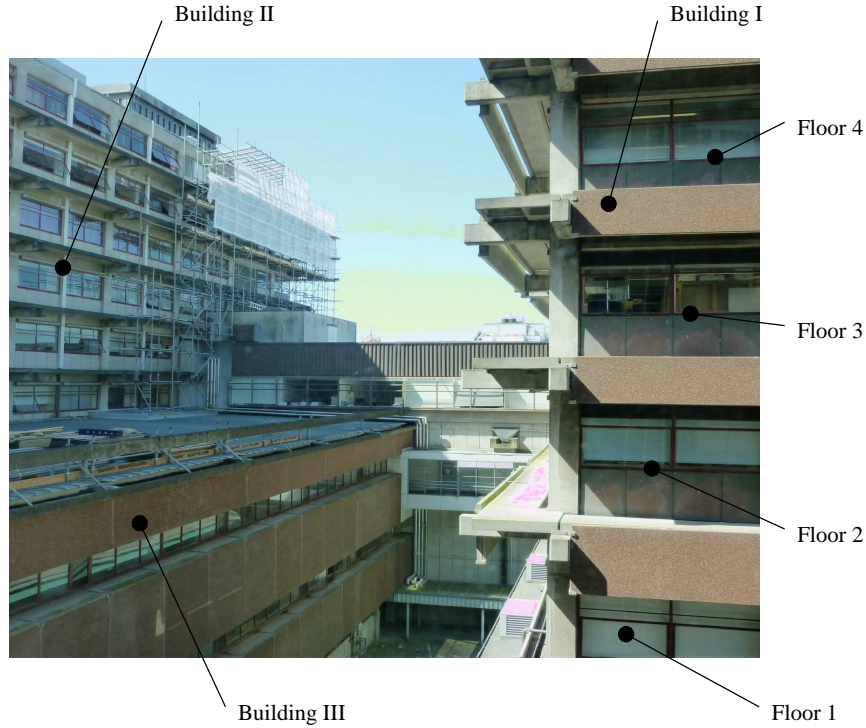


Figure 7.1: Photograph of the environment considered in this chapter, identifying the back face of the Chemistry Building (I) and the surrounding Buildings (II and III). The scaffolding visible in the photograph on Building II was not present at the time of the experimental study.

apart. The glass windows are 5 mm thick<sup>3</sup>, and are modelled as dielectric slabs with  $\epsilon_r = 3.0$ , and  $\sigma_e = 2 \text{ mS/m}$ . The metal roof is modelled as a 10 mm thick sheet with  $\sigma_e = 10^7 \text{ S/m}$ . Numerical dispersion is minimised by ensuring the lattice density is at least  $12 \text{ cells}/\lambda_{min}$  [11].

The simulations were conducted at centre frequencies of 1.0 GHz and 4.5 GHz. Sections §7.3 and §7.4 present the results obtained when exciting the lattice with a 1.0 GHz centre frequency pulse, while section §7.6 compares the 4.5 GHz simulation results to measurements conducted at that frequency. For the 4.5 GHz simulations, the lattice size is 2 mm, the time step 4.48 ps, and the total time simulated is 400 ns (90,000 time steps). At 1.0 GHz the lattice size can be relaxed to 5 mm.

### 7.3 Narrowband Results (1.0 GHz)

Fig. 7.2(a) shows the distribution of steady-state complex field amplitude (for an  $E_z$  component) in a  $\text{TM}_z$  polarised lattice at 1.0 GHz. The corresponding grey-scale intensity plot of the phase is shown in Fig. 7.2(b), where white corresponds to a phase of  $+\pi$ , and black is  $-\pi$ . Similar plots for a  $\text{TE}_z$  polarised lattice are shown in Figs. 7.3(a) and (b). The field distributions outside the buildings are complex, and indicate the presence of strong multi-path phenomena. However, within Building I the results suggest propagation to a lower storey is dominated by penetration through the concrete floors, and reflection/scattering from the external faces of Buildings II and III. On an immediately adjacent floor—and for both  $\text{TM}_z$  and  $\text{TE}_z$  lattices—the phase fronts generally remain centred on the antenna, indicating the dominant propagation path in

<sup>3</sup>At 4.5 GHz the lattice size is 2 mm. In this case the window thickness was reduced to 4 mm.

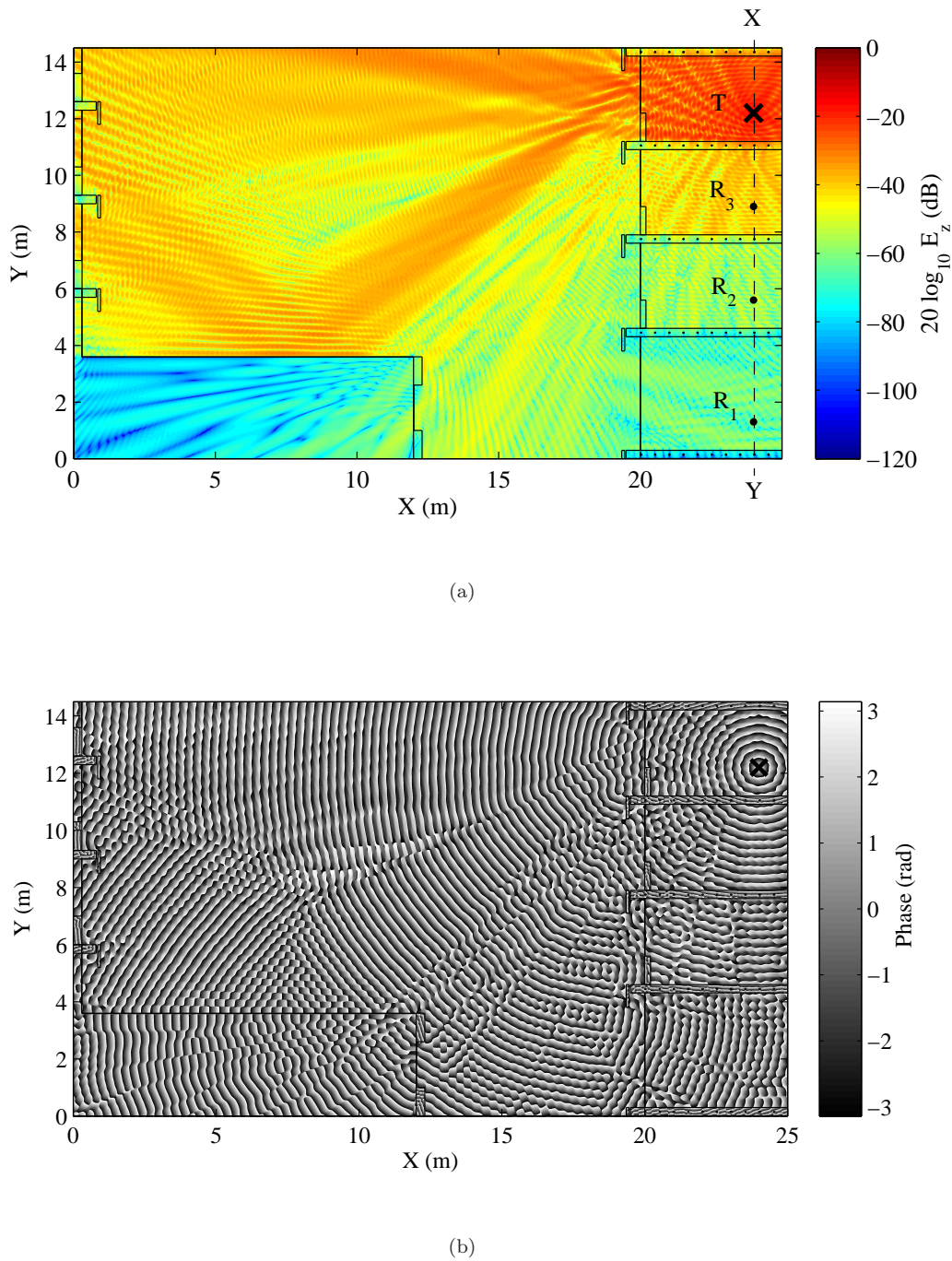


Figure 7.2: (a) Complex field amplitude (in dB units relative to the source) and (b) Phase of an  $E_z$  component in a  $\text{TM}_z$  polarised lattice. The location of the transmitter is marked with  $\times$ . The impulse response is recorded at points  $R_1$ - $R_3$  (discussed in section §7.4).

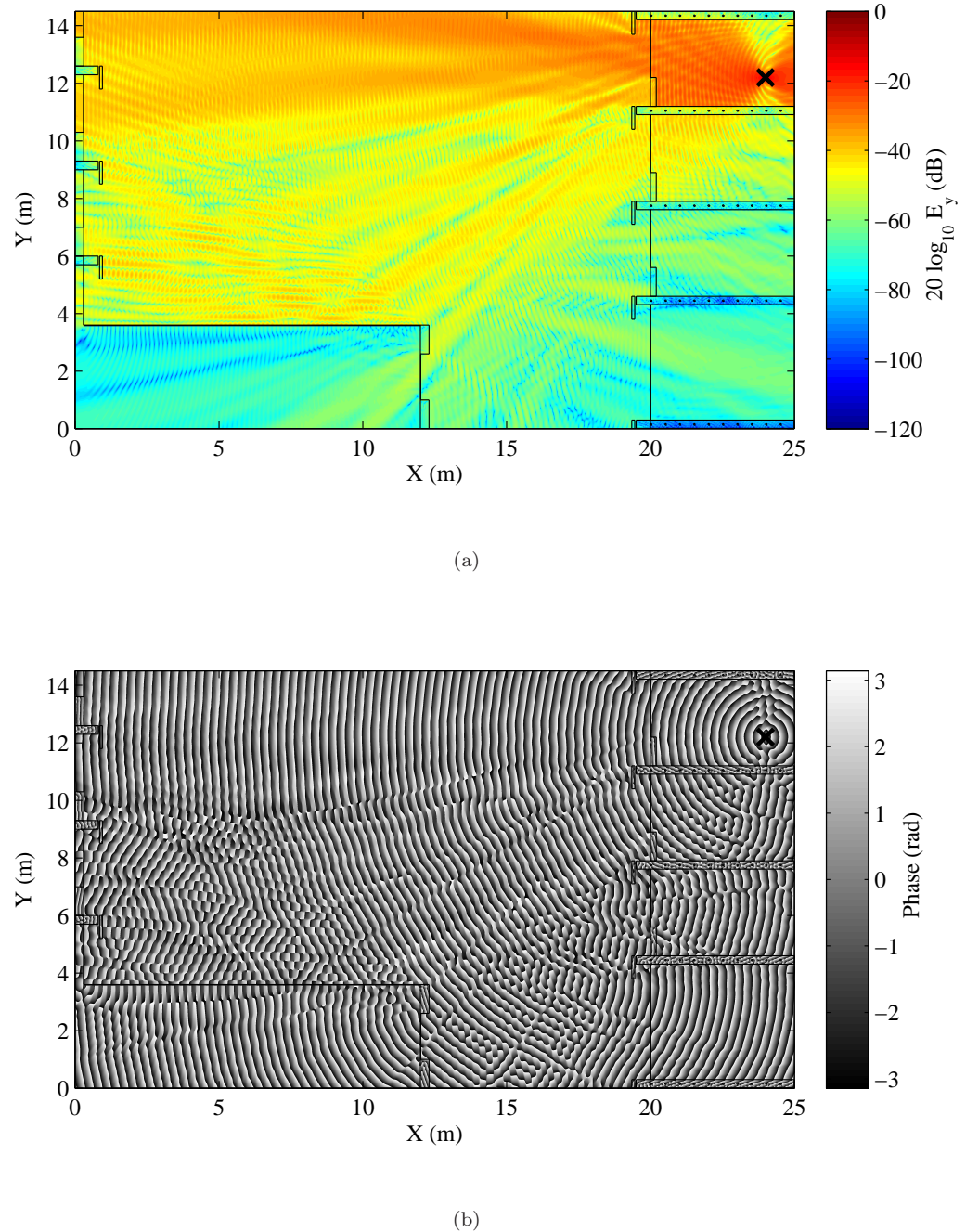
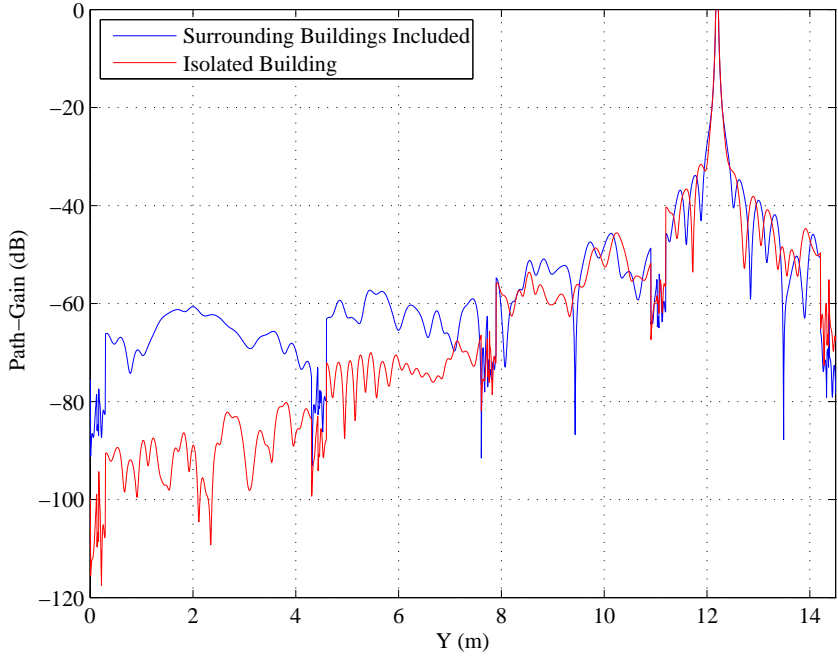
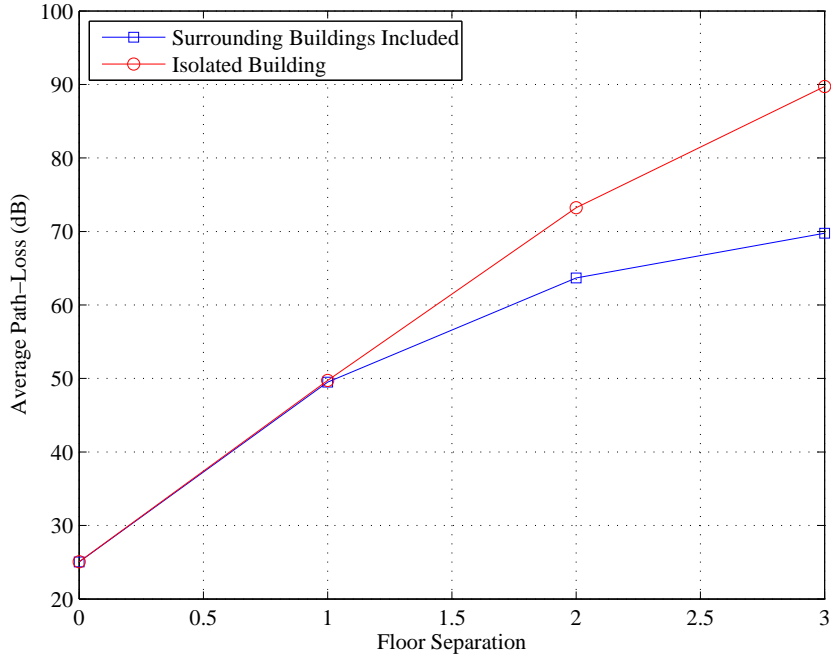


Figure 7.3: (a) Complex field amplitude (in dB units relative to the source) and (b) Phase of an  $E_y$  component in a  $TE_z$  polarised lattice. The location of the transmitter is marked with  $\times$ .



(a)



(b)

Figure 7.4: (a) FDTD modelled path-gain at 1.0 GHz along the path XY in Fig. 7.2(a) with and without surrounding buildings. (b) Average path-loss recorded across each floor with and without the surrounding buildings. In both cases TE<sub>z</sub> polarisation is assumed.

these regions is penetration through the floors<sup>4</sup>. Similar to the results reported in chapter 6, localised shadowing effects from the rebar are also observed, however the dominant propagation path remains penetration through the floors.

In the geometry considered the reflection paths are largely free-space and consequently may carry higher power, relative to paths penetrating through the floors. Density plots of the field strength show bands of greater magnitude recorded across each floor, and these can be attributed to reflections from the surrounding buildings. Furthermore, although the power recorded on adjacent floors decreases, the net floor attenuation is lower than expected (compared to the isolated building considered in chapter 6). The reflections are also evident in the grey-scale density plots of electric field phase. When surrounding buildings are modelled, as shown in Fig. 7.2(b) and Fig. 7.3(b), the curvature of the phase-fronts are not centred on the transmitting antenna. The angle of arrival and curvature of the phase in these regions indicates this observation is caused by reflections from the surrounding buildings. On the second and third floors, both penetrating and reflecting components are visible in the phase plot, while on the first floor reflections dominate completely, suggesting that as more floors are penetrated, the relative strength of the reflected component increases.

Fig. 7.4 shows the path-gain<sup>5</sup> recorded along the line XY in Fig. 7.2(a), which passes through all four floors—for TE<sub>z</sub> polarisation at 1.0 GHz. Also included in Fig. 7.4 is the power along a similar slice when the surrounding buildings are not included in the simulation geometry. It is observed that power along line XY is discontinuous at the dielectric boundaries, and occurs as the concrete floors are orthogonal to the E<sub>y</sub> field components. In the absence of surrounding buildings the attenuation introduced by each floor is approximately 19 dB and relatively constant. In contrast, when the surrounding buildings are included, the (apparent) attenuation introduced by each floor decreases significantly. Fig. 7.4(b) compares the average path-loss recorded across each floor when the nearby buildings are included in the geometry. It is evident that the surrounding buildings can reduce the path-loss recorded on adjacent (and nearly adjacent) floors. However, this finding is based on two-dimensional FDTD simulations; in reality, spreading in the third (orthogonal) dimension will reduce the power carried on long delay paths. This issue is discussed further in section §7.6.2 and appendix E.

## 7.4 Wideband Results

The impulse response was measured by applying a modulated Gaussian pulse, defined by

$$p(t) = \exp \left[ -\left( \frac{t - t_0}{t_w} \right)^2 \right] \sin(2\pi f_0 t),$$

to the vertical electric field component at T in Fig. 7.2(a). The pulse parameters are:  $f_0 = 1.0$  GHz,  $t_w = 1.24$  ns and  $t_0 = 5t_w$  s, producing a pulse with a 150 MHz 3-dB bandwidth. The E<sub>y</sub> component of the electric field was sampled on each floor directly under the transmitter, at the points R<sub>1</sub>, R<sub>2</sub> and R<sub>3</sub> indicated in Fig. 7.2. The base-band impulse response was recovered by non-coherent demodulation of the received signals (essentially an envelope detector).

Fig. 7.5(a)–(h) shows the electric field strengths after 2000, 4000, 6000, 10000, 12000, 16000,

---

<sup>4</sup>It should be noted that the radiation pattern of an E<sub>y</sub> source element in a TE<sub>z</sub> polarised lattice introduces a null directly under the antenna.

<sup>5</sup>Similar to chapter 6, the two-dimensional path-gain is defined as  $20 \log_{10} |E|$ , where the source has been normalised to 1∠0 v/m.

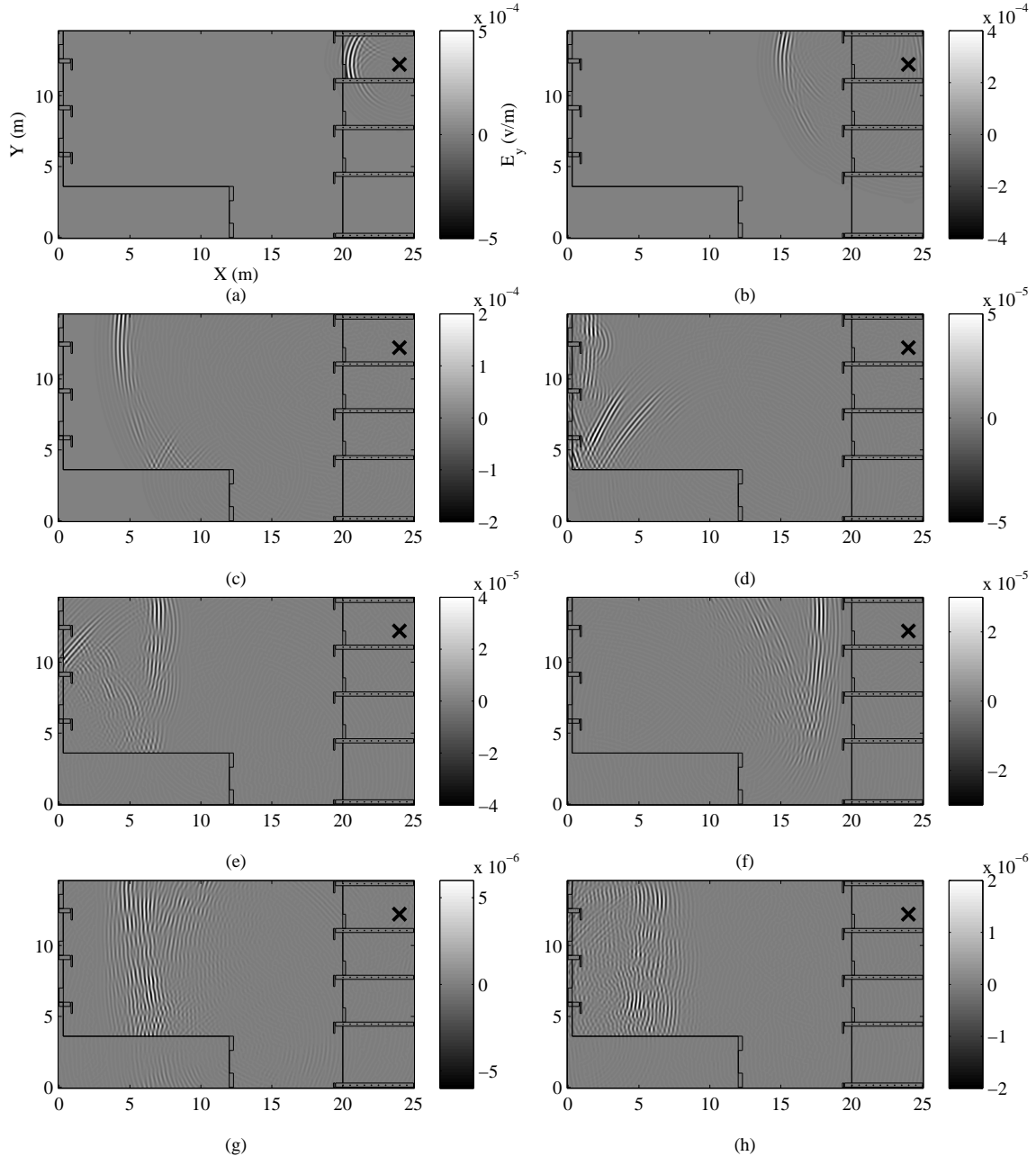
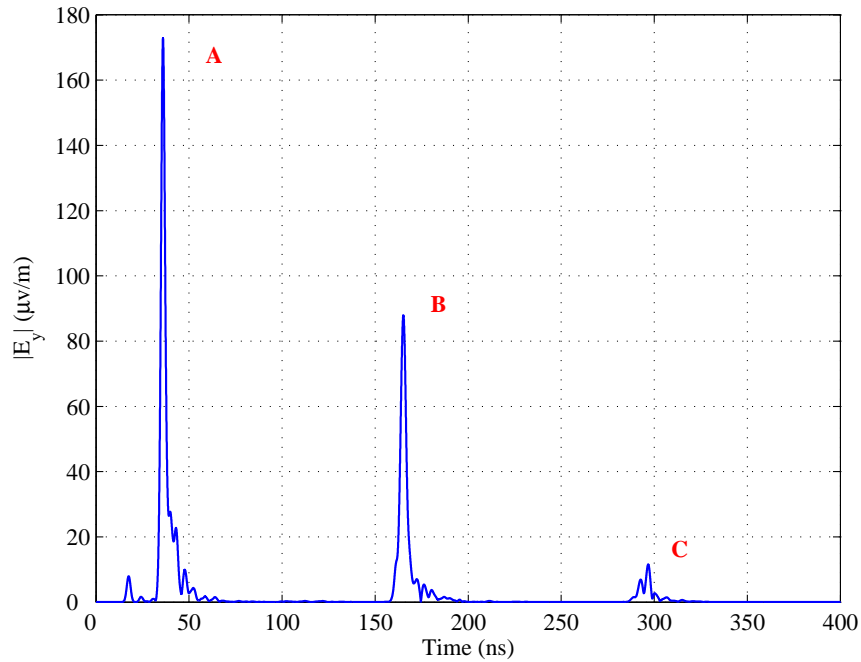
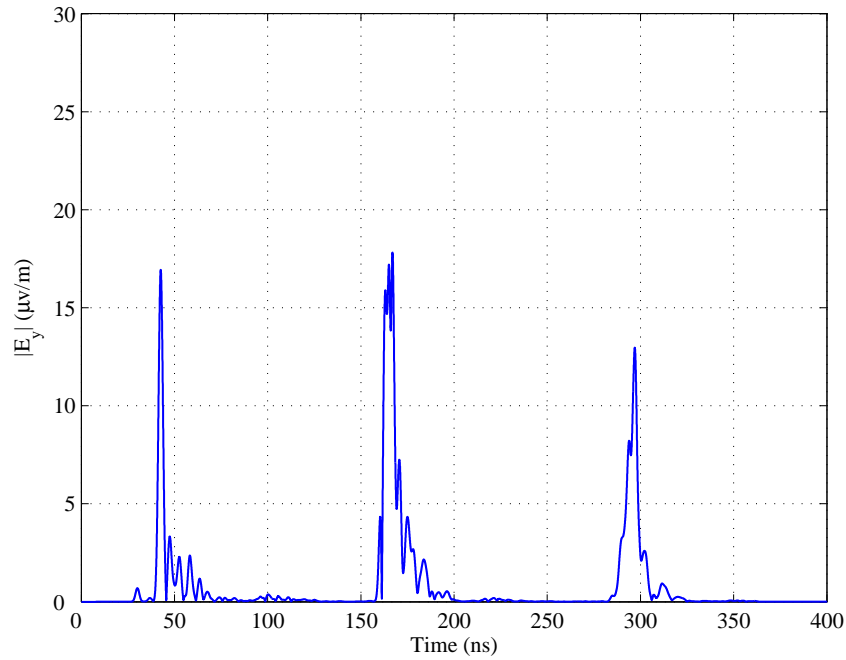


Figure 7.5:  $|E_y|$  field at (a) 2000, (b) 4000, (c) 6000, (d) 10000, (e) 12000, (f) 16000, (g) 22000 and (h) 26000 time-steps. Separate scales are required for each plot as spreading reduces the pulse magnitude.

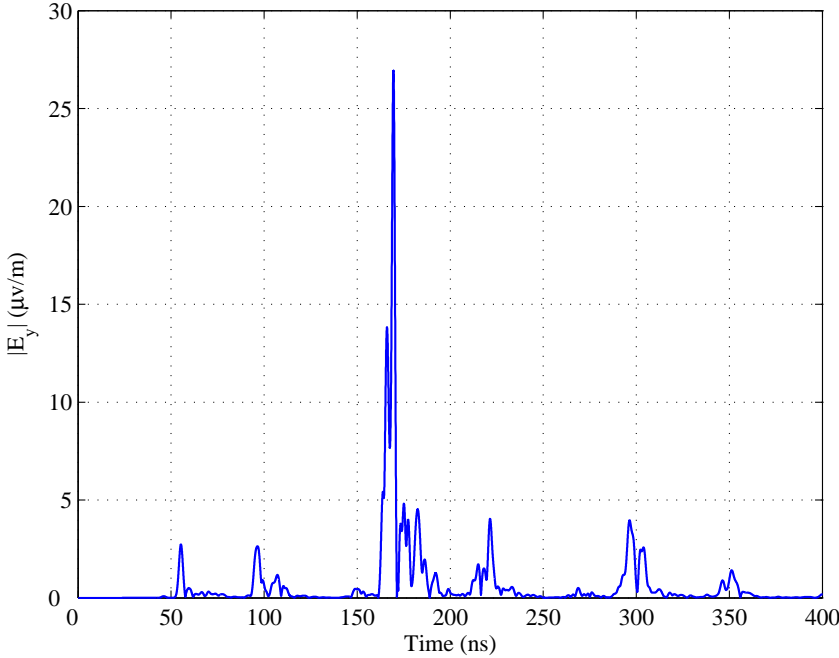


(a) Transmitter one floor above.



(b) Transmitter two floors above.

Figure 7.6: FDTD simulated impulse responses recorded at points (a) R<sub>3</sub>, (b) R<sub>2</sub> and (c) R<sub>1</sub>.



(c) Transmitter three floors above.

Figure 7.6: FDTD simulated impulse responses recorded at points (a)  $R_3$ , (b)  $R_2$  and (c)  $R_1$ .

22000 and 26,000 time steps respectively. The modulated Gaussian pulse propagates away from the source and interacts with the surrounding buildings. It is observed that strong reflections onto lower floors are supported. Before reflecting at Building II, the wave-fronts remain circular and centred on the source point. The external surface of Building II has been modelled in some detail, and as a result the reflected pulse width widens considerably. As shown in Fig. 7.5(f), the returning pulse is reflected off Building I, leading to a double reflection at Buildings II and III.

Fig. 7.6(a), (b) and (c) show the base-band impulse response at points  $R_3$ ,  $R_2$  and  $R_1$  respectively. In each location a number of distinct pulses are visible, but these can be grouped into three sets, which are marked A, B and C on Fig. 7.6(a). By examining the evolution of the pulse, and by computing path-length from the time-delay, it is possible to associate each pulse with a distinct path. Pulse set A represents the signal travelling directly through the floors, while pulse sets B and C represent single and double reflections at the face of Building I respectively. As shown in Fig. 7.6(b), on lower floors the received signal is increasingly dominated by pulses arriving on long delay paths (pulses B and C). The smaller pulses between A, B and C represent diffraction from the corner of Building II (since no direct reflection path is possible).

The fraction of the total received power arriving on each component across each floor is estimated in Table 7.1. The power arriving on a particular path is calculated by summing the squared electric field over the appropriate time interval, and the fraction computed by dividing this value by the total received power across the floor. The time intervals are identified through inspection, and as time delays are sufficiently spread, overlaps are avoided. The components reflected at the face of the surrounding buildings have been divided into single (B) and double

Table 7.1: Percentage of power arriving on each component.

		Floor 1	Floor 2	Floor 3
Direct (A)		0.6%	10.6%	89.9%
	Total	94.3%	89.0%	10.1%
Reflections	Single Bounce (B)	92.6%	88.2%	10.1%
	Double Bounce (C)	1.7%	0.8%	0.0%
Diffraction		5.2%	0.4%	0.0%

(C) reflections.

For a single floor separating the transmitter and receiver the majority of received power arrives through the floor, while only 10.1% arrives on reflected paths. As more floors separate the transmitter and receiver, the relative strengths of reflected pulses increases<sup>6</sup>. On the second floor, 89.0% of the total received power is reflected, and on the third floor, only 0.6% is due to floor penetration. The majority of the reflected power arrives on single-bounce paths, with double-bounce reflections delivering at most 1.7% of the total power. It must also be noted that diffraction at the corner contributes a maximum 5.2% of the total received power on the first floor, and is negligible on higher floors. This indicates diffraction does not make a major contribution in this environment. As the reflected paths remain external to the building, they are largely free-space, resulting in similar amplitudes on lower floors.

## 7.5 Development of a Mechanistic Model

The results presented in sections §7.3 and §7.4 indicate the power arriving on adjacent floors in a multi-storey building (with nearby buildings present) is dominated by a component penetrating through the floors and another component reflected by nearby buildings. Based on these findings, a simplified GO-based, mechanistic model to predict the path-loss on adjacent floors is proposed. The results have also indicated that double-reflections and edge diffraction can increase the received power; however their contribution is not significant and can be excluded from consideration in the mechanistic model. Thus the model consists of two components, both of which are based on the Friis equation [2, pp. 70–73]. For the computation of spatially averaged power, the two components are treated as uncorrelated and are added together on a power basis, given by

$$PL_{\text{total}} = PL_{\text{direct}} + PL_{\text{reflected}} \text{ (W).} \quad (7.1)$$

The path-loss of the direct component is estimated by

$$PL_{\text{direct}} = \left( \frac{\lambda}{4\pi d_d} \right)^2 \kappa^{2n} \text{ (W),} \quad (7.2)$$

where  $d_d$  is the distance between the transmitter and receiver when the wave penetrates through the floors,  $n$  is the number of floors penetrated and  $\kappa$  is the (linear) attenuation through a single floor. Measurement and simulation results indicate  $\kappa$  (in log-units) is approximately 22 dB/floor, which is consistent with observations made by other researchers [6, 38, 84]. The

---

<sup>6</sup>It should be noted that the results presented in Table 7.1 are calculated from two-dimensional FDTD simulations. In reality spreading in the third dimension will reduce the power carried on long paths.

path-loss of the component reflected back from the surrounding buildings is estimated by

$$PL_{\text{reflected}} = \sum_{b=1}^B \left( \frac{\lambda}{4\pi d_b} \right)^2 \prod |\Gamma|^2 \prod |\tau|^2 \text{ (W)}, \quad (7.3)$$

where  $B$  is the number of adjacent buildings parallel to an external face,  $d_b$  is the distance between the transmitter and receiver when the wave reflects from surrounding building  $b$ <sup>7</sup>,  $\Gamma$  is the reflection coefficient at the building face, and  $\tau$  is the transmission coefficient through the glass windows. Measurements and simulations indicate transmission through two sets of glass windows reflection at a glass-fronted building reduces the received power by 18 dB, and can be modelled by reflection and transmission coefficients of 0.5.

## 7.6 Experimental Validation

### 7.6.1 Narrow-band Comparison

The path-gains predicted by the mechanistic model proposed in (7.1)–(7.3) have been compared against experimental measurements of the received power on the lower three floors of Building I. The transmitting antenna was located 4.0 m from the windows on the third floor, and the received power was measured at 20 points on each of the lower floors. The measurements were taken at 4.5 GHz using bi-conical antennas, and—similar to the approach discussed in chapter 6—the receiving antenna was rotated over a  $9\lambda$  circular locus to determine the sector mean by averaging the effects of multi-path fading. Fig. 7.7 compares the measured sector averaged path-gain with values predicted by the mechanistic model. The RMS error between the path-gains predicted by the mechanistic model and measurements is 3.5 dB for a single floor separation, and 2.8 dB for two floor separations, indicating a high degree of prediction accuracy is possible with the mechanistic model. Also included in Fig. 7.7 are predictions made with only the direct (penetrating) component. In the case shown, significantly lower powers are predicted when the reflecting components are ignored.

Directional measurements were also used to determine the angular distribution of received power on the lower floors of Building I. Fig. 7.8(a) shows a floor-plan with the relative positions of the transmitter, receiver<sup>8</sup> and surrounding buildings identified. A bi-conical antenna was used to transmit the signal at 4.5 GHz, while a pyramidal horn antenna<sup>9</sup> was used to record the received power. The horizontal 3 dB beam-width of the horn antenna is  $10^\circ$ , and the fields were sampled for every  $10^\circ$  antenna rotation. Fig. 7.8(b) shows the pattern of the received power (in linear units) with antenna rotation for a single floor separation. It is observed that the majority of the power arrives at approximately  $180^\circ$ , in the direction of the surrounding buildings. The smaller lobe observed at  $90^\circ$  can also be attributed to a similar reflection at the face of another building.

### 7.6.2 Wide-band Comparison

The simulation findings presented in section §7.4 were confirmed with experimental measurements of the channel impulse response. The impulse response was measured using a sliding

<sup>7</sup>Given the source and observation points,  $d_b$  can be determined by doing a search for the reflection point.

<sup>8</sup>In the case examined the transmitting and receiving antennas were vertically aligned.

<sup>9</sup>The decision to use a pyramidal horn antenna was influenced by the available equipment inventory at the time of the measurement campaign.

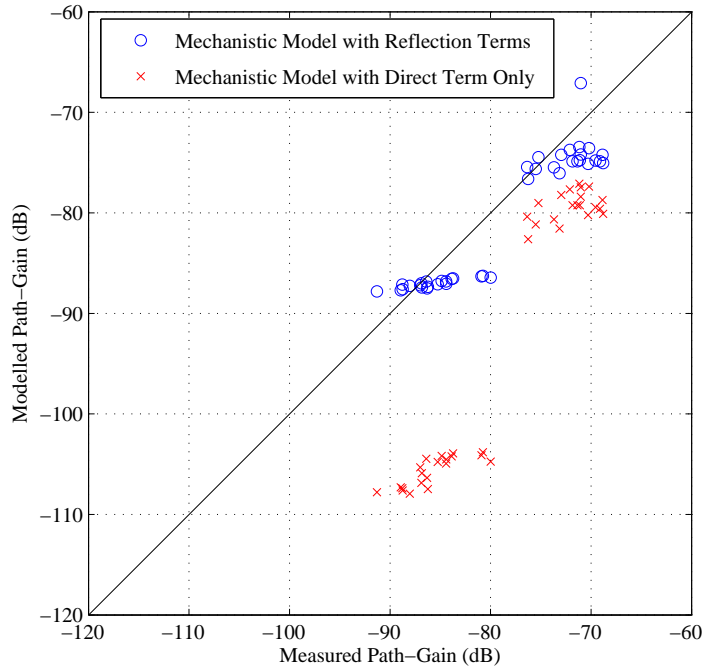


Figure 7.7: Measured path-gain versus the mechanistic models given by (7.1)–(7.3).

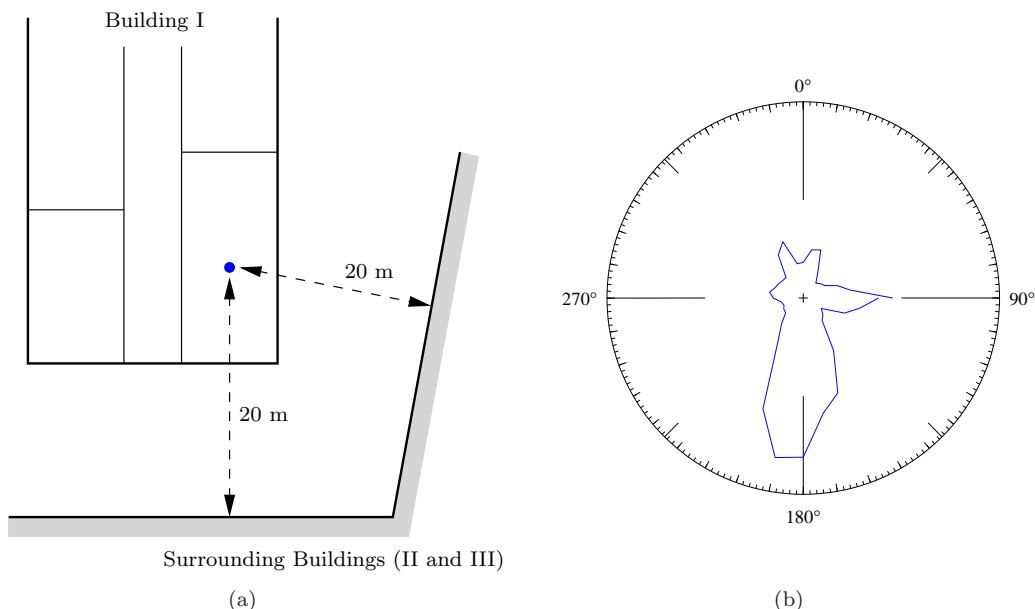


Figure 7.8: (a) Floor plan showing the relative positions of transmitter (marked with ●) and the surrounding buildings. (b) Received power recorded at ● (one floor below the transmitter) as a function of angle.

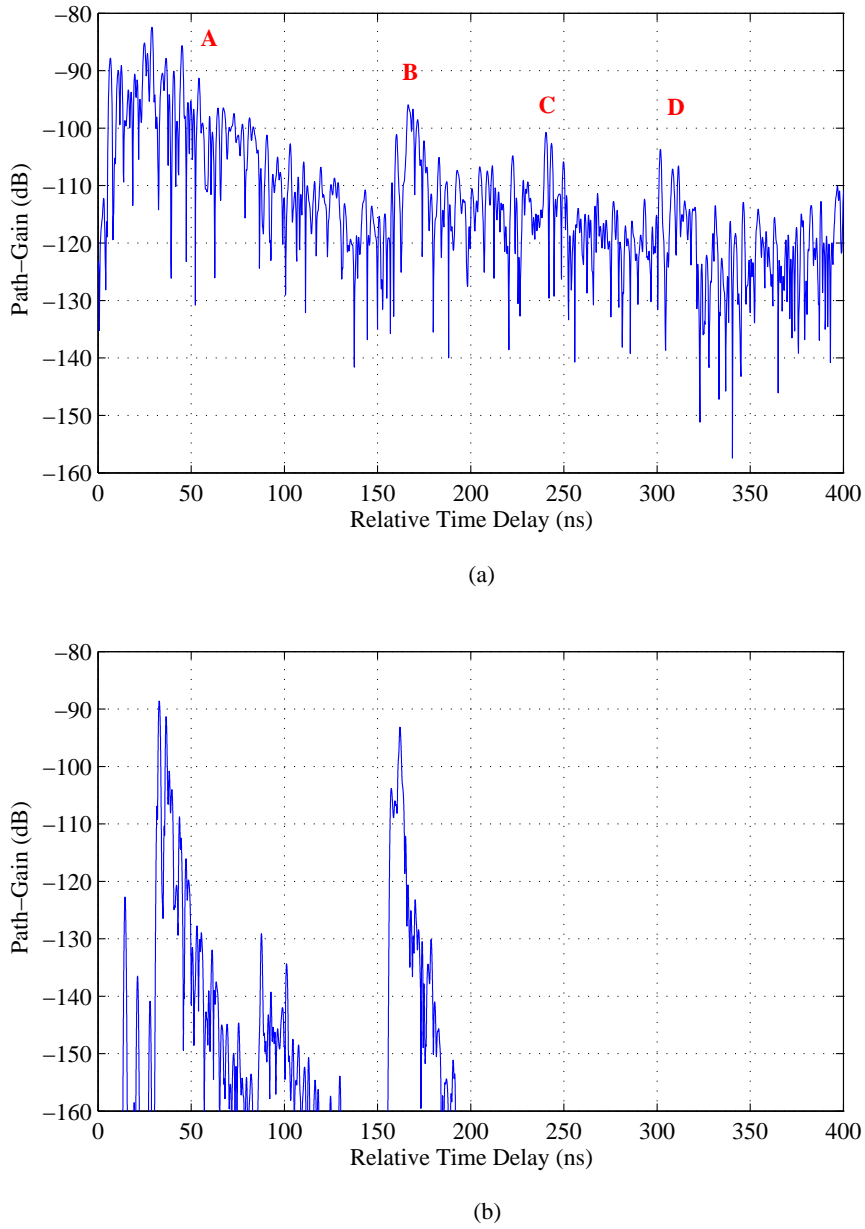


Figure 7.9: Comparisons between the (a) experimentally measured and (b) FDTD simulated impulse response for one floor separation.

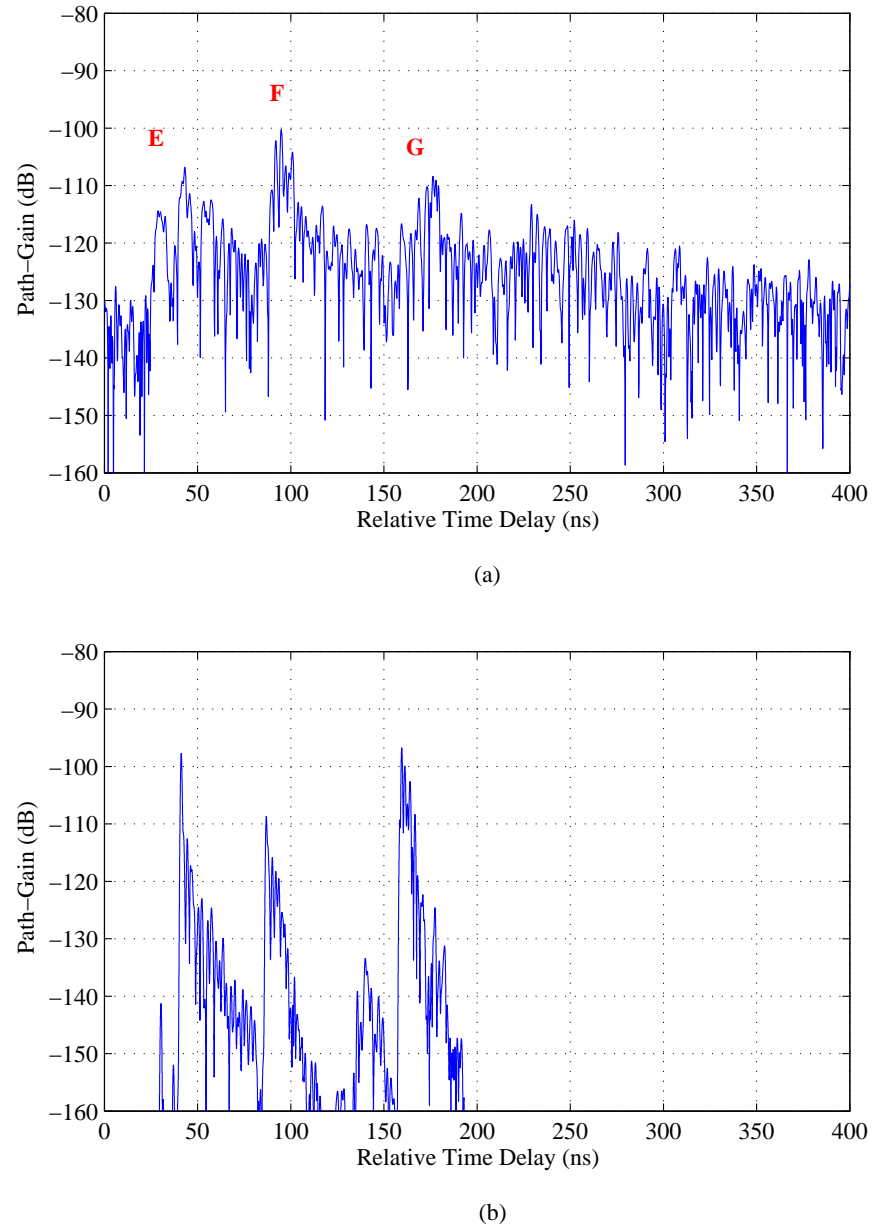


Figure 7.10: Comparisons between the (a) experimentally measured and (b) FDTD simulated impulse response for two floor separations.

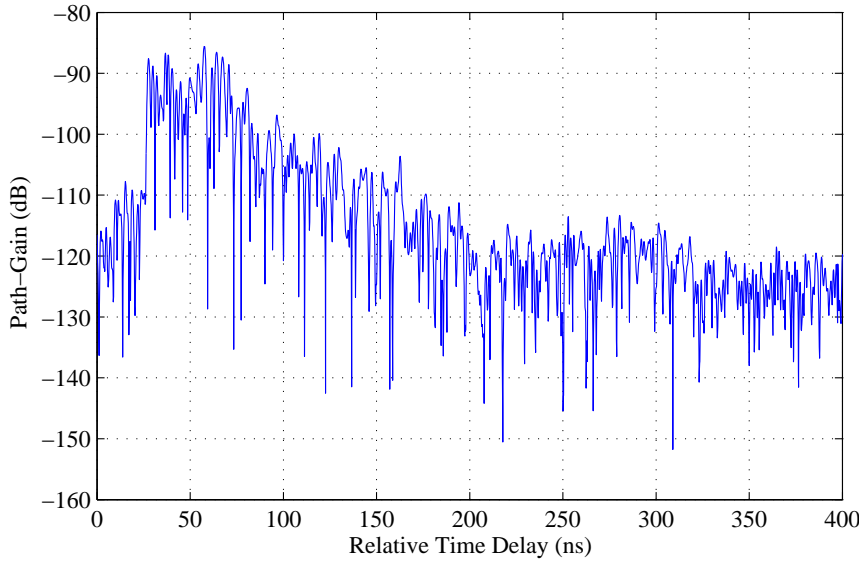


Figure 7.11: Impulse response measured at the front face, where there are no surrounding buildings.

correlator channel sounder with a 511-bit PN sequence clocked at 800 MHz<sup>10</sup>. The centre frequency of the system was 4.5 GHz, and the 3 dB signal bandwidth was approximately 700 MHz. The theoretical dynamic range for the system is 43.33 dB [89], however, in practise it was approximately 30 dB. To express the results in path gain, and to remove the linear system response, the raw data was calibrated against free-space measurements made in an anechoic chamber. The measurements were time-averaged to minimise the effects of time-varying scatterers in the environment. Wide-band antennas were used: a vertically-orientated bi-cone as the transmitter and a pyramidal horn as the receiver. By taking measurements with a directional receiving antenna, only signals arriving in the beam-width will contribute to the received signal. Significantly, this will limit the effect of signals arriving from other directions and allows a valid comparison with simulation results. For the purposes of comparison, the two-dimensional FDTD results were extended to 2.5-dimensions<sup>11</sup> by assuming isotropic spreading in the (orthogonal) third dimension. This procedure is detailed in appendix E.

The transmitter was located on the third floor, and the impulse response measurements were taken on the first and second floors. Similar to the FDTD simulations, both antennas were vertically aligned and positioned 4.0 m from the windows and 1.0 m above the floor. The measurements were repeated at the front face of Building I (where there are no nearby buildings). The measured impulse response on the first and second floors at the back face are shown in Fig. 7.9(a) and Fig. 7.10(a). The salient features have been labelled. For comparison, the 4.5 GHz FDTD simulation results (with 700 MHz 3 dB pulse bandwidth) are shown beneath in Fig. 7.9(b) and Fig. 7.10(b). It is observed that there are significant differences in the signal magnitude (up to 10 dB) between the simulations and the measurements, however, there is generally good agreement in the time-domain. For both sets of measurement data the noise floor

<sup>10</sup>The design of the channel sounder was not considered in this thesis. The measurements were taken with the channel sounder described in [89], on loan from Dr Pirkil and The Georgia Institute of Technology.

<sup>11</sup>In the context of this thesis 2.5-dimensions refers to a pseudo three-dimensional expansion described in appendix E.

(and dynamic range) of the system is 35 dB below the maximum peak (approximately  $-115$  dB and  $-135$  dB). The measurements have a higher noise floor and significantly lower dynamic range than the FDTD simulations, however the dominant pulses are clearly visible. Furthermore, Fig. 7.11 shows the impulse response measured for a single floor separation when the horn antenna was directed outwards, toward the street, and no long delay paths are observed.

In Fig. 7.9(a) there are two distinct sets of pulses, identified by A and B, and these are centred at 35 ns and 165 ns. These correspond to the components of the signal travelling through the floor and reflected by Building I respectively. This is supported by FDTD results, and the time difference—indicating an excess path length of 39 m—agrees well with reflection from Building I, 20 m away. The smaller pulses at 240 ns and 310 ns (identified by C and D) are thought to be caused by higher order reflections since time delays agree well with FDTD simulations, but, as these are close to the noise floor, no firm conclusions can be drawn. In Fig. 7.10(a) three sets of pulses—identified by E, F and G and centred at 45 ns, 90 ns and 170 ns respectively—are observed. These correspond to penetration through the floors, scattering from Building II, and reflection at Building I respectively. The temporal alignment with the FDTD simulation results in Fig. 7.10(b) is good; however the magnitudes of some components are different.

The differences between the simulations and measurements are largest when two floors separate the transmitter and receiver; for a single floor separation the differences are smaller, approximately 3 dB. This suggests that much of the error is introduced by not including some features of the first floor environment in the FDTD simulation. The first floor environment is heavily cluttered by industrial equipment (e.g. motor/generators, gantry cranes), which was not included in the FDTD model. This type of environment tends to scatter the energy and lower the peak power arriving on a single component [2, pp. 123–125]. Furthermore, the detailed scatter on the roof of Building II was not modelled in the FDTD simulations. It should also be noted that expanding the FDTD results to 2.5-dimensions will underestimate the distance travelled (and thus overestimate the received power) when the wave travels through a dielectric material.

## 7.7 Discussion

It is observed that reflections from nearby buildings can significantly increase the average received power on adjacent floors (compared to the case when no surrounding buildings are present). After 1–2 floor separations the reflected signals are of similar magnitude to those penetrating the floors<sup>12</sup>. This finding could have significant implications for in-building wireless systems. If frequencies are reused on adjacent floors, reflections can provide low-loss paths, which will increase the levels of co-channel interference, lowering the SIR and thereby reducing system performance. Furthermore, as more floors separate the transmitter and receiver, an increasing proportion of the power arrives on long delay paths, manifesting as strong echoes in the impulse response. In addition to causing rapid fading of the signal envelope, the time delayed echoes overlap, causing symbol errors in digital communication systems due to inter-symbol-interference. The increased delay-spread due to reflections from nearby buildings potentially decreases maximum transmission rates.

The mechanistic model outlined in (7.1)–(7.3) is appropriate when adjacent buildings are

---

<sup>12</sup>It is also important to note that the external reflecting surfaces do not need to be smooth. Results indicate strong reflected components are possible from electrically rough building faces.

present to support reflection onto lower floors, and when the construction materials and architectural styles are similar. Other paths, both internal (e.g. propagation down stairwells and lift shafts) and external (e.g. diffraction at floor edges) have not been considered in this chapter, as the adjacent building reflections tend to dominate the received signal. However, in the absence of surrounding buildings, other mechanisms will need to be considered.

## 7.8 Summary

This chapter has extended the propagation study examined in chapter 6 to consider possible reflection paths from nearby buildings, however, the size of the problem has restricted the FDTD analysis to a two-dimensional vertical slice. The FDTD results indicate strong reflected paths exist and can dominate the signal received on adjacent (or nearly adjacent) floors. A mechanistic model to characterise this behaviour can be formulated using two-components to account for paths penetrating through the floors and reflecting from nearby buildings. Experimental measurements of the path-loss on lower floors show a good agreement with the mechanistic model. Wide-band measurements of the channel impulse response are also compared with the FDTD simulation results, and the differences can be attributed to details/clutter in the environment not considered in the two-dimensional geometry. Chapter 8 will analyse inter-floor radio-wave propagation using a three-dimensional implementation of the FDTD method (however, nearby buildings will not be considered).

# Chapter 8

## Propagation Study C: Within the Building Perimeter (3D)

### 8.1 Introduction

The propagation studies presented in chapters 6 and 7 have largely focused on two-dimensional characterisations of the indoor radio channel. As noted in chapter 4, the high computational requirements of the FDTD method often restricts analysis of electrically large problems (such as propagation within buildings [41, 56, 58, 59, 62, 64]) to two-dimensions. It is important to note that, unlike the single-floor case, no single two-dimensional slice through a realistic multi-floor geometry can correctly account for all possible propagation paths. For example, many buildings have concrete shafts containing elevators and stairwells, and, as indicated in chapter 6, propagation to adjacent floors around (or through) such shafts can only be thoroughly examined in three-dimensions. Clutter in the propagation environment, such as office furniture, is also difficult to model in two-dimensions, and furthermore is frequently ignored. Accordingly, the propagation study presented in this chapter uses a three-dimensional parallel implementation of the FDTD method to fully capture the propagation mechanisms present within a multi-storey building. Due to the high computational requirements, only three floors have been considered, and all propagation paths are assumed to be contained within the building perimeter. In this regard, the research presented in this chapter is an extension of the problem considered in chapter 6.

Section §8.2 outlines the FDTD simulation parameters and describes the basic and detailed internal geometries considered in this chapter. Propagation on the same floor as the transmitter is examined in section §8.3, while section §8.4 considers propagation to adjacent floors. In both sections §8.3 and §8.4, streamline visualisations of the Poynting vector are used to investigate the existence of dominant propagation mechanisms, and to show how clutter in the environment alters the propagation paths. Section §8.5 compares the FDTD simulation results with experimental measurements of the path-loss, and simplified distance-dependency models to characterise the path-loss for both the simulations and measurements are developed in §8.6. Section §8.7 discusses the differences in the Rician fading distributions for both the basic and detailed geometries and compares these to experimental measurements. A brief summary of the major findings of the chapter is presented in section §8.8.

## 8.2 Description of the Environment Investigated

Three floors of the Engineering School Tower have been considered (a more detailed description of this indoor propagation environment can be found in chapter 6). The FDTD simulation volume for this problem is  $18 \times 18 \times 9 \text{ m}^3$ . A cubic lattice with  $\Delta = 1 \text{ cm}$  ( $\approx \lambda_{\min}/15$ ) is used, which results in approximately 3 billion mesh cells. Using the parallel three-dimensional FDTD code outlined in chapter 4, this problem takes 48 hours to solve to an approximate steady state (15,000 time-steps<sup>1</sup>), using 64 processors (Intel Xeon 2.66 GHz) and approximately 180 GB of memory.

Previous applications of time-domain methods to model propagation within buildings have assumed these buildings to be empty [12, 41, 54–56, 58, 60–62] (though [54, 60, 61] did assess the impact of different wall types). However, typical office buildings contain variable amounts of furniture and other metallic and dielectric clutter. In this chapter comparisons are made between a *basic* geometry (with a similar level of detail to models in the existing literature) and a more *detailed* geometry that includes some furniture and other environmental details. Fig. 8.1(a) and (b) show wire-frame representations of the basic and detailed geometries respectively.

The 0.20 m thick concrete floors, 1 cm thick exterior glass, and the hollow concrete shaft are common to both geometries. The basic geometry adds internal walls (modelled as 6 cm solid slabs of drywall) creating a corridor around the shaft, and divides the remaining space into nine offices. The detailed geometry models the internal walls as two 1 cm sheets of drywall (separated by a 4 cm air-gap) attached to wooden frames with studs spaced 1.5 m apart. Against each wall, metal bookcases extend floor-ceiling—these contain rows of books, modelled as 0.20 m thick wooden slabs. Appendix F shows an illustration of the wall details, and the attenuation introduced propagating through various walls. Doors into the offices and shaft are modelled as wood, and extend slightly into the corridor (the elevator doors are inset and modelled as metal). Metal reinforcing bars (2 cm square) are embedded in the concrete floors on a 1 m<sup>2</sup> grid, and metal window frames (2 cm square) are spaced 1.5 m apart along the external glass windows. Three flights of concrete stairs are also included in the central shaft. The electrical properties for the materials used in both the basic and detailed geometries are listed in Table 5.1.

## 8.3 Propagation on the Same Floor

Although same floor radio-wave propagation has been studied previously with the FDTD method, most studies have limited analysis to two-dimensional ‘slices’ through the geometry [41, 55, 56, 58, 62]<sup>2</sup>. However, these results may fail to capture propagation mechanisms caused by interactions with the floor or ceiling, and also cannot be directly verified against experimental measurements. This section presents a three-dimensional analysis of same floor propagation using the FDTD method, specifically focusing on the impacts of including clutter in the model; inter-floor propagation is discussed in section §8.4.

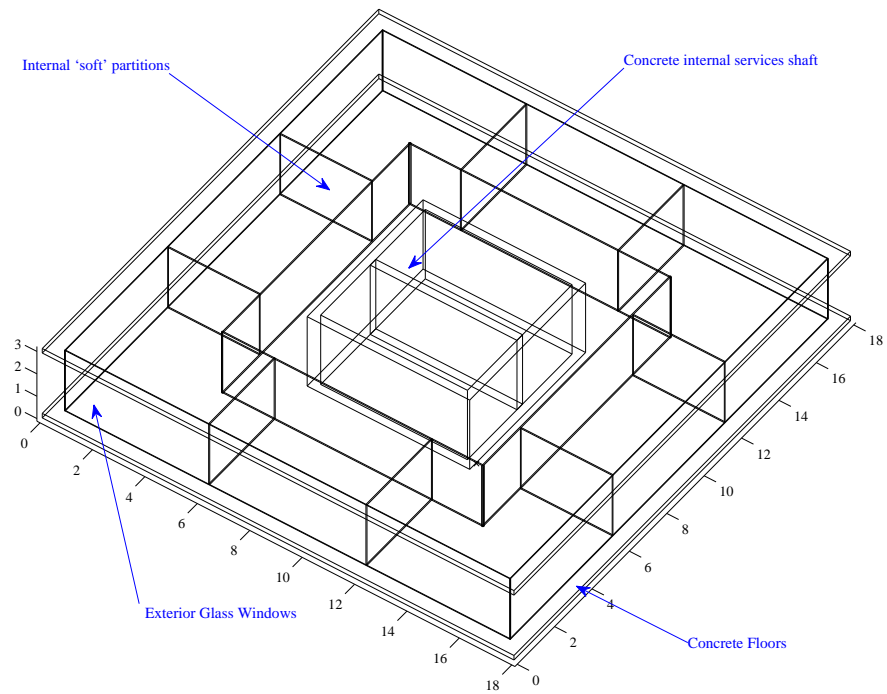
### 8.3.1 The Effects of Clutter

Fig. 8.2(a) and (b) plot the path-loss (in dB units) on horizontal slices through the basic and detailed internal geometries. The slices are positioned 1.50 m from the floor, in the plane of

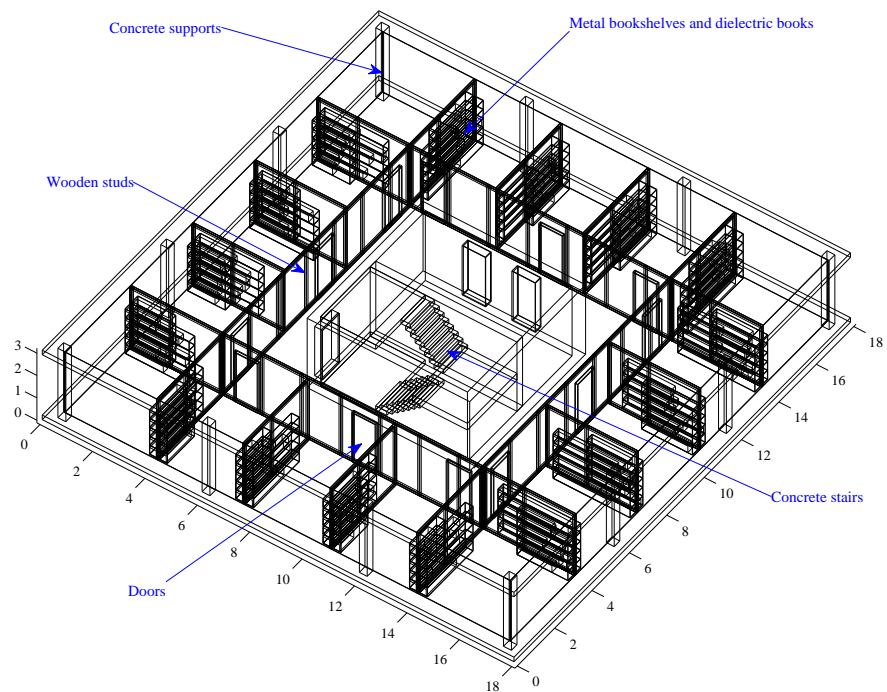
---

<sup>1</sup>The total simulation time is thus 0.27  $\mu\text{s}$ , allowing a maximum path length of approximately 82 m.

<sup>2</sup> $\text{TM}_z$  lattice polarisation is usually assumed as the radiation pattern of an  $E$  field source in a  $\text{TM}_z$  lattice is isotropic in the horizontal plane.



(a)



(b)

Figure 8.1: Wire-frame representations of the (a) basic and (b) detailed geometries.

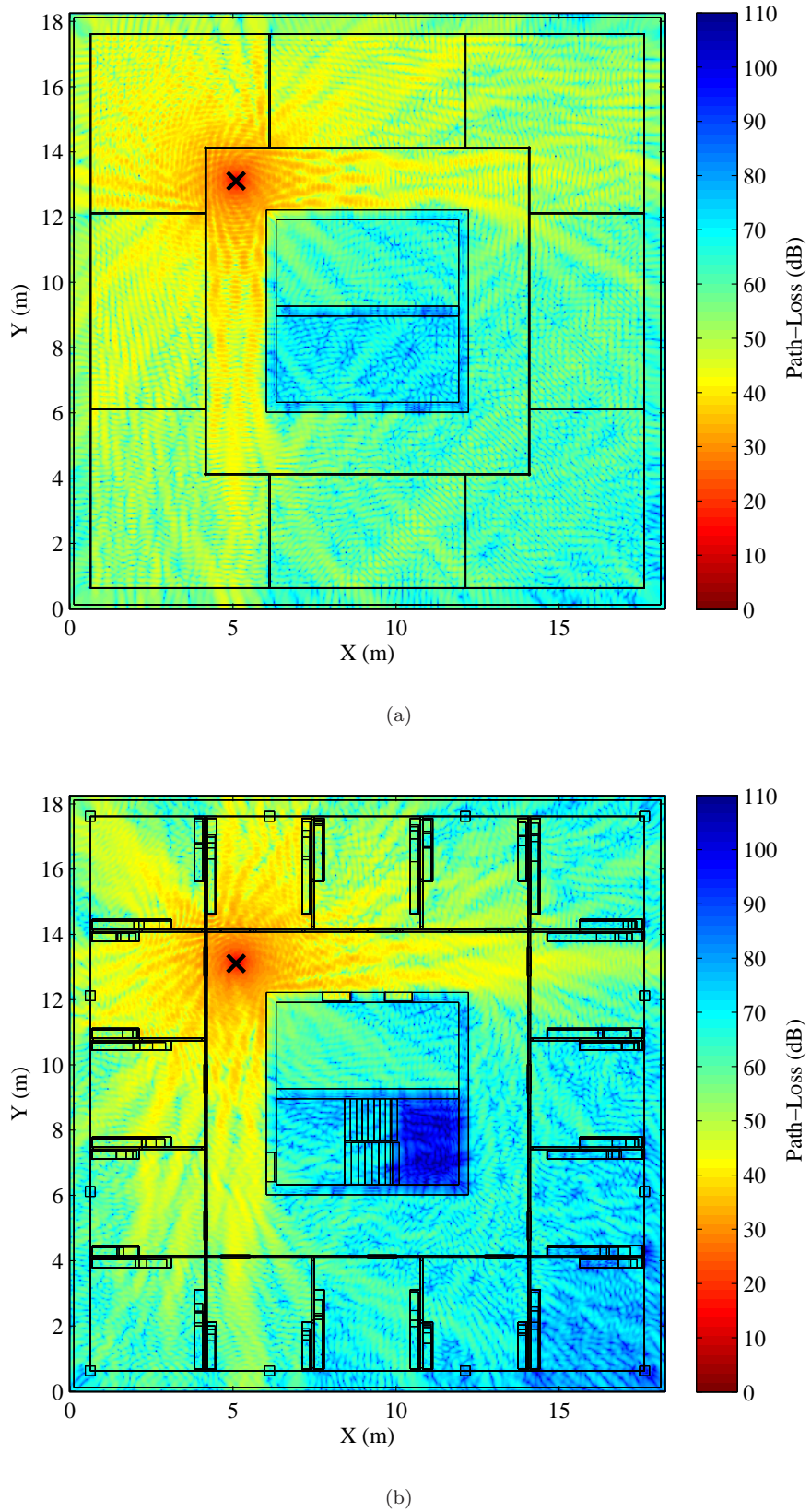


Figure 8.2: FDTD simulated path-loss on a horizontal slice through (a) basic internal geometry, and (b) detailed internal geometry.

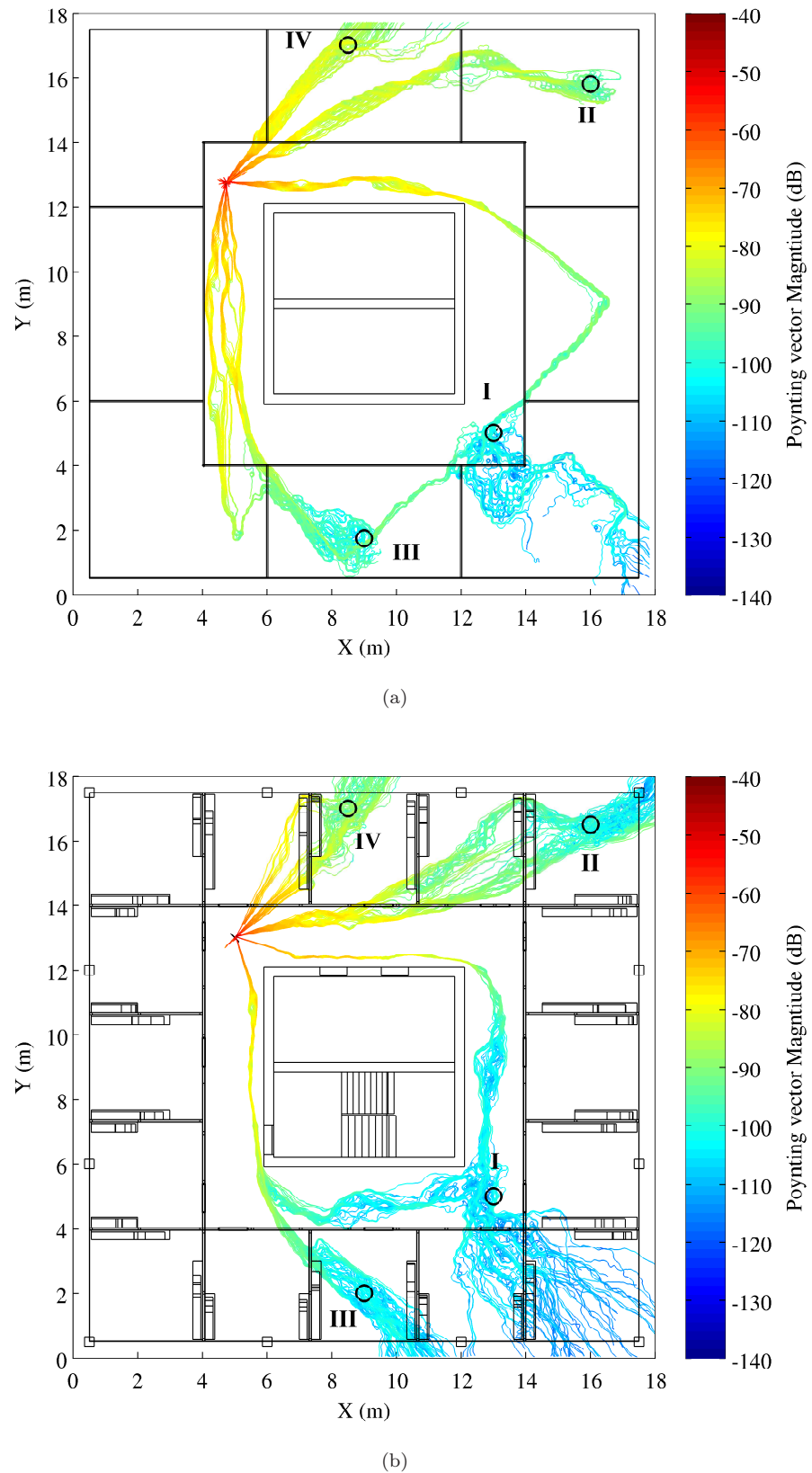


Figure 8.3: Streamlines of energy flow through the single floor environment: (a) basic geometry and (b) detailed geometry. Seed points are marked with  $\circ$ .

the transmitting antenna (located at  $\times$ ). Fig. 8.3(a) and (b) show streamlines (I–IV) of energy flow, calculated using (5.5)–(5.6) for both internal geometries. Initial points ( $\circ$ ) were selected such that streamlines I and III are shadowed by the central shaft, and II and IV are separated from the transmitter by soft partitions. The central services shaft is observed to significantly shadow waves propagating across the floor when the transmitters are diagonally positioned. Paths penetrating through the shaft are highly attenuated by the thick lossy concrete walls, and consequently, signals received in the shadowed regions are dominated by paths propagating around the shaft.

Energy reaching the shadowed regions in the basic geometry is observed to penetrate through the soft partitioned offices and reflects off the exterior glass windows. This is supported in both Fig. 8.2(a) and Fig. 8.3(a), where strong specular reflections from the glass are visible—for example, in Fig. 8.3(a), the incident and reflection angles streamlines I and II make against the glass normal are identical. The presence of strong reflected paths agrees well with previous two-dimensional FDTD simulations of empty buildings [41, 56, 62]. The problem is nominally symmetric and reflections from both sides of the building contribute equal amounts of power; the resulting  $(3\lambda)^3$  sector-averaged path-loss in the shadowed regions is approximately 65 dB.

Comparing Fig. 8.2(a) with 8.2(b) and Fig. 8.3(a) with 8.3(b) shows a distinct change in the propagation mechanisms, namely strong reflected paths from the windows and drywall are no longer visible. When shelves and books are included against the internal walls, the reflected paths are attenuated to such an extent that (in this case) diffraction around the corners of the concrete shaft is observed to dominate propagation into the shadow regions. Paths involving diffraction exist in the basic geometry, but contribute a small proportion of the total received power. The inclusion of metal window frames also perturbs specular reflection from the glass. The sector averaged path-loss recorded in shadowed regions is up to 15 dB higher than the basic geometry. As shown in appendix F, the attenuation introduced by a single layer of clutter in the environment only slightly reduces the received power. However, the accumulation of many such effects has the potential to cast significant radio shadows, and may result in other propagation mechanisms dominating. Clutter in the detailed geometry is also observed to introduce strong multi-path components when propagating through the walls, e.g. streamlines II and IV in Fig. 8.3(a) and (b). This behaviour also alters the fading distributions, and is discussed in further detail in section §8.7.

### 8.3.2 Propagation in Corridors

For both the basic and detailed internal geometries, the corridors have been modelled as largely clutter free. The sides of the corridors can be considered electrically smooth, and thus have potential to act as over-moded waveguides. This mechanism has previously been observed experimentally for relatively long ( $> 30$  m) corridors [15]. In Fig. 8.2(a) and (b) the  $3\lambda$  sector-average path-loss is observed to increase from 30 dB to 45 dB when moving 1.5–8.5 m away from the antenna, along the corridor. These values are between 3–5 dB lower than expected for free-space and can be attributed to the reflections from the walls, ceiling and floor.

For both geometries, moving into the shadow of the corner increases the path-loss by approximately 10 dB, and it continues to increase moving further away down the intersecting corridor. This observation is consistent with the analysis presented in [15]—a significant decrease in received power is expected in the intersecting corridor until the modal distribution reaches a steady-state. Results suggest for the relatively short distances considered in this building, waveguide modes are not fully established and propagation in corridors is largely governed

by the free-space path (with the inclusion of an appropriate diffraction loss at intersections). At longer distances the angle of incidence becomes increasingly glancing and true waveguide modes may be formed.

## 8.4 Propagation to Adjacent Floors

Fig. 8.4 shows the path-loss on horizontal slices (a) one floor and (b) two floors above the transmitter for the detailed geometry (similar to Fig. 8.2, the slices are positioned 1.5 m above each floor). Comparing the distribution of path-loss one and two floors above the transmitter, Fig. 8.4(a) and (b), with the same floor case, Fig. 8.2(b), shows many similarities. In particular, the radio shadow cast by the shaft remains a dominant feature of the indoor environment, and propagation into the shadowed regions remains governed by diffraction at the corners of the shaft. Similar observations can be made for the basic geometry presented in appendix G. Clutter in the environment is also observed to introduce strong local shadowing and multi-path. These results suggest that many of the mechanisms identified in the same floor case still dominate propagation to adjacent floors. However, it is noted that the attenuation introduced by each floor is not constant and varies depending on the location of the receiver.

Fig. 8.5(a) shows the path-loss on a vertical ‘slice’ through the three-floor detailed geometry; the location of the slice is indicated by - - - in Fig. 8.4(a). The radiation pattern of the short dipole antenna (located at  $\times$ ) causes greater path-loss in regions above the antenna. The lower path-loss around point ‘A’ can be attributed to reflection and scattering from the metal elevator doors. The metal rebar is observed to introduce local scattering, supporting the findings of [77], which showed greater multi-path is present when the rebar embedded in the concrete is included in the analysis. However, similar to the two-dimensional analysis presented in chapter 6, the dominant propagation path—penetration through the concrete—remains largely unchanged. Fig. 8.5(b) shows streamline visualisations of the Poynting vector for four seed points (indicated by  $\circ$ , and centred on the vertical slice) located one and two floors above the transmitter. These streamlines largely follow line-of-sight (LOS) paths (though refraction is also visible at the air-concrete and concrete-air interfaces), indicating the dominant propagation mechanism (in this region) is penetration through the floors.

As more floors separate the transceivers, alternative propagation paths involving the lift-shafts and stairwells may contribute significant amounts of power, and may explain the variations in attenuation across each floor. Results indicate these paths are not dominant for a single floor separation. However, as indicated in Fig. 8.5(c), propagation into the lift-shaft can provide a comparable level<sup>3</sup> of power two floors above the transmitter. As the walls of the shaft are thicker than the floors, these paths are only visible after two floor penetrations. If the geometry was extended to four floors, paths propagating through the shaft would be expected to dominate the received signal.

## 8.5 Comparisons with Experimental Measurements

To confirm the findings made with the FDTD method, experimental measurements were conducted at 1.8 GHz over three floors of the Engineering building. Details about the experimental setup were discussed in chapter 6. Fig. 8.6 shows contour plots of the measured path-loss, when

---

<sup>3</sup>Streamline visualisations of the Poynting vector show the *net* energy flow, and for both paths to be present they have to contribute roughly equal power.

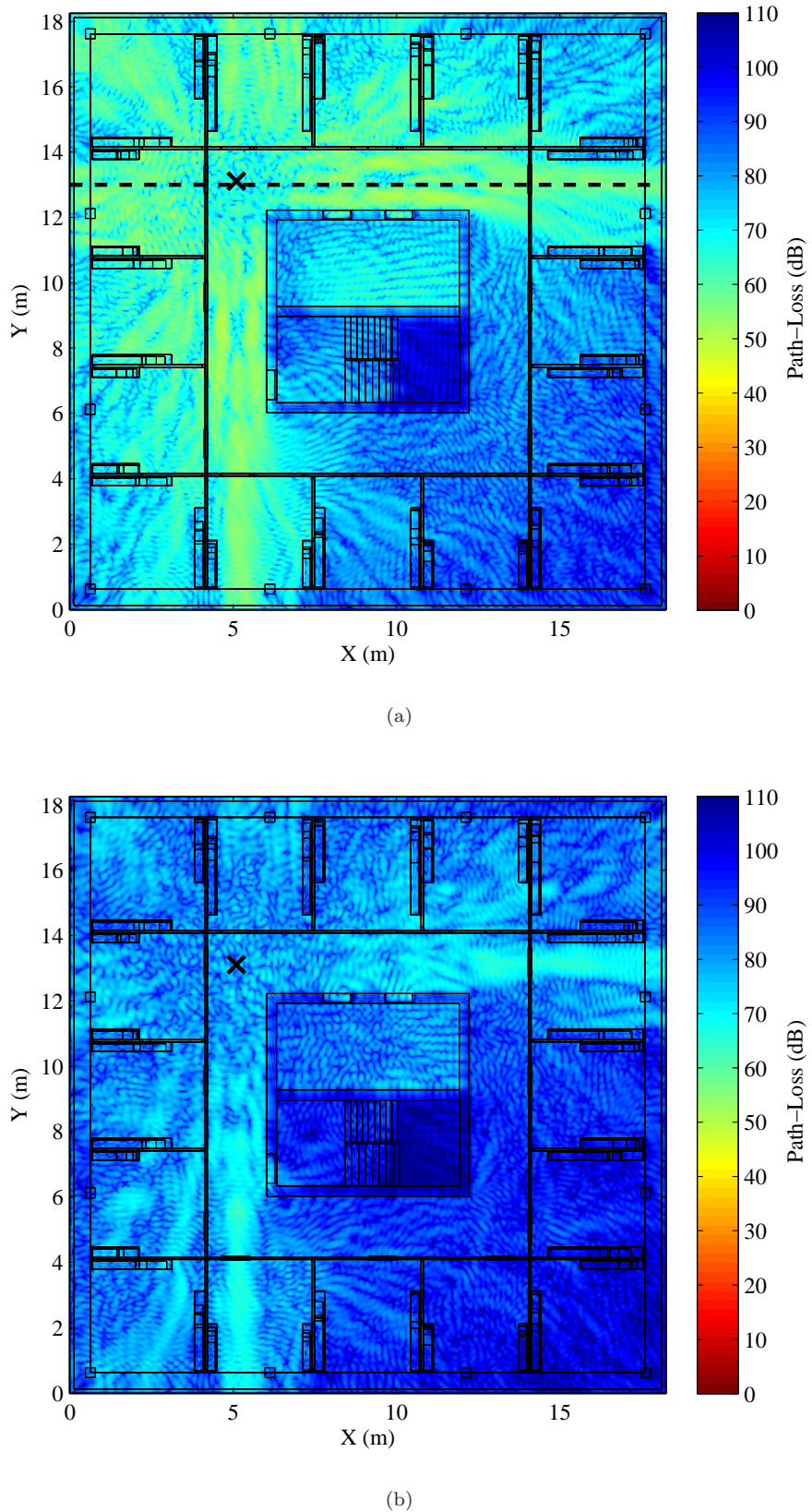


Figure 8.4: FDTD simulated path-loss (detailed geometry) for (a) one floor separating the transmitter and receiver, and (b) two floors separation.

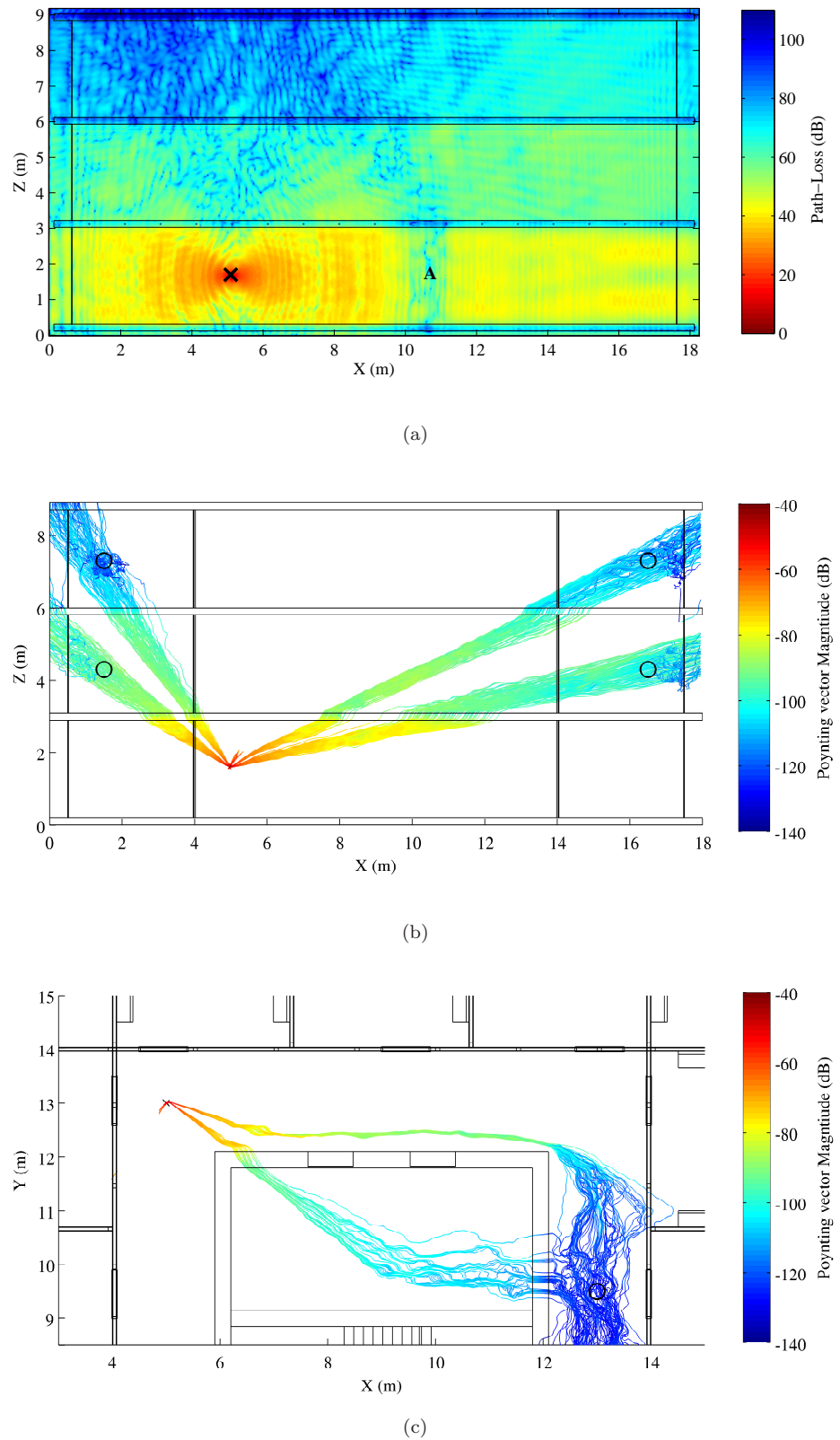


Figure 8.5: (a) Vertical slice through the three-floor detailed geometry. (b) Poynting vector streamlines on the vertical slice. (c) Propagation paths (to the third floor) via the shaft.

the transmitter is located at  $\times$  on (a) the same floor, (b) one floor above, and (c) two floors above. The contours are only indicative of the power measured at locations marked by  $\bullet$ , in reality stepwise changes in path-loss will occur when the propagating wave passes through a wall or another dielectric object.

### 8.5.1 Qualitative Comparisons

A qualitative comparison between the measured path-loss, presented in Fig. 8.6, and the simulated path-loss in Fig. 8.2 and Fig. 8.4 shows the FDTD generally provides a good prediction of the distribution of path-loss (for both internal geometries). However, the limited spatial resolution of the measured data is unable to show if diffraction around the dielectric corner, or reflection from the windows is the dominant mechanism. Three measurements were made inside the shaft; the path-loss inside the shaft is higher than points outside, confirming the dominant energy path is not penetration through the concrete walls.

It is observed that the FDTD simulations underestimate the path-loss for some regions. This underestimation cannot be accounted for in the frequency difference, and is largest in regions furthest from the transmitter on highly cluttered paths, particularly paths shadowed by the shaft or passing through multiple partitions. For example in the single-floor case, measurement points deeply shadowed by the shaft experience between 80–90 dB path-loss. When the problem is simulated with the basic geometry, a sector averaged path-loss of between 60–70 dB is observed; including the internal details increases the path-loss to 70–80 dB<sup>4</sup>. Similar observations can be made for propagation to adjacent floors. Adding internal details improves the prediction accuracy. For example, in regions separated from the transmitter by multiple soft partitions the measured path-loss varies between 70–80 dB, the basic geometry between 45–55 dB and detailed between 55–65 dB. On adjacent floors, the received power is still overestimated in the same regions, however the difference is larger<sup>5</sup>. The over-estimation of received power may limit the direct applicability of the FDTD method for modelling indoor propagation, particularly for interference prediction purposes.

### 8.5.2 Direct Comparisons

As the material properties do not change significantly over the 1.0–1.8 GHz frequency range [32], a direct comparison between the path-loss for 1.0 GHz FDTD simulations and 1.8 GHz experimental measurements only needs to account for the increased free-space loss (5.1 dB). Fig. 8.7 shows a point-wise comparison between the average path-loss recorded at the 156 experimental measurement points, and  $(3\lambda)^3$  sector averaged FDTD simulations of the path-loss made at the same locations. Adding internal details improves the prediction accuracy—as shown in Fig. 8.7 the RMS error between the measurements and simulation is 14.4 dB for the basic geometry; this is reduced to 10.5 dB when the details are included. This result is significant, as it shows to correctly predict the path-loss, a significant level of detail present in the indoor propagation environment must be considered when applying full-wave electromagnetic methods. The sensitivity of the FDTD simulation results to the level of detail included in the environment is discussed further in chapter 10.

---

<sup>4</sup>It should be noted that the additional free-space loss (5.1 dB) between 1.0 and 1.8 GHz will not account for the additional diffraction loss.

<sup>5</sup>This observation suggests a higher value for the concrete conductivity is required.

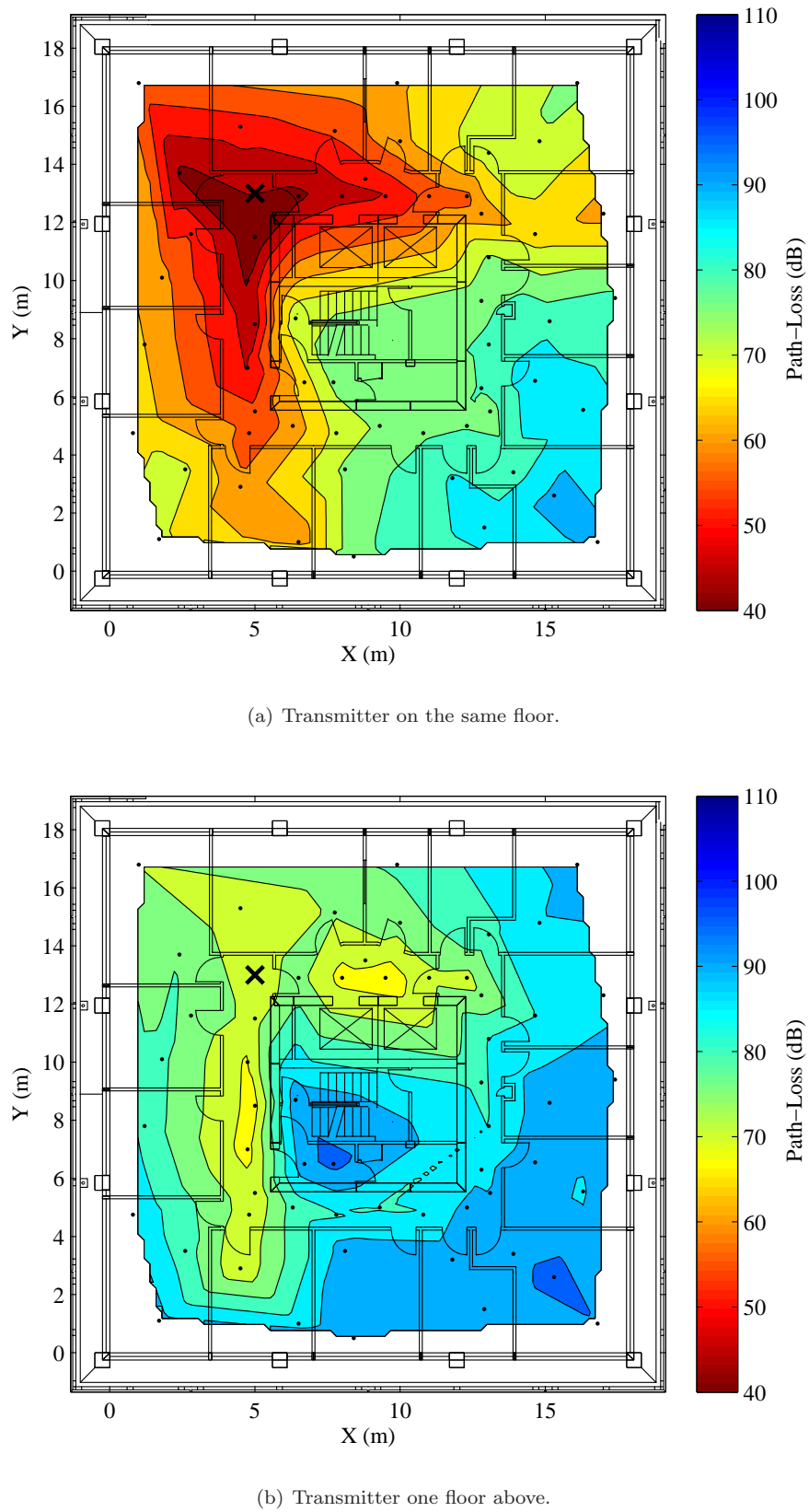
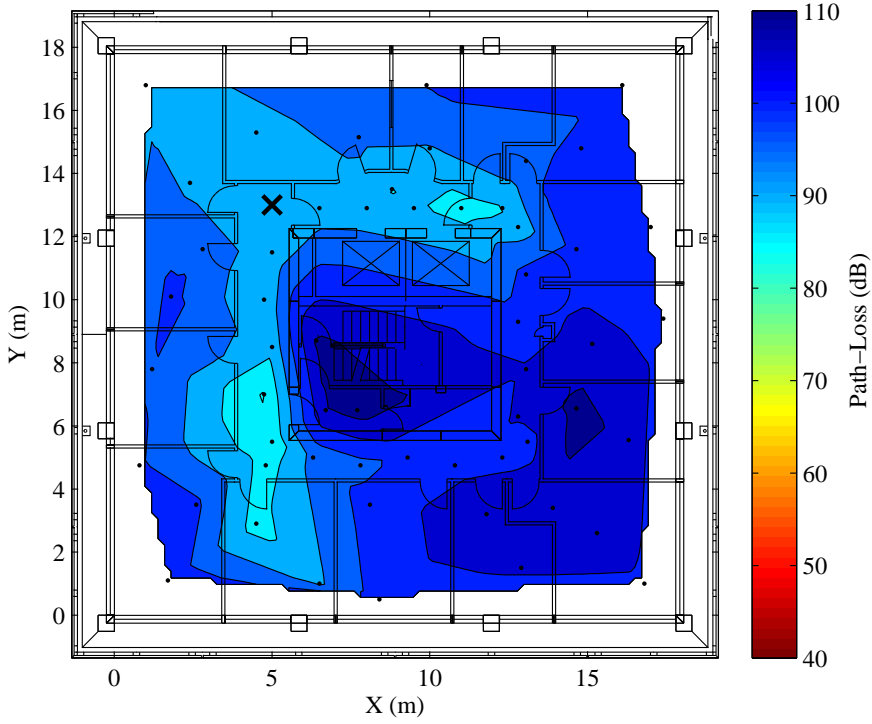


Figure 8.6: Experimental measurements of the sector-averaged path-loss in the Engineering building at 1.8 GHz. The location of the transmitter is marked with  $\times$ .



(c) Transmitter two floors above.

Figure 8.6: Experimental measurements of the sector-averaged path-loss in the Engineering building at 1.8 GHz. The location of the transmitter is marked with  $\times$ .

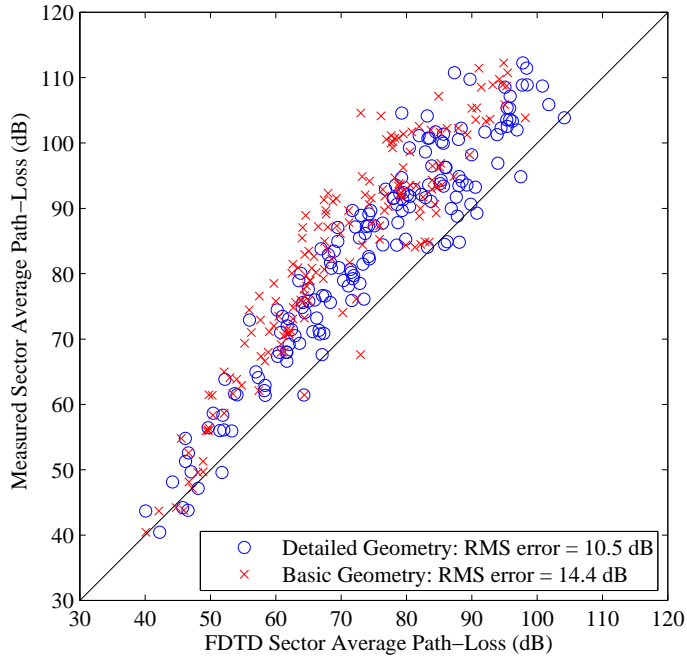


Figure 8.7: Scatter plot comparing sector-averaged measurements of the path-loss with values obtained from FDTD simulations in the same locations.

## 8.6 Path-Loss Prediction Models

### 8.6.1 Path-Loss versus Distance

Fig. 8.8 shows scatter plots of the  $(3\lambda)^3$  sector-averaged path-loss (in dB) versus the transmitter-receiver separation distance for (a) the basic geometry, and (b) the detailed geometry. The path-loss for sectors on all three floors have been included and points located inside the concrete services shaft have been ignored. The attenuation introduced by the floors separates the path-loss into three subsets, and it is noted in some circumstances, the path-loss on deeply shadowed or cluttered paths (on the same floor as the transmitter) can exceed the path-loss recorded on immediately adjacent floors. The clutter in the detailed geometry also increases the range of path-loss values recorded across each floor. For one and two floor separations, it is observed that the sector-averaged path-loss initially decreases with distance. These sectors are all located directly above the transmitter, and this behaviour can be explained by considering the radiation pattern of the dipole antenna, as noted in Fig. 8.5(a).

Higher path-losses are observed in the detailed geometry, particularly on longer paths. Based on the results presented in sections §8.3 and §8.4, the change in propagation mechanism from reflection at the glass windows to diffraction at the concrete corner is responsible for the increased path-loss; and as demonstrated in appendix F, the attenuation introduced by clutter in the environment can also increase the path-loss. In Fig. 8.8 there are several sectors (in both geometries) with distance dependency exponents,  $n < 2.0$ . These sectors occur in the corridors and are caused by strong reflections from the walls, ceiling and floor; similar observations have been made in [41]. For both geometries and experimental measurements, the sector-averaged path-loss across a floor can vary by over 30 dB. Consequently, developing computationally-simple mechanistic models to reliably predict this behaviour—especially on longer paths—is a challenge.

### 8.6.2 Distance-Dependency Models

As discussed in chapter 3, empirical models in the form  $d^n$  are typically used to relate the average path-loss with the transmitter-receiver separation distance. This section examines fitting the sector-averaged path-loss calculated from the FDTD data to the widely used Seidel model [7], given by

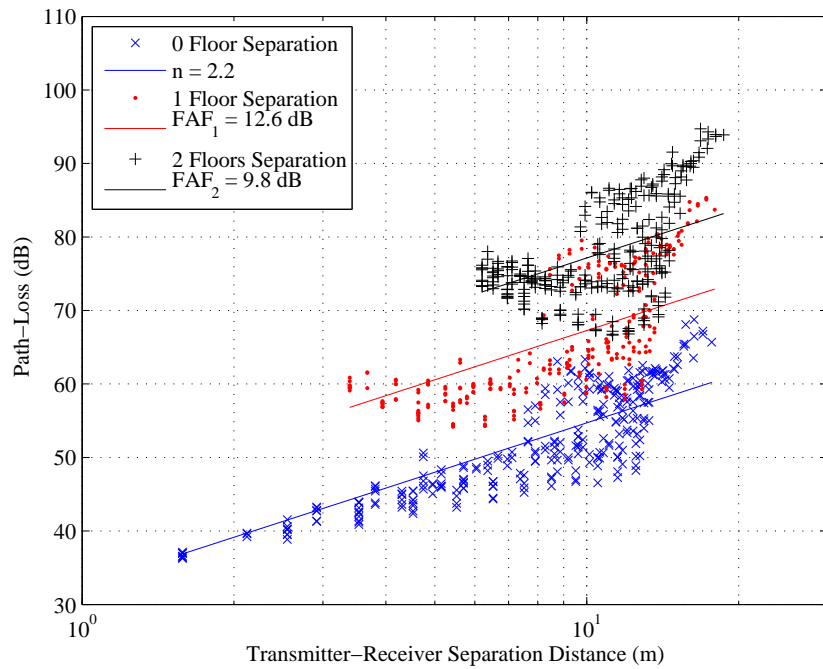
$$PL(d) = PL(d_0) + 10 \times n \times \log_{10} \left( \frac{d}{d_0} \right) + \sum_{f=1}^F \text{FAF}_f \quad (\text{dB}), \quad (8.1)$$

where  $PL(d_0)$  is the path-loss at reference distance  $d_0 = 1.0$  m,  $n$  is the distance dependency exponent for data collected on the same floor as the transmitter,  $d$  is the transmitter-receiver separation distance,  $\text{FAF}_f$  is the floor attenuation encountered propagating through the  $f^{\text{th}}$  floor, and  $F$  is the number of floor separations considered. The parameters  $n$  and  $\text{FAF}_f$  are found by fitting (8.1) to the data via linear regression, given  $PL(d_0 = 1\text{m}) = 32.4$  dB<sup>6</sup>.

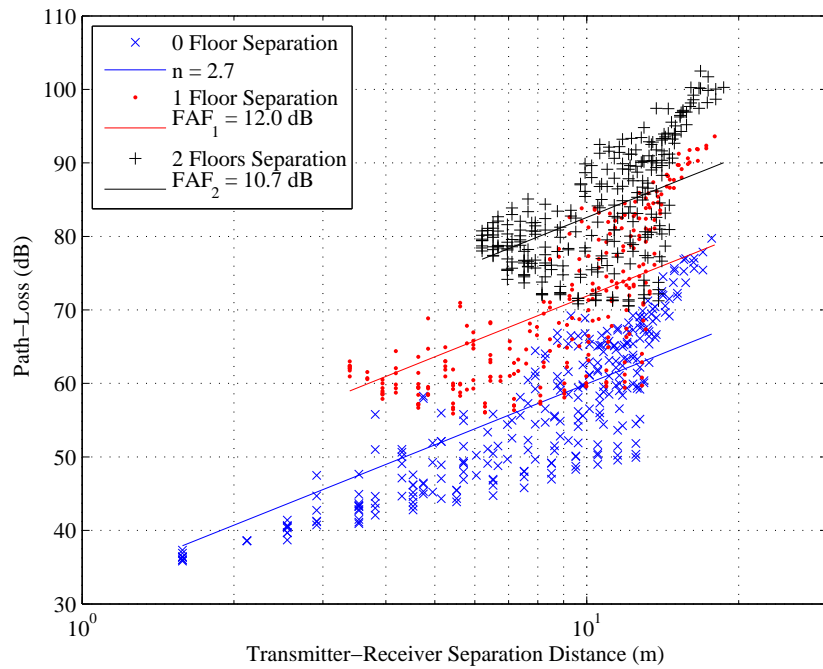
Table 8.1 shows the least-squares best-fit distance dependency exponents, floor attenuation factors and RMS error between (8.1) and the FDTD and experimental data. The data collected across the floor has been divided into two regions, *lit* and *shadowed*, based on the position of the receiver relative to the transmitter and the concrete services shaft. Scatter plots of the

---

<sup>6</sup>As the electric field values have been converted to path-loss, this value is the free-space path-loss at  $d_0 = 1.0$ , as calculated by the Friis equation (5.3) assuming isotropic antennas and no feeder cable losses. For the 1.8 GHz experimental measurements  $PL(d_0 = 1\text{m}) = 37.6$  dB.



(a)



(b)

Figure 8.8: Scatter plots of  $(3\lambda)^3$  path-loss versus distance for (a) basic and (b) detailed internal geometries. The solid lines represent a Seidel model [84] fitted to the simulated data.

Table 8.1: Parameters for the Seidel Model [84].

		Basic Geometry	Detailed Geometry	Experimental Measurements
All Regions	$n$	2.2	2.7	3.6
	FAF <sub>1</sub> (dB)	12.6	12.0	11.8
	FAF <sub>2</sub> (dB)	9.8	10.7	11.0
	RMS error (dB)	5.3	6.5	7.4
Lit Regions	$n_{lit}$	1.9	2.3	2.9
	FAF <sub>1</sub> (dB)	11.8	11.9	14.6
	FAF <sub>2</sub> (dB)	11.0	12.1	14.2
	RMS error (dB)	3.0	4.4	6.1
Shadowed Regions	$n_{shadowed}$	2.6	3.2	4.2
	FAF <sub>1</sub> (dB)	15.3	14.1	9.0
	FAF <sub>2</sub> (dB)	8.3	8.9	6.6
	RMS error (dB)	3.6	4.1	4.8

path-loss versus distance, where the regions have been explicitly separated, are provided in appendix H.

When all regions are considered, the same floor distance dependency exponent increases for the detailed model due to increased attenuation through the clutter. The increase in RMS error for the detailed geometry also indicates scattering off the clutter introduces greater variability around (8.1). It is also observed that FAF<sub>2</sub> < FAF<sub>1</sub> for both geometries and the experimental measurements. If the only propagation path was through the floors, and if the floors were identical, FAF<sub>1</sub> = FAF<sub>2</sub>, however, the observed decrease is between 1–3 dB. In other buildings, a greater decrease in the FAF is observed (e.g. FAF<sub>1</sub> = 12.9 dB and FAF<sub>2</sub> = 5.8 dB [7]), and this behaviour is difficult to explain experimentally [7]. As noted in chapters 6 and 7, other propagation mechanisms can reduce the apparent FAF. However, the geometry considered in this chapter only supports internal propagation paths, i.e. floor edge diffraction and external reflection paths are not possible. For the geometry examined in this chapter, combining the lit and shadowed regions essentially averages the effects of both; a better understanding may be gained by considering the two regions separately.

As shown in Fig. 8.5(b), penetration through the floors is the dominant propagation mechanism in the lit regions (for both internal geometries), and consequently FAF<sub>1</sub> ≈ FAF<sub>2</sub>. In the basic geometry  $n_{lit} = 1.9$ , which is close to free-space ( $n = 2.0$ ). The streamline visualisations of the Poynting vector presented in section §8.3 show the dominant propagation path in lit regions is largely LOS. The soft partitions do not perturb the propagating waves or introduce appreciable attenuation. However, in the detailed geometry  $n_{lit} = 2.3$ , which tends to indicate clutter in the environment introduces additional attenuation. This is also supported by examining streamlines II and IV in Fig. 8.3, which show the energy tends to propagate on non-LOS paths in the lit regions.

The streamlines presented in Fig. 8.5(c) indicate other (lower-loss) propagation paths may dominate in the shadowed region. It is thought the presence of such paths is (partly) responsible for the decrease in FAF between one and two floor separations. It is noted that  $n_{shadowed} > n_{lit}$  for both geometries and experimental measurements. However, as energy no longer travels on LOS paths (e.g. diffraction at the corners of the shaft), models based on a simple distance-dependency relationship may no longer be appropriate.

## 8.7 Fading Distributions

As discussed in chapter 2, to reliably predict system performance (the outage probability), knowledge of both the sector mean and the variation in received signal about the sector mean are required. The research presented in this chapter so far has focused on gaining reliable estimates for the sector mean; this section focuses on characterising multi-path fading. The Rayleigh and Rician probability distributions (introduced in chapter 2) are frequently used to stochastically characterise multi-path fading in indoor environments [6, 21] [14, pp. 201–202], and are repeated here for convenience.

The Rician distribution assumes a strong (e.g. LOS) component dominates the received signal<sup>7</sup>. The PDF of the Rician distribution is

$$f(x) = \frac{x}{\sigma^2} \exp\left(\frac{-x^2 + s^2}{2\sigma^2}\right) I_0\left(\frac{xs}{\sigma^2}\right),$$

where  $s^2$  is the power of the dominant component,  $2\sigma^2$  is the mean scattered power, and  $I_0$  is the zero-th order Bessel function of the first kind. The Rician  $K$ -factor is defined as the ratio of specular power to scattered power,  $K = \frac{s^2}{2\sigma^2}$ , and can be determined using [21]

$$\frac{\mathbb{E}[x]}{\mathbb{E}[x^2]} = \sqrt{\frac{\pi}{4(K+1)}} \exp\left(-\frac{K}{2}\right) \left[ (1+K)I_0\left(\frac{K}{2}\right) + KI_1\left(\frac{K}{2}\right) \right], \quad (8.2)$$

where  $\mathbb{E}[x^2]$  is the average square amplitude,  $\mathbb{E}[x]$  is the average amplitude, and  $I_m$  is the  $m$ -th order Bessel function of the first kind.

Fig. 8.9 shows cumulative distribution functions (CDF) of received signal envelope (in dB) for both internal geometries and experimental measurements. Also shown in Fig. 8.9 is a floor plan; the data was collected in the shaded sectors—located within an office, approximately 5 m from the transmitter. Rician distributions are fitted to these data sets using (8.2). In the basic geometry  $K$  is 2.6—this indicates a strong dominant component exists—whereas, in the detailed geometry and measurements  $K = 0$ , suggesting more energy is being scattered in this case. The experimental data set consists of 400 points, whereas the simulated data set has  $2.5 \times 10^5$  points. Consequently, there is a greater variability between the experimental and theoretical CDFs, particularly at lower signal powers.

The differences in Rician  $K$ -factor for the basic and detailed geometries can be explained by examining streamline visualisations of the Poynting vector. Fig. 8.10 shows streamlines for the (a) basic; and (b) detailed geometries, reaching the same sectors considered in Fig. 8.9. In the basic geometry it is observed that the energy is travelling on the LOS path with some attenuation when penetrating through the soft partitions; accordingly,  $K$  is greater than zero. The same streamline in the detailed geometry shows the LOS path is blocked by bookshelves. The increased attenuation allows additional scattered paths (of similar magnitude to the attenuated-LOS path) to exist and accordingly, the PDF of the signal envelop follows a Rayleigh distribution. Similar phenomena are observed in other locations shadowed by clutter.

Fig. 8.11 shows CDFs of Rician  $K$ -factors recorded over  $(3\lambda)^3$  sectors, on the same and an immediately adjacent floor, for both internal geometries. It is observed that when the details

---

<sup>7</sup>In the case where no single component dominates, the PDF of the signal envelope follows a Rayleigh distribution, given by

$$f(x) = \frac{x}{\sigma^2} \exp\left(\frac{-x^2}{2\sigma^2}\right),$$

where  $\sigma^2$  is the mean power. The Rayleigh distribution is thus a special case of the Rician distribution ( $K = 0$ ).

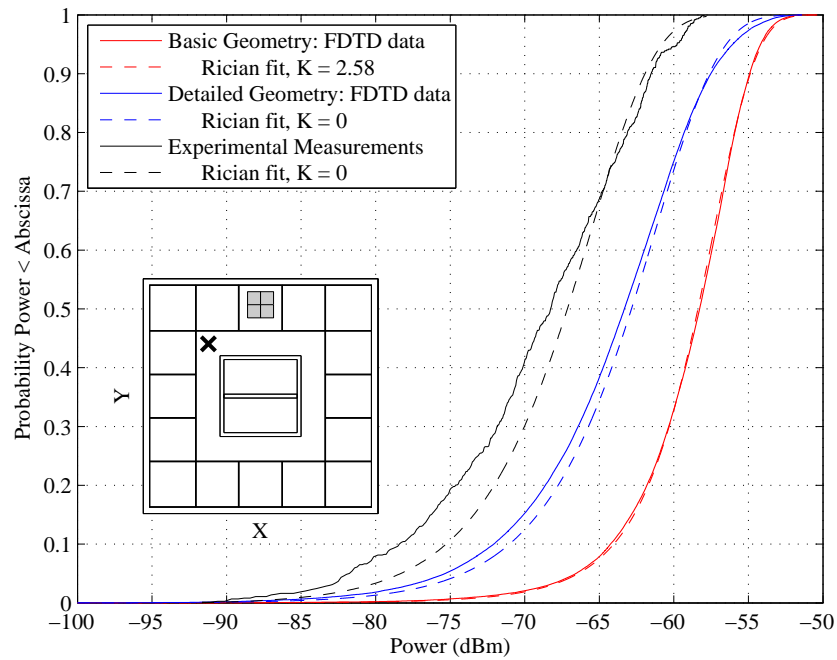


Figure 8.9: Cumulative distribution functions of the  $E_z$  field envelope for both internal geometries and experimental measurements compared with exact Rician distributions. The  $E_z$  field data was recorded in the shaded regions on the same floor as the transmitter (located at  $\times$ ).

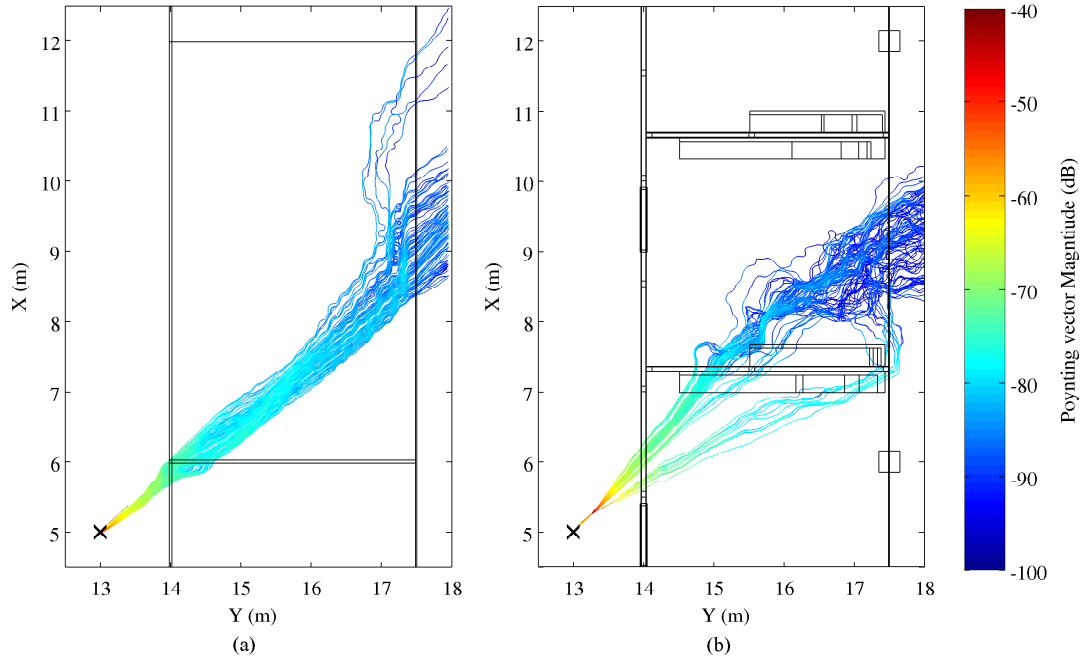


Figure 8.10: Streamline visualisations of the Poynting vector for (a) basic and (b) detailed internal geometries.

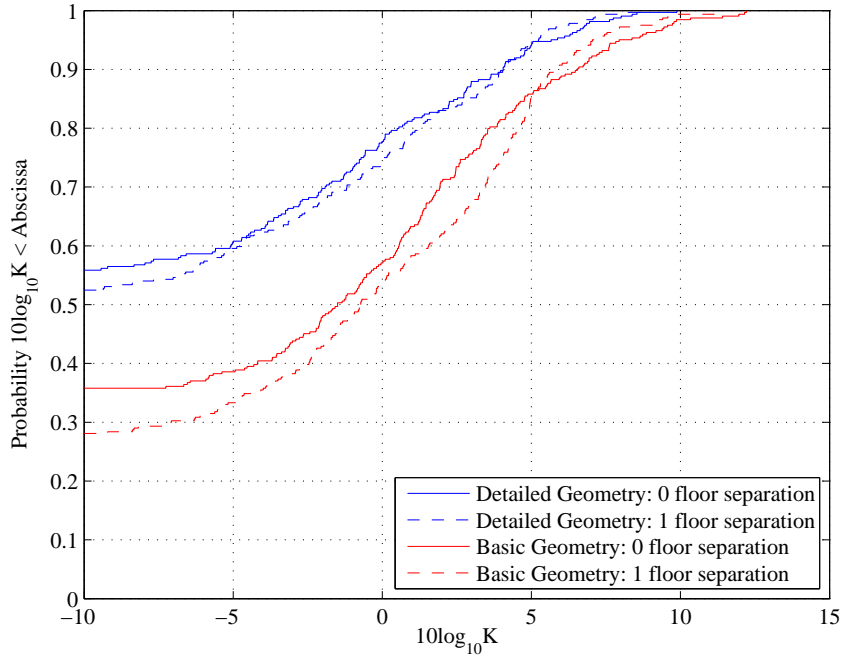


Figure 8.11: CDFs of the Rician  $K$ -factor recorded on the same and an immediately adjacent floor for both internal geometries.

are included, a greater proportion of sectors have lower  $K$ -factors, suggesting the proportion of scattered energy is higher. In the detailed geometry, the signal envelope of approximately 56% of the occupied space on the same floor, and 52% on an adjacent floor, can be characterised by a Rayleigh distribution ( $K = 0$ ); by contrast, in the basic geometry, the percentage of sectors with  $K = 0$  are 36% on the same floor, and 29% on an adjacent floor.

## 8.8 Summary

Unlike the propagation studies presented in chapters 6 and 7, this chapter uses a three-dimensional implementation of the FDTD method to investigate inter-floor propagation between three floors of a generalised multi-storey building. The chapter focuses on characterising propagation mechanisms that cannot be fully examined using two-dimensional geometries, specifically, inter-floor propagation around large shadowing obstacles (such as a concrete central services shaft), and the impacts of including internal clutter. In the building examined, the inclusion of metallic and lossy dielectric clutter alters the dominant propagation mechanisms, causing increases in the sector-averaged path-loss and distance-dependency exponents. The details also reduce Rician  $K$ -factors across the floor. Ignoring the clutter in the environment will result in optimistic estimates of the path-loss and fading distributions, and potentially under designed systems (with respect to coverage). Chapter 9 examines the use of the FDTD method to estimate system performance in the presence of interference.

# Chapter 9

# System Performance Estimation for Indoor Wireless Systems with the FDTD Method

## 9.1 Introduction

The performance of contemporary indoor wireless systems is largely limited by interference from other systems (and devices) operating over the same frequency bands. In order to predict system performance in the presence of interference, estimates of the desired and interfering signal strengths from transceivers operating within the building are required. As noted in chapters 6–8, the FDTD method is well suited to modelling radio-wave propagation in two- and three-dimensional representations of multi-storey buildings. However, as many fixed-transmitter<sup>1</sup> locations need to be considered (requiring multiple simulation runs), the high computational costs of the FDTD method largely restricts interference analysis to two-dimensional geometries and smaller three-dimensional problems. The high computational costs also preclude the use of the FDTD method for optimising base-station deployment strategies, or the optimal placement of metal shielding to occlude interfering signals. While this chapter sits outside the main focus of this thesis—the development of mechanistic propagation models—it returns to the primary motivations by examining the application of the FDTD method to directly estimate system performance in the presence of interference. Due to computational limitations, this chapter is considered a feasibility study to help plan future investigations.

Section §9.2 identifies metrics typically used to assess system performance in the presence of interference, and discusses how these can be predicted with the FDTD method. An assessment of various base-station deployment strategies is examined in section §9.3 using two-dimensional models of multi-storey buildings. Three-dimensional deployment strategies are considered in section §9.4, however, computational limitations restrict the analysis to three floors; the simulation results are also compared against experimental measurements. Section §9.5 assesses the use of partial metal shielding to occlude possible interfering paths, thereby improving system performance. Correlated shadowing between the desired and interfering transmitters is discussed in section §9.6. Section §9.7 briefly discusses the implications of the findings, and the chapter is summarised in section §9.8.

---

<sup>1</sup>Hereafter referred to as base-stations.

## 9.2 Modelling Interference for Indoor Wireless Systems

### 9.2.1 Interference Within Buildings

As discussed in chapter 2, the increasing demand for wireless services often necessitates reuse of the frequency spectrum. Frequency reuse causes interference, which is detrimental to system performance, reducing the reliability, throughput and the number of users that can be supported [4, pp. 16–19]. Compared to outdoor cellular mobile networks, wireless systems operating indoors—such as Wireless Local Area Networks (WLANs)—are generally more susceptible to interference, as the transceivers are in usually in closer physically proximity [6]. Multi-storey buildings also encourage three-dimensional deployment strategies, with frequency channels often reused on adjacent (or nearly adjacent) floors. Furthermore, the deployment of systems operating in unlicensed frequency bands (e.g. the ISM and U-NII radio bands) tends to be *ad hoc*, and usually little or no consideration is given to reducing interference.

Estimates of the carrier-to-interference ratio (CIR) and outage probability are often used as metrics to assess the performance of wireless systems in the presence of interference [6, 22]. The CIR is largely a function of the propagation environment, whereas the outage probability—the probability that a mobile receiver fails to achieve adequate reception [24]—also depends on the specific system<sup>2</sup>. This chapter limits the outage probability analysis to Direct-Sequence Code-Division Multiple-Access (CDMA) systems, as the mechanisms by which interference arises in other systems—such as Orthogonal Frequency-Division Multiplexing (OFDM)—are considerably more complicated [90], and outside the scope of this thesis.

Although the propagation environment remains the same, the CIR also depends on whether interfering signals are originating from other base-stations (down-link), or from other users (up-link). Up-link and down-link channels are typically operated on separate frequency bands, and therefore do not usually interfere with each other. The down-link CIR is evaluated at all possible mobile-user locations, and as a result, largely depends on the base-station configuration; whereas, the up-link CIR is evaluated at the base-stations, and primarily depends on the number and location of the users. The analysis presented in this chapter only focuses on the down-link channel<sup>3</sup> (and hereafter references to CIR or outage probability are assumed to be for the down-link case).

### 9.2.2 FDTD Propagation Analysis

Similar to the propagation studies examined in chapters 6 and 8, the building models are based on the Engineering Tower at The University of Auckland (photographs and a more thorough description of the building can be found in section §6.2). Table 9.1 summarises the FDTD simulations parameters for the two- and three-dimensional geometries. The two-dimensional geometry is based on a vertical ‘slice’ through the building and consists of metal-reinforced concrete floors, glass exterior windows and hanging panels (as described in section §6.3). The central services shaft has also been examined, however, all propagation paths are assumed to be contained within the building perimeter (i.e. reflection/scattering paths from nearby buildings have been ignored).  $\text{TM}_z$  polarisation is assumed, and a single  $E_z$  component is used to excite the lattice, thus waves propagate cylindrically away from the source.

<sup>2</sup>The CIR can also depend on the system, e.g. limited levels of interference may be introduced if adjacent channels overlap.

<sup>3</sup>It should be noted that mobile-users transmitting on the up-link channel are usually power-controlled to limit interference. An investigation of various power-control algorithms is presented in [91].

Table 9.1: FDTD Simulation Parameters.

	<b>2D</b>	<b>3D</b>
Frequency ( $f$ )	1.8 GHz	1.0 GHz
Lattice size ( $\Delta$ )	5 mm	10 mm
Time Step ( $\Delta t$ )	9.15 ps	18.3 ps
Number of Floors	8	3
Problem Size	$27 \times 25 \text{ m}^2$	$18 \times 18 \times 9 \text{ m}^3$
Memory	620 MB	180 GB
Wall-Time <sup>a</sup>	2 hours	48 hours
Processors	22 cores	64 cores

<sup>a</sup>The wall-time is the actual time taken by a computer/cluster to complete the simulation; an estimate of the CPU-time is wall-time  $\times$  processors.

Due to high computation requirements, the three-dimensional geometry only models three stories of Engineering Tower. The central services shaft, glass windows and gib-board internal partitions have been included (similar to the *basic* geometry examined in chapter 8). Although the results presented in chapter 8 demonstrate that dielectric and metallic clutter (such as bookshelves and other office furniture) can significant alter the fields, these have been ignored here for simplicity.

### 9.2.3 Carrier-to-Interference Ratio

Users operating in the building are assumed to connect to the base-station with the strongest received signal, and therefore other base-stations transmitting over the same frequency range appear as interference. The interfering signals from the other base-stations can be treated as uncorrelated, and are added together on a power basis [66]. The power is spatially averaged over  $3\lambda \times 3\lambda$  sectors to remove multi-path fading [17], and the CIR is computed for each sector by dividing the sector-averaged power from the strongest base-station by the sum of the (sector-averaged) power produced by base-stations on the other seven floors, as described by

$$\text{CIR}_n^{(x)} = \frac{\max \left\{ P_n^{(x)} \in x \right\}}{\sum_x P_n^{(x)} - \max \left\{ P_n^{(x)} \in x \right\}}, \quad (9.1)$$

where  $n$  identifies the sector and  $x$  represents the set of base-station locations.

### 9.2.4 Outage Probability

CDMA is a spread-spectrum technique where multiple users are separated in signal-space with orthogonal spreading codes [4, pp. 457–459]. Therefore, the desired signal for one user will appear as ‘noise-like’ wide-band interference to every other user. CDMA systems are resilient to narrow-band interference, but the cumulative effects of this wide-band interference from other users will degrade system performance. Down-link channels for CDMA systems are affected by two sources of interference. *Intra-cellular* interference originates from transmissions to other users connected to the same base-station, whereas *inter-cellular* interference is caused by transmissions to users connected to co-channel base-stations. Both inter- and intra-cellular

interference are affected by the processing gain ( $N$ , assumed to be 511), voice activity factor ( $\alpha$ , assumed to be 0.5), and the number of active users ( $K$ , assumed to be 30/floor); however only inter-cellular interference is affected by the locations of the base-stations and users [92]. Specifically, the instantaneous signal-to-interference ratio (SIR) is given by [92]

$$\text{SIR} = \frac{1}{\sqrt{\frac{\alpha}{3N}(K - 1 + \frac{KP_{\text{int}}}{P_{\text{des}}})}}, \quad (9.2)$$

where  $P_{\text{int}}$  and  $P_{\text{des}}$  are the interfering and desired signal powers respectively. The mean values of  $P_{\text{int}}$  and  $P_{\text{des}}$  are predicted from FDTD simulations of the indoor environment. Superimposed on the sector-mean is multi-path fading, modelled as an exponentially distributed random variable<sup>4</sup>. As indoor environments are often cluttered, the incident wave is locally scattered around the receiver, and an exponential distribution to characterise the multi-path fading is appropriate [93, pp. 13–19]. Furthermore, FDTD simulations of propagation in generalised three-dimensional geometries (presented in chapter 8) also indicate the fading envelope can be adequately characterised by an exponential distribution in most cases.

For a large number of active users and high processing gain, the CDMA bit-error-rate (BER) can be approximated by a Gaussian function of the composite intra- and inter-cellular SIR [92]. An outage is assumed to occur if the instantaneous BER is above  $10^{-3}$ , i.e. if the instantaneous SIR drops below the receiver protection margin  $r_p$ , calculated by solving (9.2) for the  $\frac{KP_{\text{int}}}{P_{\text{des}}}$  term<sup>5</sup> [22]. The outage probability is found by determining the probability that  $P_{\text{des}}$  is less than  $r_p P_{\text{int}}$ . For an exponentially distributed desired signal and  $n$  exponential interfering signals the outage probability is given by [24]

$$\begin{aligned} P_{\text{out}}^n &= 1 - P_{\text{ser}}^n \\ &= 1 - \int_0^\infty P(I_1) \int_0^\infty P(I_2) \cdots \int_0^\infty P(I_n) \times \\ &\quad \int_{\sum_{i=1}^n I_i r_p}^\infty p(w) dw dI_n \cdots dI_2 dI_1, \end{aligned} \quad (9.3)$$

where

$$p(w) = \frac{1}{A} \exp\left(-\frac{w}{A}\right), \quad (9.4)$$

and

$$p(I_i) = \frac{1}{B_i} \exp\left(-\frac{I_i}{B_i}\right) \quad (9.5)$$

are the probability density functions for the exponentially distributed desired and  $i^{\text{th}}$  interfering signal powers;  $A$  is the mean desired signal and  $B_i$  the mean of the  $i^{\text{th}}$  interferer. Substituting (9.4) and (9.5) in (9.3) gives

$$P_{\text{out}}^n = 1 - \prod_{i=1}^n \frac{\Lambda_i}{\Lambda_i + r_p}, \quad (9.6)$$

where  $\Lambda_i$  is the mean desired-signal/interfering-signal ratio,  $\Lambda_i = \frac{A}{B_i}$ . The expression for CDMA outage probability depends largely on the CIR, and higher outage is experienced in locations where desired and interfering signals have comparable magnitude.

<sup>4</sup>When considered in terms of power, the Rayleigh distributed multi-path fading envelope can be modelled as an exponentially distributed random variable.

<sup>5</sup>For a BER threshold of  $10^{-3}$ ,  $r_p = -19.3$  dB.

## 9.3 Deployment Strategies (2D)

The two-dimensional vertical ‘slice’ is shown in Fig. 9.1(a), with the locations of the base-stations marked by  $\times$ . Two base-station locations per floor have been considered, and these are positioned 1.0 m above the floor, and 1.5 m from the windows on either side of the building. The base-station transmitting antennas are assumed to be omni-directional—operating at 1.8 GHz with identical transmit powers—and are modelled by exciting a single  $E_z$  field component in a two-dimensional  $TM_z$  lattice. For an eight storey building, assuming only one base-station operates per floor, there are 256 possible deployment strategies. However, by symmetry there are only 128 unique strategies, and each has been examined. It is assumed frequencies are reused on each floor, though in practise it may be possible to increase the reuse distance.

### 9.3.1 Isolated Building

Fig. 9.1 shows density plots of the CIR for three different base-station deployment strategies. Regions of high CIR are indicated in red; whereas blue represents regions of low CIR. When the base-station antennas are vertically aligned, Fig. 9.1(a) shows that the CIR remains relatively constant across the floors, with an average value of 14 dB. The CIR is higher around the base-stations, and lower in regions within the concrete floors, or outside the building perimeter. By vertically aligning base-stations, the desired and interfering signals travel similar distances to the user. However, interfering signals from adjacent floors experience approximately 15 dB attenuation passing through the reinforced concrete. The high inter-floor isolation ensures high CIR; and low outage probabilities across the floor are also observed. The increasingly glancing angle of incidence on the concrete floor increases the CIR by approximately 3–4 dB as the user moves away from the base-station. Results also indicate that most of the interference comes from base-stations operating on immediately adjacent floors. Base-stations more than two storeys away contribute, at most, 3.0% of the total interfering power.

Fig. 9.1(b) shows vertically staggering the base-stations has a major impact on the CIR, producing greater extremes in the values observed across a floor. When the user is closer than 3.5 m to the base-station, the CIR is larger than the vertically aligned case. However, as the user moves across the floor, the CIR is observed to decrease significantly, reaching values as low as  $-1.5$  dB. Both these effects are caused by the relative distance between the user and the desired and interfering base-stations. In regions where the CIR is weak, signals from adjacent floors are substantially stronger due to increased proximity, and consequently are comparable in magnitude (despite the 15 dB floor attenuation) to signals propagating across the floor. The situation is reversed for regions where the CIR is strong. Plots of the CIR cumulative distribution function (CDF)—for vertically aligned and staggered base-station configurations—are shown in Fig. 9.3, where only sectors within the building perimeter have been considered. The CDF can be used to compare and quantify the difference between various base-station configurations. It is observed that an increased proportion of the building has low ( $< 5$  dB) CIR when the base-station configuration is changed from aligned to staggered. When the base-stations are vertically aligned, 3.0% of sectors have CIR less than 5 dB, while staggering base-stations increases this to 22.2%.

Fig. 9.2 shows the outage probability within the building when the base-stations are vertically staggered. Extremely localised regions of high outage are observed. The outage probability is lowest around the transmitters (approximately  $10^{-6}$ – $10^{-5}$ ), and increases as the user moves further across a floor. When the mobile user is approximately 7–8 m away from the base-

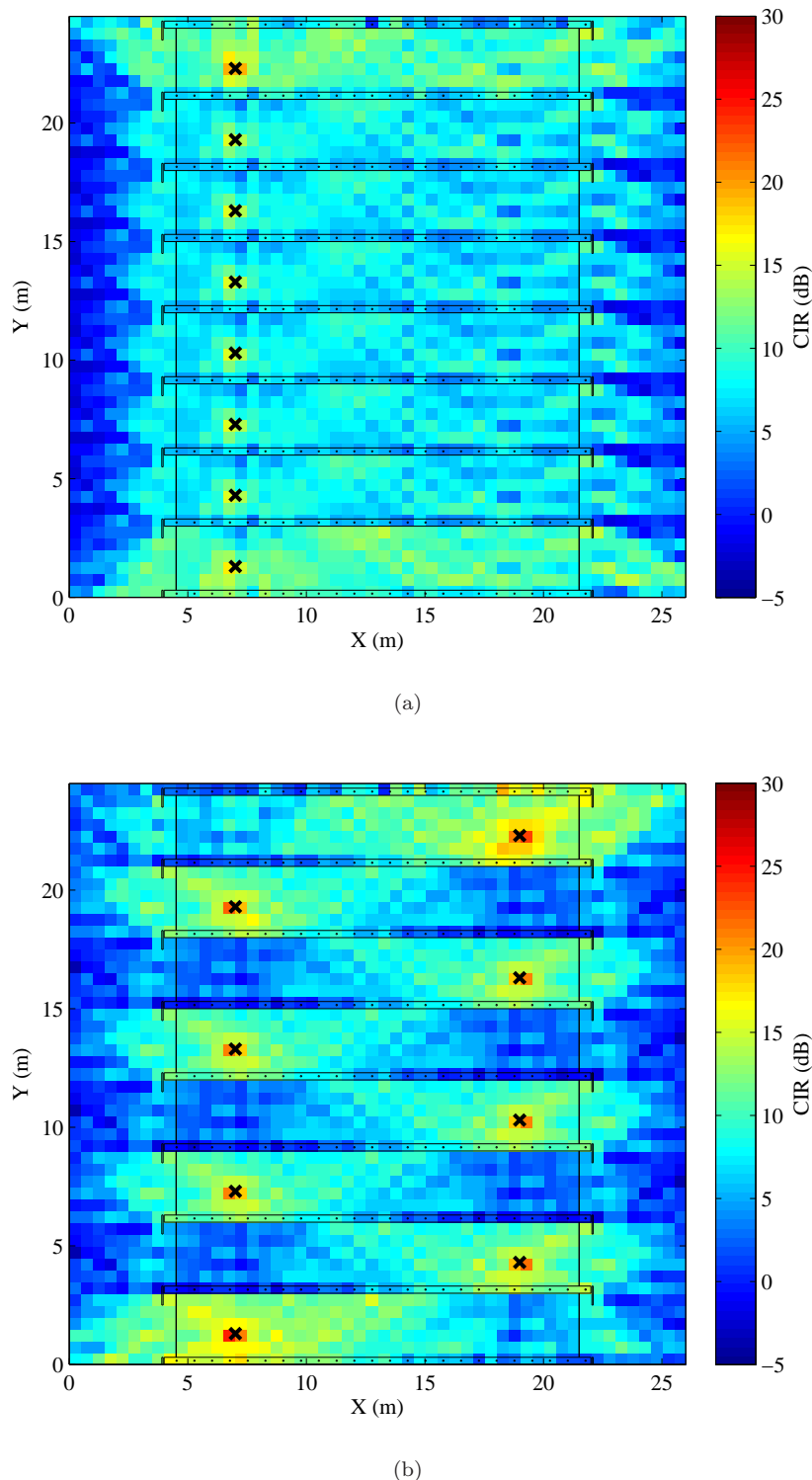
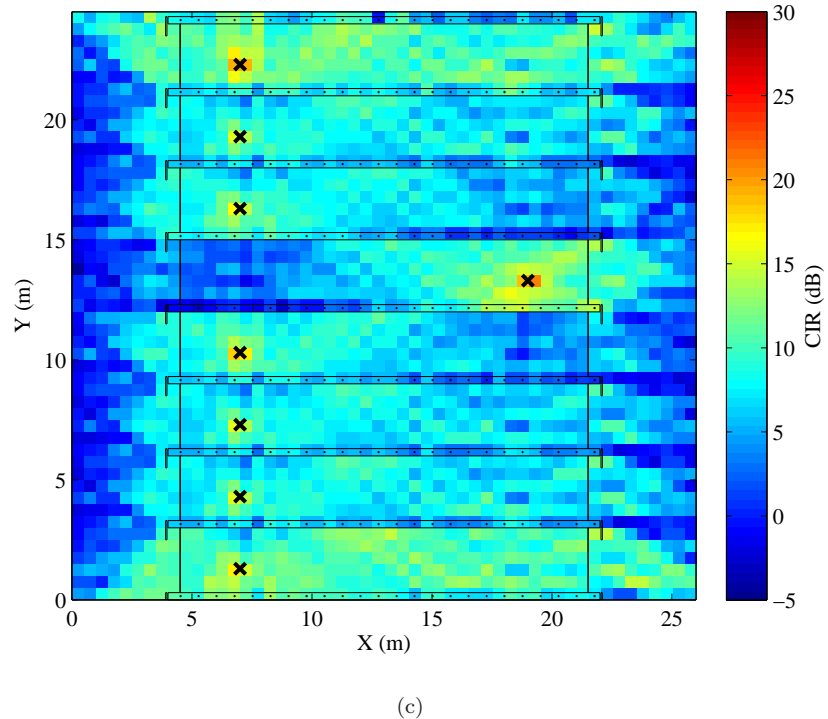


Figure 9.1: Down-link CIR density plots: (a) vertically aligned, (b) vertically staggered base-station antennas, and (c) a single antenna out of alignment. base-station locations are marked with  $\times$ .



(c)

Figure 9.1: Down-link CIR density plots: (a) vertically aligned, (b) vertically staggered base-station antennas, and (c) a single antenna out of alignment. base-station locations are marked with  $\times$ .

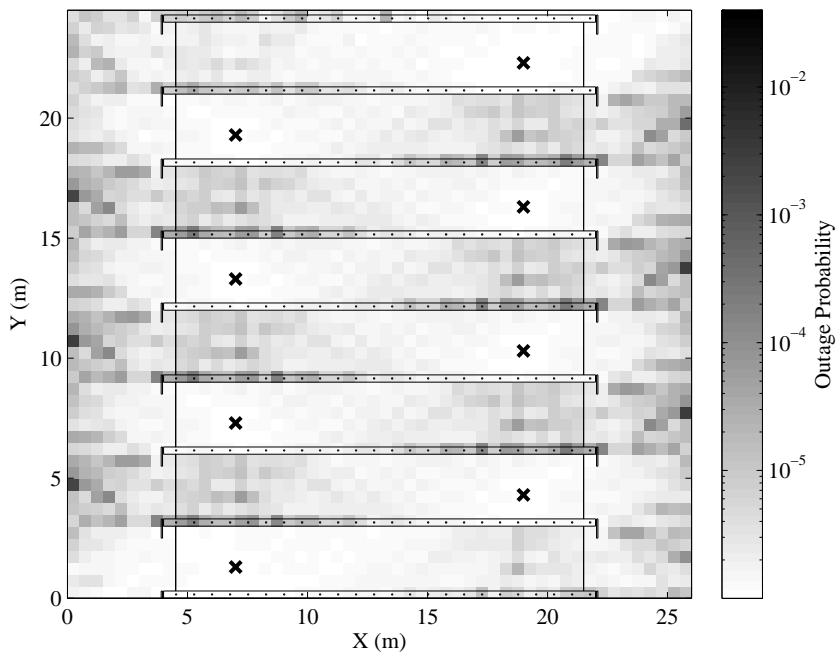


Figure 9.2: Down-link outage probability density plot for vertically staggered base-stations. Base-stations locations are marked with  $\times$ .

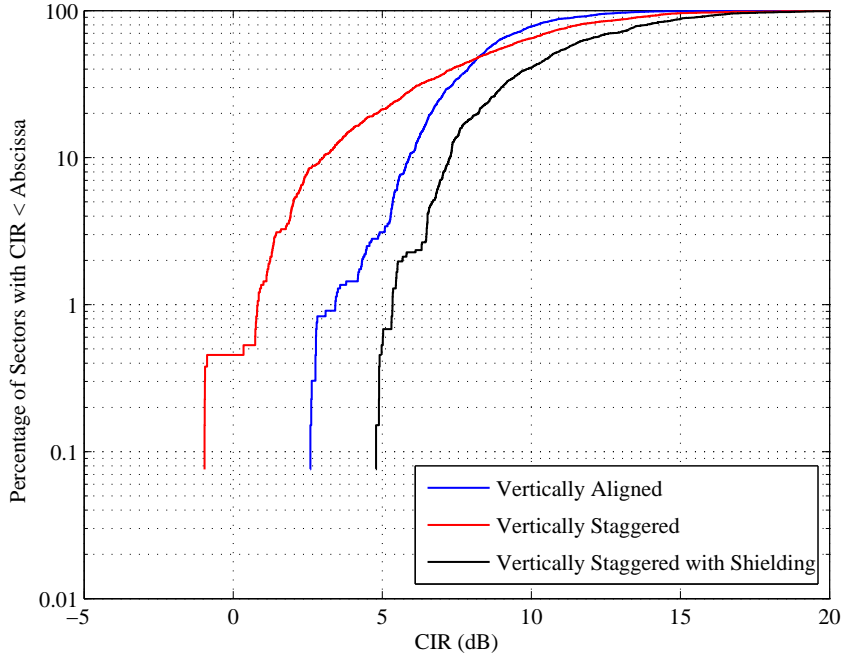


Figure 9.3: CIR cumulative distribution with vertically aligned and staggered base-stations. Also shown is the improvement with the deployment of partial metal shielding.

station, the outage probability rises considerably to reach a maximum of 0.02. A comparison against Fig. 9.1(b) suggests that CDMA systems experience very little outage if the CIR can be kept above 5 dB. By contrast, if the CIR drops below 5 dB, the outage rises considerably. Results also indicate that a single base-station not vertically aligned will increase that floors' outage probability (and to a lesser extent, that of adjacent floors). As shown in Fig. 9.1(c) the localised increase in outage probability can be similar to the vertically staggered case. Similar findings—increased outage for vertically staggered base-stations, compared to the aligned case—have also been observed in experimental studies [6]. However, as a Monte-Carlo method was used to calculate the average outage probability across a floor, the results were not detailed enough to show localised effects [6].

### 9.3.2 Propagation through Internal Shafts

Fig. 9.4 shows density plots of the outage probability when the services shaft is included in the simulation model. When all base-station antennas are vertically aligned, as in Fig. 9.4(a), regions of the floor on the left side of the shaft have low outage, whereas substantially increased outage occurs in regions on the right side (and within the shaft itself). Higher outage within the shaft is of less concern, as most users would not be operating in this environment for long periods. The services shaft reduces inter-floor isolation by providing low attenuation paths for signals originating on other floors. Therefore, signals from adjacent floors passing through the shaft have comparable power, leading to increased outage.

By examining all permutations, base-stations can be deployed to ensure the entire building can be serviced with low outage. An example of one such configuration is shown in Fig. 9.4(b), where the base-stations are staggered but grouped in pairs. Low interference is maintained,

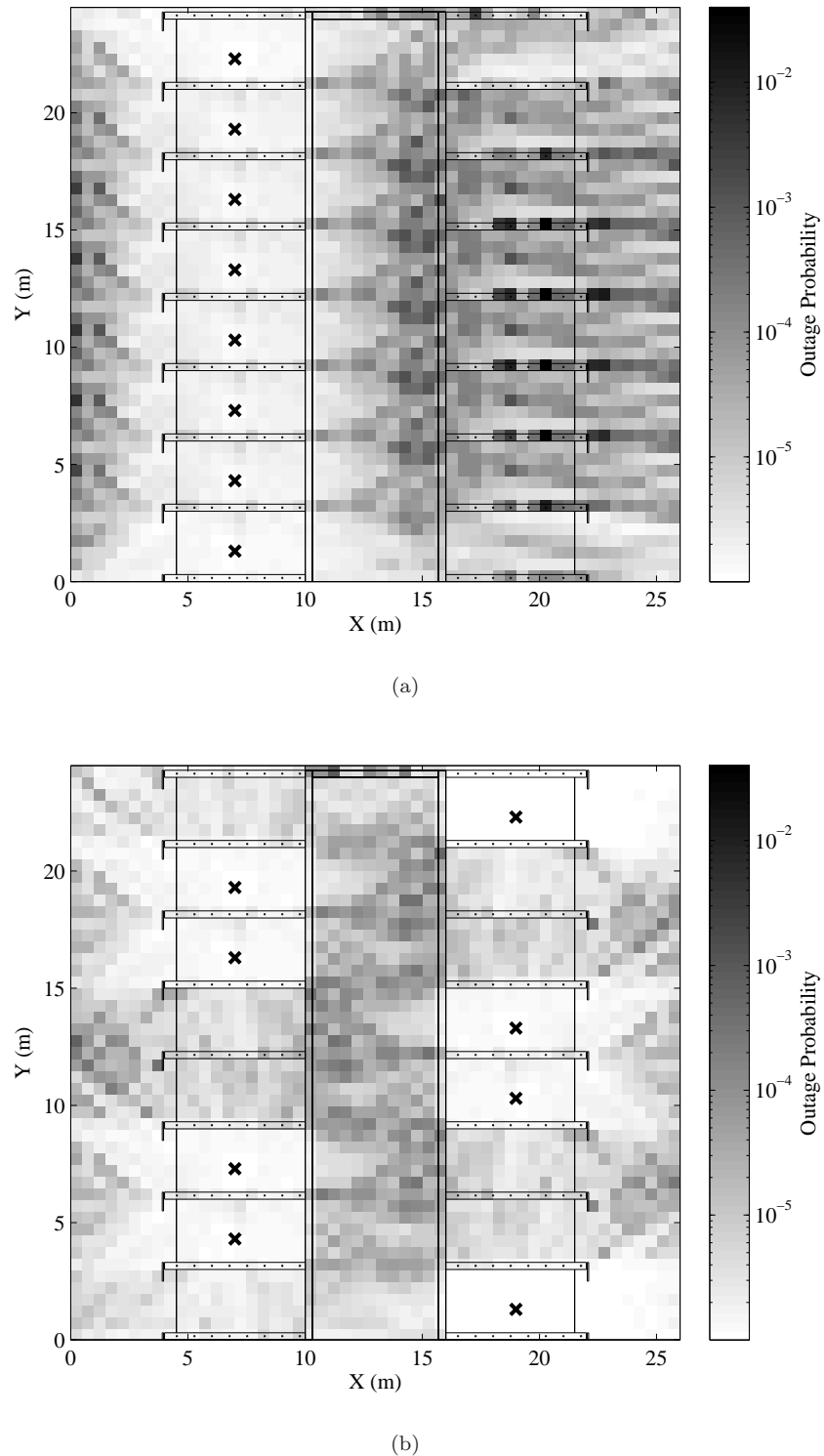


Figure 9.4: Density plots of outage probability when the central services shaft is included: (a) vertically-aligned base-stations and (b) base-stations optimised to minimise outage probability. The locations of the base-stations are marked with  $\times$ .

as each base-station is also servicing a portion of the floor vertically adjacent. In this case the shaft is being used to isolate base-stations on the left and right sides, and the interfering signals from across the shaft are attenuated more than the desired signals (which only have to penetrate a single floor). Regions within the shaft still experience high levels of outage. It should be noted that this two-dimensional characterisation of the services shaft does not account for propagation paths travelling around the shaft (e.g. diffraction at the corners or reflection from the windows). The presence of these paths could significantly alter the CIR and outage probability, but can only be captured using a three-dimensional geometry, which is considered in section §9.4.

## 9.4 Deployment Strategies (3D)

The results presented in chapters 6 and 8 indicate no single two-dimensional slice through a multi-storey building can correctly account for all propagation paths. In particular, propagation around (or through) internal services shafts can only be thoroughly examined in three-dimensions<sup>6</sup>. Accordingly, a three-dimensional implementation of the FDTD method is used estimate the desired and interfering signals in a multi-storey building. Due to the high computational requirements, only three floors have been considered. Fortunately, as noted in section §9.3, the majority of inter-floor interference arrives from base-stations operating on immediately adjacent floors, so such an analysis is valid.

In the scenarios considered in this section a further restriction is added. One fixed base-station operates on each floor (as before), however, the mobile users cannot connect to base-stations on adjacent floors, i.e. each floor is treated as a separate network<sup>7</sup>. The CIR and outage probability results in this section are presented with respect to users operating on Floor 2; the co-channel interfering<sup>8</sup> base-stations are located on Floors 1 and 3.

### 9.4.1 Staggered and Aligned Base-Stations

Fig. 9.5 shows density plots of the  $(3\lambda)^3$  sector-averaged CIR for (a) vertically aligned and (b) vertically staggered base-stations. The location of the desired and interfering base-stations are marked by  $\square$  and  $\times$  respectively. When the base-stations are vertically aligned, the average CIR across the floor is 18.7 dB (with a standard deviation of 6.2 dB). The CIR is highest (32.8 dB) around the desired base-station, while the lowest CIR (6.4 dB) is recorded in the services shaft. Low outage is expected when the base-stations are vertically aligned, as though the propagation paths around the shaft are similar for signals originating from either the desired or interfering base-stations, the concrete floor attenuates the interfering signals, thereby introducing 15–20 dB isolation.

Vertically staggering the base-stations—as shown in Fig. 9.5(b)—significantly alters the CIR. In particular, low CIR is observed in regions where the desired signal is shadowed by the services shaft. As noted in chapter 8, propagation paths penetrating through the shaft are highly attenuated by the thick lossy concrete walls, and consequently, signals received in the shadowed regions are dominated by paths propagating around the shaft. In the geometry considered, specular reflection from the glass exterior windows dominates, and the average

<sup>6</sup>Furthermore, the three-dimensional simulation results can be directly compared against experimental measurements.

<sup>7</sup>This is more realistic, as floors may be occupied by different companies/groups of users.

<sup>8</sup>This is the limiting/worse-possible case as it is assumed frequencies are reused on each floor.

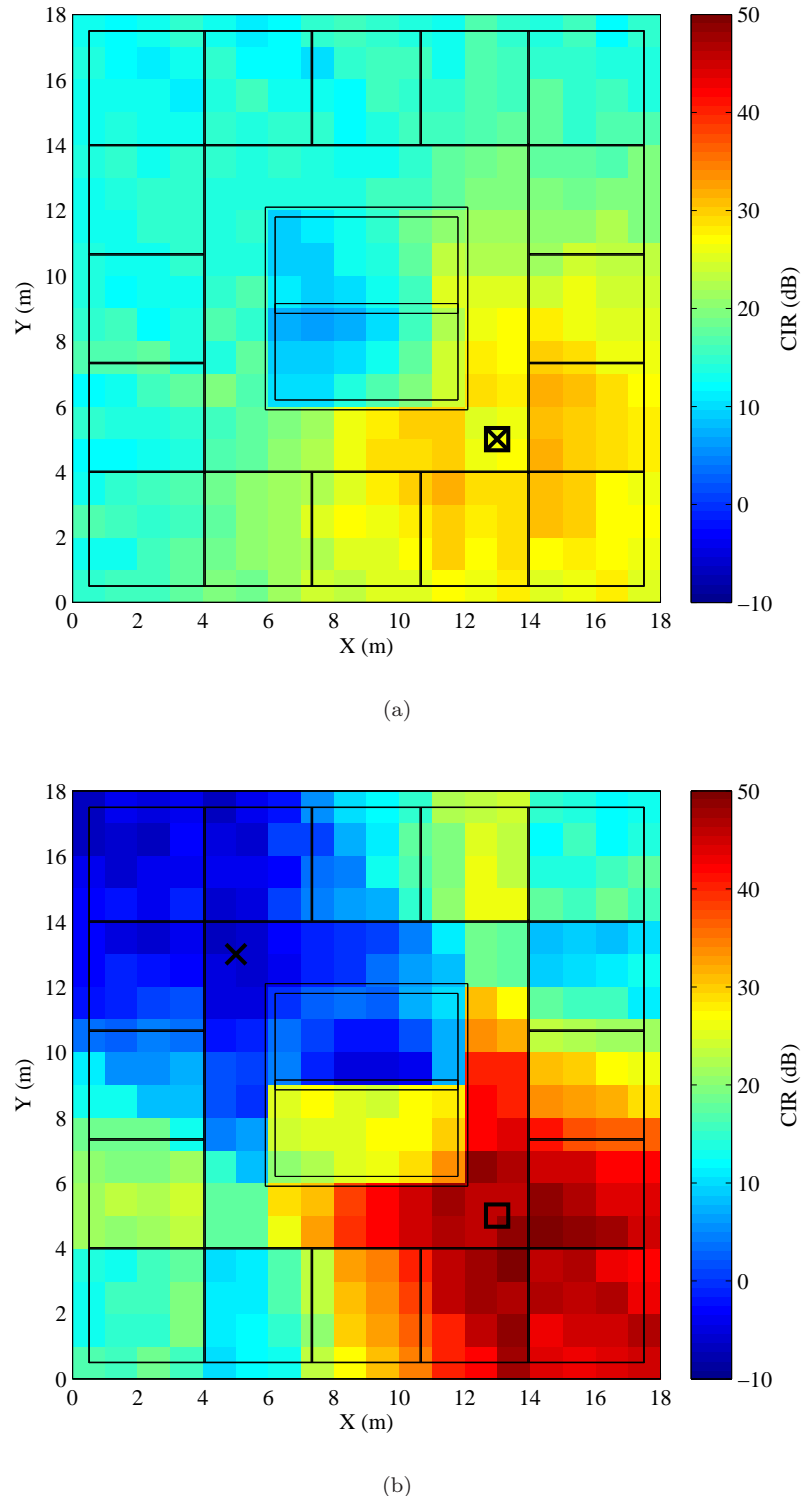


Figure 9.5: CIR density plots for (a) vertically aligned and (b) vertically staggered base-stations. The location of the desired and interfering base-stations are marked by  $\square$  and  $\times$  respectively.

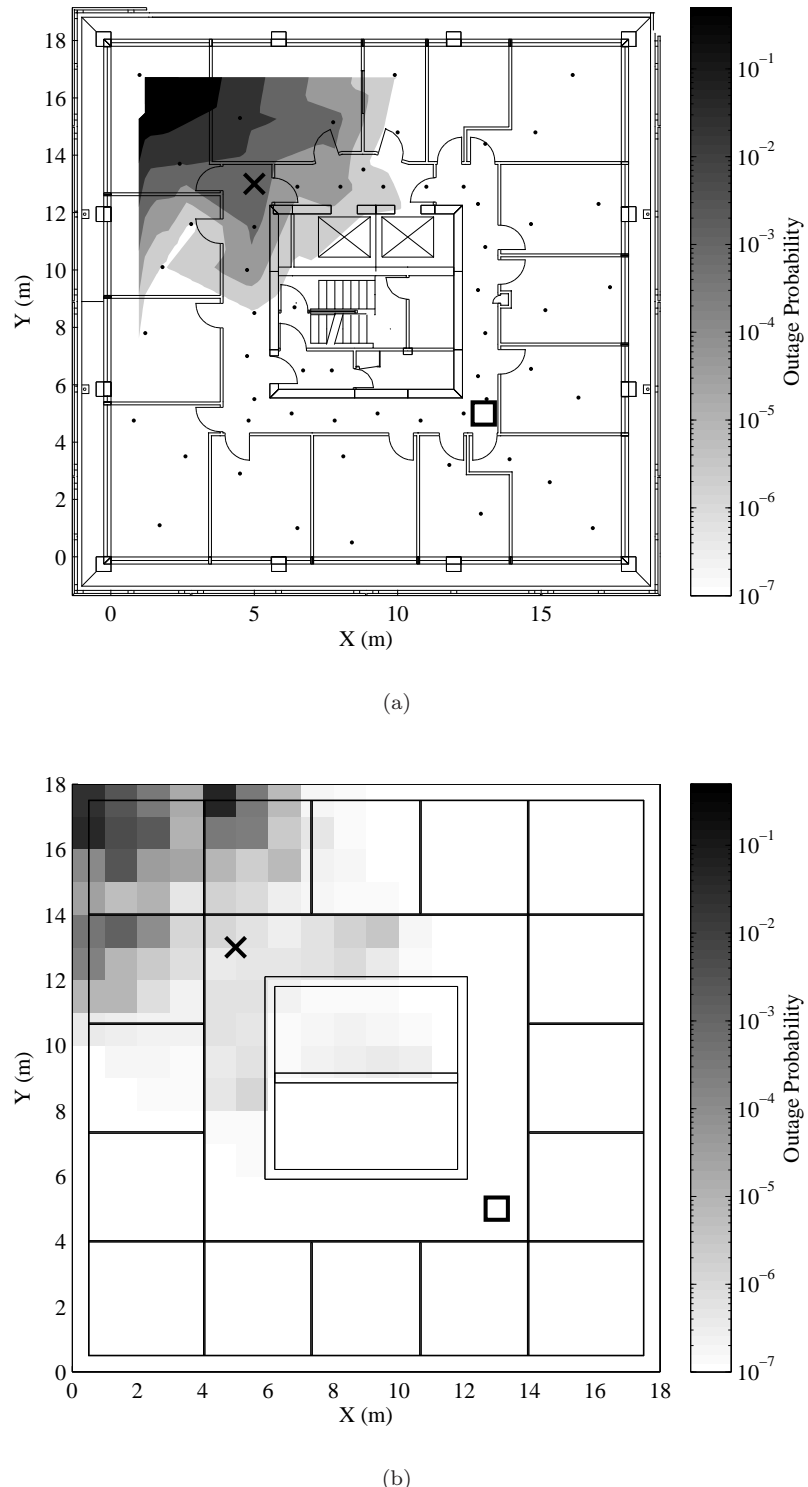


Figure 9.6: Density plots for the outage probability: (a) experimental measurements (1.8 GHz) and (b) FDTD simulations (1.0 GHz). The location of the desired and interfering base-stations are marked by  $\square$  and  $\times$  respectively.

path-loss is typically between 60–70 dB. In the shadowed regions, the isolation between the desired and interfering signals is reduced, and for a number of sectors the CIR is negative (i.e. the interfering signals are stronger than the desired). In regions where line-of-sight (LOS) paths from the desired base-station exist<sup>9</sup>, higher CIR is observed (in most cases above 10 dB). Similar to the vertically aligned case, the highest CIR is observed in regions around the desired base-station.

#### 9.4.2 Comparisons with Experimental Measurements

To confirm the findings presented in section §9.4.1, experimental measurements of the path-loss in the Engineering Tower (at 1.8 GHz) were used to compute the outage probability for a CDMA system. Similar to [6], multiple transmitters were deployed throughout the building, and the sector-averaged power was recorded at 52 locations across the sixth floor (further details of the experimental setup can be found in section §6.5.2). Fig. 9.6(a) shows a density plot of the measured outage probability across the sixth floor, for the case when the base-stations are vertically staggered. It should be noted that, although the plot shows a smooth variation, the outage will change abruptly at material interfaces. The location of the desired and interfering base-stations are marked by  $\square$  and  $\times$  respectively. Regions directly above/below the interfering base-stations are observed to have significantly higher levels of outage compared to the rest of the floor. The highest outage probability measured is 0.69, while lower outage is measured in regions closer to the desired base-station. When base-stations are vertically aligned, the outage probability remains relatively constant (approximately  $10^{-5} - 10^{-4}$ ) across the entire floor. The simulated outage probability—shown in Fig. 9.6(b)—generally agrees well with the experimental measurements. However, it should be noted that clutter (e.g. office furniture and fittings), usually present in the indoor propagation environment, have been ignored. The results presented in chapter 8 show that clutter in the environment can introduce significant attenuation, particularly on longer paths, which would tend to further increase the outage probability.

## 9.5 Interference Mitigation

The use of frequency selective surfaces (FSS) within buildings to selectively block certain frequency bands has been suggested previously [28–30]. By using FSSs to occlude co-channel interference paths, system performance may be improved. The results presented in sections §9.3 and §9.4 indicate high outage is generally localised to (relatively) small regions directly above or below the interfering base-stations. In this section, electromagnetic shielding—in the form of thin metal sheets<sup>10</sup> embedded within the concrete floors—is deployed to increase the inter-floor isolation. Previous research has shown the length/area of shielding applied is proportional to the improvement in outage probability [22], and though it is possible to completely isolate each floor by covering the ceiling (or floor) with shielding, this approach has not been considered for reasons of applicability and practicality. Instead, partial shields are examined, and modelled in the FDTD lattice as thin layers of metal with  $\sigma_E = 10^7$  S/m. At the operating frequencies

<sup>9</sup>Propagation paths penetrating through internal partitions are also considered LOS, as the gib-board does not introduce significant attenuation.

<sup>10</sup>As noted in chapter 2, metal shields can be considered *ideal* frequency selective surfaces operated in their resonant state [22]

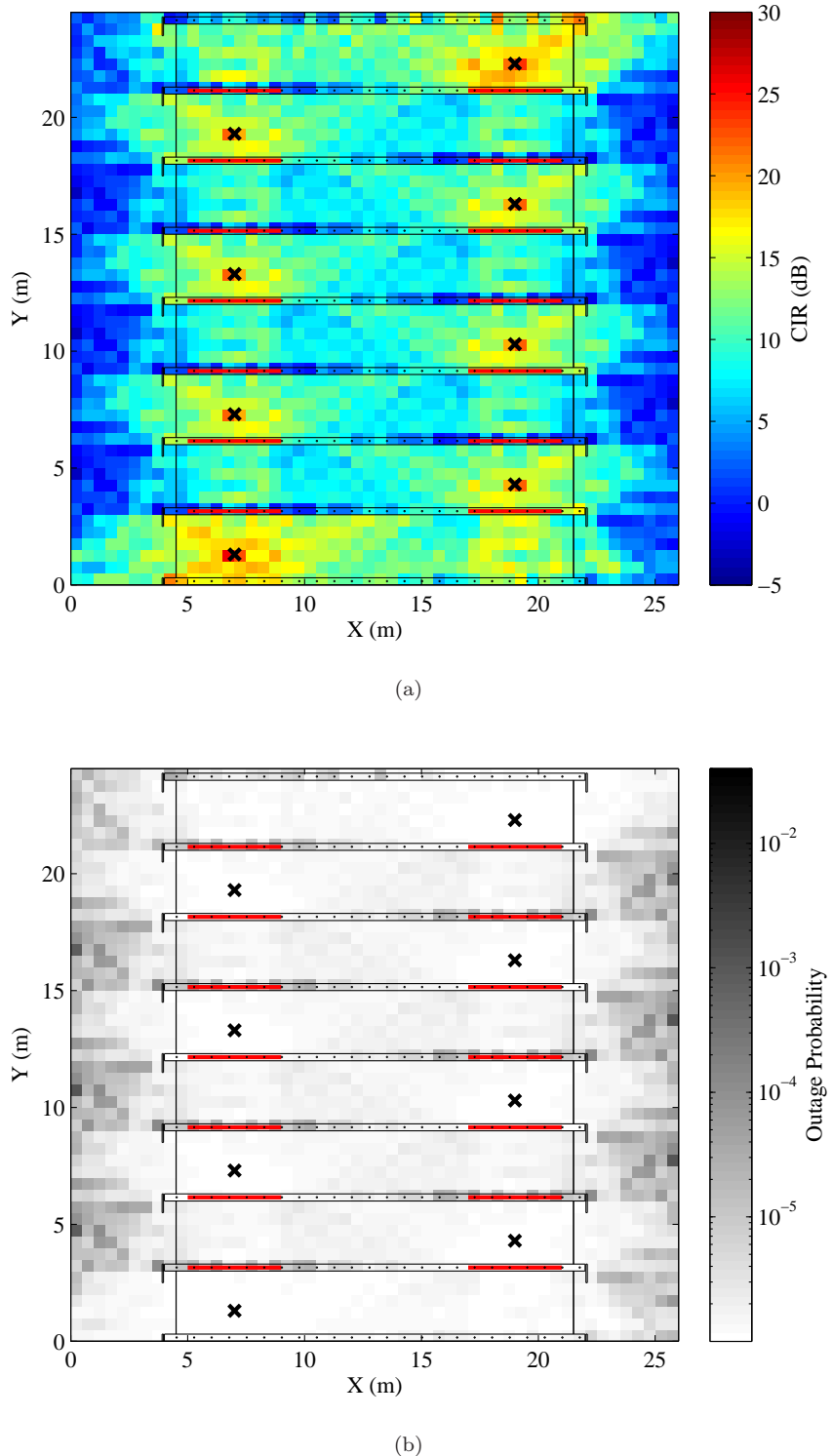


Figure 9.7: Density plots of (a) CIR and (b) CDMA outage probability with metal shields, marked by — (the thickness has been exaggerated for clarity), embedded in each floor. The locations of the base-stations are marked by  $\times$ , and users are assumed to connect to the strongest base-station.

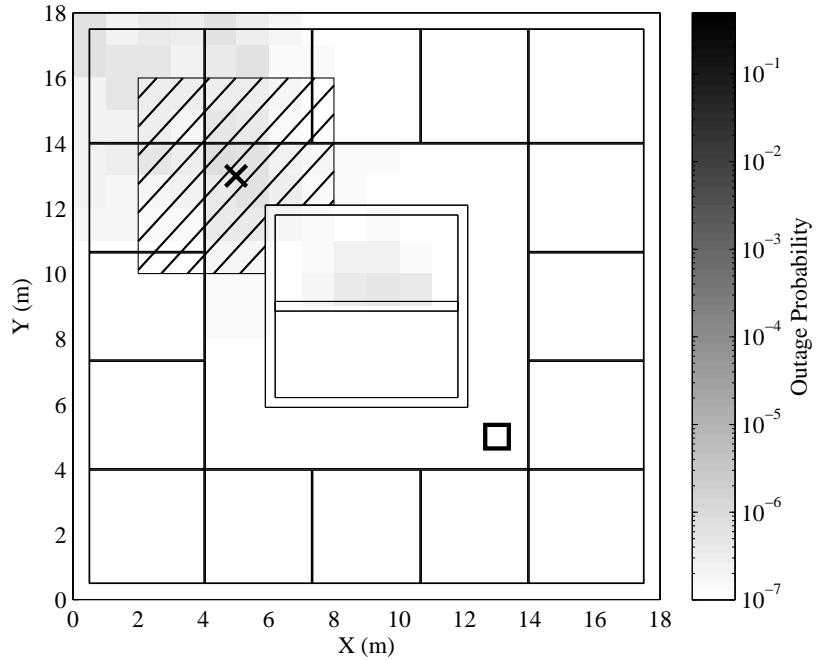


Figure 9.8: Density plot of the CDMA outage probability with metal shields (cross-hatched region) embedded in each floor. The location of the desired and interfering base-stations are marked by  $\square$  and  $\times$  respectively.

considered in this chapter, the thickness of the metal sheet (assumed to be one FDTD cell) is considerably larger than the skin depth.

Fig. 9.7(a) shows the CIR on a two-dimensional slice with vertically staggered base-stations and partial metal shielding embedded in the concrete floors. The locations of the shields are indicated by  $-$ , and the thickness has been exaggerated for clarity. The shields are 4.0 m in length and centred above each base-station. It is observed that the shielding increases the inter-floor isolation. In particular, regions in the building where—without shielding—low CIR was experienced now have considerably higher CIR, and the results are comparable to the case when the base-stations are vertically aligned. Comparing Fig. 9.7(a) with Fig. 9.1(b) shows shielding can increase the CIR directly above/below interfering base-stations by approximately 15 dB. A plot of the CIR cumulative distribution for vertically staggered base-stations with partial metal shielding is shown in Fig. 9.3. It is noted that less than 1% of the sectors within the building perimeter have a CIR below 5 dB; this represents a substantial improvement from the staggered configuration (22.2%). The improvement in CIR is also reflected in the density plot of outage probability, shown in Fig. 9.7(b). The outage probability is observed to decrease by an order of magnitude, compared to the case without shielding. The isolation is not perfect, as some energy will diffract around the edges of the shield, and these effects are visible in Figs. 9.7(a) and (b). However, the energy carried on diffracted paths is substantially weaker, and therefore has minimal impact on the outage probability.

The three-dimensional shield is a  $6 \times 6$  m square, centred directly above or below the interfering base-stations (as noted in Fig. 9.8, the shield does not extend into the services shaft). Fig. 9.8 shows a density plot of the outage probability—calculated with (9.5), with interfering base-stations located on immediately adjacent floors—across the floor when the

shields are deployed. Comparing Fig. 9.8 with Fig. 9.6(b) shows the shielding significantly lowers the outage probability. The low levels of outage (already present) in regions away from the interfering base-station have not been affected by the shielding.

## 9.6 Correlated Shadowing

When the transmitters are vertically staggered—as depicted in Fig. 9.1(b)—an increased proportion of sectors have low or negative CIR. This finding agrees well with experimental observations and previous studies [6, 39]. It has been suggested that correlated shadowing in the indoor environment is responsible for this behaviour [39]. Correlated shadowing (of the sector-averaged mean) is thought to occur when the desired and interfering signals travel over very similar propagation paths, i.e. encountering the same shadowing obstacles [39]. When the co-channel base-stations are vertically aligned, significant positive correlation between the desired and interfering signals can exist, i.e. as the desired signal strength increases, so does the interference and vice-versa. However, if the desired and interfering base-stations are not aligned, it is possible that when the desired signal is weak the interfering signals are strong (and vice-versa), thereby producing negative correlation. The central services shaft is thought to play a significant role in the strong correlations observed [39]. The correlation between a pair of desired and interfering base-stations can be quantified by [6]<sup>11</sup>

$$\rho = \frac{\sum_k (L_{dk} - \bar{L}_{dk})(L_{ik} - \bar{L}_{ik})}{\sqrt{\sum_k (L_{dk} - \bar{L}_{dk})^2} \sqrt{\sum_k (L_{ik} - \bar{L}_{ik})^2}}, \quad (9.7)$$

where  $L_{dk}$  (dB) and  $L_{ik}$  (dB) are the sector-averaged path-losses between the user location ( $k$ ) and the desired and interfering base-stations respectively. Table 9.2 lists values of the correlation coefficients calculated using (9.7) for the experimental measurements and FDTD simulations (with a single floor separating the desired and interfering base-stations). Strong positive correlation exists when the base-stations are vertically aligned; and by contrast, staggered base-stations display strong negative correlation. It is interesting to note that positive and negative correlations exist even when the core is omitted from the simulation model.

Table 9.2: Correlation Coefficients between Desired and Interfering Signals.

	$\rho_{\text{aligned}}$	$\rho_{\text{staggered}}$
Two-dimensional FDTD (no core)	0.62	-0.39
Two-dimensional FDTD (core)	0.79	-0.71
Three-dimensional FDTD	0.94	-0.70
Experimental Measurements	0.85	-0.62

Fig. 9.9 demonstrates that strong positive and negative correlations are artifacts of the distance-dependency relationship between user locations and base-stations, and are not specific to any building layout. Fig. 9.9(a) shows a representative diagram of two floors of a multi-storey building; the desired base-station operates on Floor 1 and two possible locations for the

<sup>11</sup>The equations provided in [6, 39] have typographical errors; (9.7) is correct.

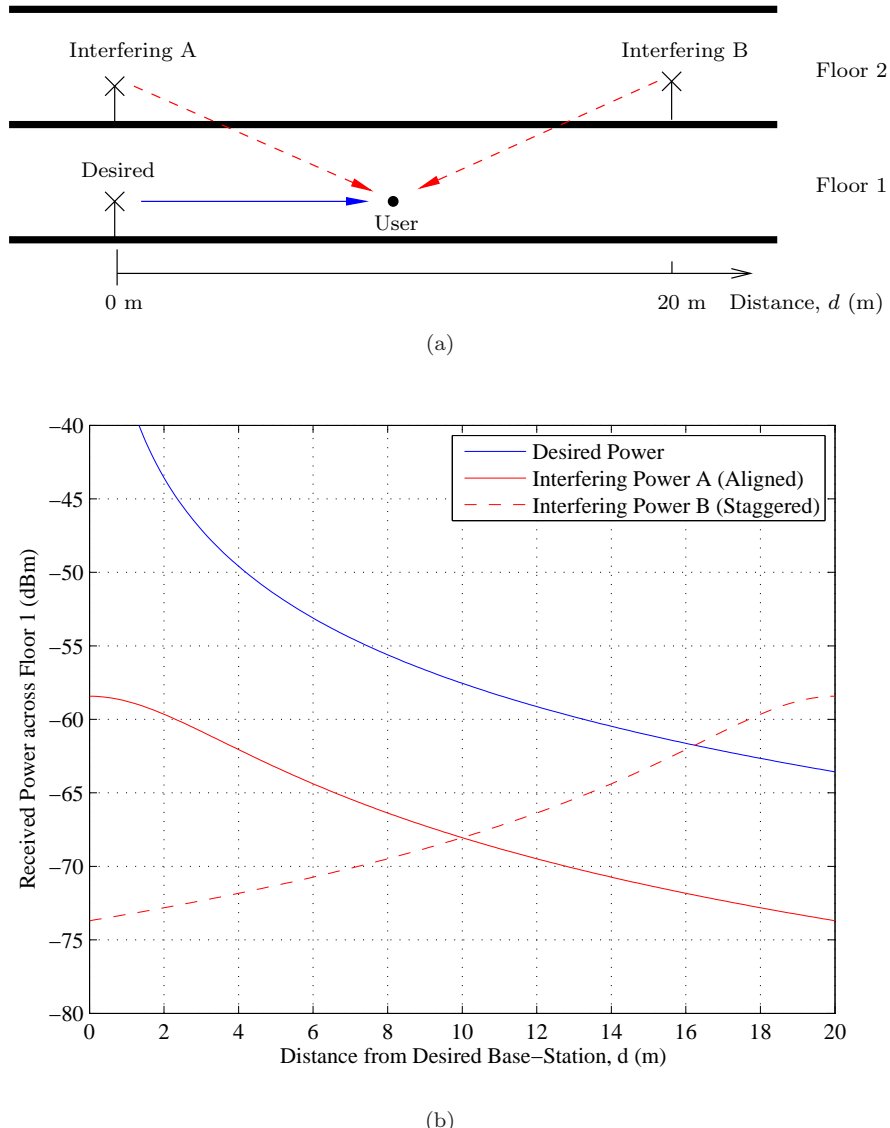
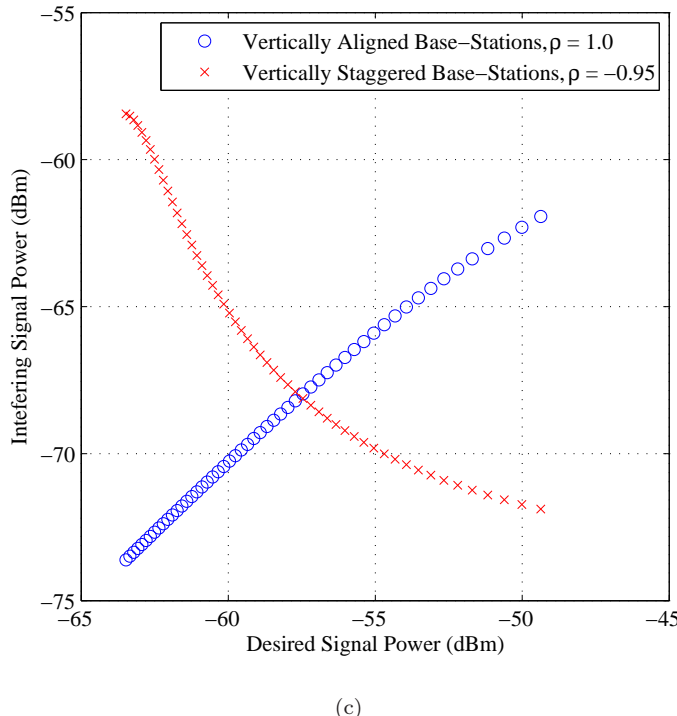


Figure 9.9: (a) Representative diagram of inter-floor interference from vertically aligned and staggered base-stations to a user operating on Floor 1. (b) Power recorded (in dBm) from the desired and interfering base-stations. (c) Scatter-plot of the interfering power versus the desired power for vertically aligned and staggered base-stations.



(c)

Figure 9.9: (c) Scatter-plot of the interfering power versus the desired power for vertically aligned and staggered base-stations.

interfering base-station are considered; vertically aligned (A) and vertically staggered/offset (B). The results presented in chapter 6 suggest an appropriate propagation model to describe the power received on Floor 1 (from either the desired or interfering base-stations) is free-space with an appropriate attenuation—in this case 10 dB—to account for penetration through the lossy concrete.

Fig. 9.9(b) shows the power received on Floor 1 from the desired and interfering base-stations. As expected, the desired power decreases exponentially with distance; similarly, the power from interfering base-station A also decreases exponentially with distance (with 10 dB isolation). However, the power received from interfering base-station B increases with distance away from the desired base-station. As shown in Fig. 9.9(c), this introduces very strong positive and negative correlation between the desired and interfering signals. This result suggests that the strong correlation values previously observed [6, 39] are artifacts of the relative distance between the user and the desired and interfering base-stations<sup>12</sup>. It also helps explains why the regions of low CIR (and high outage) are highly localised above/below interfering base-stations, and why only a (relatively) small region of the floor needs to be shielded. It should be noted that in reality, propagation around the services shaft (or other shadowing obstacles) will tend to decrease the strength of the desired signal on longer paths, thereby reducing the high correlation values.

<sup>12</sup>These results also suggest that the internal structure of the building is actually responsible for *lowering* the correlation (in particular for staggered base-stations). However, a detailed investigation is outside the scope of this thesis.

## 9.7 Consequences for System Planning

Although the primary purpose of this chapter was a feasibility study, several of the findings presented herein can be generalised and applied to other buildings in the form of heuristic rules<sup>13</sup>. The results indicate that to minimise interference the base-stations should (where possible) be vertically aligned; by contrast, the worst (in general) deployment strategy is a vertically staggered configuration. The FDTD simulation results also indicate that inter-floor interference paths can be occluded by shielding specific areas of the floor with thin layers of metal foil<sup>14</sup>. In general, this shielding should be located directly above/below the interfering base-stations. However, it should be noted that metal shielding will only increase the inter-floor isolation when it is used to occlude the dominant sources of interference. For example, external buildings can support strong reflections to adjacent floors, and in this case shielding the floor or ceiling will not significantly reduce the levels of interference.

At the present time the FDTD method remains too computationally expensive to be used in practise for optimising base-station deployment strategies, or the location (and dimensions) of metal shielding to minimise interference from co-channel systems. Optimisation algorithms, such as binary integer programming or genetic algorithms, may require many possible trials before an optimal deployment strategy is reached. The comparatively low computational requirements of ray-based methods (GO/UTD) makes them more attractive for optimisation purposes. For example, GO/UTD have been applied to optimise the locations of base-stations [94], and the deployment of metal shielding [22] within buildings. However, as noted in section §3.3.2, ray-based methods must be applied with caution, as many of the approximations and assumptions in their derivation are not valid for typical indoor environments (e.g. the study in [22] ignores diffraction from all dielectric edges). *Mechanistic* models, such as those proposed in chapters 6–8, potentially satisfy the trade-off between accuracy and computational cost. However, these are not yet at a stage of development that will allow localised field distributions to be predicted accurately (as required for the deployment of shielding).

## 9.8 Summary

This chapter has extended the propagation studies considered in chapters 6–8 to estimate the performance of indoor wireless systems (specifically those based on CDMA technology) in the presence of interference. Computational limitations have restricted analysis to two-dimensional slices through a multi-storey building and smaller three-dimensional geometries. The chapter has focused on base-station deployment strategies to minimise the overall levels of interference within a multi-storey building. The simulation results have been compared with experimental measurements of the outage probability and a good agreement was found for most cases. It was noted that regions of high interference were very localised, and the performance of partial metal shielding (in the form of thin metal sheets) was simulated. The shielding occludes the interfering signal paths, increasing the inter-floor isolation, and thereby reducing interference. The use of the FDTD method to estimate the performance of indoor wireless systems is the last stage in the road-map of propagation studies outlined in chapter 5. Chapter 10 discusses the implications of the findings presented within this thesis and makes recommendations for future investigations.

---

<sup>13</sup>Several of these results have already been reported in the literature, e.g. [6], but these were based on experimental studies and the transportability of the findings to other buildings remains a concern.

<sup>14</sup>The experimental verification of this finding is outside the scope of this thesis.



# Chapter 10

# Discussion and Recommendations for Future Investigation

## 10.1 Introduction

The two major objectives of this thesis are the characterisation radio-wave propagation within buildings using two- and three-dimensional implementations of the FDTD method; and generalising these results to develop appropriate mechanistic models. To address these goals, three propagation studies—based on simplified two- and three-dimensional representations of multi-storey buildings—have been considered. Each propagation study has focused on a different aspect of the indoor radio channel, and although the major objectives have been achieved there is scope for further development. This chapter discusses some of the key findings presented in chapters 6–9 from a system planning perspective, and discusses recommendations for future investigation.

Section §10.2 provides an overview of the mechanistic modelling approach and briefly summarises the main findings from chapters 6–8. Also examined in section §10.2 are applicability bounds for the FDTD method and the mechanistic models. Recommendations for future investigation are outlined in section §10.3, focusing on the refinement of the mechanistic models, techniques/methods to reduce the computational costs, and the characterisation of clutter in the indoor propagation environment. The chapter is briefly summarised in section §10.4.

## 10.2 Mechanistic Propagation Models—A Review from a System Planning Perspective

### 10.2.1 Overview

Chapters 2 and 3 established the need for accurate, yet computationally efficient, models to characterise radio-wave propagation within buildings. In particular (to reliably predict the system performance) accurate estimates of the sector-averaged desired and interfering signal powers are required. Currently, empirical models remain widely used for system planning purposes, as they are relatively straightforward to apply. However, many of the terms and parameters in these models generally lack an electromagnetic basis, and can vary considerably between buildings, thereby complicating transportability. Computational electromagnetic techniques, such

as the FDTD method, offer increased accuracy, and can provide a physical basis for previous experimental observations. However, it must be understood that, due to high computational costs, the FDTD technique is **not** being suggested as a practical method to model the indoor radio channel. Instead, the mechanistic modelling approach outlined in this thesis uses the FDTD method to determine the dominant propagation paths in simplified models of multi-storey buildings. These results can be generalised to form mechanistic models by developing simple ray-optical<sup>1</sup> approximations to describe each dominant path/mechanism. The resulting mechanistic models are computationally efficient, but retain the accuracy of their electromagnetic foundations. It should also be noted that the mechanistic models are developed to predict the local/sector-averaged mean power over a small region, not the instantaneous received power at a point. Variations in the signal about the mean-level can be included by superimposing statistical distributions that describe the fading envelope.

### 10.2.2 Propagation Studies—Summary

#### Propagation Study A: Within the Building Perimeter (2D)

Study A considers propagation on a simplified two-dimensional vertical ‘slice’ through an eight storey office tower, consisting of multiple concrete floors (modelled as homogeneous dielectric slabs). A thorough investigation with the FDTD method (for both  $\text{TM}_z$  and  $\text{TE}_z$  lattice polarisations) indicates two mechanisms dominate the power received on immediately (and nearly) adjacent floors: direct penetration through the floors, and diffraction at the floor-edges. Generally, penetration dominates for the first 4–5 floor separations; beyond five floors diffraction dominates<sup>2</sup>. The addition of further details (such as metal rebar, glass windows, hanging panels and internal walls) were shown to alter the local fields, but do not significantly change the dominant components. The inclusion of a central services shaft (containing elevators and stairwells) significantly attenuates signals propagating across the floor, but also introduces lower-loss propagation paths to adjacent floors.

#### Propagation Study B: External to the Building Perimeter (2D)

Study B extends the two-dimensional slice examined in study A to consider possible reflection and scattering paths from nearby buildings. FDTD simulation results indicate that strong reflection paths can exist (even from the electrically rough external faces), and are capable of delivering significant levels of power back to immediately (and nearly) adjacent floors. In particular, the reflected path is largely free-space, and consequently tends to dominates the received signal after 2–3 floor separations. A two-component mechanistic model to describe the power received on a lower floor is based on ray-optical approximations of the penetrating and reflecting paths.

#### Propagation Study C: Within the Building Perimeter (3D)

Study C significantly reduces the scale of the problem, but extends the geometry to three-dimensions (computational limitations restrict the geometry to three floors). In three-dimensions

---

<sup>1</sup>Ray-methods (such as GO/UTD) are not used directly as this would *a priori* assume all propagation paths can be characterised using rays.

<sup>2</sup>The transition between penetration and diffraction depends on the material properties and frequency; for typical values of the concrete permittivity and conductivity this is around 4–5 floors separations.

the signals can propagate around the central services shaft, and in ‘lit’ regions the results suggest a free-space model with (constant) floor attenuation terms is appropriate. However, in the ‘shadowed’ regions, additional loss terms are required to account for propagation around the services shaft. It is also noted that as the floor separation increases, propagation paths travelling within the shaft contribute an increasing proportion of the received power. Study C also focused on characterising propagation in the presence of clutter, such as office furniture and fittings. Clutter in the propagation environment is difficult to adequately characterise in two-dimensions and has frequently been ignored in previous investigations. However, the limited inclusion of clutter in the three-dimensional geometry is shown to significantly alter the propagation paths. For example, in the absence of clutter, propagation into the shadowed regions is dominated by reflection from the exterior glass windows; by contrast, clutter in the environment strongly attenuates these paths, and the received signal is dominated by diffraction at the corners of the shaft. Developing mechanistic models for this behaviour is complicated by the inherent randomness in the position (and properties) of the clutter.

### 10.2.3 Assumptions and Applicability

As noted, the mechanistic modelling approach approximates the dominant propagation paths (identified from FDTD simulations of the indoor radio channel) with ray-methods. This approach is valid provided the dominant propagation paths remain ray-optical. However, several situations could arise where the dominant components do not follow ray-optical trajectories. For example, the UTD is known to fail when predicting diffraction over multiple co-linear knife edges (where each diffracting edge is in the transition region of the previous edge) [86, 87]. Propagation down the outside face of a building—over multiple floor edges—could be considered a similar geometry. However, results in this case indicate an adequate level of accuracy is possible by only considering diffraction at the edges of the first and last floor. Other deviations from ray-optical trajectories can be identified using visualisation techniques developed to infer the dominant propagation paths. For example, streamline projections through the Poynting vector represent the *net* energy flow, and while local distortions (over  $1-2\lambda$ ) are expected due to multi-path phenomena, strongly curved streamlines would tend to indicate the propagation path cannot be characterised using ray-optics. However, in many cases the streamlines are observed to follow straight paths, e.g. propagation to adjacent floors as depicted in Fig. 8.5(b). Furthermore, predictions of the sector-averaged power using the mechanistic models agree well with full-wave FDTD simulations, suggesting in many cases (examined to date) the propagation phenomena can be adequately characterised using ray-optics.

Central to the development of mechanistic models is a thorough assessment of the limitations of the FDTD method to characterise the indoor radio channel. Although this topic has been covered in the preceding chapters, at this stage it is appropriate to briefly summarise several of the key limitations which may have implications for future investigations. In particular, propagation studies A and B have largely focused on two-dimensional characterisations of the buildings. Two-dimensional geometries assume the structure being modelled is infinite in extent, i.e. the fields propagate on a ‘slice’ through the problem. Propagation paths orthogonal to the slice direction cannot be captured or characterised, and results show that in some circumstances these mechanisms may be significant. However, in many other regions the propagation mechanisms identified using two-dimensional geometries are identical (or at least very similar) to those identified in three-dimensions.

It should also be noted that two-dimensional FDTD simulations cannot be directly com-

pared against experimental measurements. Direct comparisons have thus focused on the three-dimensional results<sup>3</sup> presented in chapter 8. In some regions the difference in the sector-averaged power between the FDTD simulations and measurements is as large as 25 dB. However, it is also observed that the RMS error between the measurements and simulations decreases as a greater level of internal details/clutter are modelled. Furthermore, the dielectric properties ( $\epsilon_r$  and  $\sigma$ ) of many construction materials are usually not known exactly, and results indicate the field distributions are sensitive to the material properties. These results tend to suggest the limiting factor for FDTD simulations of the indoor radio channel is the availability of an accurate ‘database’ of the locations, composition and properties of walls/floors *and* environmental details/clutter<sup>4</sup>. It should be noted that this finding is not specific to the FDTD method, and applies to any other electromagnetic technique used to model propagation within buildings.

### 10.3 Recommendations for Future Investigation

At this stage in the thesis it is appropriate to consider recommendations for future investigation. Similar to the goals of this thesis, the recommendations focus on developing appropriate models to characterise the indoor radio channel, and are grouped around three major themes:

1. Refining the mechanistic models;
2. Investigating methods to reduce the computational requirements; and
3. Developing techniques to characterise the effects of clutter.

Each of these categories is now considered.

#### 10.3.1 Refinement of the Mechanistic Models

##### Alternative Building Geometries

Both buildings considered in this thesis (the Engineering Tower and Chemistry Building at The University of Auckland) were erected in the mid 1960’s and share the same *Brutalist* architectural style<sup>5</sup> and construction materials, specifically steel-reinforced concrete. The internal structure of both buildings is also very similar, and consists of concrete floors<sup>6</sup> and structural supports (which may also contain services shafts<sup>7</sup> for lifts and stairwells), with false ceilings carrying facilities and services, such as heating, lighting and water. The remaining internal space is divided into corridors and offices/laboratories with ‘soft’ partitions (gib-board/drywall nailed to timber frames). The offices and laboratories also tend to be cluttered with a range of metallic and dielectric objects.

As both buildings studied are very similar, the mechanisms identified with the FDTD method may be specific to this style of architecture, i.e. the resulting mechanistic models may

---

<sup>3</sup>Computational limitations set the maximum simulated frequency to 1.0 GHz, while the measurements have been conducted at 1.8 GHz. The additional free-space loss has been accounted for in the comparisons.

<sup>4</sup>The impracticality of recording the locations and property of the clutter is noted, and methods to characterise the effects of clutter form part of the recommendations for future investigation.

<sup>5</sup>*Brutalist* architecture is characterised by angular ‘blocky’ structures and extensive use of poured concrete [95, 262–268].

<sup>6</sup>Concrete floors can be formed by pouring concrete over a rigid metal frame. In this case, propagation paths through the concrete are highly attenuated and other mechanisms to adjacent floors may dominate.

<sup>7</sup>In this thesis the services shafts have been centred on the floor. Although the field distribution around an off-centre shaft is likely to be very similar to cases already examined, larger portions of the floor could be characterised using two-dimensional models.

be ‘tuned’ and not as transportable to other buildings. Consequently, further studies in other buildings (with different architectural styles) are recommended. In particular:

- Steel frames provide much of the structural support in modern buildings, which accordingly use less concrete. Propagation studies A–C have focused exclusively on concrete-framed buildings, with the results indicating many propagation mechanisms are strongly influenced by concrete structures. In buildings with less concrete, other propagation mechanisms may dominate, and many previous findings may not be (directly) applicable.
- Large atrium areas and open plan offices are also common in many modern buildings. Accurate models to predict coverage and interference in these areas are important as the user density is typically high. Although the propagation environment can be considered (largely) free-space, most users will be operating 1–2 m above the floor and surrounded by local clutter.

Experimental measurements in other buildings to validate the FDTD results and mechanistic models is also recommended.

### Incorporation of Experimental Measurements

It is unlikely any modelling approach will completely eliminate the need for experimental measurements. For example, the mechanistic models developed in this thesis were validated against extensive site surveys of the received power. However, it may be possible to develop models that require a smaller number of validation measurements. As noted in chapter 6, variations in the material properties or geometry can result in significant changes to the received power, however, in most circumstances the dominant mechanisms are not observed to change. By characterising these mechanisms with terms that can be determined using a small number of tuning measurements the models may be more transportable to a wider range of buildings. For example, the attenuation introduced by a concrete floor<sup>8</sup> can be accurately determined with several measurements of the sector-averaged power/path-loss in a small region directly above/below a transmitter. Similarly, additional terms could be introduced to better model regions in a building where the mechanistic models are known to introduce significant prediction errors, e.g. behind large shadowing objects.

### 10.3.2 Reducing Computational Requirements

#### Subgridding and Non-Uniform Meshing

As previously noted, one of the major limitations of the FDTD method—particularly when applied to electrically large problems, such as three-dimensional models of buildings—is high computational costs. High spatial and temporal<sup>9</sup> sampling densities are required to ensure numerical stability and accurate results. Typically a sampling density of 15 cells/ $\lambda$  is used to reduce dispersion error; in this case  $\lambda$  is the wavelength of the highest frequency of interest in the most optically dense material. Consequently, if a fixed lattice size is used, free-space regions are often gridded in excess of the  $\lambda/15$  requirement.

---

<sup>8</sup>Directly measuring the concrete conductivity is considerably more complicated and generally requires specialised equipment [78].

<sup>9</sup>Alternative time-stepping algorithms, such as the Alternating Direction Implicit (ADI) scheme can be used to increase the time-step, however this also increases computational complexity [11, 888–891].

The lattice cells can be subdivided to increase the sampling density in regions where additional spatial resolution is required, e.g. within dielectric materials, or where the objects of interest are smaller than a lattice cell. In this case large cells could be used in the free-space regions. Subgridding could significantly reduce the computational requirements and allow larger buildings to be examined at higher frequencies. However, many sub-gridding techniques introduce spurious reflections at the interface of the regular and subgridded lattices [11, 505–507], or late-time numerical instability [96]. Alternatively, non-uniform triangular lattices can be used to increase the sampling density by locally conforming the mesh around/within dielectric materials, or objects with complicated/curved geometries. However, drawbacks of triangular lattices include a reduced time-step to ensure numerical stability [97], increased local error [11, p. 464], and difficulties in formulating absorbing boundary conditions (accurate results have been reported for a triangular mesh terminated with periodic boundary conditions [97]).

### The Pseudo-Spectral Time-Domain Method

The Pseudo-Spectral Time-Domain (PSTD) method uses a discrete Fourier Transform<sup>10</sup> (DFT) to evaluate the spatial derivatives of Maxwell's curl equations on a computational lattice [11, pp. 150–151]. In contrast to the FDTD algorithm outlined in chapter 4, the electric and magnetic field components are co-located. The spatial derivatives can be calculated using the differentiation property of the Fourier Transform [11, pp. 150–151]

$$\frac{\partial U}{\partial x} \Big|_i = -\mathcal{F}^{-1}(jk_x \mathcal{F}[U_i]),$$

where  $\mathcal{F}$  and  $\mathcal{F}^{-1}$  represent the forward and inverse DFTs respectively,  $U_i$  are the field values along a  $x$ -directed cut through the lattice, and  $k_x$  is the  $x$ -component of the wave-vector. The set of spatial derivatives along the  $x$ -directed cut can be evaluated in a single step. As the DFT assumes periodicity of the set, values will ‘wrap-around’, producing spurious results. However, these numerical artifacts can be removed (to a certain extent) by implementing a perfectly matched layer absorbing boundary condition on the other edges of the computational lattice [48]. It should also be noted that discontinuities in the fields (e.g. at material interfaces) introduce strong Gibbs' phenomena, reducing the accuracy of the algorithm. Non-uniform DFTs have been suggested to improve spatial sampling at the interfaces, but are difficult to calculate efficiently [48].

Similar to the Yee leapfrog algorithm, the **E** and **H** fields are interleaved in time, with the magnetic fields evaluated at integer time steps and the electric fields at half-integer time steps. However, in contrast to the FDTD algorithm, the dispersion constraint is  $\Delta < \lambda/2$  (for the FDTD method this is typically  $\Delta < \lambda/15$ ). The corresponding reduction in computational requirements is approximately  $8^D$ , where  $D$  is the dimensionality of the problem [11, pp. 150–151]. Although parallelising the PSTD method may be more difficult<sup>11</sup> than the FDTD algorithm, the reduction in computational requirements may allow electrically large (three-dimensional) indoor environments to be solved without requiring high performance computer clusters.

---

<sup>10</sup>The Fast Fourier Transform (FFT) can also be applied to improve computational efficiency.

<sup>11</sup>The spatial derivatives of the PSTD method are evaluated on one-dimensional cuts through the lattice, and for two- and three-dimensional implementations these cuts are interleaved, making it difficult to subdivide the lattice for efficient parallelisation.

### Hybrid GO/FDTD Methods

Numerical electromagnetic techniques based on approximating the propagating fields as rays (e.g. GO/UTD) can accurately predict many propagation phenomena—such as line-of-sight propagation, reflection and diffraction—and are often considerably more computationally efficient than the FDTD method. However, ray-methods have difficulty modelling propagation around/through inhomogeneous dielectric objects with complicated geometry. Furthermore, approximations to describe diffraction (such as the UTD) are only valid for perfectly conducting wedges. However, a hybrid GO/FDTD approach could provide both a greater accuracy than a purely GO solution, and lower computational costs than a purely FDTD solution. An example of a possible application of hybrid GO/FDTD methods would be a more computationally efficient analysis of reflection from surrounding buildings (propagation study B). In this case a large portion of the path is free-space and can be well modelled using GO; while propagation within the building—and reflection at the electrically rough face of the external building—would be better characterised with the FDTD method. Several approaches have been proposed for converting FDTD field components to GO point sources and vice versa [52, 53, 59, 60], however, difficulties in ensuring accurate coupling between the fields limits applicability of hybrid GO/FDTD methods. The potential reductions in computational requirements warrant further investigation.

#### 10.3.3 Modelling Propagation in the Presence of Clutter

The results obtained from a three-dimensional characterisation of the indoor radio channel suggest local clutter and scatter—which have largely been ignored in RF planning tools for indoor environments [18], or been incorporated by altering the material properties of the large-scale geometry [43]—not only significantly reduce the received power, but also alter the propagation mechanisms observed. The results indicate indoor propagation is governed by both the large-scale geometry—the effects of which are largely deterministic—and the cumulative effects of small-scale clutter, which have essentially random size, position and properties, but can cause significant changes to received power. The inherent variation in building layout, internal clutter and material properties complicate the analysis. However, based on the findings reported in this thesis the question should not be *what is the level of detail required to accurately predict path-loss?* but *what is the expected variation in path-loss caused by uncertainty in the problem being modelled?*

A statistical characterisation of propagation in cluttered environments was proposed in [65], where scattering by walls and local clutter was modelled probabilistically using the Boltzmann or diffusion equations. However, some regions, particularly corridors, are largely clutter free and will promote free-space or possibly waveguiding behaviour. Simply modelling the entire environment as a probability ‘cloud’ of local clutter will not capture this behaviour. Similarly, large material inhomogeneities (such as a concrete lift shaft) have potential to cast significant radio shadows across large areas of a building. Combining a statistical approach to account for the details with deterministic electromagnetic methods to predict large-scale field strengths may yield useful results.

Monte Carlo techniques have been used in conjunction with the FDTD method to determine the average scattering parameters from random two-dimensional surfaces [98]. The effects of changes in the geometry and material properties on propagation mechanisms and received power could be quantified by running multiple simulations varying the input parameters ap-

propriately. However, applying FDTD/Monte Carlo methods to non-trivial three dimensional indoor propagation problems is not feasible with current computing hardware. A study applying Monte Carlo techniques to determine the sensitivity of a mechanistic model to the input parameters (in this case the material properties) for a two-dimensional geometry is shown in appendix I. Other uncertainty analysis techniques (such as polynomial chaos and the method of moments) have also been used to quantify the standard deviation in the outputs when applying the FDTD method to generalised problems with variable inputs [99], and may be more computationally amenable.

## **10.4 Summary**

In this chapter, the implications of the findings described in chapters 6–9 are discussed. In particular, the mechanistic modelling approach has been assessed from a systems perspective and limitations identified. Based on the results presented in this thesis, recommendations for future investigation have been suggested. The recommendations are focused on developing appropriate models to characterise the indoor radio channel, and include refining the existing mechanistic models, reducing computational requirements, and modelling propagation in the presence of clutter. Chapter 11 provides some concluding remarks.

# Chapter 11

## Conclusions

The commercial success of mobile radio systems has led to significant interest in understanding and predicting radio-wave propagation in urban areas, and increasingly within buildings. The performance of these systems is limited by noise, the physical environment, and—as the uptake of wireless technology increases—interference from other users and devices. Interference is an important issue in the design of wireless communication systems employing frequency reuse. This reuse of frequencies occurs spatially, and therefore insufficient isolation between co-channel systems can result in unacceptable levels of interference which detrimentally affect quality and capacity. Wireless systems designed to operate indoors—such as pagers, cordless phones, cellular systems (in particular femto-cells) and WLANs—are particularly susceptible to interference, as all transceivers are usually in close proximity. Knowledge of how radio waves propagate within buildings is important to assess the impact of interference, and plays an important role in the design and performance evaluation of wireless systems. This thesis has applied computational electromagnetics—specifically two- and three-dimensional implementations of the FDTD method—to investigate and characterise the indoor radio channel.

The indoor radio channel can be divided into two categories: *a*) propagation on the same floor as the transmitter; and *b*) propagation to adjacent floors. Accurately characterising both ‘channels’ is important when considering interference, as the desired signal usually originates from a base-station on the same floor, while interference typically arises from neighbouring co-channel systems operating on immediately, or nearly, adjacent floors. For example, underestimating the strength of the desired signals could result in an over-designed system, where the coverage extends beyond the expected range (potentially causing interference to other systems); while underestimating the strength of the interfering signals could reduce system performance.

This thesis has largely focused on characterising and modelling propagation between the floors of generalised multi-storey buildings. Although models to characterise the inter-floor propagation paths have been developed from experimental measurements and ray-optical approximations, relatively little research has been directed toward applying full-wave computational electromagnetic techniques, such as the FDTD method. However, the FDTD method is (generally) too computationally expensive to be applied for day-to-day system planning purposes. Therefore, this thesis has also focused on generalising the numerical simulation results to determine the dominant paths governing propagation between the floors of multi-storey buildings. This knowledge is then used to formulate computationally efficient *mechanistic* models, which may be more transportable to other buildings.

Inter-floor propagation paths can be characterised in two-dimensions by taking a vertical

‘slice’ through a multi-storey building. Depending on the position and orientation of this slice, various features (e.g. internal services shafts) of the building can be isolated and examined separately. At the very least the vertical slice contains the floors (in contemporary multi-storey buildings these are usually made from concrete) and a two-dimensional representation of the transmitting antenna. Depending on the polarisation of the slice the radiation pattern can be omni-directional, or similar to that of a short-dipole antenna. The significant attenuation introduced by the concrete floors means, that in many circumstances, lower loss propagation paths may dominate the received signal on adjacent floors, e.g. diffraction down the outside face of the building, reflection and scattering from external buildings, and propagation into internal shafts. Fortunately, many of these propagation mechanisms can be adequately characterised using simplified ray-optical models. The FDTD simulation results have also been used to examine optimal base-station deployment strategies to minimise interference throughout the building, and to explore the possibility that metal shielding could be used to occlude the dominant interfering paths. The findings reported in this thesis suggest metal shielding could be very successful if deployed in real buildings, and further research is recommended.

Results present in this thesis indicate many of the propagation mechanisms identified in two-dimensions still dominate when the geometry is extended to three-dimensions. However, a direct comparison between the measured sector-averaged path-loss and those predicted with the FDTD method show significant differences. Generally the FDTD method overestimates the received power, and in some regions the differences can be greater than 15 dB. This behaviour is thought to be caused by clutter in the indoor environment, the cumulative effects of which are observed to significantly attenuate certain propagation paths, thereby altering the dominant mechanisms, i.e. the FDTD method is incorrectly identifying the dominant propagation paths. This finding has also been confirmed by comparing streamline visualisations of the Poynting vector with the simulated (and measured) Rician K-factors. When the clutter is ignored, the fading envelope for most locations in the building can be characterised by a Rician distribution; by contrast, clutter in the environment introduces strong multi-path and the fading envelope is better characterised by a Rayleigh distribution. These findings have significant implications for the use of deterministic methods (e.g. computational electromagnetics) to model the indoor radio channel, as it suggests a considerably greater level of detail must be included to achieve the desired accuracy. A feasibility study to statistically characterise the sensitivity of the results to the input parameters—by combining a Monte-Carlo approach with the FDTD method—was shown to yield useful results.

In the century since the first demonstration of radio-waves to carry information, a multitude of technological advancements have made wireless communications a ubiquitous part of the modern world. The increasing demand for wireless access is likely to drive technological developments in the foreseeable future. However, the propagation of radio-waves remains the integral part of any wireless technology. Propagation within buildings is difficult to model experimentally, and consequently this thesis has focused on applying computational electromagnetics to investigate and characterise the indoor radio channel. The results presented herein may find application in the deployment of existing wireless systems, or help guide the development of future technologies.

## Appendix A

# FDTD Update Equations

In the case where  $\Delta x = \Delta y = \Delta z = \Delta$ , four terms can be defined, namely

$$\begin{aligned} c_1|_{i,j,k} &= \frac{2\epsilon_0\epsilon_r|_{i,j,k} - \Delta t\sigma_{\text{E}}|_{i,j,k}}{2\epsilon_0\epsilon_r|_{i,j,k} + \Delta t\sigma_{\text{E}}|_{i,j,k}} \\ c_2|_{i,j,k} &= \frac{2\Delta t}{\Delta(2\epsilon_0\epsilon_r|_{i,j,k} + \Delta t\sigma_{\text{E}}|_{i,j,k})} \\ c_3|_{i,j,k} &= \frac{2\mu_0\mu_r|_{i,j,k} - \Delta t\sigma_{\text{M}}|_{i,j,k}}{2\mu_0\mu_r|_{i,j,k} + \Delta t\sigma_{\text{M}}|_{i,j,k}} \\ c_4|_{i,j,k} &= \frac{2\Delta t}{\Delta(2\mu_0\mu_r|_{i,j,k} + \Delta t\sigma_{\text{M}}|_{i,j,k})}, \end{aligned}$$

and the FDTD update equations can be written as

$$\begin{aligned} E_x|_{i+0.5,j,k}^{n+0.5} &= c_1|_{i+0.5,j,k} \times E_x|_{i+0.5,j,k}^{n-0.5} + c_2|_{i+0.5,j,k} \times \left[ H_z|_{i+0.5,j+0.5,k}^n \right. \\ &\quad \left. - H_z|_{i+0.5,j-0.5,k}^n - H_y|_{i+0.5,j,k+0.5}^n + H_y|_{i+0.5,j,k-0.5}^n \right] \end{aligned} \quad (\text{A.1})$$

$$\begin{aligned} E_y|_{i,j+0.5,k}^{n+0.5} &= c_1|_{i,j+0.5,k} \times E_y|_{i,j+0.5,k}^{n-0.5} + c_2|_{i,j+0.5,k} \times \left[ H_x|_{i,j+0.5,k+0.5}^n \right. \\ &\quad \left. - H_x|_{i,j+0.5,k-0.5}^n - H_z|_{i+0.5,j+0.5,k}^n + H_z|_{i-0.5,j+0.5,k}^n \right] \end{aligned} \quad (\text{A.2})$$

$$\begin{aligned} E_z|_{i,j,k+0.5}^{n+0.5} &= c_1|_{i,j,k+0.5} \times E_z|_{i,j,k+0.5}^{n-0.5} + c_2|_{i,j,k+0.5} \times \left[ H_y|_{i+0.5,j,k+0.5}^n \right. \\ &\quad \left. - H_y|_{i-0.5,j,k+0.5}^n - H_x|_{i,j+0.5,k+0.5}^n + H_x|_{i,j-0.5,k+0.5}^n \right] \end{aligned} \quad (\text{A.3})$$

$$\begin{aligned} H_x|_{i,j+0.5,k+0.5}^{n+1} &= c_3|_{i,j+0.5,k+0.5} \times H_x|_{i,j+0.5,k+0.5}^n + c_4|_{i,j+0.5,k+0.5} \times \\ &\quad \times \left[ E_y|_{i,j+0.5,k+1}^{n+0.5} - E_y|_{i,j+0.5,k}^{n+0.5} - E_z|_{i,j+1,k+0.5}^{n+0.5} + E_z|_{i,j,k+0.5}^{n+0.5} \right] \end{aligned} \quad (\text{A.4})$$

$$\begin{aligned} H_y|_{i+0.5,j,k+0.5}^{n+1} &= c_3|_{i+0.5,j,k+0.5} \times H_y|_{i+0.5,j,k+0.5}^n + c_4|_{i+0.5,j,k+0.5} \\ &\times [E_z|_{i+1,j,k+0.5}^{n+0.5} - E_z|_{i,j,k+0.5}^{n+0.5} - E_x|_{i+0.5,j,k+1}^{n+0.5} + E_x|_{i+0.5,j,k}^{n+0.5}] \end{aligned} \quad (\text{A.5})$$

$$\begin{aligned} H_z|_{i+0.5,j+0.5,k}^{n+1} &= c_3|_{i+0.5,j+0.5,k} \times H_z|_{i+0.5,j+0.5,k}^n + c_4|_{i+0.5,j+0.5,k} \\ &\times [E_x|_{i+0.5,j+1,k}^{n+0.5} - E_x|_{i+0.5,j,k}^{n+0.5} - E_y|_{i+1,j+0.5,k}^{n+0.5} + E_y|_{i,j+0.5,k}^{n+0.5}] \end{aligned} \quad (\text{A.6})$$

These equations form the basis of the FDTD method outlined in §4.2

## Appendix B

# The Uniaxial Perfectly Matched Layer

### B.1 Derivation of the Update Equations

In the frequency domain Maxwell's equations can be expressed as

$$\nabla \times \check{\mathbf{H}} = j\omega\epsilon\bar{s}\check{\mathbf{E}} \quad (\text{B.1})$$

$$\nabla \times \check{\mathbf{E}} = -j\omega\mu\bar{s}\check{\mathbf{H}}, \quad (\text{B.2})$$

where  $\check{U}$  represents a field in the frequency domain,  $j$  is the imaginary unit,  $\omega$  is natural frequency, and  $\bar{s}$  is a material tensor characterising the UPML medium.

It can be shown [11, 285–288], that defining  $\bar{s}$  as follows, specifies a simultaneously lossy, uniaxial and anisotropic medium matched to free-space in the edge and corner regions of the three dimensional computational lattice (in the main problem space  $\bar{s}$  reduces to the unit dyad):

$$\bar{s} = \begin{bmatrix} \frac{s_y s_z}{s_x} & 0 & 0 \\ 0 & \frac{s_x s_z}{s_y} & 0 \\ 0 & 0 & \frac{s_x s_y}{s_z} \end{bmatrix}, \quad (\text{B.3})$$

where  $s_x$ ,  $s_y$  and  $s_z$  are components of the diagonal elements of  $\bar{s}$ , given by

$$s_w = \kappa_w + \frac{\sigma_w}{j\omega\epsilon} \quad w \in \{x, y, z\}. \quad (\text{B.4})$$

The terms  $\kappa_w$  and  $\sigma_w$  are expressed as one-dimensional functions,

$$\kappa_w(w) = \begin{cases} \kappa'_w(w) & w \leq w_{\min}, w \geq w_{\max} \\ 1 & w_{\min} < w < w_{\max} \end{cases}$$

$$\sigma_w(w) = \begin{cases} \sigma'_w(w) & w \leq w_{\min}, w \geq w_{\max} \\ 0 & w_{\min} < w < w_{\max} \end{cases}.$$

To reduce spurious reflections at the PML interface, the UPML parameters  $\sigma'(w)$  and  $\kappa'(w)$

are graded within the PML [11, pp. 292–294] [71], starting with low values at the interface and reaching a maximum after 10–15 cells. The UPML implemented in this thesis uses polynomial grading, given by

$$\begin{aligned}\sigma'_w(w) &= \sigma_{\max} \left( \frac{w}{p} \right)^m \\ \kappa'_w(w) &= 1 + (\kappa_{\max} - 1) \left( \frac{w}{p} \right)^m,\end{aligned}$$

where  $p$  is the thickness of the UPML and  $\kappa_{\max}$  and  $\sigma_{\max}$  are the values of  $\kappa'_w(w)$  and  $\sigma'_w(w)$  on the outer boundaries respectively.

Direct substitution of (B.3) and (B.4) into (B.1) would require computationally expensive time domain convolution. The expression can be simplified by defining appropriate constitutive equations,

$$\begin{aligned}\check{D}_x &= \epsilon_0 \frac{s_z}{s_x} \check{E}_x \\ \check{D}_y &= \epsilon_0 \frac{s_x}{s_y} \check{E}_y \\ \check{D}_z &= \epsilon_0 \frac{s_y}{s_z} \check{E}_z.\end{aligned}\tag{B.5}$$

Eqn (B.1) can thus be written as

$$\begin{bmatrix} \frac{\partial \check{H}_z}{\partial y} - \frac{\partial \check{H}_y}{\partial z} \\ \frac{\partial \check{H}_z}{\partial y} - \frac{\partial \check{H}_y}{\partial z} \\ \frac{\partial \check{H}_z}{\partial y} - \frac{\partial \check{H}_y}{\partial z} \end{bmatrix} = j\omega \begin{bmatrix} s_y & 0 & 0 \\ 0 & s_z & 0 \\ 0 & 0 & s_x \end{bmatrix} \begin{bmatrix} \check{D}_x \\ \check{D}_y \\ \check{D}_z \end{bmatrix}.\tag{B.6}$$

Substituting (B.4) into (B.6) and applying the inverse Fourier transform yields

$$\begin{bmatrix} \frac{\partial H_z}{\partial y} - \frac{\partial H_y}{\partial z} \\ \frac{\partial H_z}{\partial y} - \frac{\partial H_y}{\partial z} \\ \frac{\partial H_z}{\partial y} - \frac{\partial H_y}{\partial z} \end{bmatrix} = \frac{\partial}{\partial t} \begin{bmatrix} \kappa_y & 0 & 0 \\ 0 & \kappa_z & 0 \\ 0 & 0 & \kappa_x \end{bmatrix} \begin{bmatrix} D_x \\ D_y \\ D_z \end{bmatrix} + \frac{1}{\epsilon_0} \begin{bmatrix} \sigma_y & 0 & 0 \\ 0 & \sigma_z & 0 \\ 0 & 0 & \sigma_x \end{bmatrix} \begin{bmatrix} D_x \\ D_y \\ D_z \end{bmatrix}.\tag{B.7}$$

A similar expression for the magnetic fields can be derived starting from (B.2). The set of partial differential equations (B.7) can be discretised on the Yee lattice, for example, the update equation for  $D_z$  is

$$\begin{aligned}D_z|_{i,j,k+0.5}^{n+0.5} &= \left( \frac{2\epsilon_0\kappa_x - \Delta t\sigma_x}{2\epsilon_0\kappa_x + \Delta t\sigma_x} \right) D_z|_{i,j,k+0.5}^{n-0.5} + \left( \frac{2\epsilon_0\Delta t}{2\epsilon_0\kappa_x + \Delta t\sigma_x} \right) \\ &\times \left[ \frac{H_y|_{i+0.5,j+0.5,k+0.5}^n - H_y|_{i-0.5,j+0.5,k+0.5}^n}{\Delta x} - \frac{H_x|_{i,j+0.5,k+0.5}^n - H_x|_{i,j-0.5,k+0.5}^n}{\Delta y} \right].\end{aligned}\tag{B.8}$$

The update equation for  $E_z$  is derived by substituting (B.4) in (B.5), giving

$$\left[ \kappa_z + \frac{\sigma_z}{j\omega\epsilon} \right] \check{D}_z = \epsilon_0 \left[ \kappa_y + \frac{\sigma_y}{j\omega\epsilon} \right] \check{E}_x.$$

Transforming into the time domain yields,

$$\frac{\partial}{\partial t} (\kappa_z D_z) + \frac{\sigma_z}{\epsilon} D_z = \epsilon_0 \left[ \frac{\partial}{\partial t} (\kappa_y E_z) + \frac{\sigma_y}{\epsilon} E_z \right].$$

The update equation for the  $E_z$  component is then

$$\begin{aligned} E_z|_{i,j,k+0.5}^{n+0.5} &= \left( \frac{2\epsilon_0\kappa_y - \Delta t\sigma_y}{2\epsilon_0\kappa_y + \Delta t\sigma_y} \right) E_z|_{i,j,k+0.5}^{n-0.5} + \left( \frac{1}{\epsilon(2\epsilon_0\kappa_y + \Delta t\sigma_y)} \right) \\ &\quad \times \left[ (2\epsilon_0\kappa_z + \Delta t\sigma_z) D_z|_{i,j,k+0.5}^{n+0.5} - (2\epsilon_0\kappa_z - \Delta t\sigma_z) D_z|_{i,j,k+0.5}^{n-0.5} \right]. \end{aligned} \quad (\text{B.9})$$

Similar update expressions can be derived for the remaining **E**, **D**, **H** and **B** field components and are shown in the following sections. Updating the electric fields in the UPML is now a two step process,  $D_z$  is evaluated using the adjacent magnetic fields components with (B.8), and  $E_z$  is updated using the newly calculated  $D_z$  field components with (B.9). The UPML can be reduced to two dimensions by setting  $\kappa_z = 1$ ,  $\sigma_z = 0$  and reducing all  $\frac{\partial}{\partial z}$  terms in (B.7) to zero.

It should be noted that the auxiliary fields are only required in the UPML regions [11, p. 302], and to reduce memory consumption each region should be specified separately. However it is difficult to scale this approach to three dimensions, for example, in the two dimensional case, fields for 24 auxiliary regions must be specified; in three dimensions this rises to 312. Furthermore, terminating lossy materials in the UPML requires storage of the  $U|^{n-0.5}$  and  $U|^{n-1.5}$  field components [11, 290–291], further increasing the computational overhead.

## B.2 UPML Update Equations

Defining  $\psi_w = 2\epsilon_0\kappa_w + \Delta t\sigma_w$  and  $\rho_w = 2\epsilon_0\kappa_w - \Delta t\sigma_w$ , where  $w \in \{x, y, z\}$  and  $\kappa_w$  and  $\sigma_w$  are the UPML parameters defined in section §4.3.1, allows the UPML update equations to be written as

$$\begin{aligned} D_x|_{i+0.5,j,k}^{n+0.5} &= \frac{\rho_y}{\psi_y} \times D_x|_{i+0.5,j,k}^{n-0.5} + \frac{2\epsilon_0\Delta t}{\Delta\psi_y} \times \left[ H_z|_{i+0.5,j+0.5,k}^n - H_z|_{i+0.5,j-0.5,k}^n \right. \\ &\quad \left. - H_y|_{i+0.5,j,k+0.5}^n + H_y|_{i+0.5,j,k-0.5}^n \right] \end{aligned} \quad (\text{B.10})$$

$$\begin{aligned} D_y|_{i,j+0.5,k}^{n+0.5} &= \frac{\rho_z}{\psi_z} \times D_y|_{i,j+0.5,k}^{n-0.5} + \frac{2\epsilon_0\Delta t}{\Delta\psi_z} \times \left[ H_x|_{i,j+0.5,k+0.5}^n - H_x|_{i,j+0.5,k-0.5}^n \right. \\ &\quad \left. - H_z|_{i+0.5,j+0.5,k}^n + H_z|_{i-0.5,j+0.5,k}^n \right] \end{aligned} \quad (\text{B.11})$$

$$\begin{aligned} D_z|_{i,j,k+0.5}^{n+0.5} &= \frac{\rho_x}{\psi_x} \times D_z|_{i,j,k+0.5}^{n-0.5} + \frac{2\epsilon_0\Delta t}{\Delta\psi_x} \times \left[ H_y|_{i+0.5,j,k+0.5}^n - H_y|_{i-0.5,j,k+0.5}^n \right. \\ &\quad \left. - H_x|_{i,j+0.5,k+0.5}^n + H_x|_{i,j-0.5,k+0.5}^n \right] \end{aligned} \quad (\text{B.12})$$

$$B_x|_{i,j+0.5,k+0.5}^{n+1} = \frac{\rho_y}{\psi_y} \times B_x|_{i,j+0.5,k+0.5}^n + \frac{2\epsilon_0 \Delta t}{\Delta \psi_y} \times \left[ E_y|_{i,j+0.5,k+1}^{n+0.5} - E_y|_{i,j+0.5,k}^{n+0.5} - E_z|_{i,j+1,k+0.5}^{n+0.5} + E_z|_{i,j,k+0.5}^{n+0.5} \right] \quad (\text{B.13})$$

$$B_y|_{i+0.5,j,k+0.5}^{n+1} = \frac{\rho_z}{\psi_z} \times B_y|_{i+0.5,j,k+0.5}^n + \frac{2\epsilon_0 \Delta t}{\Delta \psi_z} \times \left[ E_z|_{i+1,j,k+0.5}^{n+0.5} - E_z|_{i,j,k+0.5}^{n+0.5} - E_x|_{i+0.5,j,k+1}^{n+0.5} + E_x|_{i+0.5,j,k}^{n+0.5} \right] \quad (\text{B.14})$$

$$B_z|_{i+0.5,j+0.5,k}^{n+1} = \frac{\rho_x}{\psi_x} \times B_z|_{i+0.5,j+0.5,k}^n + \frac{2\epsilon_0 \Delta t}{\Delta \psi_x} \times \left[ E_x|_{i+0.5,j+1,k}^{n+0.5} - E_x|_{i+0.5,j,k}^{n+0.5} - E_y|_{i+1,j+0.5,k}^{n+0.5} + E_y|_{i,j+0.5,k}^{n+0.5} \right] \quad (\text{B.15})$$

$$E_x|_{i+0.5,j,k}^{n+0.5} = \frac{\rho_z}{\psi_z} E_x|_{i+0.5,j,k}^{n-0.5} + \frac{1}{\epsilon \psi_z} \times \left[ \psi_x D_x|_{i+0.5,j,k}^{n+0.5} - \rho_x D_x|_{i+0.5,j,k}^{n-0.5} \right] \quad (\text{B.16})$$

$$E_y|_{i,j+0.5,k}^{n+0.5} = \frac{\rho_x}{\psi_x} E_y|_{i,j+0.5,k}^{n-0.5} + \frac{1}{\epsilon \psi_x} \times \left[ \psi_y D_y|_{i,j+0.5,k}^{n+0.5} - \rho_y D_y|_{i,j+0.5,k}^{n-0.5} \right] \quad (\text{B.17})$$

$$E_z|_{i,j,k+0.5}^{n+0.5} = \frac{\rho_y}{\psi_y} E_z|_{i,j,k+0.5}^{n-0.5} + \frac{1}{\epsilon \psi_y} \times \left[ \psi_z D_z|_{i,j,k+0.5}^{n+0.5} - \rho_z D_z|_{i,j,k+0.5}^{n-0.5} \right] \quad (\text{B.18})$$

$$H_x|_{i,j+0.5,k+0.5}^{n+1} = \frac{\rho_z}{\psi_z} H_x|_{i,j+0.5,k+0.5}^{n-0.5} + \frac{1}{\mu \psi_z} \times \left[ \psi_x B_x|_{i,j+0.5,k+0.5}^{n+1} - \rho_x B_x|_{i,j+0.5,k+0.5}^n \right] \quad (\text{B.19})$$

$$H_y|_{i+0.5,j,k+0.5}^{n+1} = \frac{\rho_x}{\psi_x} H_y|_{i+0.5,j,k+0.5}^n + \frac{1}{\mu \psi_x} \times \left[ \psi_y B_y|_{i+0.5,j,k+0.5}^{n+1} - \rho_y B_y|_{i+0.5,j,k+0.5}^n \right] \quad (\text{B.20})$$

$$H_z|_{i+0.5,j+0.5,k}^{n+1} = \frac{\rho_y}{\psi_y} H_z|_{i+0.5,j+0.5,k}^n + \frac{1}{\mu \psi_y} \times \left[ \psi_z B_z|_{i+0.5,j+0.5,k}^{n+1} - \rho_z B_z|_{i+0.5,j+0.5,k}^n \right] \quad (\text{B.21})$$

## Appendix C

# Free-Space Calibration

### C.1 Two-Dimensions

In two-dimensional free-space, the fields predicted when exciting the FDTD lattice with a point source differ from the theoretical Green's Function (found by solving the two-dimensional scalar wave equation) by a multiplicative scaling factor,  $C$ , that depends on the frequency and cell size ( $\Delta$ ) [100]. A numerical comparison indicates that the *effective radius* of a point source is approximately  $0.2\Delta$  (over the range  $\frac{\lambda}{5} \leq \Delta \leq \frac{\lambda}{40}$ ) [11, p. 175]. The scaling factor ( $C$ ) to adjust the FDTD electric field to the theoretical values is thus [100]

$$C = \left| \frac{j}{4} H_0^{(2)}(kr_e) \right|,$$

where  $H_0^{(2)}(kr_e)$  is the two-dimensional Green's Function for free-space (Hankel Function of the second kind),  $k$  is the wavenumber and  $r_e$  the effective radius ( $r_e \approx 0.2\Delta$ ). In order to make effective comparisons between simulations run at different frequencies, lattice size and polarisation, the correction factor,  $C$ , must be applied.

### C.2 Three-Dimensions

As noted in section §5.2.2, to make appropriate comparisons against experimental measurements, the simulated field values must be converted to power (path-loss). In three-dimensions, the radiation pattern of the dipole antenna complicates a theoretical analysis of this problem. An alternative approach is to find the appropriate calibration factor via a free-space simulation. Table C.1 shows the gains required to calibrate the FDTD calculated field results to path-loss for commonly used lattice sizes and frequencies.

Table C.1: 3D FDTD Lattice Gains ( $E_z$  Source)

$f$ (GHz)	$\Delta$ (mm)	$g = G_t G_r$	$g$ (dB)
1.0	5	$1.80 \times 10^{-4}$	-37.44
	10	$1.86 \times 10^{-5}$	-47.31
1.8	5	$1.23 \times 10^{-5}$	-49.11
	10	$1.19 \times 10^{-6}$	-59.24



## Appendix D

# Including Details in the Propagation Environment

### D.1 Reinforcing Bars

Metal reinforcing bars (rebar) are often embedded within concrete structures to provide additional tensile strength; Fig. D.1(a) shows a two-dimensional arrangement of the rebar within the concrete floors. The square bars with dimensions  $A \times A$  are modelled as metal ( $\sigma_E = 10^7$  S/m), positioned in the centre of each slab and spaced  $s$  m apart. Fig. D.1(b) shows the steady-state power (for the  $E_y$  component in a  $TE_z$  lattice) recorded along a line directly under reinforced and non-reinforced floors; in this case  $A = 4$  cm,  $T = 0.30$  m and  $s = 0.75$  m. Compared to the slab-only geometry, the addition of rebar is observed to increase scattering, in particular, deeper fades are visible in the regions directly under the transmitter. Although the rebar alters the fading distributions, the dominant energy path remains propagation through the floors. Similar results are obtained when considering  $TM_z$  polarisation, or varying the dimensions and spacing. The results presented in Fig. D.1 tend to indicate the presence of metal rebar can be largely ignored in two-dimensions<sup>1</sup>. This finding agrees with previous analytical studies (Greens Function/MoM) [79] and FDTD simulations [77] of metal embedded in dielectric slabs. In both investigations it was found embedding the rebar contributes towards scatter, however, the net effect on sector-averaged fields is minimal.

### D.2 Hanging Panels

The photograph of the Engineering Tower in Fig. 6.1(a) shows large concrete panels hanging from the ends of the floors (these panels serve no structural purpose and exist purely as external decoration). The analysis presented in the section §6.2 shows that (in many circumstances) energy can propagate down the side of the building via diffraction at the edges of the floors. Hanging panels, such as those identified in Fig. 6.1(a), could perturb this mechanism, thereby altering the power received on adjacent (or nearly adjacent) floors.

Fig. D.2(a) and (b) show the steady-state  $E_z$  phase ( $TM_z$  polarisation) recorded at 1.0 GHz for diffraction over 10 concrete partial-floors (0.2 m thick, with  $\epsilon_r = 6.0$  and  $\sigma_E = 50$  mS/m)

---

<sup>1</sup>It should be noted that in reality, the rebar forms a three-dimensional mesh, and this aspect will be investigated in chapter 8.

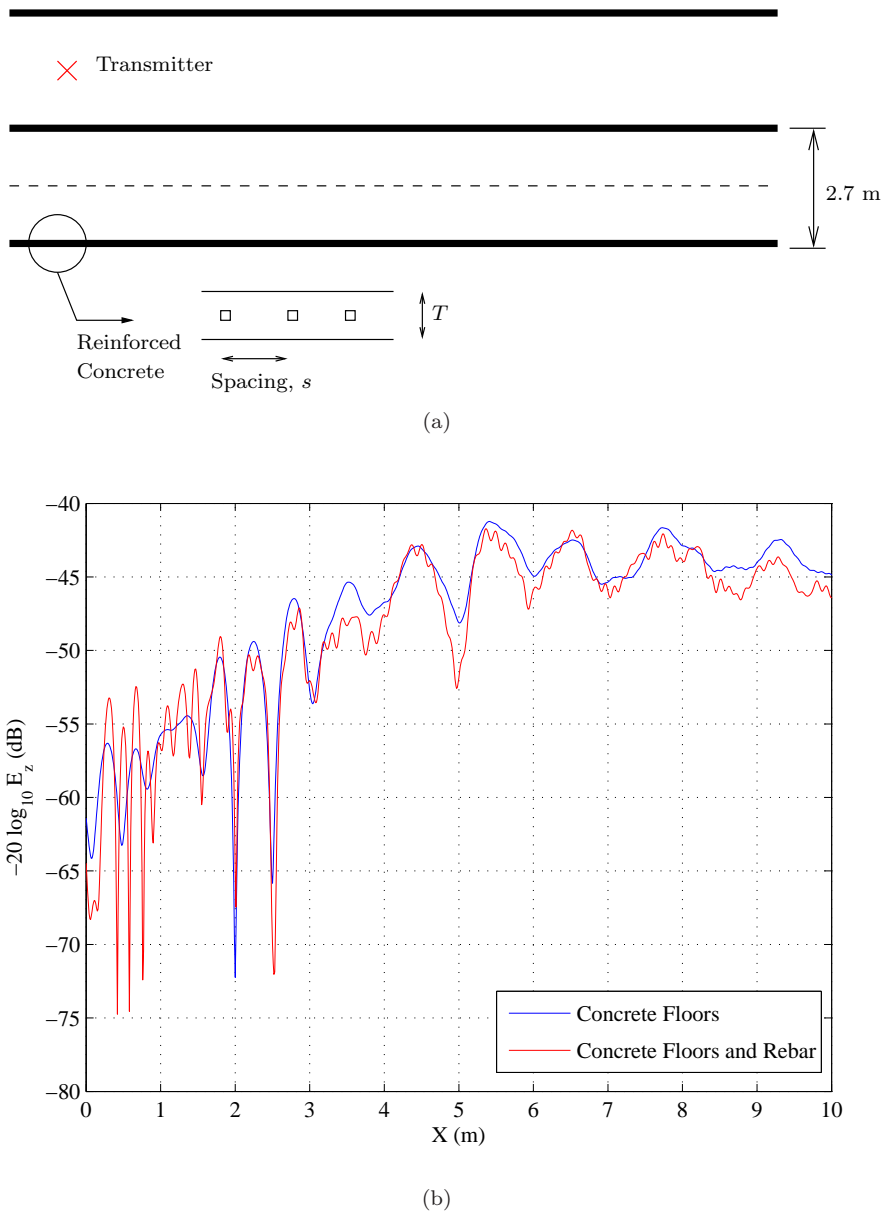


Figure D.1: (a) Depiction of the metal reinforcing bars. (b) Power (in dB) for a  $TE_z$  polarised lattice recorded along - - - with  $T = 0.30$  m and  $s = 0.75$  m.

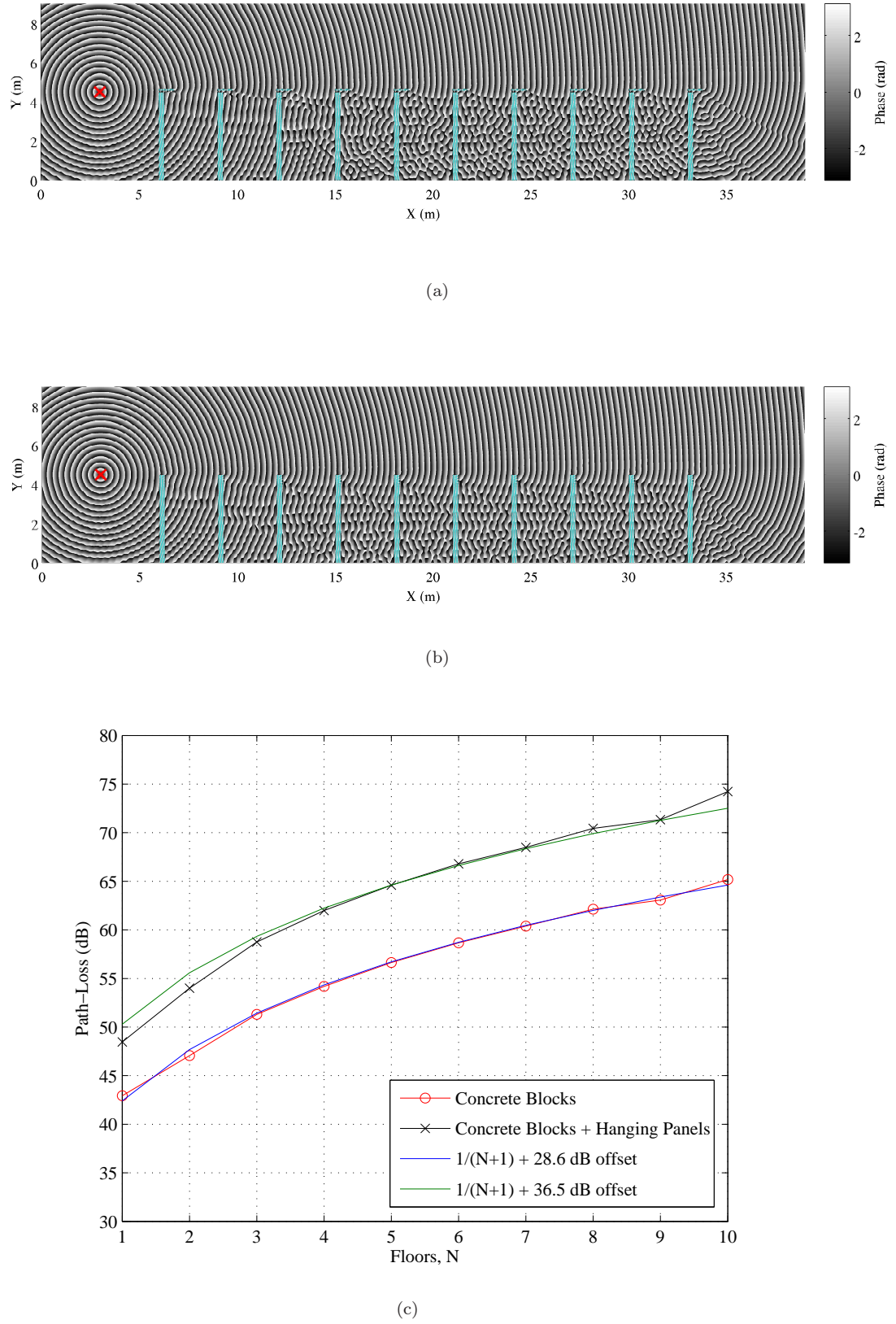


Figure D.2: (a) Steady-state  $E_z$  phase over 10 concrete floors (with hanging panels included). (b) Steady-state  $E_z$  phase without the hanging panels. (c) Steady-state two-dimensional path-loss (in dB) recorded at the tip of each floor.

with and without the hanging panels respectively<sup>2</sup>. The phase remains radially centred on the source for 1–3 floor separations; beyond three separations the radial phase pattern is distorted by the diffracted components (strong reflections from the concrete floors are also present). Diffraction at the floor vertices is less distinct when the hanging panels are included in the geometry. This finding is supported by examining the received power. Fig. D.2(b) shows a plot of the two-dimensional path-loss recorded at the top of each floor. It is observed that the panels introduce an average 7.9 dB increase in the path-loss. In both cases the FDTD simulated values agree well with the theoretical field diffracted over  $N$  identical co-linear knife edges, given by  $\frac{1}{N+1}$  [101].

---

<sup>2</sup>The FDTD simulation space is 9 m in the  $y$ -direction, as sufficient clearance over the top of the diffracting edges is needed to account for the Fresnel zones.

## Appendix E

### 2.5D Field Expansion

The high computational requirements for the three-dimensional FDTD method necessarily restricts analysis to two-dimensional geometries in many cases. However directly applying the two-dimensional FDTD method can lead to incorrect conclusions in many circumstances. For example, in three-dimensions, the Green's Function is proportional to  $\frac{1}{r}$ ; whereas, in two-dimensions, the Green's Function is proportional to  $H_0^{(2)}(kr)$  (where  $H_0^{(2)}$  is the zero-th order Hankel function of the second kind and  $k$  is the wave-number), and  $\lim_{r \rightarrow \infty} H_0^{(2)}(kr) \propto \frac{1}{\sqrt{r}}$ . Hence, the power received on longer paths (e.g. reflections from nearby buildings) will be overestimated with two-dimensional simulations.

However, the two-dimensional simulation results can be extended to pseudo-2.5D by considering isotropic spreading in the third dimension. This assumes there are no changes to the geometry in the third dimension. For the electric field, the additional divergence term is  $\frac{1}{\sqrt{d}}$ , where  $d$  is approximated from the total elapsed time,  $d = c_0 t$ . The spreading term can be incorporated into the calculation for the steady state magnitude by rewriting (5.2) as

$$U_{f_0}^{2.5D}|_{i,j,k} = U_{f_0}^{2.5D}|_{i,j,k} + \frac{u_{i,j,k}^n}{\sqrt{c_0 n \Delta t}} \exp(-j2\pi f_0 n \Delta t). \quad (\text{E.1})$$

The approach outlined in (E.1) operates in the time-domain, and consequently is very sensitive to dispersion error (particularly at longer distances). Fig. E.1 shows the steady-state path-loss calculated over a distance of 100 m in a two-dimensional  $\text{TM}_z$  FDTD lattice; the Friis equation and 2.5D FDTD expansion are also shown. It is observed, for distances greater than 3.0 m ( $10\lambda$ ), the distance dependency exponent of the 2.5D FDTD expansion approaches that of the three-dimensional Friis equation; below  $10\lambda$  near-field effects dominate.

As observed in Fig. E.1 the dispersion error manifests as an offset in the distance-dependency curve, and can be calibrated out with an appropriate test-run in free-space, similar to the procedure outlined in section §5.2.2. Furthermore, the additional divergence term will overestimate the distance, and hence attenuation, for paths passing through dielectric material<sup>1</sup>. Therefore, this approach is only strictly valid in free-space, though the error observed for paths encountering dielectric material is often small in comparison to the total path-loss.

---

<sup>1</sup>The propagation velocity decreases proportional to  $\sqrt{\epsilon_r}$ , thus increasing the time-delay, and hence the correction factor applied.

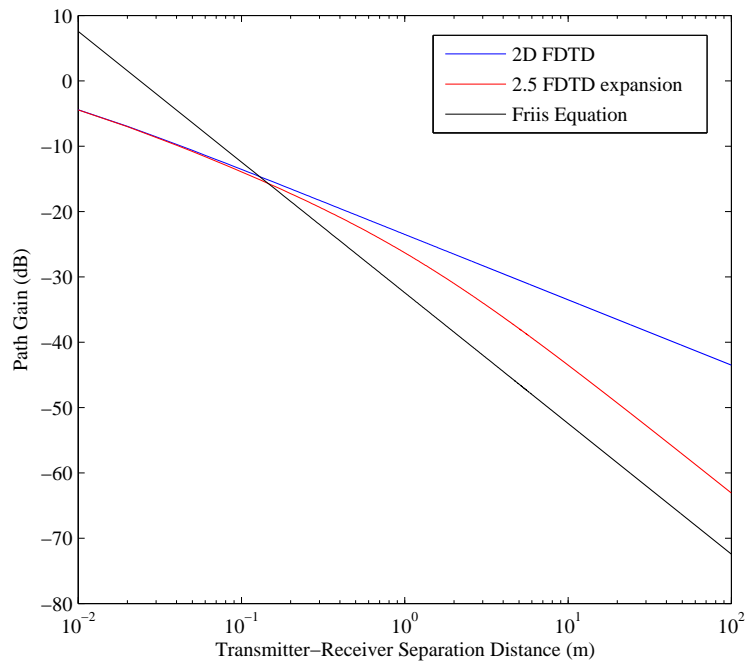


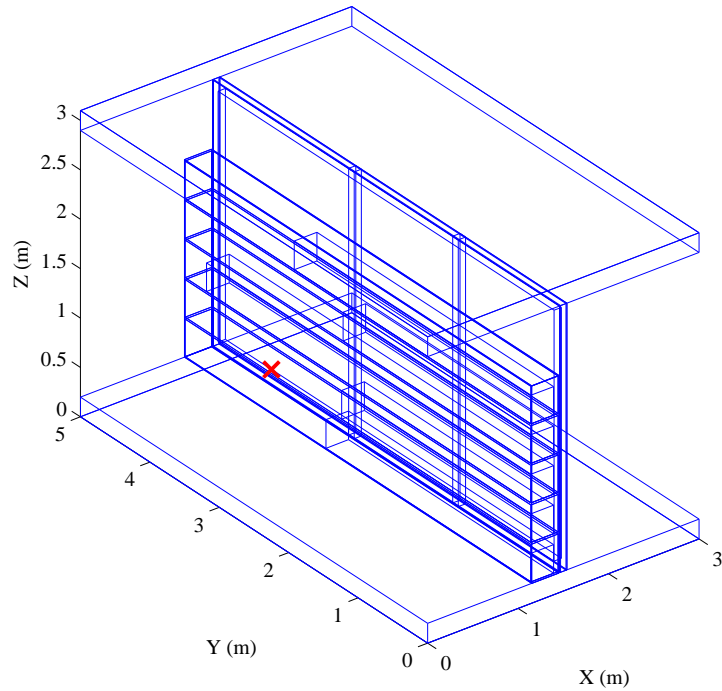
Figure E.1: Distance dependency relationships for 2D and 2.5D FDTD simulation results and the Friis equation ( $P_t = 1.0$  W) for  $f_0 = 1.0$  GHz and  $\Delta = 0.01$  m in free-space.

## Appendix F

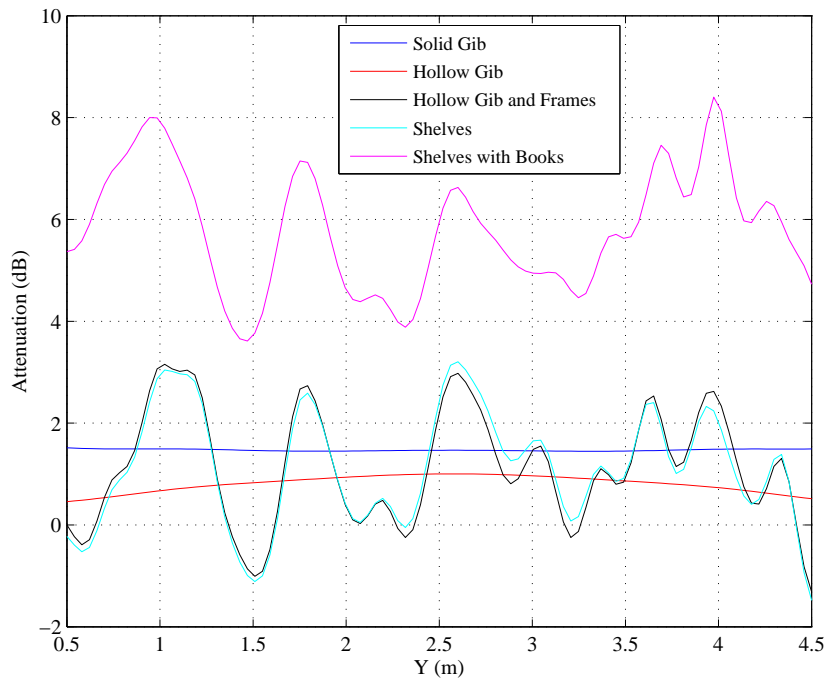
# Localised Effects of Clutter—An Illustrative Example

Fig. F.1(a) shows an illustration of the wall and clutter details considered in the detailed geometry. The path-loss from the vertically-orientated dipole source (located at  $\times$ , 1.2 m in front of the wall) is measured along a line 1.0 m behind the wall. The power is averaged over  $3\lambda$  to remove any height effects and normalised against the free-space path-loss to determine the attenuation. Fig. F.1(b) shows the attenuation introduced by various cluttered walls.

In isolation the hollow and solid partitions introduce 0.8 and 1.5 dB attenuation respectively. The lower attenuation for the hollow walls is expected given the low relative permittivity and thickness of the gib-board walls. Including the wooden frames, studs and metal shelves perturbs the fields, but this detail does not significantly alter the attenuation or the dominant energy flow through the walls. The vertical studs are observed to cast localised radio shadows behind the partition, for example, the null at  $y = 1.5$  m is caused by propagation around (and through) a vertical stud. Interesting, the behaviour introduced by the studs persist even as further details, such as the bookshelves, are added. When the lossy dielectric books are included, the average attenuation increases to 5.8 dB. These results suggest that to accurately predict propagation in the presence of clutter, some way of characterising the location and properties of the internal detail becomes increasingly important.



(a)



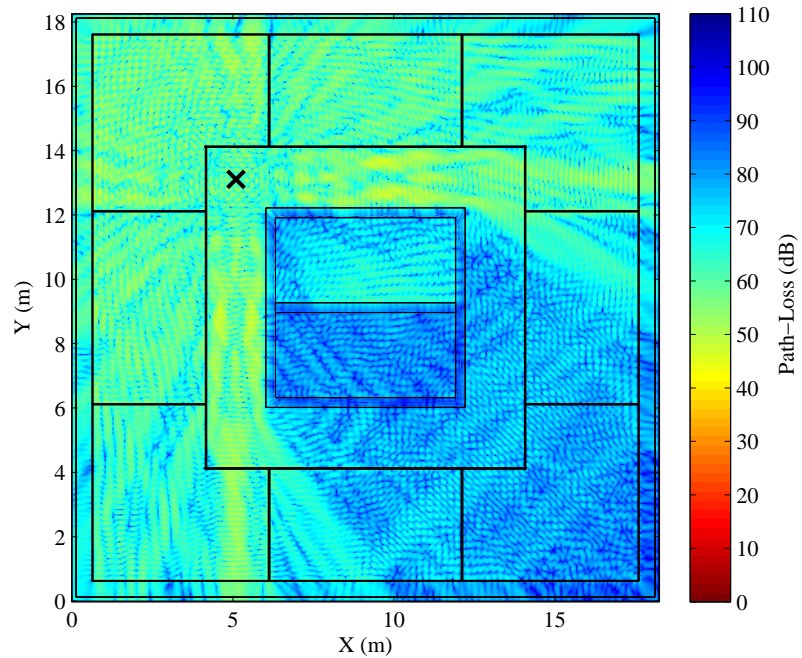
(b)

Figure F.1: (a) Illustration of the walls and bookshelves. The location of the transmitter is marked  $\times$ . (b) Attenuation (in dB) relative to free-space.

## Appendix G

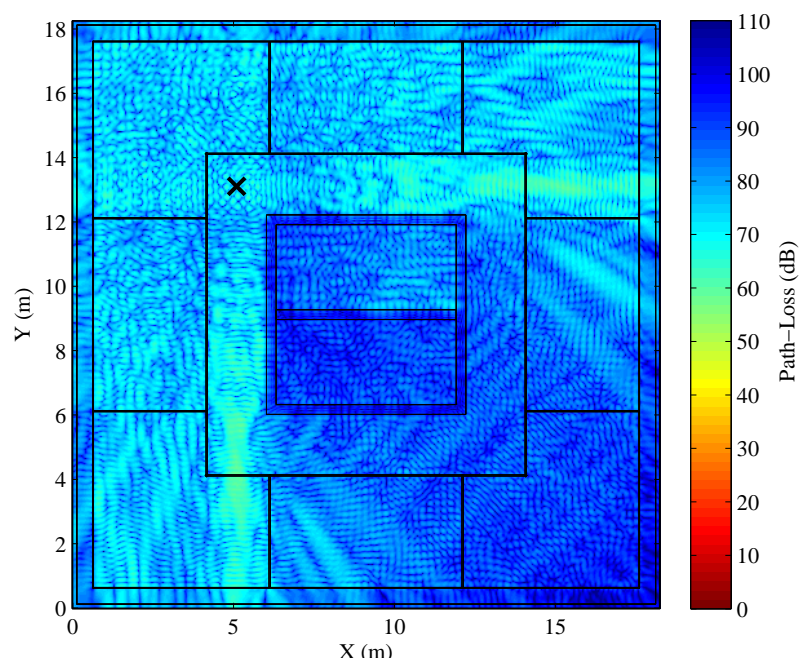
# Inter-floor Propagation: Basic Geometry

Plots of the path-loss on horizontal slices through the detailed geometry have been presented in section §8.4. This appendix presents similar slices through the path-loss for the basic internal geometry. Fig. G.1 shows the path-loss (a) one floor, and (b) two floors above the transmitter. Similar to the findings made for the detailed geometry, many of the same-floor propagation mechanisms continue to dominate when the transceiver separation is increased by one or two floors. For example, in G.1(a) and (b), strong specular reflections from the glass windows are observed, and remain the dominant propagation mechanism for regions shadowed by the services shaft.



(a) One floor above the transmitter

Figure G.1: FDTD simulated path-loss on horizontal slices through the basic geometry.



(b) Two floors above the transmitter

Figure G.1: FDTD simulated path-loss on horizontal slices through the basic geometry.

## Appendix H

# Path-Loss versus Distance

In section §8.6, it was observed that the average floor attenuation remained relatively constant propagating through either one or two floors. However, it was noted in Table 8.1 that the floor attenuation depends on the position of the transmitter relative to the receiver and the central services shaft. In particular, the additional floor attenuation decreased when propagating through two floors for points shadowed by the shaft. It was also observed that in lit regions the floor attenuation remained constant. Similar observations were also made for the experimental dataset. This appendix presents scatter plots of the path-loss versus distance, where the lit and shadowed regions have been separated.

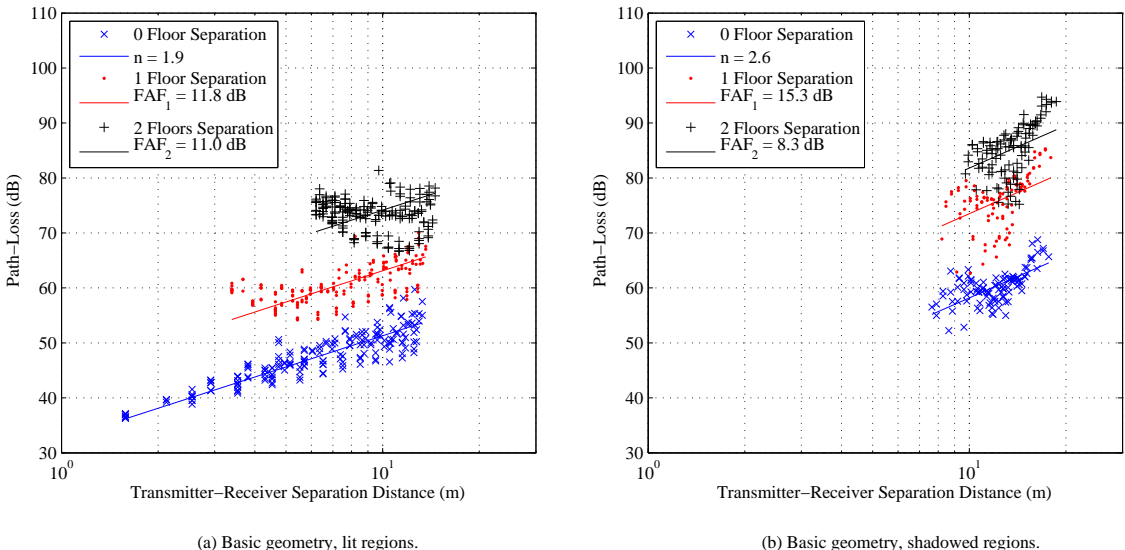
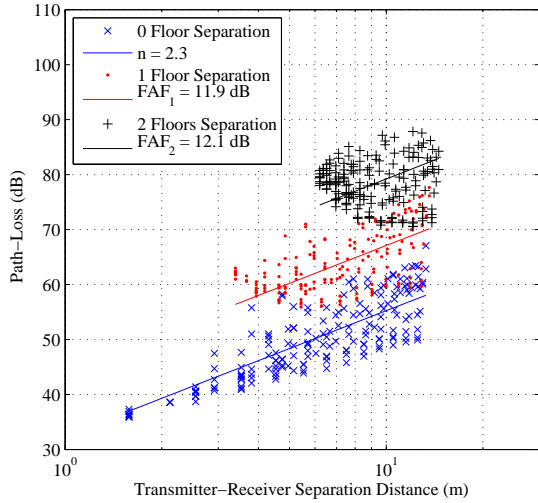
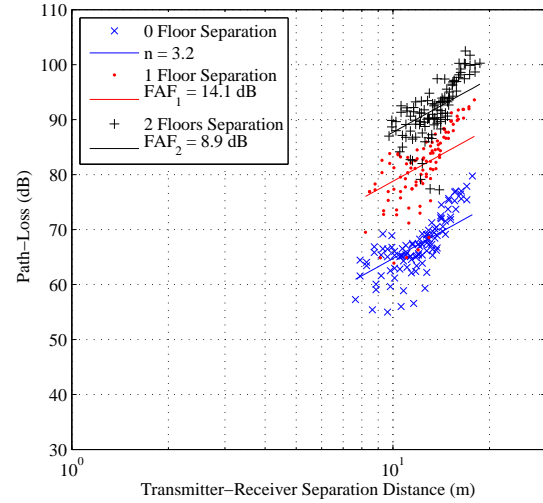


Figure H.1: Path-loss versus distance for the basic geometry. In lit regions, the FAF is constant for both floors, but is observed to decrease in the shadowed regions.

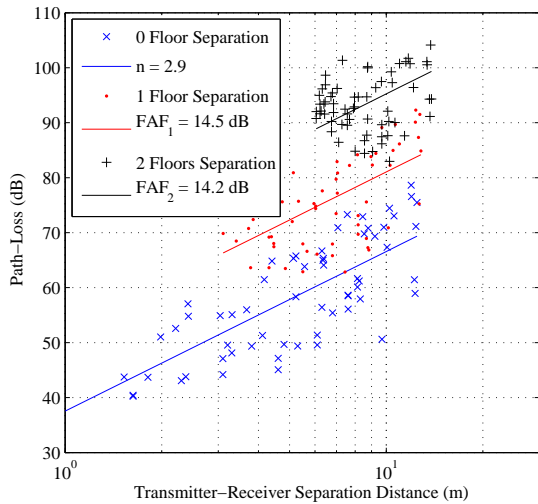


(a) Detailed geometry, lit regions.

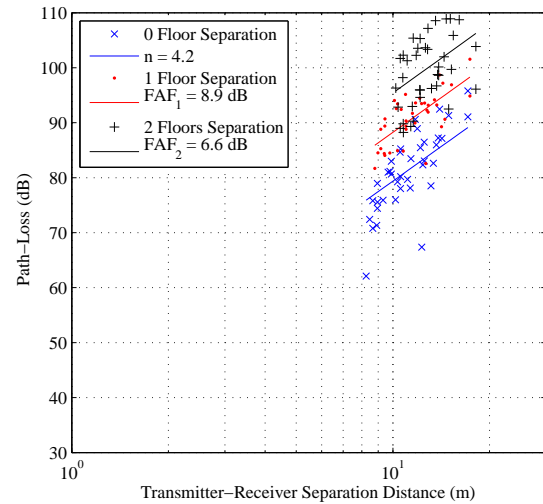


(b) Detailed geometry, shadowed regions.

Figure H.2: Path-loss versus distance for the detailed geometry. Similar to the basic geometry, the FAF decreases in the shadowed regions.



(a) Measurements, lit regions.



(b) Measurements, shadowed regions.

Figure H.3: Path-loss versus distance for 1.8 GHz experimental measurements in the Engineering tower. The decrease in FAF for shadowed regions is also observed.

## Appendix I

# Monte Carlo Sensitivity Analysis—2D Feasibility Study

As previously noted, RF propagation within buildings can be strongly affected by the geometry and material properties. The large variations in path-loss can make it difficult to develop appropriate models to characterise the indoor radio channel. One way of determining the sensitivity of the propagation model to the parameters is via a Monte Carlo analysis—where the input parameter set is varied randomly for a fixed number of trials. However, the high computational costs of the FDTD method generally restricts Monte-Carlo analysis to two-dimensions [98] at lower frequencies. In this feasibility study a two-dimensional parallel implementation of the FDTD method is used to estimate the sensitivity of a mechanistic model to variations in the material properties.

A floor plan of the geometry—identifying the concrete services shaft, glass exterior windows and gib-board internal partitions—is shown in Fig. I.1. The frequency is fixed at 1.0 GHz, and the location of the transmitter is indicated by  $\times$ . One hundred trials (for a  $\text{TM}_z$  polarised lattice) are considered, and in each case the six parameters are randomly drawn from independent uniform distributions, with the range indicated in Table I.1. The FDTD simulation of each trial requires 2.5 GB of memory, and on a parallel cluster with 20 processors allocated the wall time is 10 minutes/simulation to reach an approximate steady-state (15,000 time-steps).

Table I.1: Monte Carlo Parameters

	Range	
Concrete	$\epsilon_r$	1.0–6.0
	$\sigma_E$	0–100 mS/m
Glass	$\epsilon_r$	1.0–6.0
	$\sigma_E$	0–10 mS/m
Gib-board	$\epsilon_r$	1.0–6.0
	$\sigma_E$	0–10 mS/m

As before, the sector-averaged path-loss is calculated over a  $3\lambda \times 3\lambda$  area, and fitted to a distance dependency relationship, given by

$$PL = 10 \times n \log_{10}(d) + \beta,$$

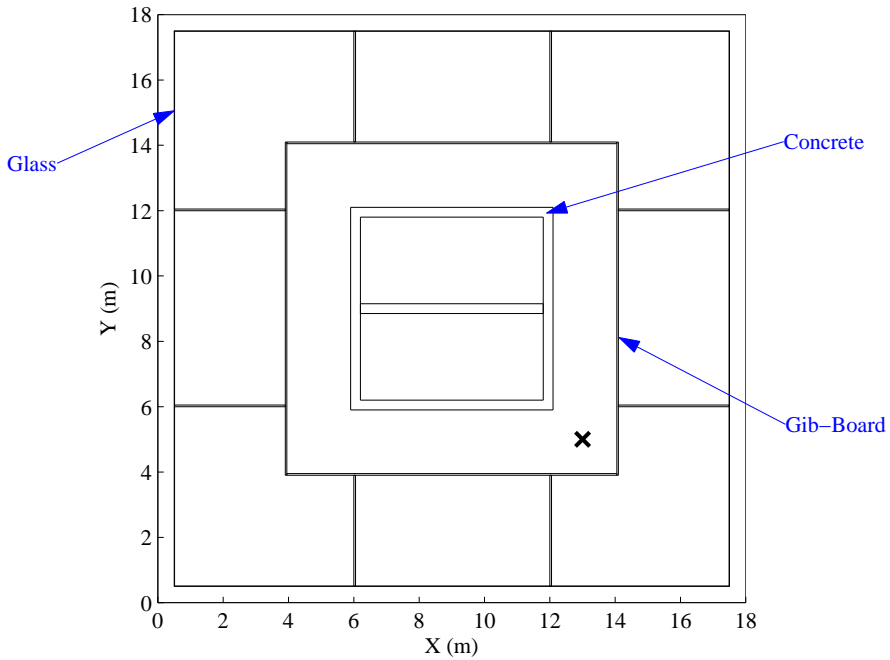


Figure I.1: Floor plan of the geometry considered with salient features labelled. The location of the transmitter is identified with  $\times$ .

where  $d$  is the transmitter-receiver separation distance,  $n$  is the distance dependency exponent, and  $\beta$  is the offset<sup>1</sup>. It should be noted that sectors located within the central services shaft have been excluded from the analysis.

Fig. I.2(a)–(f) shows scatter plots of  $n$  against the six parameters considered. It is observed that  $n$  is dependent on the glass permittivity and (to a certain extent) the concrete conductivity;  $n$  is largely independent of the other parameters. In particular,  $n$  is observed to decrease with increasing glass permittivity and increase with concrete conductivity (for  $\sigma_e < 20$  mS/m). Propagation to regions shadowed by the central services shaft is known to be strongly influenced by specular reflections from the glass. The reflection coefficient from a dielectric slab (for  $TM_z$  lattice polarisation) increases with the material permittivity [82, p. 188]. Stronger reflections deliver greater power to the shadowed regions, thereby decreasing the distance dependency exponent. Similarly, for low values of concrete conductivity, the dominant propagation path is through the services shaft. As the conductivity increases, these paths are attenuated, and  $n$  increases. However, beyond 20 mS/m,  $n$  is largely independent of the concrete conductivity (at this stage, reflections from the glass dominate propagation into the shadowed regions).

---

<sup>1</sup>In an empirical model  $\beta$  would represent the free-space loss at a reference distance from the transmitting antenna.

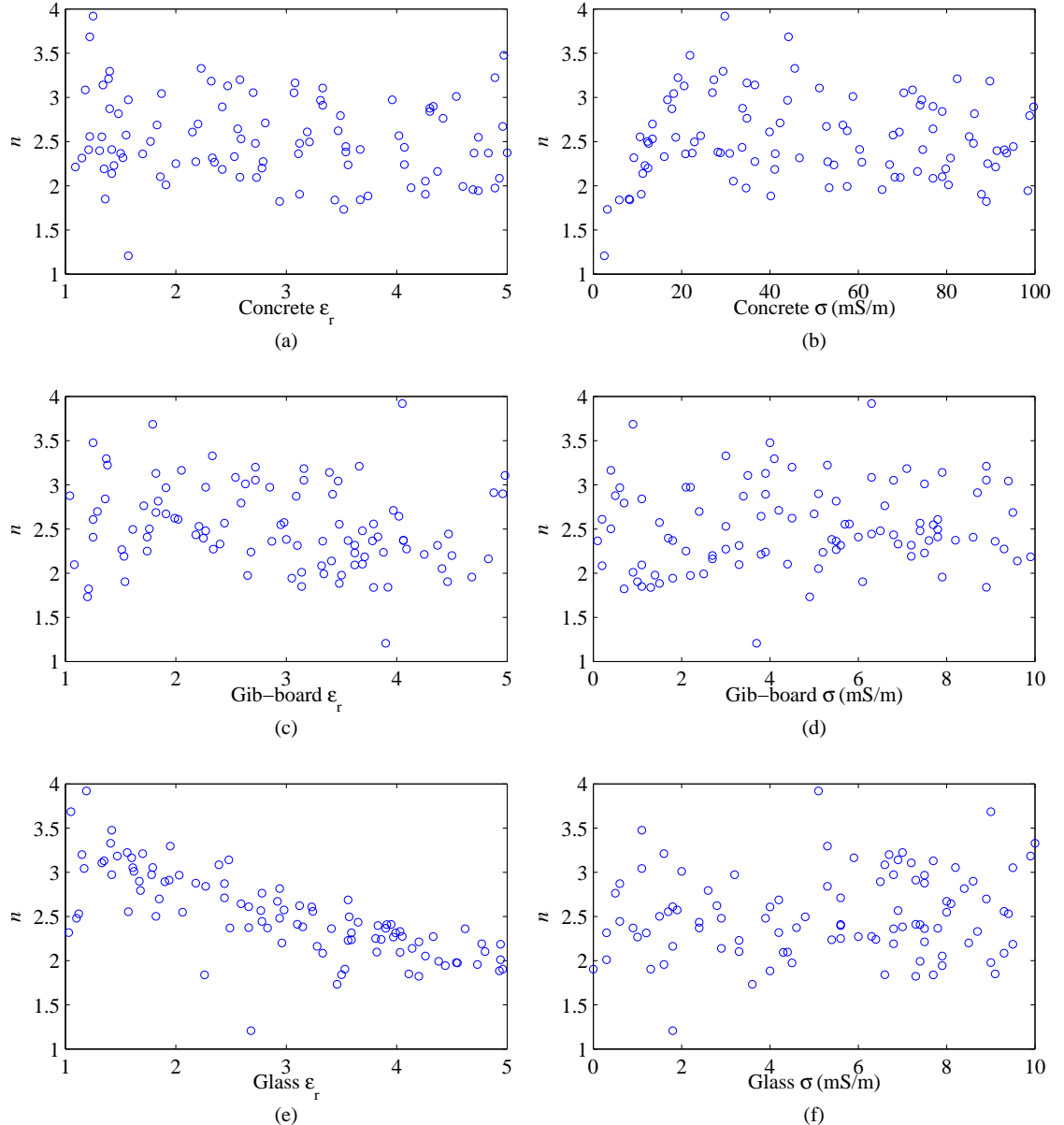


Figure I.2: Sensitivity plots of the material parameters versus  $n$ . Each  $\circ$  represents a separate trial.



# References

- [1] T. K. Sarkar, R. J. Mailloux, A. A. Oliner, M. Salazar-Palma, and D. L. Sengupta, *History of Wireless*. New Jersey: Wiley, 2006.
- [2] T. Rappaport, *Wireless Communications Principles and Practice*, 1st ed. New Jersey: Prentice-Hall, 1996.
- [3] A. Goldsmith, *Wireless Communications*. New York: Cambridge University Press, 2005.
- [4] G. L. Stüber, *Principles of Mobile Communication*, 2nd ed. Boston: Kluwer Academic Publishers, 2001.
- [5] J. Zhang and G. de la Roche, *Femtocells Technologies and Deployment*. Wiley, 2010.
- [6] K. S. Butterworth, K. W. Sowerby, and A. G. Williamson, “Base station placement for in-building mobile communication systems to yield high capacity and efficiency,” *IEEE Trans. Commun.*, vol. 48, no. 4, pp. 658–669, April 2000.
- [7] S. Y. Seidel and T. S. Rappaport, “914 MHz path loss prediction models for indoor wireless communications in multifloored buildings,” *IEEE Trans. Antennas Propag.*, vol. 40, no. 2, pp. 207–217, Feb. 1992.
- [8] J.-F. LaFortune and M. Lecours, “Measurement and modeling of propagation losses in a building at 900 MHz,” *IEEE Trans. Veh. Technol.*, vol. 39, no. 2, pp. 101–108, May 1990.
- [9] D. Fleisch, *A Student’s Guide to Maxwell’s Equations*. Cambridge: Cambridge University Press, 2008.
- [10] M. N. O. Sadiku, *Numerical Techniques in Electromagnetics*, 2nd ed. CRC Press, 2000.
- [11] A. Taflove and S. C. Hagness, *Computational Electrodynamics: The Finite-Difference Time-Domain Method*, 3rd ed. Boston: Artech House, 2005.
- [12] A. C. M. Austin, M. J. Neve, G. B. Rowe, and R. J. Pirkle, “Modeling the effects of nearby buildings on inter-floor radio-wave propagation,” *IEEE Trans. Antennas Propag.*, vol. 57, no. 7, pp. 2155–2161, July 2009.
- [13] M. J. Neve, K. W. Sowerby, A. G. Williamson, G. B. Rowe, J. C. Batchelor, and E. A. Parker, “Physical layer engineering for indoor wireless systems in the twenty-first century,” in *Proc. Loughborough Antennas Propag. Conf.*, 2010.
- [14] J. D. Parsons, *The mobile radio propagation channel*, 2nd ed. Wiley, 2000.
- [15] D. Porrat and D. C. Cox, “UHF propagation in indoor hallways,” *IEEE Trans. Wireless Commun.*, vol. 3, no. 4, pp. 1188–1198, July 2004.
- [16] P. V. Nikitin, D. D. Stancil, A. G. Cepni, O. K. Tonguz, A. E. Xhafa, and D. Brodtkorb, “Propagation model for the HVAC duct as a communication channel,” *IEEE Trans. Antennas Propag.*, vol. 51, no. 5, pp. 945–951, 2003.

- [17] R. A. Valenzuela, O. Landron, and D. L. Jacobs, "Estimating local mean signal strength of indoor multipath propagation," *IEEE Trans. Veh. Technol.*, vol. 46, no. 1, pp. 203–212, 1997.
- [18] W. Honcharenko, H. L. Bertoni, J. L. Dailing, J. Qian, and H. D. Yee, "Mechanisms governing UHF propagation on single floors in modern office buildings," *IEEE Trans. Veh. Technol.*, vol. 41, no. 4, pp. 496–504, Nov. 1992.
- [19] J. Walfisch and H. L. Bertoni, "A theoretical model of UHF propagation in urban environments," *IEEE Trans. Antennas Propag.*, vol. 36, no. 12, pp. 1788–1796, Dec. 1988.
- [20] M. J. Neve, "Mobile radio propagation prediction in built-up environments using ray-methods," Ph.D. dissertation, The University of Auckland, Auckland, New Zealand, 1992.
- [21] F. van der Wijk, A. Kegel, and R. Prasad, "Assessment of a pico-cellular system using propagation measurements at 1.9 GHz for indoor wireless communications," *IEEE Trans. Veh. Technol.*, vol. 44, no. 1, pp. 155–162, 1995.
- [22] D. C. K. Lee, M. J. Neve, and K. W. Sowerby, "The impact of structural shielding on the performance of wireless systems in a single-floor office building," *IEEE Trans. Wireless Commun.*, vol. 6, no. 5, pp. 1787–1695, May 2007.
- [23] "IEEE 802.11-2007—part 11: Wireless LAN medium access control (MAC) and physical layer (PHY) specifications," IEEE, 2007.
- [24] K. W. Sowerby and A. G. Williamson, "Outage probability calculations for multiple cochannel interferers in cellular mobile radio systems," *IEE Proc. — F*, vol. 135, no. 3, pp. 208–215, June 1988.
- [25] A. V. Pais, K. W. Sowerby, and M. J. Neve, "Outdoor-to-indoor signal correlation and its influence on indoor system performance at 2 GHz," *Electron. Lett.*, vol. 39, no. 2, pp. 236–238, 23 Jan 2003.
- [26] A. H. Wong, M. J. Neve, and K. W. Sowerby, "Performance analysis for indoor wireless systems employing directional antennas," *IEE Proc. — Commun.*, vol. 152, no. 6, pp. 890–896, 2005.
- [27] E. A. Parker, A. D. Chuprin, and R. J. Langley, "Finite element analysis of electromagnetic wave diffraction from buildings incorporating frequency selective walls," *IEE Proc. — Microw. Antennas Propag.*, vol. 146, no. 5, pp. 319–323, 1999.
- [28] M. Philippakis, C. Martel, D. Kemp, R. Allan, M. Clift, S. Massey, S. Appleton, W. Damerell, C. Burton, and E. A. Parker, "Application of FSS structures to selectively control the propagation of signals into and out of buildings," OFCOM, Tech. Rep. AY4464, March 2004.
- [29] G. H.-H. Sung, K. W. Sowerby, and A. G. Williamson, "Modeling a low-cost frequency selective wall for wireless-friendly indoor environments," *IEEE Antennas Wireless Propag. Lett.*, vol. 5, no. 1, pp. 311–314, 2006.
- [30] G. H.-H. Sung, K. W. Sowerby, M. J. Neve, and A. G. Williamson, "A frequency-selective wall for interference reduction in wireless indoor environments," *IEEE Antennas Propag. Mag.*, vol. 48, no. 5, pp. 29–37, 2006.
- [31] J. C. Vardaxoglou, *Frequency Selective Surfaces Analysis and Design*. Taunton: Research Studies Press, 1997.
- [32] Recom. ITU-R P.1238-6, "Propagation data and prediction methods for the planning of indoor radiocommunication systems and radio local area networks in the frequency range 900 MHz to 100 GHz," 2009.

- [33] K.-W. Cheung, J. H.-M. Sau, and R. D. Murch, "A new empirical model for indoor propagation prediction," *IEEE Trans. Veh. Technol.*, vol. 47, no. 3, pp. 996–1001, Aug. 1998.
- [34] A. J. Motley and J. M. P. Keenan, "Personal communication radio coverage in buildings at 900 MHz and 1700 MHz," *Electron. Lett.*, vol. 24, no. 12, pp. 763–764, 9 June 1988.
- [35] M. F. Ibrahim and J. D. Parsons, "Signal strength prediction in built up areas, part 1: Median signal strength," *IEE Proc. — F*, vol. 130, no. 5, pp. 377–391, 1983.
- [36] D. Molkdar, "Review on radio propagation into and within buildings," *IEE Proc. — H*, vol. 138, no. 1, pp. 61–73, Feb 1991.
- [37] H. Hashemi, "The indoor radio propagation channel," *Proc. IEEE*, vol. 81, no. 7, pp. 943–968, 1993.
- [38] W. Honcharenko, H. L. Bertoni, and J. Dailing, "Mechanisms governing propagation between different floors in buildings," *IEEE Trans. Antennas Propag.*, vol. 41, no. 6, pp. 787–790, June 1993.
- [39] K. S. Butterworth, K. W. Sowerby, and A. G. Williamson, "Correlated shadowing in an in-building propagation environment," *Electron. Lett.*, vol. 33, no. 5, pp. 420–422, 1997.
- [40] J. Wong, A. Mason, M. Neve, and K. Sowerby, "Base station placement in indoor wireless systems using binary integer programming," *IEE Proc. — Commun.*, vol. 153, no. 5, pp. 771–778, 2006.
- [41] A. Alighanbari and C. D. Sarris, "Rigorous and efficient time-domain modeling of electromagnetic wave propagation and fading statistics in indoor wireless channels," *IEEE Trans. Antennas Propag.*, vol. 55, no. 8, pp. 2373–2381, Aug. 2007.
- [42] S. Loredo, L. Valle, and R. P. Torres, "Accuracy analysis of GO/UTD radio-channel modeling in indoor scenarios at 1.8 and 2.5 GHz," *IEEE Antennas Propag. Mag.*, vol. 43, no. 5, pp. 37–51, 2001.
- [43] S. Y. Seidel and T. S. Rappaport, "Site-specific propagation prediction for wireless in-building personal communication system design," *IEEE Trans. Veh. Technol.*, vol. 43, no. 4, pp. 879–891, Nov. 1994.
- [44] W. K. Tam and V. N. Tran, "Propagation modelling for indoor wireless communication," *Electron. Commun. Eng. J.*, vol. 7, no. 5, pp. 221–228, 1995.
- [45] T. K. Sarkar, Z. Ji, K. Kim, A. Medouri, and M. Salazar-Palma, "A survey of various propagation models for mobile communication," *IEEE Antennas Propag. Mag.*, vol. 45, no. 3, pp. 51–82, June 2003.
- [46] H. El-Sallabi and P. Vainikainen, "Improvements to diffraction coefficient for non-perfectly conducting wedges," *IEEE Trans. Antennas Propag.*, vol. 53, no. 9, pp. 3105–3109, 2005.
- [47] K. S. Yee, "Numerical solution of initial boundary value problems involving Maxwell's Equations in isotropic media," *IEEE Trans. Antennas Propag.*, vol. 14, no. 3, pp. 302–307, 1966.
- [48] Q. H. Liu, "Large-scale simulations of electromagnetic and acoustic measurements using the pseudospectral time-domain (PSTD) algorithm," *IEEE Trans. Geosci. Remote Sens.*, vol. 37, no. 2, pp. 917–926, March 1999.
- [49] W. Yu, R. Mittra, T. Su, Y. Liu, and X. Yang, *Parallel Finite-Difference Time-Domain Method*. Boston: Artech House, 2006.
- [50] A. Lauer, A. Bahr, and I. Wolff, "FDTD simulations of indoor propagation," in *Proc. IEEE Veh. Technol. Soc. Conf.*, 1994, pp. 883–886.

- [51] A. Lauer, I. Wolff, A. Bahr, J. Pamp, and J. Kunisch, "Multi-mode FDTD simulations of indoor propagation including antenna properties," in *Proc. IEEE Veh. Technol. Soc. Conf.*, 1995, pp. 454–458.
- [52] Y. Wang, S. Safavi-Naeini, and S. K. Chaudhuri, "A hybrid technique based on combining ray tracing and FDTD methods for site-specific modeling of indoor radio wave propagation," *IEEE Trans. Antennas Propag.*, vol. 48, no. 5, pp. 743–754, 2000.
- [53] Y. Wang, S. K. Chaudhuri, and S. Safavi-Naeini, "An FDTD/ray-tracing analysis method for wave penetration through inhomogeneous walls," *IEEE Trans. Antennas Propag.*, vol. 50, no. 11, pp. 1598–1604, 2002.
- [54] Z. Yun, M. F. Iskander, and Z. Zhang, "Complex-wall effect on propagation characteristics and MIMO capacities for an indoor wireless communication environment," *IEEE Trans. Antennas Propag.*, vol. 52, no. 4, pp. 914–922, April 2004.
- [55] T. M. Schäfer and W. Wiesbeck, "Simulation of radiowave propagation in hospitals based on FDTD and ray-optical methods," *IEEE Trans. Antennas Propag.*, vol. 53, no. 8, pp. 2381–2388, Aug. 2005.
- [56] T. T. Zygoridis, E. P. Kosmidou, K. P. Prokopidis, N. V. Kantartzis, C. S. Antonopoulos, K. I. Petras, and T. D. Tsiboukis, "Numerical modeling of an indoor wireless environment for the performance evaluation of WLAN systems," *IEEE Trans. Magn.*, vol. 42, no. 4, pp. 839–842, April 2006.
- [57] Y. Zhao, Y. Hao, and C. Parini, "FDTD characterization of UWB indoor radio channel including frequency dependent antenna directivities," *IEEE Antennas Wireless Propag. Lett.*, vol. 6, pp. 191–194, 2007.
- [58] A. Alighanbari and C. D. Sarris, "Parallel time-domain full-wave analysis and system-level modeling of ultrawideband indoor communication systems," *IEEE Trans. Antennas Propag.*, vol. 57, no. 1, pp. 231–240, Jan. 2009.
- [59] M. Thiel and K. Sarabandi, "A hybrid method for indoor wave propagation modeling," *IEEE Trans. Antennas Propag.*, vol. 56, no. 8, pp. 2703–2709, Aug. 2008.
- [60] ———, "3D-wave propagation analysis of indoor wireless channels utilizing hybrid methods," *IEEE Trans. Antennas Propag.*, vol. 57, no. 5, pp. 1539–1546, 2009.
- [61] M. L. Stowell, B. J. Fasenfest, and D. A. White, "Investigation of radar propagation in buildings: A 10-billion element cartesian-mesh FETD simulation," *IEEE Trans. Antennas Propag.*, vol. 56, no. 8, pp. 2241–2250, Aug. 2008.
- [62] E. C. K. Lai, M. J. Neve, and A. G. Williamson, "Identification of dominant propagation mechanisms around corners in a single-floor office building," in *Proc. IEEE APS/URSI Int. Symp.*, 2008, pp. 424–427.
- [63] A. C. M. Austin, M. J. Neve, and G. B. Rowe, "Modelling inter-floor radio-wave propagation in office buildings," in *Proc. IEEE APS/URSI Int. Symp.*, 2008, pp. 392–395.
- [64] ———, "Modelling interference for indoor wireless systems using the FDTD method," in *Proc. IEEE APS/URSI Int. Symp.*, 2009, pp. 3231–3234.
- [65] D. Ullmo and H. U. Baranger, "Wireless propagation in buildings: a statistical scattering approach," *IEEE Trans. Veh. Technol.*, vol. 48, no. 3, pp. 947–955, May 1999.
- [66] F. Ikegami and S. Yoshida, "Analysis of multipath propagation structure in urban mobile radio environments," *IEEE Trans. Antennas Propag.*, vol. 28, no. 4, pp. 531–537, Jul 1980.

- [67] F. Ikegami, S. Yoshida, T. Takeuchi, and M. Umehira, "Propagation factors controlling mean field strength on urban streets," *IEEE Trans. Antennas Propag.*, vol. 32, no. 8, pp. 822–829, 1984.
- [68] A. Taflove and M. E. Brodwin, "Numerical solution of steady-state electromagnetic scattering problems using the time-dependent Maxwell's equations," *IEEE Trans. Microw. Theory Tech.*, vol. 23, no. 8, pp. 623–630, 1975.
- [69] C. L. Wagner and J. B. Schneider, "Divergent fields, charge, and capacitance in FDTD simulations," *IEEE Trans. Microw. Theory Tech.*, vol. 46, no. 12, pp. 2131–2136, 1998.
- [70] G. Mur, "Absorbing boundary conditions for the finite-difference approximation of the time-domain electromagnetic-field equations," *IEEE Trans. Electromagn. Compat.*, no. 4, pp. 377–382, 1981.
- [71] J.-P. Berenger, "A perfectly matched layer for the absorption of electromagnetic waves," *J. Comput. Phys.*, vol. 114, pp. 185–200, 1994.
- [72] R. Mittra and U. Pekel, "A new look at the perfectly matched layer (PML) concept for the reflectionless absorption of electromagnetic waves," *IEEE Microw. Guided Wave Lett.*, vol. 5, no. 3, pp. 84–86, 1995.
- [73] S. D. Gedney, "An anisotropic perfectly matched layer-absorbing medium for the truncation of FDTD lattices," *IEEE Trans. Antennas Propag.*, vol. 44, no. 12, pp. 1630–1639, Dec. 1996.
- [74] "MPICH2: High-performance and widely portable MPI," March 2010, <http://www.mcs.anl.gov/research/projects/mpich2/>.
- [75] H. Landstorfer, H. Liska, H. Meinke, and B. Müller, "Energiestromung in elektromagnetischen wellenfeldern," *Nachrichtentechnische Zeitschrift*, vol. 25, no. 5, pp. 225–231, 1972, (in German). English Translation: "Energy Flow in Electromagnetic Wave Fields," *NASA Technical Translation*, NASA TT F-15,955. Oct. 1974.
- [76] J. F. Nye, G. Hygate, and W. Laing, "Energy streamlines: A way of understanding how horns radiate backwards," *IEEE Trans. Antennas Propag.*, vol. 42, no. 9, pp. 1250–1256, Sep. 1994.
- [77] R. A. Dalke, C. L. Holloway, P. McKenna, M. Johansson, and A. S. Ali, "Effects of reinforced concrete structures on RF communications," *IEEE Trans. Electromagn. Compat.*, vol. 42, no. 4, pp. 486–496, Nov. 2000.
- [78] A. Safaai-Jazi, S. M. Riad, A. Muqabel, and A. Bayram, "Through-the-wall propagation and material characterization," Virginia Polytechnic Institute and State University, Tech. Rep., 2002.
- [79] R. Paknys, "Reflection and transmission by reinforced concrete — numerical and asymptotic analysis," *IEEE Trans. Antennas Propag.*, vol. 51, no. 10, pp. 2852–2861, Oct. 2003.
- [80] O. Landron, M. Feuerstein, and T. Rappaport, "A comparison of theoretical and empirical reflection coefficients for typical exterior wall surfaces in a mobile radio environment," *IEEE Trans. Antennas Propag.*, vol. 44, no. 3, pp. 341–351, 1996.
- [81] G. Daian, A. Taube, A. Birnboim, M. Daian, and Y. Shramkov, "Modeling the dielectric properties of wood," *Wood Science and Technology*, vol. 40, no. 3, pp. 237–246, 2006.
- [82] C. A. Balanis, *Advanced Engineering Electromagnetics*. New York: John Wiley, 1989.
- [83] S. Y. Tan, M. Y. Tan, and H. S. Tan, "Multipath delay measurements and modeling for interfloor wireless communications," *IEEE Trans. Veh. Technol.*, vol. 49, no. 4, pp. 1334–1341, July 2000.

- [84] S. Y. Seidel, T. S. Rappaport, M. J. Feuerstein, K. L. Blackard, and L. Grindstaff, “The impact of surrounding buildings on propagation for wireless in-building personal communications system design,” in *Proc. IEEE Veh. Technol. Soc. Conf.*, 10–13 May 1992, pp. 814–818.
- [85] J. Medbo and J.-E. Berg, “Spatio-temporal channel characteristics at 5 GHz in a typical office environment,” in *Proc. IEEE Veh. Technol. Soc. Conf.*, vol. 3, 7–11 Oct. 2001, pp. 1256–1260.
- [86] M. J. Neve and G. B. Rowe, “Contributions towards the development of a UTD-based model for cellular radio propagation prediction,” *IEE Proc. — Microw. Antennas Propag.*, vol. 141, no. 5, pp. 407–414, Oct. 1994.
- [87] ——, “Mobile radio propagation prediction in irregular cellular topographies using ray methods,” *IEE Proc. — Microw. Antennas Propag.*, vol. 142, no. 6, pp. 447–451, Dec 1995.
- [88] D. A. McNamara, C. W. I. Pistorius, and J. A. G. Malherbe, *Introduction to the Uniform Geometrical Theory of Diffraction*. London: Artech House, 1990.
- [89] R. J. Pirkle and G. D. Durgin, “Optimal sliding correlator channel sounder design,” *IEEE Trans. Wireless Commun.*, vol. 7, no. 9, pp. 3488–3497, 2008.
- [90] S. Namik, K. W. Sowerby, and M. J. Neve, “OFDM-OFDM interference analysis in in-building wireless environments,” in *Proc. Virg. Tech. Symp. on Wireless Pers. Comm.*, June 2008.
- [91] A. V. Pais, K. W. Sowerby, and M. J. Neve, “Implications of power control and successive interference cancellation on indoor DS-CDMA system deployment and performance,” *IEEE Commun. Lett.*, vol. 9, no. 3, pp. 204–206, March 2005.
- [92] L. B. Milstein, T. S. Rappaport, and R. Barghouti, “Performance evaluation for cellular CDMA,” *IEEE J. Sel. Areas Commun.*, vol. 10, no. 4, pp. 680–689, May 1992.
- [93] W. C. Jakes, *Microwave Mobile Communications*. John Wiley & Sons Inc, 1975.
- [94] Z. Yun, S. Lim, and M. F. Iskander, “An integrated method of ray tracing and genetic algorithm for optimizing coverage in indoor wireless networks,” *IEEE Antennas Wireless Propag. Lett.*, vol. 7, pp. 145–148, 2008.
- [95] K. Frampton, *Modern Architecture: A Critical History*, 4th ed. London: Thames and Hudson, 2007.
- [96] J.-P. Berenger, “A Huygens subgridding for the FDTD method,” *IEEE Trans. Antennas Propag.*, vol. 54, no. 12, pp. 3797–3804, 2006.
- [97] Y. Liu, C. D. Sarris, and G. V. Eleftheriades, “Triangular-mesh-based FDTD analysis of two-dimensional plasmonic structures supporting backward waves at optical frequencies,” *J. Lightw. Technol.*, vol. 25, no. 3, pp. 938–945, March 2007.
- [98] F. Hastings, J. Schneider, and S. Broschat, “A Monte-Carlo FDTD technique for rough surface scattering,” *IEEE Trans. Antennas Propag.*, vol. 43, no. 11, pp. 1183–1191, 1995.
- [99] R. S. Edwards, A. C. Marvin, and S. J. Porter, “Uncertainty analyses in the finite-difference time-domain method,” *IEEE Trans. Electromagn. Compat.*, vol. 52, no. 1, pp. 155–163, Feb. 2010.
- [100] G. Waldschmidt and A. Taflove, “The determination of the effective radius of a filamentary source in the FDTD mesh,” *IEEE Microw. Guided Wave Lett.*, vol. 10, no. 6, pp. 217–219, June 2000.
- [101] J. H. Whitteker, “Near-field ray calculation for multiple knife-edge diffraction,” *Radio Sci.*, vol. 19, no. 4, pp. 975–986, 1984.